



Technische Universität München
TUM School of Natural Sciences

Electromagnetic moments of neutral spin-1/2 particles in general renormalizable models

Merlin Emanuel Reichard

Vollständiger Abdruck der von der TUM School of Natural Sciences der Technischen Universität München zur Erlangung des akademischen Grades eines

Doktors der Naturwissenschaften

genehmigten Dissertation.

Vorsitz: Prof. Dr. Laura Fabbietti

Prüfer der Dissertation: 1. Prof. Dr. Alejandro Ibarra
2. Priv.-Doz. Dr. Mathias Garny

Die Dissertation wurde am 21.03.2025 bei der Technischen Universität München eingereicht und durch die TUM School of Natural Sciences am 07.05.2025 angenommen.

Abstract

Dark matter (DM) resembles a big puzzle in physics, whose origin and interactions are mostly unknown. In this dissertation, we investigate the case of electromagnetically interacting spin-1/2 DM candidates, focusing on the theory predictions of these interactions and their role in direct detection experiments. We calculate the electromagnetic (EM) moments of neutral spin-1/2 fermions at the one-loop level for scalar- and vector portals to the Standard Model (SM), finding compact expressions applicable to arbitrary Dirac- or Majorana particles. We apply these formulas to the archetypical Majorana DM candidate, the lightest neutralino, for different assumptions on the supersymmetric particle spectrum. Using the DM non-relativistic effective field theory, we formulate the signal rate at the detector in a factorized way, separating the ultraviolet physics from the experimental details. This concise formulation is employed to translate the constraints on the effective operators to the parameter space of a Dirac toy model. We find that direct detection experiments provide robust exclusion limits, especially for CP violation in the dark sector. Finally, we apply the model-independent expressions of the EM moments to neutrinos, for which we calculate the contribution from various extensions of the SM.

Zusammenfassung

Dunkle Materie (DM) stellt ein großes Rätsel in der Physik dar, deren Ursprung und Wechselwirkungen weitgehend unbekannt sind. In dieser Dissertation untersuchen wir den Fall von elektromagnetisch wechselwirkenden spin-1/2 Kandidaten für DM, wobei wir uns auf die theoretischen Vorhersagen dieser Wechselwirkungen und ihre Rolle bei Experimenten zum direkten Nachweis von DM konzentrieren. Wir berechnen die elektromagnetischen (EM) Momente von neutralen spin-1/2 Fermionen auf dem Einschleifenniveau für Skalar- und Vektorportale zum Standardmodell (SM) und finden kompakte Ausdrücke, die für beliebige Dirac- oder Majorana-Teilchen gelten. Wir wenden diese Formeln auf den archetypischen Majorana DM Kandidaten, das leichteste Neutralino, für verschiedene Annahmen über das supersymmetrische Teilchenspektrum an. Unter Verwendung der nichtrelativistischen effektiven Feldtheorie der DM formulieren wir die Signalrate am Detektor in einer faktorisierten Weise, die die ultraviolette Physik von den experimentellen Details trennt. Diese prägnante Formulierung wird verwendet, um die Beschränkungen für die effektiven Operatoren in den Parameterraum eines Dirac-Spielzeugmodells zu übertragen. Wir stellen fest, dass Experimente zum direkten Nachweis von DM robuste Ausschlussgrenzen liefern, insbesondere für CP-Verletzung im dunklen Sektor. Schließlich wenden wir die modellunabhängigen Ausdrücke der EM Momente auf Neutrinos an, für die wir den Beitrag von verschiedenen Erweiterungen des SM berechnen.

Publication List

This dissertation extends some of the ideas and results of

- [1] Merlin Emanuel Reichard. »Anapole Moment of Majorana Fermions and Implications for Direct Detection of Neutralino Dark Matter«. MA thesis. Garching, Germany: Technische Universität München, 2021.

Parts of the results presented in this dissertation have been published as

- [2] Alejandro Ibarra, Merlin Reichard and Ryo Nagai. »Anapole moment of Majorana fermions and implications for direct detection of neutralino dark matter«. In: *JHEP* 01 (2023), p. 086. DOI: 10.1007/JHEP01(2023)086. arXiv: 2207.01014 [hep-ph].
- [3] Alejandro Ibarra, Merlin Reichard and Gaurav Tomar. »Probing dark matter electromagnetic properties in direct detection experiments«. In: *JCAP* 02 (2025), p. 072. DOI: 10.1088/1475-7516/2025/02/072. arXiv: 2408.15760 [hep-ph].

Acknowledgements

I want to thank Alejandro Ibarra for the supervision, collaboration, and guidance over the past few years, which helped me grow academically, professionally, and personally.

Further, I want to thank Ryo Nagai and Gaurav Tomar for our enjoyable and successful collaborations, where I could enjoy the positive aspects of collaborative science. Also, I would like to thank Motoko Fujiwara, Lukas Treuer, and Onur Yonar for our interesting discussions over the last few years. Further, I would like to thank Yu Chen, Martin Napetschnig, Tommaso Scirpa, and all other members of the TUM HEP community for the coffee breaks, discussions, and rounds of table tennis we enjoyed together. Also, thanks to Michael and Anton for helping me understand the basic notions of physics during my Bachelor's degree.

On a personal note, I sincerely thank my father, Christian, for inspiring me to study Nature and supporting me in my physics journey, and my mother, Gabriele, for the never-ending support. Thanks to ICE for staying at my side and to Marvin and Axel for lending me an open ear over the last decades.

Contents

Publication List	v
1 Introduction	1
2 Dark matter: evidence, production and search avenues	5
2.1 Observational evidence	5
2.2 Production mechanisms	13
2.3 Non-gravitational search efforts	16
3 Electromagnetic moments of neutral spin-1/2 fermions	27
3.1 Electromagnetic moments in particle physics	27
3.2 Warm-up: diagonal electromagnetic moments	30
3.3 General electromagnetic moments of fermions	41
3.4 Numerical analysis of the general loop functions	44
4 Direct detection of dark matter with electromagnetic moments	53
4.1 Electromagnetic interactions I: simplified approach	53
4.2 Non-relativistic effective field theory	55
4.3 Electromagnetic interactions II: within the effective field theory	58
5 The lightest neutralino as an archetype of Majorana fermions	71
5.1 Supersymmetry in a nutshell	71
5.2 Particle content of the minimal supersymmetric standard model	73
5.3 Anapole moment of the lightest neutralino	78
5.4 Analysis for simplified particle spectra	81
5.5 Analysis within the full MSSM	87
6 Dirac dark matter with electromagnetic moments	91
6.1 The Dirac dark matter toy model	91
6.2 Constraints from direct detection signals	95
6.3 Constraints on the thermal relic	102
7 Electromagnetic moments of neutrinos	107
7.1 General remarks about neutrino electromagnetic moments	107
7.2 Neutrino electromagnetic moments within the SM	111

7.3	Neutrino electromagnetic moments beyond the SM	119
8	Summary and conclusions	141
A	Derivation of exclusion limits	145
A.1	XENON1T, PICO-60 and LZ	145
A.2	DarkSide-50	147
B	Analytical expressions for the loop functions of the EM moments	151
B.1	The general loop functions	151
B.2	Limit of identical external states	162
B.3	Large mass splitting between external states	163
B.4	Light external mass limit	165
C	Electromagnetic- vs. hypercharge moments	169
	Bibliography	173

Chapter 1

Introduction

The nature of dark matter (DM) remains one of the central unresolved questions in astrophysics and cosmology. Observations at galactic and cosmological scales indicate that most of the matter in our Universe is non-baryonic. However, direct evidence for its non-gravitational interactions is still lacking. Many proposed ideas attempt to explain the DM conundrum, ranging from incredibly light bosons that behave like waves to particles that interact weakly with ordinary matter and even to massive primordial black holes that can weigh as much as the Sun. This wide variety of possibilities underscores our limited understanding of DM.

As a result, various search strategies are employed to investigate this expansive landscape of models and ideas. For particle DM, these efforts include studying the byproducts of particle collisions at colliders, examining cosmic rays from both galactic and extragalactic sources, and measuring DM-induced recoil signatures in dedicated shielded underground laboratories.

Historically, one of the most studied candidates for DM has been the weakly interacting massive particle (WIMP). This hypothetical particle is expected to interact through weak-scale couplings and elegantly explains the observed abundance of DM through a process known as the “freeze-out” mechanism. WIMPs naturally emerge in several reasonable extensions of the Standard Model (SM), such as supersymmetry. However, numerous state-of-the-art direct detection experiments, including XENONnT, LUX-ZEPLIN, PandaX, and DarkSide-50, have not detected a conclusive WIMP signal. This lack of evidence challenges the minimal top-down paradigm and motivates alternative avenues.

More recent searches target lower-mass WIMPs, employing novel detection techniques—such as semiconductors or the Migdal effect—to access previously untested parameter space. Theoretical models have also broadened, encompassing ideas like boosted DM, multi-component scenarios, and interactions that do not necessarily rely on weak-scale couplings. An effective field theory (EFT) approach has become especially popular, as it parameterizes possible DM–SM interactions through higher-dimensional operators and thus allows model-independent analyses from a bottom-up perspective.

One intriguing possibility is that DM interacts indirectly, although very weakly,

with photons. Depending on the spin of the DM particle, quantum effects can give rise to various electromagnetic (EM) moments beyond a simple electric charge. If the particle is self-conjugate (for example, a Majorana fermion), only certain EM moments are permitted. This introduces the potential to differentiate between Dirac- and Majorana DM candidates.

These EM moments can be explicitly calculated within specific ultraviolet (UV) models, establishing a connection between the low-energy phenomenology characterized by the EM moments of DM and the fundamental UV model. While many searches focus on one dominant EM interaction at a time, these UV completions often generate multiple EM moments. This situation necessitates a more comprehensive approach to the EFT of electromagnetically interacting DM to effectively compare theoretical predictions with experimental results.

Neutrinos, which are part of the SM, present a parallel case. Their small but non-zero masses imply physics beyond the SM, and a key question is whether they are Majorana- or Dirac fermions. Unlike DM, some neutrino EM moments are predicted within the SM, which might be detected through scattering experiments or astrophysical observations. The Dirac- or Majorana nature of neutrinos again dictates which EM moments can appear, such that an experimental signature of neutrino EM moments could indicate their nature and, therefore, help us understand the mechanism of neutrino mass generation. Further, from a theoretical point of view, many models can increase the EM properties of the neutrinos, such that an observation deviating from the SM prediction would be a clear indication of new physics. Therefore, understanding the theoretical foundations governing these interactions is fundamental to correctly interpreting a possible signal.

This work explores the scenario of electromagnetically interacting DM and the theory prediction for the neutrino EM moments. In a model-independent way, we calculate the EM moments of neutral spin-1/2 fermions at the one-loop level and subsequently apply these formulas to the cases of DM and neutrinos. By combining experimental null signatures of DM direct detection experiments with the analytical formulas for the EM moments, we bridge between the EFT of electromagnetically interacting DM and the UV parameter space of DM models. We showcase this interplay for the archetypical WIMP candidate, the lightest neutralino, and a Dirac toy model. For the case of neutrinos, we study in-depth the prediction of various models—both within the (minimally extended) SM and beyond—for the neutrino EM moments and identify the conditions on these models to give rise to a sizeable contribution.

This dissertation is structured as follows: First, we motivate the DM conundrum in chapter 2 by providing an overview of its observational evidence, thermal production mechanisms, and search strategies. After briefly introducing the role of EM moments in particle physics, we carry out the one-loop calculation of the EM moments of neutral spin-1/2 fermions for scalar- and vector mediators and discuss the kinematical

features of the resulting expressions in chapter 3. Then, in chapter 4, we discuss the phenomenology of DM direct detection in more detail, particularizing the framework to the EM moments of spin-1/2 DM candidates. In light of these experimental constraints, we discuss in chapter 5 the theoretical prediction for the anapole moment of the lightest neutralino in the minimal supersymmetric standard model. Similarly, in chapter 6, we apply the general results of direct detection experiments to a Dirac DM toy model and map the exclusion limits of the EFT to the UV parameter space. Here, we also discuss the implications for a thermal relic. Finally, in chapter 7, we examine the EM moments of neutrinos, both within the SM and beyond. We show that our general results correctly produce the known results for the SM and some typical extensions. In the last section, we also promote a model in which the neutrinos acquire dark moments. In chapter 8, we summarize the findings of this work and provide conclusions.

Chapter 2

Dark matter: evidence, production and search avenues

Here, we briefly review the observational evidence of dark matter (DM), discuss the standard production mechanisms, and introduce present search techniques. For reviews of DM, see, for example, refs. [4–8].

2.1 Observational evidence

We review some examples of evidence hinting at DM ranging from scales of galaxies (~ 100 kpc) and galaxy clusters (~ 1 Mpc) to cosmological scales ($\sim (100 - 1000)$ Mpc). For further details, see *e.g.* refs. [6, 8–10].

2.1.1 Galaxies

Observations show that the rotation curves of spiral galaxies become flat for large distances to the center [11], see fig. 2.1. These findings contrast the expectation for the rotation curve based on the visible matter only, for which a decrease of the velocity $v(r)$ for large distances from the center is expected. This discrepancy can be solved by modifying either *i*) the gravitational force or *ii*) the matter content within a galaxy. Along the former approach is the idea of *modified Newtonian dynamics* (MOND) [12–14], which, however, is in tension with observations on the scale of galaxy clusters [15–19]. Therefore, the latter approach, assuming the presence of additional non-luminous matter, *dark matter*, to explain the measured discrepancy in rotation curves, is favored, which we will discuss in this section in detail.

In this context, we may model a galaxy to consist of three main components: the disc, the bulge, and the DM halo as schematically drawn in fig. 2.2. Although the description and proportions of these contributions strongly depend on the galaxy, we will employ simple analytical models to describe these three gravitational potentials to showcase the main argument for a galactic DM halo.

We model the bulge by an exponentially decreasing spherical mass density,

$$\rho_b(r) = \rho_b^0 e^{-r/R_b}, \quad (2.1)$$

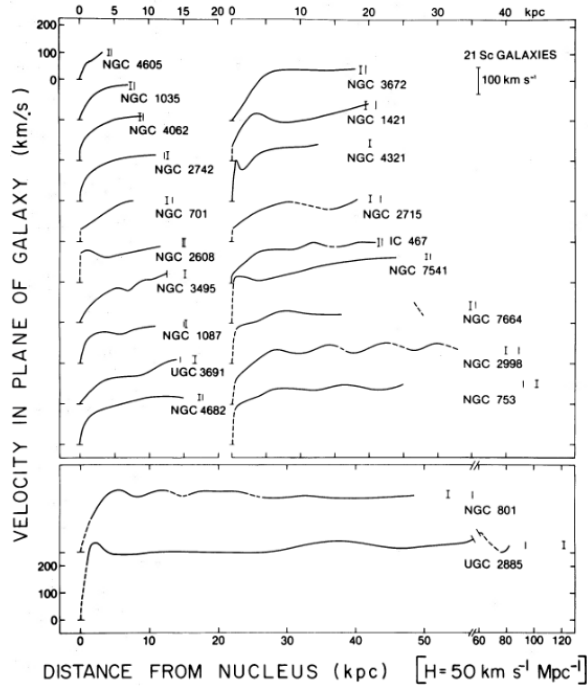


Figure 2.1: Measured rotation curves from 21 Sc galaxies. Figure taken from ref. [11] © AAS. Reproduced with permission.

and the disk by the Freeman model [20], corresponding to an exponentially flat disk with surface density

$$\Sigma(r) = \Sigma_0 e^{-r/R_d}. \quad (2.2)$$

For the DM halo, we assume the Navarro–Frenk–White (NFW) profile [21, 22]

$$\rho_\chi(r) = \frac{\rho_\chi^0}{r/R_\chi (1 + r/R_\chi)^2}, \quad (2.3)$$

however, the qualitative arguments hold, of course, also for other halo models. In the above densities, the radius R_X is the typical scale of the component $X = b, d, \chi$, and the normalization factors ρ_X^0 and Σ_0 can be related to the total masses of the component and therefore related to the observation.

To find the rotation velocity $v_X(r)$ of a point particle with mass m due to the gravitational potential of source $X = b, d, \chi$, we use the fact that the centrifugal force and the gravitational force are in equilibrium, therefore

$$v_X^2(r) = r \frac{\partial}{\partial r} \Phi_X. \quad (2.4)$$

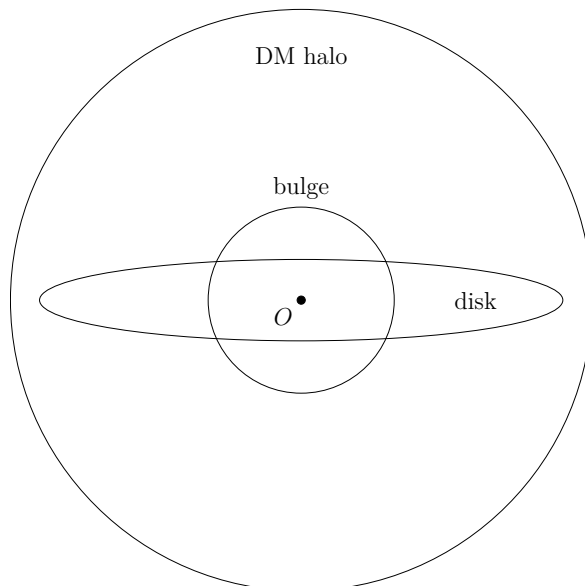


Figure 2.2: Sketch of the main components of a galaxy, where the bulge is assumed to be spherical symmetric around the origin O , a radial symmetrical disk is located at $z = 0$, and a spherical symmetrical DM halo surrounds the whole galaxy.

As the potential Φ_X is sourced by the density ρ_X we can write

$$\Phi_X(r) = -4\pi G \left[\frac{1}{r} \int_0^r dr' r'^2 \rho_X(r') + \int_r^\infty dr' r' \rho_X(r') \right] \quad (2.5)$$

for the spherical symmetrical distributions, and [23]

$$\Phi_d(r, z=0) = -4G \int_0^r \frac{da}{\sqrt{r^2 - a^2}} \int_a^\infty dr' r' \frac{\Sigma(r')}{\sqrt{r'^2 - a^2}} \quad (2.6)$$

for the disk. Calculating the potentials, therefore, allows us to determine the rotation curves due to the three different contributions outlined above.

Bulge contribution

For the bulge contribution, we find

$$v_b^2(r) = \frac{GM_b^{\text{tot}}}{r} \left[1 - e^{-r/R_b} \left(1 + \frac{r}{R_b} + \frac{1}{2} \frac{r^2}{R_b^2} \right) \right], \quad (2.7)$$

with total bulge mass $M_b^{\text{tot}} = 8\pi\rho_b^0 R_b^3$.

Disk contribution

The computation of the disk contribution turns out to be mathematically more involved than the bulge- and DM halo contribution. Plugging the exponentially flat disk surface density into eq. (2.6), we find [20, 23]

$$\Phi_d(r, z = 0) = -\pi G \Sigma_0 r [I_0(y)K_1(y) - I_1(y)K_0(y)], \quad (2.8)$$

where we defined $y = \frac{r}{2R_d}$ in the arguments of the modified Bessel functions I_ν and K_ν . Utilizing the recursion relations of these functions¹, we find for the rotation velocity [20]

$$v_d^2(r) = GM_d^{\text{tot}} \frac{r^2}{2R_d^3} \left[I_0\left(\frac{r}{2R_d}\right) K_0\left(\frac{r}{2R_d}\right) - I_1\left(\frac{r}{2R_d}\right) K_1\left(\frac{r}{2R_d}\right) \right], \quad (2.9)$$

where the total mass within the disk reads $M_d^{\text{tot}} = 2\pi \Sigma_0 R_d^2$.

DM halo contribution

For the NFW profile, we find for the potential

$$\Phi_\chi(r) = -\frac{4\pi G R_\chi^3 \rho_\chi^0}{r} \log\left(1 + \frac{r}{R_\chi}\right). \quad (2.10)$$

The rotation velocity induced by the DM in the galaxy then reads

$$v_\chi^2(r) = \frac{GM_\chi(R_\chi)}{\log(2) - \frac{1}{2}} \left[\frac{\log(1 + r/R_\chi)}{r} - \frac{1}{r + R_\chi} \right], \quad (2.11)$$

with the DM mass inside the sphere of radius R_χ being

$$M_\chi(R_\chi) = 4\pi R_\chi^3 \rho_\chi^0 \left(\log(2) - \frac{1}{2} \right). \quad (2.12)$$

In a galaxy in which these three components are the dominant sources of the gravitational potential, the rotation velocity of an object can, therefore, be described as

$$v^2(r) = v_b^2(r) + v_d^2(r) + v_\chi^2(r). \quad (2.13)$$

To compare our simplified analytical treatment of the galactic components with the measurements depicted in fig. 2.1, we infer the values for the mass scales $\{M_b^{\text{tot}}, M_d^{\text{tot}}, M_\chi(R_\chi)\}$ and scale radii $\{R_b, R_d, R_\chi\}$ from the fits conducted in ref. [24], and which are presented in table 2.1. For these values, we show in fig. 2.3 the

¹ $\frac{dI_0}{dz} = I_1$, $\frac{dK_0}{dz} = -K_1$, $\frac{dI_1}{dz} = I_0 - \frac{1}{z}I_1$ and $\frac{dK_1}{dz} = -K_0 - \frac{1}{z}K_1$, see ref. [23, appendix C].

Parameter	Value	Units
M_b^{tot}	2.3	$10^{10} M_\odot$
R_b	1.5	kpc
M_d^{tot}	5.7	$10^{10} M_\odot$
R_d	3.3	kpc
$M_\chi(R_\chi)$	22.3	$10^{10} M_\odot$
R_χ	21.6	kpc

Table 2.1: Typical values for the parameters describing a spiral galaxy’s bulge, disk, and DM profile. Data taken from ref. [24].

rotation velocities from the individual contributions and their combined prediction. We observe that the rotation curve, including the DM contribution, becomes flat for large r , whereas the disk- and bulge contributions individually become suppressed.

We conclude that the simplified analytical model of the galactic composition and the resulting rotation curve is in qualitative agreement with the measurements shown in fig. 2.1. This comparison highlights the relatively simple solution the presence of a DM halo offers to accommodate the observed flatness of the rotation curves for bodies far away from the center of galaxies.

2.1.2 Galaxy clusters

The arguably first evidence of DM was found on the scales of galaxy clusters by observations of the Coma cluster by F. Zwicky in 1933 [25–27], finding that the observed mass-to-light ratio was significantly above the expectation. This apparent discrepancy between direct observation and the mass deduced using the Virial theorem could be explained by the presence of non-luminous matter. More precise measurements of the masses of such galaxy clusters can be obtained using X-ray observations [28–30] and weak gravitational lensing effects [31]. These techniques allow mapping the gravitational sources and the visible matter, resulting in different matter distributions.

Examples of these studies include MACSJ0025.4-1222 [32] and the prominent bullet cluster, where the mass distribution deduced from visible matter differs from the mass distribution inferred from lensing data significantly, leading to a 7.6σ claim for the presence of DM in this system [33]. Further, from the DM component’s lack of deceleration, the same observations can be utilized to derive limits on the DM self-interactions [34]. In the case of the bullet cluster, self-interactions with cross-sections $\sigma_\chi/m_\chi < 0.47 \text{ cm}^2/g$ are excluded at the 95% C.L. [33].

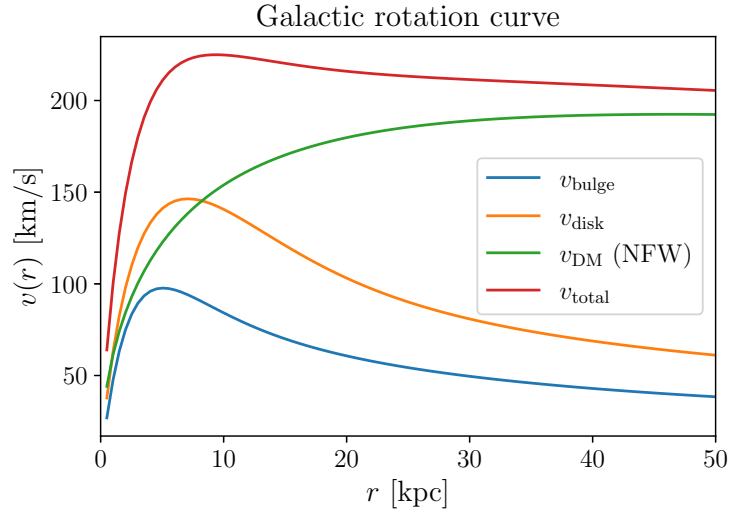


Figure 2.3: Prediction for the rotation curves of a typical galaxy using eq. (2.13) for the values shown in table 2.1.

2.1.3 Cosmic microwave background

Now, we turn to even larger scales. The omnipresent cosmic microwave background (CMB), measured in 1964 by Penzias and Wilson [35], constitutes an observational handle into the physics at the time of matter-radiation decoupling, which occurred at a temperature of $T_{\text{dec}} \simeq 0.26 \text{ eV} \simeq 3000 \text{ K}$. Today, due to redshift, these photons constitute a nearly uniform blackbody spectrum with temperature $T_{\text{dec}}^0 \simeq 2.725 \text{ K}$ with minor anisotropies of order $\delta T/T \sim 10^{-5}$ [36]. Measurements of this spectrum can be confronted with the theoretical prediction within a specific cosmological model.

Due to its simplicity and success, a popular model is the Λ CDM model, consisting of an expanding Universe with a cosmological constant Λ and cold dark matter (CDM).² The metric for the isotropic and homogeneous expanding Universe can be described by the Friedmann-Robertson-Walker (FRW) metric, defined through the line element

$$ds^2 = dt^2 - a^2 \left(\frac{dr^2}{1 - kr^2} + r^2 d\Omega^2 \right), \quad (2.14)$$

hereby, a is the scale factor describing the spatial expansion of the Universe, and $k \in \{-1, 0, 1\}$ is the space-time curvature. Assuming the Universe to behave as a perfect fluid, its evolution can be described by the Friedmann–Lemaître equations [40,

²For an introduction to cosmology, see, for example, refs. [37–39].

41]

$$H^2 = \frac{8\pi G}{3}\rho + \frac{\Lambda}{3} - \frac{k}{a^2}, \quad (2.15a)$$

$$\frac{\ddot{a}}{a} = -\frac{4\pi G}{3}(\rho + 3p) + \frac{\Lambda}{3} - \frac{k}{2a^2}, \quad (2.15b)$$

with the Hubble rate $H = \dot{a}/a$. The first equation in eq. (2.15) can be expressed as

$$H^2 a^2 (\Omega_m + \Omega_r + \Omega_\Lambda - 1) = k, \quad (2.16)$$

where the dimensionless densities for matter, radiation and dark energy are given respectively by $\Omega_m = \rho_m/\rho_c$, $\Omega_r = \rho_r/\rho_c$ and $\Omega_\Lambda = \frac{\Lambda}{8\pi G}/\rho_c$, where $\rho_c = 3H^2/8\pi G$ is the critical density. The matter density is a sum of the baryonic- and CDM contribution, $\Omega_b h^2$ and $\Omega_{\text{DM}} h^2$ respectively.

As mentioned above, measuring the temperature fluctuations over the sphere of the last scattering allows us to probe a cosmological model. Multiple physical processes can alter the measured CMB temperature fluctuations, such as acoustic oscillations and the proper description of the CMB photons propagating through the Universe, such as by including the Sachs-Wolfe effect [42]. The former describes the imprints of the baryon-photon fluid oscillating due to gravitational agglomerations. Before the photons decoupled from matter, the baryon-photon fluid was attracted by overdense regions, compressing the fluid. Competing with this compression was the resulting radiation pressure of the fluid, leading to an expansion. This resulted in a cycle of compression and expansion of the fluid, which left an imprint on the peaks of the angular CMB power spectrum.

In the Λ CDM model, the energy densities can be related to the location, width, and shape of the peaks in the spectrum [9]:

- An increase in the total energy content $\Omega_{\text{tot}} = \Omega_m + \Omega_r + \Omega_\Lambda$ moves the acoustic peaks to smaller multipole moments ℓ . The same is achieved for an increase in the dark energy density Ω_Λ .
- The matter content $\Omega_m h^2 = \Omega_b h^2 + \Omega_{\text{DM}} h^2$ affects the gravitational potential generating the acoustic oscillations. An increase in this density leads to a smoothening in the gravitational background, dampening the peaks. Further, the potential for the gravitational wells inducing the acoustic oscillations becomes steeper, which reduces the separation between high modes in the spectrum.
- The baryon density $\Omega_b h^2$ is a proxy for the mass of the baryon-photon fluid. It affects the height of the peaks.

With these considerations in mind, the data from satellites such as WMAP [43] and PLANCK [44] can be used to fit the parameters of the Λ CDM model. The most recent measurement from PLANCK leads to the following energy budget of the Universe [45]:

$$\Omega_{\text{DM}}h^2 = 0.1198 \pm 0.0015, \quad (2.17a)$$

$$\Omega_b h^2 = 0.02225 \pm 0.00016, \quad (2.17b)$$

$$\Omega_\Lambda = 0.6844 \pm 0.0091, \quad (2.17c)$$

with $h = H_0/100$ (Mpc s/km) and $H_0 = (67.27 \pm 0.66)$ km/(Mpc s) [45] being the Hubble parameter.

Thus, an expanding Universe with a cosmological constant and cold DM agrees exceptionally well with the precise measurement of the CMB power spectrum.

2.1.4 Large scale structure

Finally, evidence for DM can be found on the largest accessible scale: the large-scale structure of the Universe.³ This enormous filament-like structure of the Universe comprises superclusters of galaxies and volumes absent of matter called voids. The distribution of these structures allows us to test the cosmological model, as, during the finite time of the Universe, $t \simeq 13.8$ Gyr [45], these structures must have formed. Using observational data from analyses using weak lensing, Lyman- α , cluster counts, etc., this structure can be quantified through the *power spectrum* $P(k)$. Further, simulations can offer another handle on the clustering dynamics during the evolution of the Universe [47].

The dynamics of gravitationally interacting matter in the Universe can be described by the Vlasov equation [48]

$$\frac{\partial f}{\partial \tau} + \frac{\mathbf{p}}{am} \nabla f - am \nabla \Phi \cdot \nabla_{\mathbf{p}} f = 0, \quad (2.18)$$

where $f(\mathbf{x}, \mathbf{p})$ is the number density and Φ is the cosmological matter potential, sourcing the gravitational interactions via the perturbations, such that $\nabla^2 \Phi = \frac{3}{2} \Omega_m \mathcal{H}^2 \delta(\mathbf{x}, \tau)$, with $\delta(\mathbf{x}, \tau) = \rho(\mathbf{x}, \tau)/\bar{\rho}(\tau) - 1$ being the density contrast and $\mathcal{H} = Ha$. Further, $\tau = \int \frac{dt'}{a(t')}$ is the comoving time, and $\mathbf{x} = a\mathbf{r}$ the comoving distance.

Taking moments of the Vlasov equation, we find respectively the continuity- and

³For a comprehensive review, see, for example, ref. [46].

Euler equations describing the evolution of the density contrast

$$\frac{\partial \delta(\mathbf{x}, \tau)}{\partial \tau} + \nabla \cdot ((1 + \delta(\mathbf{x}, \tau))\mathbf{u}(\mathbf{x}, \tau)) = 0, \quad (2.19a)$$

$$\frac{\partial u_j}{\partial \tau} + \mathcal{H}u_j + u_i \nabla_i u_j = -(\nabla \Phi)_j - \frac{1}{\rho} \nabla_i (\rho \sigma_{ij}), \quad (2.19b)$$

where $\mathbf{u}(\mathbf{x}, \tau) = \mathbf{v}(\mathbf{x}, \tau) - \mathcal{H}\mathbf{x}$ is the peculiar velocity. Further, for a perfect fluid, the stress-tensor σ_{ij} vanishes at first order, such that eq. (2.19) reduces to a coupled differential equation of the density contrast $\delta(\mathbf{x}, \tau)$ and the peculiar velocity $\mathbf{u}(\mathbf{x}, \tau)$.

The matter power spectrum is defined as the correlation function between the matter fluctuations (in momentum space) at different locations

$$\langle \delta(\mathbf{k})\delta(\mathbf{k}') \rangle = (2\pi)^3 \delta^{(3)}(\mathbf{k} + \mathbf{k}') P(k), \quad (2.20)$$

i.e. it quantifies to which extent matter content at different locations is correlated and thus provides a measure for the Universe's large-scale structure. The predicted power spectrum can be compared to observations from extensive galaxy surveys mapping the large-scale structure. The conclusion is that the baryonic matter content alone cannot explain the measured large-scale structure formation. Instead, an additional gravitational source must have been present to predict a distribution similar to the measured one, which, within the Λ CDM model, is CDM.

2.2 Production mechanisms

Here, we introduce two standard production mechanisms of DM: freeze-out and freeze-in. For more details and alternative production mechanisms, see, for example, refs. [8, 9, 38, 49–53].

2.2.1 Freeze-out

The freeze-out paradigm of a weakly interacting massive particle (WIMP) is arguably the most straightforward DM production mechanism. Due to its simplicity and the fact that a DM particle with weak-scale mass $m_\chi \sim 100$ GeV and weak-scale coupling $g_{\text{dark}} \sim 0.1 - 1$ reproduces the measured relic density of $\Omega_{\text{DM}} h^2 \simeq 0.12$ [45], it is sometimes dubbed the WIMP-miracle.

In this framework, it is assumed that in the early Universe, DM had a sizable interaction with the SM, keeping the DM particles in thermal equilibrium with the remaining particles of the thermal bath via processes

$$\chi\chi \longleftrightarrow \text{SM SM}. \quad (2.21)$$

Following ref. [50], the number density of non-relativistic DM particles n_χ subject to these $2 \leftrightarrow 2$ processes follows the Boltzmann equation [38]

$$\frac{dn_\chi}{dt} + 3Hn_\chi = -\langle\sigma v\rangle (n_\chi^2 - (n_\chi^{\text{eq.}})^2), \quad (2.22)$$

with $n_\chi^{\text{eq.}}$ being the DM number density in thermal equilibrium, and [49]

$$\langle\sigma v\rangle = \frac{1}{8m_\chi^4 T K_2^2(m_\chi/T)} \int_{4m_\chi^2}^{\infty} ds \sigma(s - 4m_\chi^2) \sqrt{s} K_1(\sqrt{s}/T) \quad (2.23)$$

is the thermally averaged DM annihilation cross-section. The quadratic dependency on the number density on the right-hand side of eq. (2.22) is because we consider $2 \leftrightarrow 2$ processes, where the terms in the bracket describe the forward ($\sim n_\chi^2$) and backward ($\sim (n_\chi^{\text{eq.}})^2$) processes respectively. The term proportional to the Hubble parameter H originates from the expansion of the Universe, diluting the DM number density over time.

It is common to introduce the dimensionless abundance $Y = n_\chi/s$ and the variable $x = m_\chi/T$, with which eq. (2.22) can be cast as

$$\frac{x}{Y_{\text{eq.}}} \frac{dY}{dx} = -\frac{\Gamma_\chi}{H} \left(\left(\frac{Y}{Y_{\text{eq.}}} \right)^2 - 1 \right), \quad (2.24)$$

where the DM-bath interaction rate is given by $\Gamma_\chi = n_\chi^{\text{eq.}} \langle\sigma v\rangle$. In this form, one can identify the following behavior: in thermal equilibrium, the right-hand side vanishes, such that the yield is a constant. Once the temperature is smaller than the DM mass, the DM production becomes Boltzmann suppressed while the annihilation remains efficient, assuming that $\Gamma_\chi > H$. Then, the second term on the right-hand side of eq. (2.24) becomes negligible, resulting in the strong decrease of the yield as a function of x , following the equilibrium yield $Y \simeq Y_{\text{eq.}}$. Eventually, the Hubble rate becomes larger than the rate of DM annihilations, *i.e.* when $\Gamma_\chi \sim H$. Here, Y will decouple from its equilibrium value and experience freeze-out at the freeze-out temperature $x_f = m_\chi/T_f \sim 20 - 25$. In eq. (2.24) this can be observed as in the limit $\Gamma_\chi/H \ll 1$, the right hand side vanishes, thus, $Y \rightarrow \text{const}$.

The resulting values of the abundance today, Y_0 , are proportional to the inverse of the annihilation cross-section, as a larger annihilation rate will lead to a faster depletion of DM particles in the Universe. The prediction for the measurable DM relic density is [38]

$$\Omega_\chi h^2 \simeq 1.07 \times 10^9 \frac{\sqrt{g_*} m_\chi (n+1) \text{ GeV}^{-1}}{g_{*s} T_f M_{\text{Pl.}} \langle\sigma v\rangle}, \quad (2.25)$$

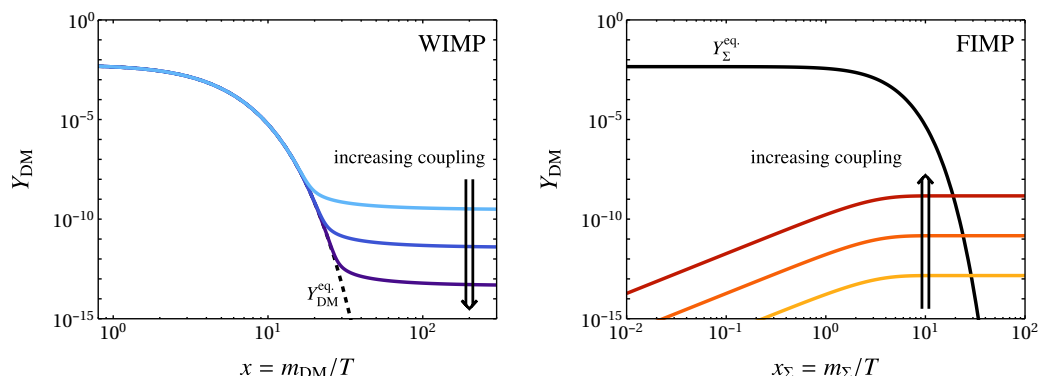


Figure 2.4: Freeze-out of the DM abundance for a thermal WIMP candidate (*left*), and the freeze-in line for a FIMP candidate (*right*) as a function of the dimensionless temperature $x = m_\chi/T$ for the WIMP and $x = m_\Sigma/T$ for the FIMP. Σ is a scalar mediator that is in thermal equilibrium with the SM, whose decay produces DM particles. Figures taken from ref. [51]; reproduced with permission from J. Herms.

where $M_{\text{Pl}} \simeq 1.2 \times 10^{19}$ GeV is the Planck mass, and g_{*s} (g_*) is the effective number of relativistic degrees of freedom of the entropy (energy density). The appearance of n accounts for the different velocity dependency the annihilation cross-section could have, as [38]

$$\langle \sigma v \rangle = \sigma_0 x^{-n}, \quad (2.26)$$

i.e. $n = 0$ corresponds to s -wave annihilation, $n = 1$ to p -wave annihilation etc.

One key feature of the freeze-out mechanism is that the larger the DM annihilation cross-section, the smaller the prediction for the DM relic density. As the cross-section is proportional to the square of the coupling between the dark sector and the SM, this relation is transferred to the coupling. This behavior can be seen in the left panel of fig. 2.4, where we show the freeze-out line of a WIMP candidate as a function of x .

2.2.2 Freeze-in

Another common production mechanism is the freeze-in mechanism. Here, the DM particles were never in thermal equilibrium with the thermal bath but instead were continuously produced by annihilations or decays of bath particles. To avoid the DM from thermalizing, this mechanism requires a very small DM-SM interaction rate and, therefore, a small coupling between the DM particle and the SM. A DM candidate that is produced via the freeze-in mechanism is sometimes dubbed a *feebly interacting massive particle* (FIMP) [54].

For a decaying bath particle $\Sigma \rightarrow \chi\chi$, the thermal history of a FIMP is described by the Boltzmann equation [50]

$$\frac{dn_\chi}{dt} + 3Hn_\chi = 2\Gamma_{\Sigma \rightarrow \chi\chi} \frac{K_1(m_\Sigma/T)}{K_2(m_\Sigma/T)} n_\Sigma^{\text{eq}}, \quad (2.27)$$

where $\Gamma_{\Sigma \rightarrow \chi\chi}$ is the decay rate of the scalar Σ and n_Σ^{eq} denotes its equilibrium number density. We can introduce similar dimensionless variables as in section 2.2.1 and cast eq. (2.27) as

$$\frac{x}{Y_\Sigma^{\text{eq}}} \frac{dY}{dx} = \frac{2\Gamma_{\Sigma \rightarrow \chi\chi}}{H} \frac{K_1(m_\Sigma/T)}{K_2(m_\Sigma/T)}. \quad (2.28)$$

The approximate solution of eq. (2.28) for the relic abundance then reads [54]

$$\Omega_\chi h^2 \simeq 1.09 \times 10^{27} \frac{g_\Sigma}{g_{*s} \sqrt{g_*}} \frac{m_\chi}{m_\Sigma^2} \Gamma_{\Sigma \rightarrow \chi\chi}, \quad (2.29)$$

where g_Σ is the intrinsic number of degrees of freedom of Σ . In contrast to the freeze-out scenario introduced in section 2.2.1, the DM relic density is proportional to the decay width of the mediator particle Σ or the production cross-section of the DM particles, constraining the couplings to be of order $g \sim 10^{-11}$ or so, depending on the scenario [54]. In the right panel of fig. 2.4, we present the freeze-in line for a FIMP candidate, showcasing the steady production of DM particles via the decay of the bath particle Σ .

2.3 Non-gravitational search efforts

As discussed in section 2.1, all observational evidence for the existence of DM comes from its gravitational interactions at different scales. Therefore, there is the worst-case possibility that this is, in fact, the only interaction DM possesses, which would severely limit our experimental reach on it. Some models accounting for this scenario include fuzzy DM [55, 56], describing ultra-light bosonic degrees of freedom, which can be produced via the misalignment mechanism [57–59], or ultra-heavy DM, being produced non-thermally via the inflaton field [60, 61].

However, as we discussed in section 2.2, within the standard WIMP- or FIMP paradigms, a DM candidate with a coupling to the SM can be produced in the early Universe, offering an attractive production mechanism. Many reasonably well-motivated UV complete models providing a DM candidate, such as the minimal supersymmetric standard model, naturally predict WIMPs. Therefore, the simplicity of these production mechanisms and the general WIMP model landscape motivates the scenario of DM interacting with the SM.

Here, we introduce the three pillars of current experimental efforts probing the non-gravitational nature of particle DM. Due to the lack of evidence pointing in other

directions, experimental studies typically consider either some benchmark (WIMP-) scenario for the analysis or try to describe the experimental results in a model-independent manner.

2.3.1 Indirect detection

In indirect detection experiments, the aim is to observe the decay- or annihilation products of DM particles originating from dense regions of the Universe, such as the galactic center, dwarf galaxies, or the core of the Sun. For more details on this subject, see, for example, refs. [8, 62–64].

The final states of the particle physics processes describing the DM decay or annihilation are strongly model-dependent, and a priori, so are the search strategies and the resulting phenomenology. However, from a practical point of view, these analyses are performed in a model-independent way, focusing on specific primary channels, such as $\chi\chi \rightarrow W^+W^-, b\bar{b}, \ell^+\ell^-,$ etc. The energy spectra at the source [8]

$$\frac{dN_{\text{SM}}}{dE} = \sum_{\text{prim}} \text{BR}_{\text{prim}} \frac{dN_{\text{SM}}^{\text{prim}}}{dE}, \quad (2.30)$$

where the primary branching ratios BR_{prim} are defined as

$$\text{BR}_{\text{prim}} = \begin{cases} \frac{\langle\sigma v\rangle_{\text{prim}}}{\langle\sigma v\rangle_{\text{tot}}} & \text{for DM annihilation} \\ \frac{\Gamma_{\text{prim}}}{\Gamma_{\text{tot}}} & \text{for DM decay} \end{cases}, \quad (2.31)$$

are the only part dependent on the DM physics via the annihilation cross-section $\langle\sigma v\rangle$ or the decay width Γ . After the annihilation (or decay), the description of these primary particles is governed by SM physics, including their decays, showering and hadronization and can be calculated using public codes such as *Pythia* [65], *Herwig* [66, 67] or *Geant4* [68]. Eventually, only the long-lived particles $e^\pm, p/\bar{p}, d/\bar{d}, \gamma, \nu_\ell/\bar{\nu}_\ell$ are left, see fig. 2.5 for a schematic presentation.

Thus, measuring the observed flux of gamma-rays, neutrinos, and other particles at Earth provides a way to study annihilating or decaying DM—assuming knowledge of the astrophysical SM background and adequately estimating the DM-induced flux.

2.3.1.1 Gamma ray searches

The differential photon flux stemming from Majorana DM annihilations in the Milky Way reads [8]

$$\frac{d\Phi}{d\Omega dE} = \frac{1}{2} \frac{r_\odot}{4\pi} \left(\frac{\rho_\odot}{m_\chi} \right)^2 J \langle\sigma v\rangle \frac{dN_\gamma}{dE}, \quad (2.32)$$

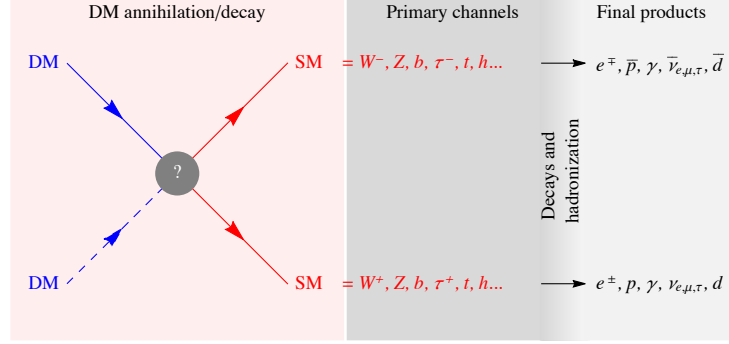


Figure 2.5: Sketch depicting annihilating (or decaying) DM into the primary particles, which further decay, shower, and hadronize. Figure taken from ref. [8].

where r_\odot is the radial distance from Earth to the Galactic Center, and ρ_\odot is the DM abundance at Earth. The differential flux at source is given in eq. (2.30), and we defined the dimensionless J -factor

$$J = \int_{\text{l.o.s.}} \frac{ds}{r_\odot} \left(\frac{\rho(r(s, \theta))}{\rho_\odot} \right)^2, \quad (2.33)$$

in which the squared DM density $\rho(r(s, \theta))$ is integrated along the line of sight (l.o.s.). The latter is parameterized in terms of the radial distance from the galactic center, $r(s, \theta) = \sqrt{r_\odot^2 + s^2 - 2r_\odot s \cos \theta}$, where r_\odot is the galactic radial coordinate of the Solar System. The flux for annihilating DM is proportional to ρ^2 because the annihilation process considered here inherently demands two DM particles in the initial state.

Similarly, if DM is decaying, the flux is expressed as

$$\frac{d\Phi}{d\Omega dE} = \frac{r_\odot \rho_\odot}{4\pi m_\chi} D \Gamma \frac{dN_\gamma}{dE}, \quad (2.34)$$

where effectively the J -factor and the thermally averaged annihilation cross-section $\langle \sigma v \rangle$ are replaced respectively by the D factor, defined by

$$D = \int_{\text{l.o.s.}} \frac{ds}{r_\odot} \frac{\rho(r(s, \theta))}{\rho_\odot}, \quad (2.35)$$

and the decay width Γ . Further, as only one parent particle is needed for the decay, the photon spectrum in this scenario is proportional to the DM density.

In practice, the differential fluxes presented for DM annihilations and DM decays in eq. (2.32) and eq. (2.34) respectively, ought to be integrated over the opening angle corresponding to the observational accessible region.

For dwarf satellite galaxies the same formulas as in eqs. (2.32) and (2.34) apply, with the relevant difference being the choice of the integration limits when integrating over the solid angle, introducing a somewhat arbitrary analysis-dependency, as the choice is not necessarily dictated by the experimental apparatus or the physical region of interest, as it is for the analysis of gamma rays from the Galactic Center.

Current generation experiments looking for an abnormal flux of gamma rays include Fermi-LAT [69, 70] and the H.E.S.S. [71], and their reach on DM-induced fluxes have been probed in refs. [72–74] and refs. [75, 76], respectively.

2.3.1.2 Neutrinos

The fluxes for neutrinos are very similar to the gamma-rays presented in eqs. (2.32) and (2.34), with the main difference being the effect of flavor oscillations. Therefore, the flux of a neutrino with a specific flavor at Earth is related to the flux at production via the neutrino oscillation probability over astrophysical distances as [77]

$$P_{\ell\ell'} = \sum_i^3 |U_{\ell i} U_{\ell' i}|^2 \simeq \begin{pmatrix} 0.55 & 0.18 & 0.27 \\ 0.18 & 0.45 & 0.38 \\ 0.27 & 0.38 & 0.35 \end{pmatrix}, \quad (2.36)$$

where we used the most recent central fit values from NuFIT 6.0 [78].⁴

For example, in a model in which DM decays into τ -neutrinos at the source, due to the propagation detectors at Earth will measure all flavors with composition $(\nu_e : \nu_\mu : \nu_\tau) \simeq (0.27 : 0.38 : 0.35)$, *i.e.* a single-flavor initial neutrino flux turns into a neutrino flux of all flavors at the detector. Dedicated search efforts exist trying to measure this DM-induced neutrino flux, such as from the IceCube collaboration [79–87] and the KM3NeT collaboration [88–90].

2.3.1.3 Charged cosmic rays

Search strategies based on charged particles typically focus on the respective anti-particle flux, as their production is less likely to occur due to non-DM-related astrophysical processes. Thus, less background is expected. Here, we comment on positrons, anti-protons, and anti-deuterons.

In contrast to photons and neutrinos, describing the propagation of charged particles from the source to Earth is more complicated, as many effects influence their propagation. The fundamental equation for the propagation is the transport

⁴See also the NuFIT website www.nufit.org.

equation for the number density per unit kinetic energy $f(\mathbf{x}, t)$, which reads [8, 91]:

$$Q(E, \mathbf{x}) = -\nabla(\mathcal{K}(E, \mathbf{x}) \cdot \nabla f) \quad (2.37a)$$

$$+ \frac{\partial}{\partial z}(\text{sgn}(z)fV_{\text{conv}}) \quad (2.37b)$$

$$- \frac{\partial}{\partial E} \left(b_{e^\pm}(E, \mathbf{x})f + v_{e^\pm}^2 \mathcal{K}_p(E, \mathbf{x}) \frac{\partial f}{\partial E} \right). \quad (2.37c)$$

The left-hand side in eq. (2.37) describes the injection of positrons into the Galactic environment and is thus referred to as *source* term. It reads

$$Q(E, \mathbf{x}) = \begin{cases} \frac{1}{2} \left(\frac{\rho}{m_\chi} \right)^2 \langle \sigma v \rangle_{\text{tot}} \frac{dN_{e^\pm}}{dE} & \text{for DM annihilation} \\ \frac{\rho}{m_\chi} \Gamma_{\text{tot}} \frac{dN_{e^\pm}}{dE} & \text{for DM decay} \end{cases}. \quad (2.38)$$

The term on the right-hand side of eq. (2.37a) is the diffusion term modeling the propagation through the inhomogeneous Galactic magnetic fields. The diffusion coefficient \mathcal{K} is typically assumed to be a scalar and may be modeled as [92]

$$\mathcal{K}(R) = \beta^\eta \mathcal{K}_0 \left(\frac{R}{\text{GeV}} \right)^\delta \left[1 + \left(\frac{R_l}{R} \right)^{(\delta - \delta_l)/s_l} \right]^{s_l} \left[1 + \left(\frac{R}{R_h} \right)^{(\delta - \delta_h)/s_h} \right]^{-s_h}, \quad (2.39)$$

where the rigidity is defined as the momentum per unit charge, $R = p/Ze$. The effect of spectral breaks [93] for low- (l) and high (h) rigidity is modeled using the 2-times broken power law. Their location is given by $R_{l/h}$; their diffusion spectral index is given by $\delta_{l/h}$, and the rate at which the spectrum changes is controlled by $s_{l/h}$. Finally, η models the dependency on the velocity $\beta = v_{e^\pm}/c$ and $\delta \sim 0.5 - 1$ is the spectral index. If the presence of the spectral breaks is neglected, the diffusion coefficient can be parameterized as (see *e.g.* refs. [94, 95])

$$\mathcal{K}(R) = \beta \mathcal{K}_0 \left(\frac{R}{\text{GeV}} \right)^\delta. \quad (2.40)$$

The term in eq. (2.37b) models the convective wind, asserting a force on the charged cosmic rays. The smaller the energy of the charged cosmic ray is, the stronger this force will act upon it. Further, the first term in eq. (2.37c) accounts for the energy loss during propagation and includes the interactions of the cosmic ray with the interstellar gas, inverse Compton scattering on photons and the CMB, and synchrotron radiation. Competing to that is the effect of re-acceleration due to the presence of diffusion centers, which can induce a second-order Fermi acceleration [96] and is modeled by the second term in eq. (2.37c).

Overall, solving the diffusion equation given in eq. (2.37) is complicated and depends on many model parameters that have to be deduced from observables such

as the boron-to-carbon ratio [97]. Furthermore, one has to resort to numerical tools such as GalProp [98, 99] or DRAGON [100, 101], or use semi-analytical approximations.

In the past, an abnormal flux of positrons was reported by the PAMELA collaboration [102] and by the AMS collaboration [103, 104], which could be explained by astrophysical processes [105–108], or by an annihilating-or decaying DM particle [109–117].

The diffusion equation of anti-protons is very similar to that of positrons given in eq. (2.37). The energy parameter E appearing in the source term Q should be replaced by the kinetic energy $K = E - m_p$ of the anti-proton and an additional term accounting for the loss of anti-protons when passing the Galactic disc due to nuclear effects,

$$2h\delta(z)(\Gamma_{\text{ann}} + \Gamma_{\text{non-ann.}})f, \quad (2.41)$$

should be added to the right hand side of eq. (2.37). Due to the abundance of protons at the Galactic disc located at $z = 0$, the anti-protons can annihilate with rate Γ_{ann} and thus be removed from the spectrum. The second rate, $\Gamma_{\text{non-ann.}}$, describes other effects that effectively remove anti-protons from the flux, such as scattering events, in which the anti-protons lose significant energy.

For the anti-deuterons, the discussion is similar to that of anti-protons, with the important difference being the estimation of the loss term eq. (2.41), owing to the different particle physics interactions. Further, as the anti-deuteron flux is expected to be tied to the anti-proton flux, the former is severely constrained by the limits on the latter [118].

2.3.2 Direct detection

Here, we briefly introduce the standard framework of DM direct detection experiments and discuss the overall features. For comprehensive reviews, see *e.g.* refs. [119, 120]. The direct detection phenomenology of electromagnetically interacting DM is discussed in detail in chapter 4.

We consider DM particles scattering off a target T with mass m_T in a laboratory on Earth. Typically, the experiment is located under an overburden, such as a mountain, to shield the detector from hindering background sources as sketched in fig. 2.6. As the interaction strength of DM with baryonic matter has to be minor, it can travel through the overburden freely until it may interact with the dedicated target of the experimental setup.

It is assumed that a flux of DM originating from the local halo with a density of $\rho_\chi \simeq 0.3 \text{ GeVcm}^{-3}$ and with a particular velocity profile may interact with targets in the experimental setup. Hereby, typically *one* type of interaction between DM and the target is assumed, which is then constrained by the absence of measured events and recoil spectra.

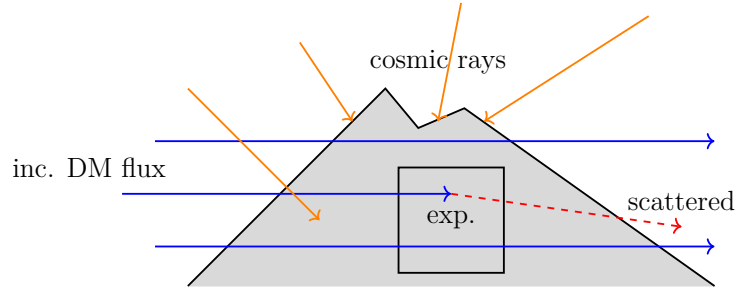


Figure 2.6: Sketch of a typical setup of an underground DM direct detection experiment (not to scale). If an incoming DM particle scatters off the target in the experiment, it deposits energy, which the detector tries to measure. The overburden shields the laboratory from cosmic rays, reducing the background noise.

The differential recoil rate from a DM particle interacting with the target via a cross-section σ with flux $\mathcal{F}(\mathbf{v})$, can be written as:

$$\frac{dR}{dE_R} = \frac{1}{m_T} \int_{v>v_{\min}} d^3v \mathcal{F}(\mathbf{v} + \mathbf{v}_E) \frac{d\sigma}{dE_R} \quad (2.42)$$

$$= \frac{\rho_0}{m_\chi m_T} \int_{v>v_{\min}} d^3v v f(\mathbf{v} + \mathbf{v}_E) \frac{d\sigma}{dE_R}. \quad (2.43)$$

In the last line, we substituted the DM velocity flux with the DM halo distribution boosted to the Earth's rest frame. A typical model—which we also assume exclusively in this dissertation—is the Standard Halo Model (SHM), which assumes a Maxwellian galactic DM distribution

$$f(\mathbf{v}) = \mathcal{N}^{-1} e^{-v^2/v_0^2} \Theta(v - v_{\text{esc}}), \quad (2.44)$$

with normalization factor

$$\mathcal{N} = \pi^{3/2} v_0^3 \left[\text{erf} \left(\frac{v_{\text{esc.}}}{v_0} \right) - \frac{2v_{\text{esc.}}}{\sqrt{\pi}v_0} e^{-\frac{v_{\text{esc.}}^2}{v_0^2}} \right]. \quad (2.45)$$

In this expression the Galactic escape velocity of DM reads $v_{\text{esc.}} = 544 \text{ km s}^{-1}$, its typical speed is given by $v_0 = 220 \text{ km s}^{-1}$ and Earth's speed is $v_E = 232 \text{ km s}^{-1}$.

The total number of scattering events can then be obtained by integrating over the energy spectrum as

$$\mathcal{N}_{\text{sig}} = w \times \int dE_R \frac{dR}{dE_R}, \quad (2.46)$$

where we assumed perfect detector efficiency. In this expression, w is the experiment's exposure typically given in units of ton \times year or gram \times days. Using

eq. (2.46), we can compare experimental results with the theoretical prediction for different models. Apart from the astrophysical information which governs the velocity distribution $\mathcal{F}(\mathbf{v} + \mathbf{v}_E)$ and the local abundance ρ_0 , the relevant quantity is the differential cross-section between DM and the target. Therefore, this inherently model-dependent quantity is the bridge between the particle description of DM and the experimental signature.

Before discussing the exclusion limits on the typical DM-nucleus cross-section, we briefly address some general remarks about the DM direct detection landscape. We sketch in fig. 2.7 a typical exclusion plot on a model parameter such as a cross-section or a coupling, highlighting the typical dominant analysis approach for the respective mass range. In such a figure, parameters above the exclusion line are excluded, and points below are allowed; in fig. 2.7, examples for such points are indicated by the red cross and green circle, respectively. The exclusion line is given at a certain confidence level (C.L.), which in the direct detection phenomenology is typically chosen to be a 90% C.L. Typically, the here-discussed nuclear recoil events dominate the spectrum for DM masses $m_\chi \gtrsim 10$ GeV. For sub-GeV DM candidates, typically, the exclusion limits using electron recoils dominate, see for example, the studies conducted in refs. [121–124] and for an effective field theoretical description of general DM-electron interactions ref. [125]. Apart from alternative proposed avenues for DM direct detection [126–131], the utilization of the Migdal effect [132] opens the possibility for studying sub-GeV DM using current detector technologies [133], which we discuss in more detail in section 4.2.1. As evident from fig. 2.7, the limits derived using this Migdal effect can bridge the gap between DM-electron and DM-nucleus scattering, albeit this can depend on the target and the interaction [123, 124].

As discussed above, to evaluate eq. (2.46), we need to assume a particular interaction between DM and the target. For now, we consider the standard scenario where the interaction between DM and the target is given by the operator $\bar{\chi}\chi\bar{N}N$ or $\bar{\chi}\gamma^\mu\chi\bar{N}\gamma_\mu N$, which are spin-independent (SI). The cross-section entering the differential rate in eq. (2.42) then reads

$$\frac{d\sigma}{dE_R} = \frac{m_T}{2\mu_T^2 v^2} \times \sigma_0^{\text{SI}} \times F_{\text{SI}}^2(E_R), \quad (2.47)$$

where μ_T is the reduced mass of the DM-target system, σ_0^{SI} is the spin-independent cross-section at zero-momentum transfer,

$$\sigma_0^{\text{SI}} = \sigma_p \frac{\mu_T^2}{\mu_N^2} \left[Z + (A - Z) \frac{f_n}{f_p} \right]^2, \quad (2.48)$$

where σ_p is the cross-section between DM and proton and here considered the free parameter which the experiment probes. Further, μ_N is the reduced mass of the WIMP-nucleon system, and f_n (f_p) is the relative interaction strength to neutrons

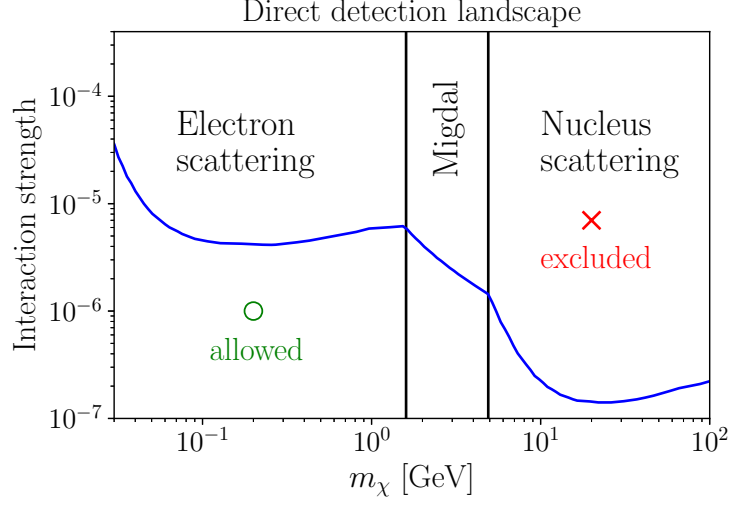


Figure 2.7: Typical exclusion landscape from DM direct experiments. The vertical axis typically denotes a coupling or cross-section; the blue line indicates the exclusion limit. We further indicate roughly the regions where electron recoils, the Migdal effect, or DM-nucleus scattering analyses provide the leading constraints.

(protons). Typically, in the standard approach, it is assumed that the DM particle couples to neutrons and protons with the same strength, such that $f_n = f_p$. This assumption is sometimes referred to as *isospin conservation*. The momentum dependency of this interaction is modeled by $F_{\text{SI}}(E_R)$, which is typically parameterized by the Helm form factor [134, 135]

$$F_{\text{SI}}(E_R) = 3 \exp(-q^2 s^2 / 2) [\sin(qr) - qr \cos(qr)] / (qr)^3, \quad (2.49)$$

with $q = \sqrt{2m_T E_R}$, $s = 1 \text{ fm}$, $r = \sqrt{R^2 - 5s^2}$ and $R = 1.2A^{1/3} \text{ fm}$. Then, for the SHM, the differential rate reads

$$\frac{dR}{dE_R} = \frac{\rho_0}{2\mu_N^2 m_\chi} \eta(v_{\min}) A^2 \sigma_p F_{\text{SI}}^2(E_R), \quad (2.50)$$

where [120]

$$\eta(v_{\min}) = \frac{v_0^3 \pi^{3/2}}{2\mathcal{N} v_E} \left[\text{erf}(\tilde{z}_+) - \text{erf}(\tilde{z}_-) - \frac{2}{\sqrt{\pi}} e^{-z_{\text{esc}}^2} (\tilde{z}_+ - \tilde{z}_-) \right] \quad (2.51)$$

is the velocity integral for the standard SI interaction and the SHM, and

$$\tilde{z}_\pm = \min(z_{\min} \pm z_E, z_{\text{esc}}), \quad (2.52)$$

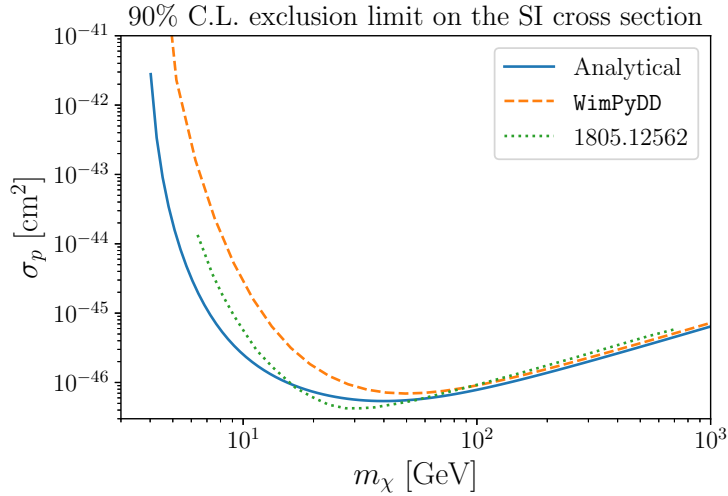


Figure 2.8: 90% C.L. exclusion limits on the DM-proton SI cross-section σ_p in the standard spin-independent scenario for the XENON1T experiment for the analytical approach outlined in this section. We also include the limit derived using the public code `WimPyDD` [136] and the result reported by the XENON1T collaboration [137].

with $z_X = v_X/v_0$.

In fig. 2.8 we present the exclusion limit on the DM-proton SI cross-section σ_p from XENON1T following the approach outlined in this section for an exposure of $w = 1 \text{ ton} \times \text{year}$ with 7 measured events and a background count of zero in the interval $[1.8, 61] \text{ keV}_{\text{nr}}$, taken from the `data` file provided by `WimPyDD` [136] (see appendix A for details on the statistical treatment). For comparison, we also show the limit derived using the public code `WimPyDD` [136] and the result presented by the XENON1T collaboration [137]. The main difference between our analytical result and the results obtained from the literature is the detector efficiency, which we neglected for simplicity.

The standard direct detection paradigm discussed so far is helpful as a benchmark for comparing different experiments. However, in practice, the type of interaction between DM and the target is model-dependent, which includes the velocity dependency, the recoil spectrum, and the potential presence of multiple types of interactions with the target, where each can have a different velocity dependency. Therefore, in general, one cannot simply recast the published limits on the standard interaction cross-section, as shown in fig. 2.8, but has to calculate the signal rates on a model-by-model basis.

Albeit designed for DM searches, direct detection experiments have recently proved their capability as neutrino observatories. The xenon-based experiments XENONnT

and PandaX-4T reported in ref. [138] and ref. [139], respectively, the first measurements of coherent elastic neutrino-nucleus scattering ($\text{CE}\nu\text{NS}$) of solar neutrinos. These neutrinos constitute an inevitable background dubbed the *neutrino floor* [140–143] or *neutrino fog* [144], whose recoil spectra can mimic DM-induced events. This background makes a statistical analysis eventually very difficult, as the needed exposure for clear discrimination between neutrinos and a DM signal is unlikely to be obtainable [145].

2.3.3 Collider searches

Finally, if DM interacts with SM particles, it could be directly produced in collider facilities such as the Large Hadron Collider (LHC) at CERN [146]. The main characteristic is a specific event's missing (transverse) energy, indicating that particles left the detectors unnoticed. Such an event could be attributed to the production of DM pairs $pp \rightarrow \chi\chi$ if the center of mass energy \sqrt{s} of the initial states allows for such a kinematic configuration. Therefore, this energy conservation argument gives a hard requirement of $\sqrt{s} > 2m_\chi$ for DM production at colliders, neglecting the energy distribution within the colliding protons. Since the LHC operates with a center of mass energy of $\sqrt{s} \sim 13.6$ TeV [146, 147], DM particles with mass $m_\chi \sim 7$ TeV would not be produced by the LHC and, therefore, be invisible to collider analyses. Key experiments at the LHC studying the potential of new physics are ATLAS [148], CMS [149] and LHCb [150, 151], which are capable of studying DM phenomenology [152–155].

Chapter 3

Electromagnetic moments of neutral spin-1/2 fermions

In this chapter, we aim to calculate the electromagnetic (EM) moments of neutral fermions in vacuum.¹ Throughout this dissertation, the term *moment* refers to one of the EM interactions of an elementary particle, which may not necessarily be related to a coefficient in a classical expansion of a charge- or current distribution. In particular, the *anapole* moment—which indeed is not a moment as it describes a non-radiating configuration—and the millicharge and charge radius are referred to as moments.

The building pieces developed here are helpful for a class of fermionic DM models, further discussed in chapters 5 and 6, and for neutrinos, both within the SM and beyond, which we discuss in chapter 7.

3.1 Electromagnetic moments in particle physics

In this section, we introduce some selected examples of EM moments of SM particles to emphasize their role in the landscape of theoretical particle physics.

EM moments of particles offer the possibility of probing the SM experimentally with high precision. One of the best-measured quantities is the anomalous magnetic moment of the electron, characterizing an electron's interaction strength with a magnetic field. It is defined through $a_e = (g_e - 2)/2$, where

$$\mu_e = -g_e \frac{e}{2m_e} \quad (3.1)$$

defines the g -factor of the electron, g_e . In Dirac theory, the prediction reads $g_e = 2$, and a deviation from this observation is attributed to quantum effects. Calculating the first-order correction in perturbation theory was one of the first quantum predictions made in 1948 by J. Schwinger [159], who obtained

$$a_e = \frac{\alpha}{2\pi} \simeq 0.001\,161\,4. \quad (3.2)$$

¹We note that medium effects could further contribute to the EM interactions of neutral fermions [156–158].

Nowadays, its value within quantum electrodynamics has been calculated up to $\mathcal{O}(\alpha^5)$ [160, 161], with further contributions arising from electroweak- and hadronic contributions. It is experimentally constrained to be [162]

$$a_e^{\text{exp.}} = 0.001\,159\,652\,180\,59(13), \quad (3.3)$$

agreeing with the SM prediction at the level of $\delta a_e \sim 0.7 \times 10^{-12}$ [162].

In contrast, the measurement of the anomalous magnetic moment of the muon seemingly differs from its SM prediction. The combined measurement of BNL [163] and FNAL [164] reads

$$a_\mu^{\text{exp.}} = 116\,592\,059(22) \times 10^{-11}, \quad (3.4)$$

being at a 5.0σ tension with the SM prediction [164]. However, some of this deviation could be attributed to the determination of the hadronic vacuum polarization [165, 166]. If, however, this tension persists, this discrepancy could be a sign of BSM physics such as supersymmetry [167]. For reviews on this subject, see, for example, refs. [168–170].

While the magnetic properties of particles reflect their interaction with magnetic fields, electric dipole moments characterize their interaction with the electric field. The electric dipole moment of the neutron, d_n , is fundamentally linked to the strong CP problem—a long-standing puzzle in quantum chromodynamics (QCD). In principle, the SM symmetries allow the QCD Lagrangian to contain the CP-violating term

$$\mathcal{L}_{\text{SM}} \supset \theta \frac{g_s^2}{32\pi^2} \tilde{G}_{\mu\nu}^a G_a^{\mu\nu}, \quad (3.5)$$

where g_s is the strong coupling constant, $G_{\mu\nu}^a$ is the gluon field-strength tensor and $\tilde{G}_{\mu\nu}^a$ its dual. As θ is a free parameter of the theory, it is expected to be of $\mathcal{O}(1)$ following the argument of naturalness [171]. As this term can be written as a total derivative of a Chern–Simons current, it will not lead to physical observables in perturbation theory [172]. However, considering the inner structure of the neutron using the chiral Lagrangian, this term induces an electric dipole moment of the neutron [173],

$$d_n \simeq 5.2 \times 10^{-16} e \text{ cm} \times \theta, \quad (3.6)$$

and is therefore proportional to the CP-violating parameter θ . Experimental searches have set extremely stringent upper limits on the neutron electric dipole moment², finding that [174]

$$|d_n| < 2.9 \times 10^{-26} e \text{ cm} \quad (90\% \text{ C.L.}), \quad (3.7)$$

implying that θ is unnaturally small, constituting the strong CP problem.

²See <https://www.psi.ch/en/nedm/edms-world-wide> for an overview of experimental efforts.

A proposed solution is the Peccei-Quinn mechanism [175, 176], where a $U(1)_{\text{PC}}$ symmetry is added to the SM. After this $U(1)_{\text{PC}}$ symmetry breaks spontaneously, a Goldstone boson is introduced to the theory. At the minimum of the potential, the presence of the Goldstone boson cancels the θ term, and the oscillations about this minimum are the axions, a DM candidate [172].

The last example of EM moments in the SM is the neutrino. Neutrinos are electromagnetically neutral particles within the SM. In contrast to the neutron, however, neutrinos are point-like elementary particles, such that no inner structure could induce an interaction with the EM field. Nevertheless, as we see in this chapter in general and explicitly in chapter 7, quantum corrections can give neutrinos up to four unique interaction form factors characterizing their interaction with a photon.

In the past, a neutrino magnetic moment was proposed as a solution to the solar neutrino problem, explaining the smallness of the measured solar electron neutrino flux, which conflicted with the prediction. A neutrino with magnetic dipole moment would interact with the Sun’s magnetic field in the convective zone, which could lead to a decrease of the flux [177–181]. As the neutrino dipole moments vanish within the SM, this solution to the solar neutrino problem necessitated BSM physics to generate a relatively large neutrino magnetic dipole moment.

In contrast, the SM predicts a non-zero charge radius and anapole moment³ for a Dirac neutrino. Historically, their calculation was plagued by apparent inconsistencies, such as gauge dependency and the appearance of UV divergent terms, which raised the question about whether these quantities are physical or not [185–198]. We comment on this problem in more detail in section 3.2 and discuss the theoretical prediction for all EM moments of neutrinos in different models in chapter 7.

Finally, the consideration of EM moments also found its way into the DM model landscape, in particular, in the context of direct detection phenomenology of spin-1/2 WIMPs [199–208]. Similar to the neutrino, DM candidates can have interactions with the EM current at the quantum level. For a spin-1/2 candidate, these include millicharges, magnetic dipole moments, electric dipole moments, charge radii, and anapole moments, where the details depend on the UV model and whether the fermion satisfies the Majorana condition. These EM properties can give rise to interactions by coupling to the charge- or the magnetic dipole moment of the targets in direct detection experiments. Further, in multicomponent DM models, the dipole moments can induce radiative decay between the different DM states [209–211], which could produce gamma lines observable in indirect detection experiments [212].

Consequently, EM multipoles have been generalized to higher spin DM particles. In refs. [213, 214], a comprehensive study of spin-1 DM candidates, including po-

³An anapole moment is a P- and C-violating interaction corresponding to a non-radiating configuration; first proposed in 1956 by Y. B. Zel’Dovich [182], which has been measured in cesium [183] and ytterbium [184].

tential signals from direct detection experiments and astrophysical and cosmological sources, has been conducted. The possibility of EM moments of gravitinos, *i.e.* spin-3/2 particles, was discussed in refs. [215–217], and an analysis of direct detection, collider physics, and thermal production for Majorana particles with EM moments was conducted in ref. [218] for spin $s \leq 2$.

3.2 Warm-up: diagonal electromagnetic moments

3.2.1 The EM vertex and the EFT

Now we turn to the calculation of the diagonal EM moments of a neutral spin-1/2 fermion, allowing processes with an off-shell photon of the type $\chi(p_1) \rightarrow \chi(p_2) + \gamma(q)$.

The most general vertex of a fermion with the EM field can be written as (see for example refs. [219–223])

$$\mathcal{M}_\mu(q) = (\gamma_\mu - q_\mu \not{q}/q^2) [f_Q(q^2) + f_A(q^2)q^2\gamma^5] + i\sigma_{\mu\nu}q^\nu [f_M(q^2) + if_E(q^2)\gamma^5], \quad (3.8)$$

where f_Q , f_A , f_M and f_E are respectively the charge-, anapole-, magnetic dipole- and electric dipole form factor and $q^\mu = (p_1 - p_2)^\mu$ is the outgoing photon momentum. Further, $\not{q} = \gamma_\mu q^\mu$, $\gamma^5 = i\gamma^0\gamma^1\gamma^2\gamma^3$ and $\sigma^{\mu\nu} = \frac{i}{2}[\gamma^\mu, \gamma^\nu]$.

In the on-shell limit, these form factors reduce to their respective EM moment:

$$f_Q(q^2 \rightarrow 0) = eQ_\chi + q^2 b_\chi, \quad f_A(q^2 \rightarrow 0) = \mathcal{A}_\chi, \quad (3.9a)$$

$$f_M(q^2 \rightarrow 0) = \mu_\chi, \quad f_E(q^2 \rightarrow 0) = d_\chi, \quad (3.9b)$$

where Q_χ is the charge of χ in units of $e > 0$, b_χ is its charge radius⁴, \mathcal{A}_χ its anapole moment and μ_χ and d_χ are respectively its magnetic- and electric dipole moment.

If the scale of momentum transfer is small compared to the scales generating the EM moments, $q^2 \ll \Lambda^2$, the phenomenology of the fermion-photon interaction can be described by these EM moments via the effective Lagrangian

$$\mathcal{L}_{\text{eff.}} = eQ_\chi \bar{\chi} \gamma^\mu \chi A_\mu \quad (3.10a)$$

$$+ \frac{\mu_\chi}{2} \bar{\chi} \sigma^{\mu\nu} \chi F_{\mu\nu} + \frac{d_\chi}{2} \bar{\chi} \sigma^{\mu\nu} \gamma^5 \chi F_{\mu\nu} \quad (3.10b)$$

$$+ b_\chi \bar{\chi} \gamma^\mu \chi \partial^\nu F_{\mu\nu} + \mathcal{A}_\chi \bar{\chi} \gamma^\mu \gamma^5 \chi \partial^\nu F_{\mu\nu}. \quad (3.10c)$$

In eq. (3.10), χ is the spinor describing the neutral fermion, A_μ is the photon field and $F_{\mu\nu} = \partial_\mu A_\nu - \partial_\nu A_\mu$ its field strength tensor. Note that the charge radius operator has the same dimension as the anapole operator, therefore motivating the need to

⁴The term charge radius stems from the interpretation of the charge form factor as the Fourier transform of the charge distribution $\rho(\mathbf{x})$, whose second term in the expansion is proportional to the charge radius, such that $b_\chi = \frac{1}{6} \int d^3x r^2 \rho(\mathbf{x}) \equiv \frac{1}{6} \langle r_\chi^2 \rangle$ [223].

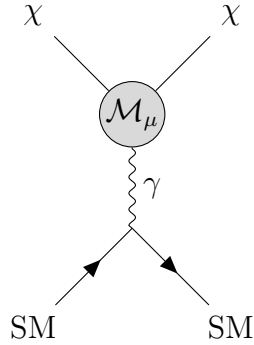


Figure 3.1: A fermion χ interacting with the SM via the photon γ .

expand the charge form factor to the second order in q^2 in eq. (3.9a). This effective Lagrangian results in a portal to the SM, as depicted in fig. 3.1.⁵

In the light of experimental efforts, the hierarchy $q^2 \ll \Lambda^2$ may not be satisfied. In direct detection facilities, the transferred momentum can be of order $\mathcal{O}(100 \text{ MeV})$, such that light quarks or electrons in the loop ($\Lambda = m_q$ or $\Lambda = m_e$) spoil this condition. In this case, one should model the photon interaction with the form factors, introducing an explicit q -dependency. For an approximation, one can set the light masses in the loop expression to zero, in which case the finite photon momentum regularizes the loop integral [225]. However, the limit $q^2 \rightarrow 0$ can safely be taken to calculate the inherent EM moments.

If CP is conserved, the electric dipole moment vanishes, and if χ satisfies the Majorana condition, all but the P- and C-violating anapole moment vanish [219, 226–228]. We discuss this case in more detail in section 3.3.2.

3.2.2 Extraction of the EM moments

The amplitude \mathcal{M}^μ for the $\chi \rightarrow \chi + \gamma$ process can be calculated up to some order in perturbation theory, resulting diagrammatically in

$$i\mathcal{M}^\mu = \begin{array}{c} \chi \\ \diagdown \\ \textcircled{1L} \\ \diagup \\ \chi \\ \vdots \\ \gamma \end{array} + \begin{array}{c} \chi \\ \diagdown \\ \textcircled{2L} \\ \diagup \\ \chi \\ \vdots \\ \gamma \end{array} + \dots, \quad (3.11)$$

⁵The Feynman diagrams in this dissertation were drawn using TikZ-Feynman [224].

where 1L (2L) denotes the one-loop (two-loop) contribution, and we omitted higher-order terms. These loop diagrams can be computed in a specific UV model, resulting in complicated combinations of the kinematic variables, the gamma matrices and loop-integrals. As the EM form factors correspond to the pre-factors of certain combinations of the gamma matrices (see eq. (3.8)), we cannot directly extract them from a given amplitude. We would have to resort to Gordon-like identities to properly re-express the amplitude via the contained EM form factors.

Alternatively, we can use the fact that the matrices

$$\Gamma \in \{\mathbb{1}, \gamma_\mu, i\gamma_5, \gamma_\mu\gamma_5, \sigma_{\mu\nu}\} \quad (3.12)$$

make up a basis [229], and define projection operators $\mathcal{P}_{\mathbb{M}}^\mu$, whose coefficients are determined by matching to the Lorentz structure of a specific EM form factor. Then, this projector can extract the EM form factors from the perturbative amplitude in eq. (3.11).

To determine the projectors, we first express the canonical vertex of eq. (3.8) in terms of the following form factors [1, 230, 231]

$$\begin{aligned} \mathcal{M}^\mu &= F_1(q^2)(\gamma^\mu q^2 - q^\mu \not{q}) + \frac{i}{2m} \sigma^{\mu\nu} q_\nu F_2(q^2) + \frac{1}{m} q^\mu F_3(q^2) \\ &+ G_1(q^2)(\gamma^\mu q^2 - q^\mu \not{q})\gamma^5 + \frac{i}{2m} G_2(q^2) \sigma^{\mu\nu} q_\nu \gamma^5 + \frac{1}{m} G_3(q^2) q^\mu \gamma^5, \end{aligned} \quad (3.13)$$

which are related to the canonical definition as

$$f_Q(q^2) = q^2 F_1(q^2), \quad f_A(q^2) = G_1(q^2), \quad (3.14a)$$

$$f_M(q^2) = \frac{1}{2m} F_2(q^2), \quad f_E(q^2) = -\frac{i}{2m} G_2(q^2). \quad (3.14b)$$

With respect to the vertex parameterization given in eq. (3.13), we may define the projector as [1, 230–232]

$$\begin{aligned} \mathcal{P}_{\mathbb{M}}^\mu &= (\not{p}_1 + m) \left[\left(a_1^{\mathbb{M}} \gamma^\mu + a_2^{\mathbb{M}} \frac{P^\mu}{2m} + a_3^{\mathbb{M}} \frac{q^\mu}{2m} \right) \gamma^5 \right. \\ &\quad \left. + b_1^{\mathbb{M}} \gamma^\mu + b_2^{\mathbb{M}} \frac{P^\mu}{2m} + b_3^{\mathbb{M}} \frac{q^\mu}{2m} \right] (\not{p}_2 + m) \end{aligned} \quad (3.15)$$

$$\equiv (\not{p}_1 + m) \tilde{\mathcal{P}}_{\mathbb{M}}^\mu (\not{p}_2 + m), \quad (3.16)$$

with $\mathbb{M} \in \{G_1, G_2, G_3, F_1, F_2, F_3\}$, $P^\mu = p_1^\mu + p_2^\mu$ and the factors $(\not{p}_{1,2} + m)$ ensure that the spinors satisfy the Dirac equation. We can determine the coefficients $a_i^{\mathbb{M}}$ and $b_i^{\mathbb{M}}$ by solving the equation

$$\text{tr}(\mathcal{P}_{\mathbb{M}}^\mu i\mathcal{M}_\mu) = \mathbb{M} \quad (3.17)$$

using the vertex parameterization of eq. (3.13) and the kinematics

$$p_1^2 = p_2^2 = m^2, \quad p_1 \cdot p_2 = (2m^2 - q^2)/2, \quad q \cdot p_1 = q^2/2, \quad q \cdot p_2 = -q^2/2. \quad (3.18)$$

We find the following projectors⁶:

$$\tilde{\mathcal{P}}_{F_1}^\mu = -i \frac{6mP^\mu + (q^2 - 4m^2)\gamma^\mu}{4q^2(4m^2 - q^2)^2}, \quad \tilde{\mathcal{P}}_{G_1}^\mu = i \frac{q^2\gamma^\mu - 2mq^\mu}{4q^2(4m^2 - q^2)}\gamma^5, \quad (3.19a)$$

$$\tilde{\mathcal{P}}_{F_2}^\mu = im \frac{m(4m^2 - q^2)\gamma^\mu - (2m^2 + q^2)P^\mu}{q^2(4m^2 - q^2)^2}, \quad \tilde{\mathcal{P}}_{G_2}^\mu = -i \frac{mP^\mu}{q^2(4m^2 - q^2)}\gamma^5, \quad (3.19b)$$

$$\tilde{\mathcal{P}}_{F_3}^\mu = -i \frac{mq^\mu}{2q^2(4m^2 - q^2)}, \quad \tilde{\mathcal{P}}_{G_3}^\mu = -i \frac{mq^\mu}{2q^4}\gamma^5. \quad (3.19c)$$

Note that these projectors can safely be defined in $D = 4$ as the amplitude \mathcal{M}^μ they multiply is inherently convergent in $D = 4$ [233].

Therefore, by projecting out the form factors and taking the photon on-shell, we can map the UV physics generating the loops to the coefficients in the effective field theory, whose Lagrangian is given by eq. (3.10).

3.2.3 Diagonal EM moments of neutral spin-1/2 fermions

To showcase the projector method, we derive here the one-loop contribution to the EM moments \mathbb{M} of a neutral Dirac fermion χ due to a t -channel mediator.⁷ For now, we ignore the exact model or the origin of this interaction and leave this for the upcoming chapters, in which we apply these results to concrete UV models of DM and neutrinos. In that sense, this section's results can be considered the building blocks to easily calculate the EM moments in a generic model where the fermion interacts via a t -channel mediator with the photon. Note that these classes of models do not generate a millicharge Q_χ .

Concretely, we consider the following interactions via a charged scalar S ,

$$\mathcal{L} = \bar{\chi} \left[c_L P_L + c_R e^{i\phi_{\text{CP}}} P_R \right] S^* f + \text{h.c.}, \quad (3.20)$$

and a vector boson V^μ

$$\mathcal{L} = \bar{\chi} \gamma^\mu \left[v_L P_L + v_R e^{i\Phi_{\text{CP}}} P_R \right] \chi^- V_\mu^+ + \text{h.c.}, \quad (3.21)$$

leading to the *scalar*- and *vector* contribution \mathbb{M}^S and \mathbb{M}^V , respectively.⁸ Here, $c_{L/R}$ and $v_{L/R}$ are real Yukawa-type couplings, parameterizing the strength with which

⁶The anapole projector $\tilde{\mathcal{P}}_{G_1}^\mu$ was already derived in ref. [1].

⁷The symbol $\mathbb{M} \in \{Q_\chi, \mu_\chi, d_\chi, \mathcal{A}, b_\chi\}$ denotes from now on the canonical EM moments.

⁸To calculate the full contribution to the EM moments from a vector boson, one has to include the diagrams with associated Goldstone bosons.

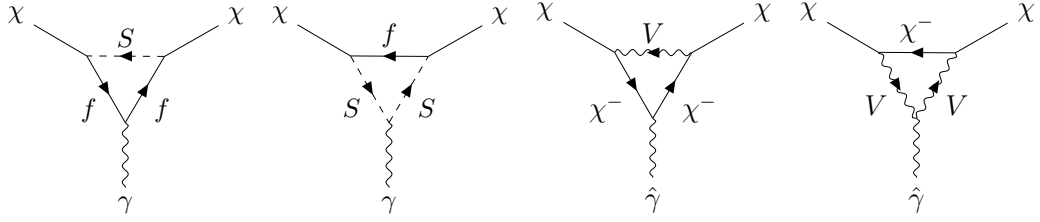


Figure 3.2: Interaction between the neutral fermion χ with the photon at one-loop level. Note that depending on the exact model, the external states may be either Dirac- or Majorana fermions. For the latter case, the charge-conjugated diagrams have to be included. Note that for the two rightmost diagrams, a background photon replaces the external photon; see text for details.

the neutral fermion χ interacts via the left/right ($P_{L/R}$) component of the fermion f or χ^- . For simplicity, we assume that the fermions f and χ^- are color singlets; if $f = q$, a color factor has to be added to the EM moments accordingly. Furthermore, Φ_{CP} and ϕ_{CP} are CP-violating phases, which could, for example, originate from fermion- or scalar mixing, respectively. We discuss the latter case in more detail in chapter 6; the former case was considered in ref. [234] for a $\text{SU}(2)_L \times \text{SU}(2)_R \times \text{U}(1)$ gauge theory, where a relative CP phase between the $W_{L/R}$ bosons can introduce a physical CP phase Φ_{CP} , affecting the dipole moments of neutrinos.

Both eq. (3.20) and eq. (3.21) generate EM moments at the one-loop level via the diagrams depicted in fig. 3.2. If the external neutral fermion χ is self-conjugated, all EM moments except the anapole moment vanish. Furthermore, in this scenario, the anapole moment of a Majorana fermion is twice the anapole moment of a Dirac fermion, *i.e.* $\mathcal{A}_M = 2 \times \mathcal{A}_D$ [223, 226–228]. In the language of the Feynman diagrams, this relationship manifests itself by including the respective self-conjugate diagrams. Using the Feynman rules for Majorana fermions introduced in refs. [235, 236], the contributions to the dipole moments and the charge radius cancel exactly, whereas the anapole moment is doubled in value [1, 2]. We discuss this formalism in more detail in section 3.3.2.

A naive evaluation of the diagrams depicted in fig. 3.2 with vector boson V leads to a UV-divergent, gauge-dependent, and thus unphysical result for the dimension-6 operators. These issues have been encountered in the past in the evaluation of the charge radius and anapole moment of neutrinos [185–196, 237], which have been ultimately resolved by using the Pinch Technique (PT)⁹ [190, 193, 194], or, equivalently, the background field method (BFM) [239–241].

This elegant equivalence was used for many calculations to tame apparent unphysical results. Using the BFM, the W boson contribution to the anapole moment of

⁹See ref. [238] for a review of the PT.

the lightest neutralino was conducted in refs. [1, 2] and the electric dipole moments of fermions in the two-Higgs doublet model was calculated in a gauge-invariant way in refs. [242, 243]. In ref. [244], the magnetic dipole moment of fermions was calculated using the PT, emphasizing the simplicity and the strength to explicitly test the gauge dependency. It is also noted that the standard calculation procedure cannot account for the gauge dependency of the off-shell form factors. Therefore, besides reproducing the standard results for the dipole moments, the PT or BFM is crucial in consistently calculating the momentum-dependent dipole form factors.

Thus, for the vector interaction in eq. (3.21), we evaluate the diagrams in the background field Feynman gauge to obtain a gauge-independent and UV convergent expression for the charge radius and the anapole moment. Effectively, this is achieved by replacing the photon with its background field analog, $\gamma \rightarrow \hat{\gamma}$, such that at the one-loop order in the background Feynman gauge, the following vertices are adjusted as [245]

$$i\hat{\Gamma}_{\gamma VV}^{\mu\nu\rho}(k_1, k_2, k_3) = -ie [g_{\nu\rho}(k_3 - k_2)_\mu + g_{\mu\nu}(k_2 - k_1 + k_3)_\rho + g_{\rho\mu}(k_1 - k_3 - k_2)_\nu] \quad (3.22)$$

and

$$i\hat{\Gamma}_{\gamma GV}^{\mu\nu\rho}(k_1, k_2, k_3) = 0, \quad (3.23)$$

where G denotes the Goldstone mode associated with the spontaneous symmetry breaking, giving rise to the mass of the gauge boson V .

Following the outlined procedure above, we calculate the amplitude $i\mathcal{M}$ corresponding to the diagrams shown in fig. 3.2 and extract the contributions to the diagonal EM moment \mathbb{M} using the projectors of eq. (3.19) and the relations of eq. (3.14), where we used `FeynCalc` [246–248] for the Dirac algebra and loop reduction, `Package-X` [232, 249] for the analytical simplification of the loop integrals, and `FeynHelpers` [250] for linking these packages. In the following, we report the results for the diagonal EM moments of a neutral Dirac fermion.

For the scalar mediator, similar calculations of the EM moments of DM have been reported in refs. [1–3, 225, 251–256]. For the vector mediator, the anapole moment of Majorana fermions was calculated in refs. [1, 2].

Magnetic dipole moment

We find that the scalar contribution to the magnetic moment can be written as

$$\mu_\chi^S = \frac{-eQ_f}{32\pi^2 m_\chi} \left[(c_L^2 + c_R^2) \mathcal{F}_1^S \left(\frac{m_f}{m_\chi}, \frac{m_S}{m_\chi} \right) + 2c_L c_R \cos \phi_{\text{CP}} \mathcal{F}_2^S \left(\frac{m_f}{m_\chi}, \frac{m_S}{m_\chi} \right) \right], \quad (3.24)$$

where we defined the loop functions

$$\begin{aligned} \mathcal{F}_1^S(\mu, \eta) = & -1 + \frac{1}{2}(\mu^2 - \eta^2) \log(\mu^2/\eta^2) \\ & - \frac{(\eta^2 - 1)(\eta^2 - 2\mu^2) - \mu^2(3 - \mu^2)}{\sqrt{\Delta}} \operatorname{arctanh} \left(\frac{\sqrt{\Delta}}{\eta^2 + \mu^2 - 1} \right) \end{aligned} \quad (3.25)$$

and

$$\mathcal{F}_2^S(\mu, \eta) = \mu \left[\frac{1}{2} \log \left(\frac{\mu^2}{\eta^2} \right) + \frac{\eta^2 - \mu^2 + 1}{\sqrt{\Delta}} \operatorname{arctanh} \left(\frac{\sqrt{\Delta}}{\eta^2 + \mu^2 - 1} \right) \right], \quad (3.26)$$

and we introduced $\Delta = (\mu^2 - \eta^2 + 1)^2 - 4\mu^2$.¹⁰

Similarly, the vector contribution reads

$$\mu_\chi^V = \frac{-eQ_f}{16\pi^2 m_\chi} \left[(v_L^2 + v_R^2) \mathcal{F}_1^V \left(\frac{m_{\chi^-}}{m_\chi}, \frac{m_V}{m_\chi} \right) + 2v_L v_R \cos \Phi_{\text{CP}} \mathcal{F}_2^V \left(\frac{m_{\chi^-}}{m_\chi}, \frac{m_V}{m_\chi} \right) \right], \quad (3.27)$$

with

$$\begin{aligned} \mathcal{F}_1^V(\mu, \eta) = & -1 + \frac{1}{2}(\mu^2 - \eta^2 + 2) \log(\mu^2/\eta^2) \\ & - \frac{(\eta^4 - \eta^2(2\mu^2 + 3) + \mu^4 + \mu^2 + 2)}{\sqrt{\Delta}} \operatorname{arctanh} \left(\frac{\sqrt{\Delta}}{\eta^2 + \mu^2 - 1} \right), \end{aligned} \quad (3.28)$$

and

$$\mathcal{F}_2^V(\mu, \eta) = -2\mu \left[\frac{1}{2} \log \left(\frac{\mu^2}{\eta^2} \right) + \frac{\eta^2 - \mu^2 - 1}{\sqrt{\Delta}} \operatorname{arctanh} \left(\frac{\sqrt{\Delta}}{\eta^2 + \mu^2 - 1} \right) \right]. \quad (3.29)$$

Both contributions scale as $\sim m_\chi^{-1}$ with the remaining kinematical dependency included in the loop functions $\mathcal{F}_{1,2}^{S,V}$. For large mediator mass $m_{S,V} \gg m_\chi$ or $m_{f,\chi^-} \gg m_\chi$, the overall scaling is $\mu_\chi \sim m_X^{-1}$ (see appendix B.4), where X denotes the heaviest state amongst S (V) and f (χ^-).

Note that the magnetic moment can be generated via two different loop functions. The first, $\sim \mathcal{F}_1^{S,V}$, can be interpreted as originating from a mass-insertion occurring at an external leg, whereas the term $\sim \mathcal{F}_2^{S,V}$ is due to an internal mass-insertion. The interpretation comes from the observation that the former term scales as $\mu_\chi \sim m_\chi$ for $m_\chi \ll m_X$, whereas the latter scales as $\mu_\chi \sim m_f$ in the same limit.

¹⁰We note that this result can also be obtained using the expressions for the anomalous magnetic moment of the muon [257].

Electric dipole moment

For the electric dipole moment, we find respectively the scalar and vector contribution

$$d_\chi^S = \frac{eQ_f}{16\pi^2 m_\chi} c_L c_R \sin \phi_{\text{CP}} \mathcal{F}_2^S \left(\frac{m_f}{m_\chi}, \frac{m_S}{m_\chi} \right) \quad (3.30)$$

and

$$d_\chi^V = \frac{eQ_f}{8\pi^2 m_\chi} v_L v_R \sin \Phi_{\text{CP}} \mathcal{F}_2^V \left(\frac{m_{\chi^-}}{m_\chi}, \frac{m_V}{m_\chi} \right). \quad (3.31)$$

As expected, if the theory preserves CP, *i.e.* $\phi_{\text{CP}} = \Phi_{\text{CP}} = 0$, both contributions yield a zero electric dipole moment.

Anapole moment

For the anapole moment of the Dirac fermion, the result reads

$$\mathcal{A}_\chi^S = \frac{-eQ_f}{192\pi^2 m_\chi^2} \left[|c_L|^2 - |c_R|^2 \right] \mathcal{F}_3^S \left(\frac{m_f}{m_\chi}, \frac{m_S}{m_\chi} \right) \quad (3.32)$$

for the scalar contribution and

$$\mathcal{A}_\chi^V = \frac{-eQ_f}{96\pi^2 m_\chi^2} \left[|v_L|^2 - |v_R|^2 \right] \mathcal{F}_3^V \left(\frac{m_{\chi^-}}{m_\chi}, \frac{m_V}{m_\chi} \right) \quad (3.33)$$

for the vector contribution. The anapole loop functions are defined as

$$\mathcal{F}_3^S(\mu, \eta) = \frac{3}{2} \log \left(\frac{\mu^2}{\eta^2} \right) + \frac{3\eta^2 - 3\mu^2 + 1}{\sqrt{\Delta}} \operatorname{arctanh} \left(\frac{\sqrt{\Delta}}{\eta^2 + \mu^2 - 1} \right) \quad (3.34)$$

and

$$\mathcal{F}_3^V(\mu, \eta) = \frac{3}{2} \log \left(\frac{\mu^2}{\eta^2} \right) + \frac{3\eta^2 - 3\mu^2 - 7}{\sqrt{\Delta}} \operatorname{arctanh} \left(\frac{\sqrt{\Delta}}{\eta^2 + \mu^2 - 1} \right). \quad (3.35)$$

The expressions we find for the anapole moment, are $\sim (|c_L|^2 - |c_R|^2)$ and $\sim (|v_L|^2 - |v_R|^2)$, *viz.* they respectively vanish if $|c_L| = |c_R|$ or $|v_L| = |v_R|$, making the P violation explicit. Therefore, to generate a large anapole moment of a fermion χ , the UV theory itself has to violate P to a large extent, as the amount of P violation is transferred to the magnitude of the anapole moment. For example, in the SM, the neutrino anapole moment is generated via the weak interaction, which maximally violates parity, see chapter 7.

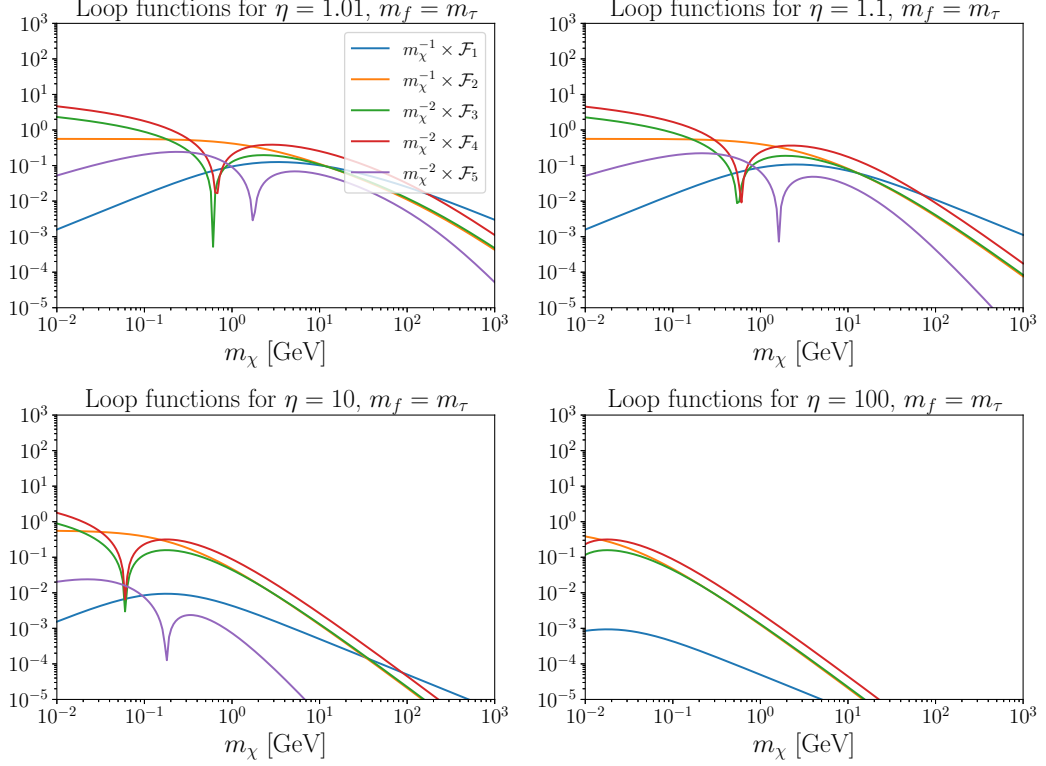


Figure 3.3: All loop functions \mathcal{F}_i^S generating the EM moments in our scalar toy model for different values of $\eta = m_S/m_\chi$ and $m_f = m_\tau$, rescaled by the power of m_χ entering the respective moment.

Charge radius operator

We find for the charge radius operator the scalar contribution

$$b_\chi^S = \frac{-eQ_f}{384\pi^2 m_\chi^2} \left[(c_L^2 + c_R^2) \mathcal{F}_4^S \left(\frac{m_f}{m_\chi}, \frac{m_S}{m_\chi} \right) + 2c_{LCR} \cos \phi_{CP} \mathcal{F}_5^S \left(\frac{m_f}{m_\chi}, \frac{m_S}{m_\chi} \right) \right], \quad (3.36)$$

where we defined the loop functions

$$\begin{aligned} \mathcal{F}_4^S(\mu, \eta) &= \frac{2(8\Delta^2 + \Delta(9\eta^2 + 7\mu^2 - 5) - 4\mu^2(3\eta^2 + \mu^2 - 1))}{\Delta^{3/2}} \operatorname{arctanh} \left(\frac{\sqrt{\Delta}}{\eta^2 + \mu^2 - 1} \right) \\ &+ \frac{4(4\Delta + \eta^2 + 3\mu^2 - 1)}{\Delta} + (8\mu^2 - 8\eta^2 - 1) \log \left(\frac{\eta^2}{\mu^2} \right) \end{aligned} \quad (3.37)$$

and

$$\mathcal{F}_5^S(\mu, \eta) = 8\mu \left[\frac{\Delta + \eta^2(-\Delta + 2\mu^2 + 1) + \mu^2(\Delta - 2\mu^2 + 3) - 1}{\Delta^{3/2}} \operatorname{arctanh} \left(\frac{\sqrt{\Delta}}{\eta^2 + \mu^2 - 1} \right) \right. \quad (3.38)$$

$$\left. + \frac{\mu^2 - \eta^2}{\Delta} + \frac{1}{2} \log \left(\frac{\eta^2}{\mu^2} \right) \right]. \quad (3.39)$$

The vector contribution reads

$$b_\chi^V = \frac{-eQ_f}{192\pi^2 m_\chi^2} \left[(v_L^2 + v_R^2) \mathcal{F}_4^V \left(\frac{m_{\chi^-}}{m_\chi}, \frac{m_V}{m_\chi} \right) + 2v_L v_R \cos \Phi_{\text{CP}} \mathcal{F}_5^V \left(\frac{m_{\chi^-}}{m_\chi}, \frac{m_V}{m_\chi} \right) \right], \quad (3.40)$$

with loop functions

$$\begin{aligned} \mathcal{F}_4^V(\mu, \eta) = & \frac{4(4\eta^4 - \eta^2(8\mu^2 + 7) + 4\mu^4 - 5\mu^2 + 3)}{\Delta} - (8\eta^2 - 8\mu^2 - 5) \log(\eta^2/\mu^2) \\ & + 2\Delta^{-3/2} \operatorname{arctanh} \left(\frac{\sqrt{\Delta}}{\eta^2 + \mu^2 - 1} \right) \times \left[- (32\eta^2 + 19)\mu^6 + (48\eta^4 + 9\eta^2 + 19)\mu^4 \right. \\ & \left. + (\eta^2 - 1)^2(8\eta^4 - 13\eta^2 + 9) - (32\eta^6 - 39\eta^4 + 14\eta^2 + 17)\mu^2 + 8\mu^8 \right] \end{aligned} \quad (3.41)$$

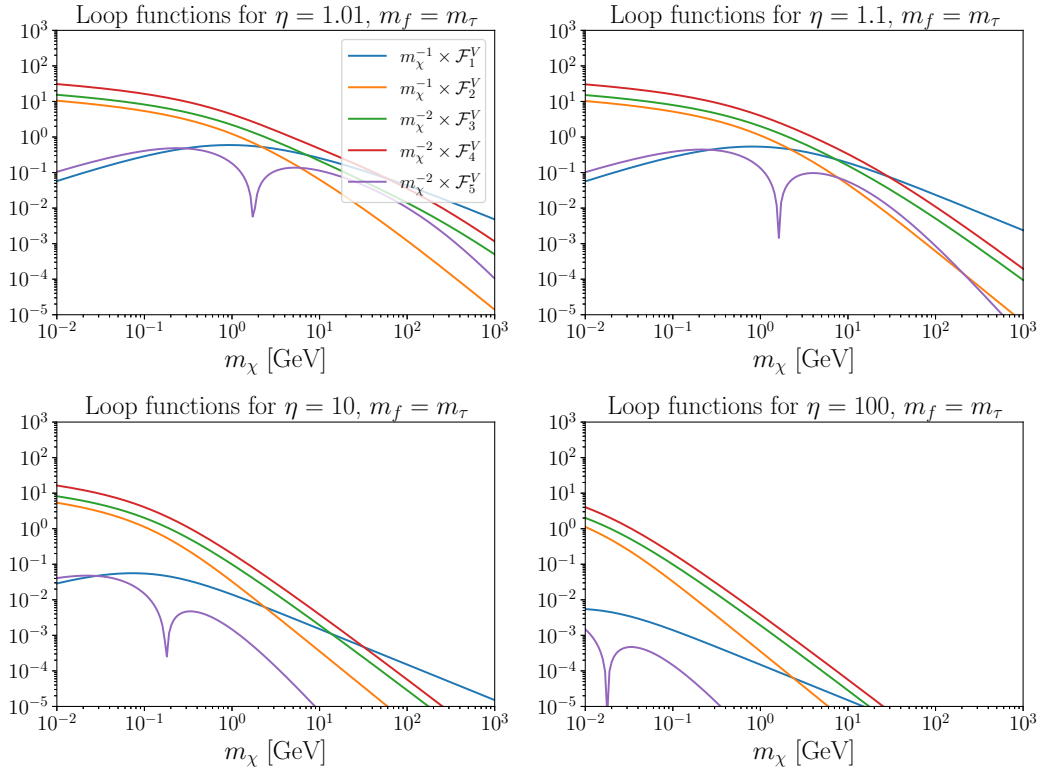
and

$$\begin{aligned} \mathcal{F}_5^V(\mu, \eta) = & 16\mu \left[\frac{\eta^2 - \mu^2}{\Delta} + \frac{1}{2} \log(\mu^2/\eta^2) \right. \\ & \left. + \frac{(\eta^2 - \mu^2)(\eta^4 - \eta^2(2\mu^2 + 3) + \mu^4 - 3\mu^2 + 2)}{\Delta^{3/2}} \operatorname{arctanh} \left(\frac{\sqrt{\Delta}}{\eta^2 + \mu^2 - 1} \right) \right]. \end{aligned} \quad (3.42)$$

We show the functional behavior of all loop functions $\mathcal{F}_i^S(\mu, \eta)$ ($\mathcal{F}_i^V(\mu, \eta)$) in fig. 3.3 (fig. 3.4) for fixed $\eta \in \{1.01, 1, 10, 100\}$ and a tau-philic model ($f = \tau$), where we rescaled the loop functions with the power of m_χ entering the EM moments to allow for better comparison of their relative sizes.

All loop functions are enhanced for small mass-splittings $\eta \rightarrow 1$ or $\mu \rightarrow 1$, as long as the other particle in the loop is light. The physical interpretation is that for such mass configurations, the loop particles can be on-shell [225].

Finally, we note from figs. 3.3 and 3.4 that multiple moments can be of comparable size simultaneously. Therefore, the typical EFT assumption of having only one


 Figure 3.4: Same as fig. 3.3, but for the vector loop functions \mathcal{F}_i^V .

moment dominate the interaction with the photon is only valid in some particular regions in parameter space. We will discuss this point further in the context of the Dirac DM candidate and its potential signature in DM direct detection experiments in chapter 4.

3.3 General electromagnetic moments of fermions

In the previous section, we discussed the diagonal EM form factors and the calculation of the corresponding moments for the building block Lagrangians eqs. (3.20) and (3.21) and presented the results in terms of loop functions. Here, we generalize this approach for processes $\chi_1 \rightarrow \chi_2 + \gamma$, which includes the diagonal elements from section 3.2 and the transition moments between the neutral fermions χ_1 and χ_2 .

3.3.1 Dirac fermions

Conceptually, we follow the steps outlined in detail in section 3.2, but keep the external fermions generic. In the general case the form factors of eq. (3.8) are now matrices, containing the *diagonal* and *transition-* or *off-diagonal* EM form factors,

$$\begin{aligned} \mathcal{M}_{ji}^\mu = & (\gamma^\mu - q^\mu \not{q}/q^2) [(f_Q)_{ji}(q^2) + (f_A)_{ji}(q^2)q^2\gamma^5] \\ & + i\sigma^{\mu\nu}q_\nu [(f_M)_{ji}(q^2) + i(f_E)_{ji}(q^2)\gamma^5], \end{aligned} \quad (3.43)$$

where i (j) labels the initial (final) external mass eigenstate and the form factors f_Q , f_A , f_M , and f_E are now matrix-valued. For small outgoing momentum transfers $q^2 = (p_1 - p_2)^2 \simeq 0$, the form factors reduce to their respective static analog,

$$(f_Q)_{ji}(q^2 \rightarrow 0) = eQ_{ji} + q^2 b_{ji}, \quad (f_A)_{ji}(q^2 \rightarrow 0) = \mathcal{A}_{ji}, \quad (3.44a)$$

$$(f_M)_{ji}(q^2 \rightarrow 0) = \mu_{ji}, \quad (f_E)_{ji}(q^2 \rightarrow 0) = d_{ji}. \quad (3.44b)$$

If $j = i$, the moment is referred to as *diagonal* moment, whereas for $j \neq i$, it is a *transition* or *off-diagonal* moment.

For the building blocks, we consider the generalized versions of eqs. (3.20) and (3.21),

$$\mathcal{L} = \bar{\chi}_i [c_L^i P_L + c_R^i P_R] f S^* + \text{h.c.}, \quad (3.45)$$

and

$$\mathcal{L} = \bar{\chi}_i \gamma^\mu [v_L^i P_L + v_R^i P_R] f V_\mu^\dagger + \text{h.c.}, \quad (3.46)$$

respectively and consider the couplings $c_{L/R}^i$ and $v_{L/R}^i$ to be complex from now on.

At the one-loop level, the interactions given in eqs. (3.45) and (3.46) generate a portal to the photon, which we depict in fig. 3.5. We evaluate these diagrams using `Package-X` [232, 249] and extract their contribution to the EM moments \mathbb{M}_{ji}^S .

We find that the EM moments generated by the scalar mediator can be written compactly as

$$\begin{aligned} \mathbb{M}_{ji}^S = & \frac{eQ_f}{32\pi^2} \left\{ \left[c_L^j (c_L^i)^* \pm c_R^j (c_R^i)^* \right] \mathcal{F}_{\mathbb{M}}^S \left(\frac{m_f}{m_{\chi_1}}, \frac{m_S}{m_{\chi_1}}, \frac{m_{\chi_2}}{m_{\chi_1}} \right) \right. \\ & \left. + \left[c_L^j (c_R^i)^* \pm c_R^j (c_L^i)^* \right] \mathcal{G}_{\mathbb{M}}^S \left(\frac{m_f}{m_{\chi_1}}, \frac{m_S}{m_{\chi_1}}, \frac{m_{\chi_2}}{m_{\chi_1}} \right) \right\}, \end{aligned} \quad (3.47)$$

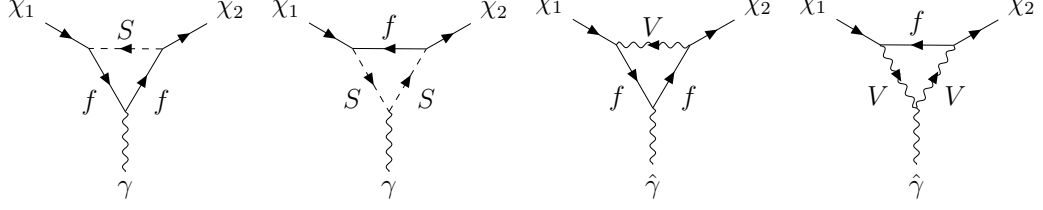


Figure 3.5: One-loop transition diagrams generating the EM moments; for the diagrams with vector bosons, we employ the background field method; see section 3.2 for details.

and for the vector mediator as

$$\begin{aligned} \mathbb{M}_{ji}^V = \frac{eQ_f}{32\pi^2} \left\{ \left[v_L^j(v_L^i)^* \pm v_R^j(v_R^i)^* \right] \mathcal{F}_{\mathbb{M}}^V \left(\frac{m_f}{m_{\chi_1}}, \frac{m_V}{m_{\chi_1}}, \frac{m_{\chi_2}}{m_{\chi_1}} \right) \right. \\ \left. + \left[v_L^j(v_R^i)^* \pm v_R^j(v_L^i)^* \right] \mathcal{G}_{\mathbb{M}}^V \left(\frac{m_f}{m_{\chi_1}}, \frac{m_V}{m_{\chi_1}}, \frac{m_{\chi_2}}{m_{\chi_1}} \right) \right\}, \end{aligned} \quad (3.48)$$

where the upper sign (+) is for $\mathbb{M} = \mu, b$ and the lower sign (-) for $\mathbb{M} = d, \mathcal{A}$.

Because the EM current is hermitian, so are the EM moments [223]

$$\mathbb{M}^{S,V} = (\mathbb{M}^{S,V})^\dagger. \quad (3.49)$$

Thus, the loop functions satisfy

$$\mathcal{F}_{\mathbb{M}}^{S,V} \left(\frac{m_f}{m_{\chi_1}}, \frac{m_{S,V}}{m_{\chi_1}}, \frac{m_{\chi_2}}{m_{\chi_1}} \right) = \mathcal{F}_{\mathbb{M}}^{S,V*} \left(\frac{m_f}{m_{\chi_2}}, \frac{m_{S,V}}{m_{\chi_2}}, \frac{m_{\chi_1}}{m_{\chi_2}} \right), \quad (3.50a)$$

$$\mathcal{G}_{\mathbb{M}}^{S,V} \left(\frac{m_f}{m_{\chi_1}}, \frac{m_{S,V}}{m_{\chi_1}}, \frac{m_{\chi_2}}{m_{\chi_1}} \right) = \pm \mathcal{G}_{\mathbb{M}}^{S,V*} \left(\frac{m_f}{m_{\chi_2}}, \frac{m_{S,V}}{m_{\chi_2}}, \frac{m_{\chi_1}}{m_{\chi_2}} \right). \quad (3.50b)$$

Similarly, the EM moments for anti-fermions, denoted by $\overline{\mathbb{M}}$, can be obtained from the EM moments of fermions by employing CPT-invariance [223], resulting in

$$\begin{aligned} \overline{Q}^{S,V} &= -(Q^{S,V})^*, \\ \overline{\mu}^{S,V} &= -(\mu^{S,V})^*, \quad \overline{d}^{S,V} = -(d^{S,V})^*, \\ \overline{\mathcal{A}}^{S,V} &= (\mathcal{A}^{S,V})^*, \quad \overline{b}^{S,V} = -(b^{S,V})^*. \end{aligned} \quad (3.51)$$

Without loss of generality, we therefore focus on the matrices $\mathbb{M}_{ji}^{S,V}$ for the remaining part of the analysis.

We provide the loop functions $\mathcal{F}_{\mathbb{M}}^{S,V}$ and $\mathcal{G}_{\mathbb{M}}^{S,V}$ in the general case in appendix B.1, for the diagonal case in appendix B.2, for large mass-splittings between χ_1 and χ_2 in appendix B.3, and finally for the limit of small external masses in appendix B.4. Note that eq. (3.48) does not include the Goldstone modes, which are model-dependent and have to be included using eq. (3.47).

3.3.2 Majorana fermions

The calculation of EM moments for $\chi_{1,2}$ being Majorana fermions follows a similar approach to the Dirac case. We extract the form factors from one-loop diagrams that describe the coupling to the photon and take the on-shell limit $q^2 \rightarrow 0$. As noted in section 3.2.3, the resulting form factors differ fundamentally, owing to the following crucial differences between Dirac- and Majorana fermions:

- The number of diagrams is doubled because reversed processes must also be considered. Following the conventions proposed in refs. [235, 236], we adopt a global fermion flow and modify the vertices and propagators for reversed diagrams. This results in diagrams similar to those in fig. 3.5, but with opposite charge flows relative to the fixed fermion flow. For these diagrams, the vertices and propagators are adjusted as:

$$\Gamma' = \mathcal{C}\Gamma^T\mathcal{C}^{-1}, \quad (3.52)$$

$$S'(p) = \mathcal{C}S(p)^T\mathcal{C}^{-1} = S(-p), \quad (3.53)$$

where \mathcal{C} represents the charge-conjugation matrix, Γ is a vertex, and $S(p)$ the fermion propagator. The total amplitude for the Majorana case is then the sum of the “Dirac-like” diagrams and the reversed (or conjugated) diagrams.

- Under charge conjugation, a Majorana spinor satisfies

$$\lambda^*\psi = \psi^c = \mathcal{C}\bar{\psi}^T, \quad (3.54)$$

where λ is an arbitrary phase factors [258–260], set to unity in refs. [235, 236]. However, sometimes it can be convenient to keep this phase explicit, which translates into a phase factor in the plane wave expansion

$$\psi = \int \frac{d^3p}{(2\pi)^3 2E_p} \sum_{s=\pm\frac{1}{2}} \left(f_s(\mathbf{p})u_s(\mathbf{p})e^{-ip\cdot x} + \lambda f_s^\dagger(\mathbf{p})v_s(\mathbf{p})e^{ip\cdot x} \right), \quad (3.55)$$

and thus affects the reversed diagrams [209, 228, 258, 261] and seemingly the total amplitude. Of course, physical results are independent of the choice of this phase [258, 262]. Following ref. [234], we initially leave these phases implicit and discuss their explicit incorporation subsequently.

Taking these adjustments for the Majorana case into consideration, we find that the EM moments of two Majorana fermions can be written as

$$(\mathbb{M}_{ji}^{S,V})^M = (\mathbb{M}_{ji}^{S,V})^D \mp (\mathbb{M}_{ji}^{S,V})^D (c_{L/R}^{i,j} \rightarrow (c_{L/R}^{i,j})^*, v_{L/R}^{i,j} \rightarrow (v_{L/R}^{i,j})^*), \quad (3.56)$$

where the upper and lower signs correspond to $\mathbb{M} = \mu, b$ and $\mathbb{M} = d, \mathcal{A}$, respectively, and $(\mathbb{M}_{ji}^{S,V})^D$ denotes the EM moments for Dirac fermions given in eqs. (3.47) and (3.48). In terms of the loop functions, eq. (3.56) reads

$$\begin{aligned}
 (\mathbb{M}_{ji}^S)^M = i \frac{eQ_f}{16\pi^2} \left\{ \text{Im} \left(c_L^j (c_L^i)^* + c_R^j (c_R^i)^* \right) \mathcal{F}_{\mathbb{M}}^S \left(\frac{m_f}{m_{\chi_1}}, \frac{m_S}{m_{\chi_1}}, \frac{m_{\chi_2}}{m_{\chi_1}} \right) \right. \\
 \left. + \text{Im} \left(c_L^j (c_R^i)^* + c_R^j (c_L^i)^* \right) \mathcal{G}_{\mathbb{M}}^S \left(\frac{m_f}{m_{\chi_1}}, \frac{m_S}{m_{\chi_1}}, \frac{m_{\chi_2}}{m_{\chi_1}} \right) \right\} \quad (3.57)
 \end{aligned}$$

for $\mathbb{M} = \mu, b$, and for $\mathbb{M} = d, \mathcal{A}$ we find

$$\begin{aligned}
 (\mathbb{M}_{ji}^S)^M = \frac{eQ_f}{16\pi^2} \left\{ \text{Re} \left(c_L^j (c_L^i)^* - c_R^j (c_R^i)^* \right) \mathcal{F}_{\mathbb{M}}^S \left(\frac{m_f}{m_{\chi_1}}, \frac{m_S}{m_{\chi_1}}, \frac{m_{\chi_2}}{m_{\chi_1}} \right) \right. \\
 \left. + \text{Re} \left(c_L^j (c_R^i)^* - c_R^j (c_L^i)^* \right) \mathcal{G}_{\mathbb{M}}^S \left(\frac{m_f}{m_{\chi_1}}, \frac{m_S}{m_{\chi_1}}, \frac{m_{\chi_2}}{m_{\chi_1}} \right) \right\}, \quad (3.58)
 \end{aligned}$$

with similar expressions for the vector contribution $(\mathbb{M}_{ji}^V)^M$.

As noted above, alternatively, the creation phase can be made explicit, leading to an additional factor of λ_i in the Feynman rules for the reversed diagrams. Then, eq. (3.56) can be written as

$$(\mathbb{M}_{ji}^{S,V})^M = (\mathbb{M}_{ji}^{S,V})^D \mp \lambda_{ij} \times (\mathbb{M}_{ji}^{S,V})^D \left(\tilde{c}_{L/R}^{i,j} \rightarrow (\tilde{c}_{L/R}^{i,j})^*, \tilde{v}_{L/R}^{i,j} \rightarrow (\tilde{v}_{L/R}^{i,j})^* \right), \quad (3.59)$$

where $-\lambda_{ij}$ for $\mathbb{M} = \mu, b$ and $+\lambda_{ij}$ for $\mathbb{M} = d, \mathcal{A}$, we defined $\lambda_{ij} = \lambda_i^* \lambda_j$ and $\tilde{c}_{L/R}^{i,j}$ and $\tilde{v}_{L/R}^{i,j}$ are the couplings in the new basis in which the creation phases are factored out. We discuss these two formalisms in more detail when applying the general findings of this section to Majorana neutrinos in section 7.2.2.

3.4 Numerical analysis of the general loop functions

We found in section 3.3 that the EM moments for Dirac- and Majorana fermions can be expressed in terms of prefactors that depend only on the couplings, as well as the loop functions $\mathcal{F}_{\mathbb{M}}^{S,V}$ and $\mathcal{G}_{\mathbb{M}}^{S,V}$ carrying all the dependency on the mass parameters.

In this section, we discuss the numerical evaluation¹¹ of the EM loop functions $\mathcal{F}_{\mathbb{M}}^{S,V}$ and $\mathcal{G}_{\mathbb{M}}^{S,V}$ in the general case as well discuss the analytical approximations for two phenomenologically motivated limits. In the numerical analyses, the dipole loop functions carry units of GeV^{-1} , and the loop functions associated with the anapole moment and charge radius have units of GeV^{-2} .

¹¹We evaluated the Passarino-Veltman functions with `LoopTools` [263].

3.4.1 General loop functions

We present in figs. 3.6 to 3.9 the scalar- and vector loop functions as function of $m_{S,V}/m_{\chi_1} - 1$ and $m_{\chi_2}/m_{\chi_1} - 1$ for fixed $m_{\chi_1} = 100 \text{ GeV}$ and $m_f = m_\tau$. For similar plots in which we present the loop functions for fixed m_{χ_1} and m_{χ_2} and vary $\mu = m_f/m_{\chi_1}$ and $\eta = m_{S,V}/m_{\chi_1}$, see figs. B.1 to B.3 and figs. B.4 to B.6 for the scalar- and vector loop functions respectively in appendix B.1.

Figures 3.6 to 3.9 indicate that the loop functions have unique dependencies on the masses (apart from $\mathcal{G}_d^{S,V}$ differing from $\mathcal{G}_\mu^{S,V}$ by a phase factor) and are suppressed for large m_S or large m_{χ_2} . Therefore, generally, a non-trivial interplay between these loop functions can be expected for the overall amplitude \mathcal{M}^μ governing the coupling to the photon.

For values of m_S or m_{χ_2} close to m_{χ_1} on the other hand, most of the loop functions become enhanced, with the notable exceptions being $\mathcal{G}_A^{S,V}$ and $\mathcal{F}_d^{S,V}$, which are suppressed for small $m_{\chi_2} \rightarrow m_{\chi_1}$. This observation is expected, as we have not encountered these loop functions when discussing the diagonal EM moments in section 3.2. Further, we find that the loop functions related to the dipole moments are typically numerically larger than the ones for the anapole and charge radius. As we evaluated the loop functions for a τ -lepton in the loop, the fermion mass is fixed to $m_f = m_\tau$, resulting in the maxima positioned in the lower left corner of the panels in figs. 3.6 to 3.9.

To quantify the location of the maxima, we present the scalar loop functions as functions of m_{χ_2}/m_{χ_1} in fig. 3.10 for some fixed values of m_S and m_f , highlighting the resonance occurring in the general case, corresponding to the divergence of the function

$$\tilde{F}(\xi, \mu, \eta) = \frac{2\sqrt{\lambda(\xi^2, \eta^2, \mu^2)}}{\xi^2} \operatorname{arctanh} \left(\frac{\sqrt{\lambda(\xi^2, \eta^2, \mu^2)}}{(\eta + \mu)^2 - \xi^2} + i\epsilon \right), \quad (3.60)$$

where $\lambda(x, y, z)$ is the Källén function [264]. The resonance condition then amounts to

$$(\mu + \eta)^2 \simeq \xi^2. \quad (3.61)$$

This resonance feature is the origin of the omnipresent enhancement in the lower left corners in figs. 3.6 to 3.9, resulting for $\eta = m_S/m_{\chi_1} = 1.01$ in the value of $(m_{\chi_2}/m_{\chi_1} - 1)_{\max} \simeq 2.8 \times 10^{-2}$ for the which loop functions are enhanced.

A further feature of the loop functions is the observation that $\mathcal{G}_{A,b}^{S,V}$ vanish for $\mu = \eta$, which can be seen by the absence of points along the diagonal in the plots depicted in figs. B.2 and B.5. Looking at the analytical expressions, this is expected as exact cancellation occurs here. We note that all loop functions become mass-suppressed as $1/m_X^n$, where X is the heaviest state among the loop particles f , S or V , and the power n depends on the loop function. A further suppression $\sim 1/m_{\chi_2}^{n'}$ occurs the

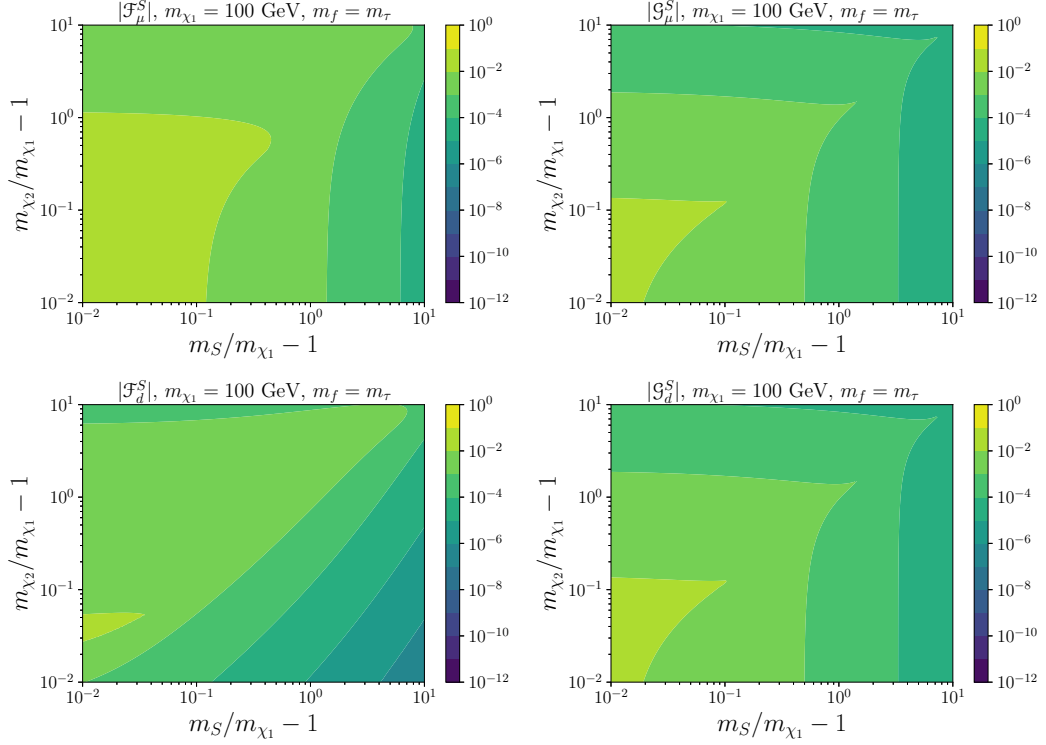


Figure 3.6: Scalar loop functions for the dipole moments for $m_{\chi_1} = 100$ GeV and $m_f = m_\tau$ as a function of the mass-splitting between χ_1 and the scalar S , and between χ_1 and χ_2 .

larger the mass-splitting between the two external fermions is. This suppression is, of course, expected from general EFT arguments, as here, the effective operators are inversely proportional to some power of the mass of the heaviest state in the loop.

3.4.2 Large mass-splitting between external states

The first limiting case we discuss is the scenario where the external states separate a large hierarchy: $m_{\chi_1} \gg m_{\chi_2}$. The loop functions for the opposite hierarchy can be obtained trivially using eq. (3.50). Applications for this case could include a very heavy DM state decaying into a lighter, the decay of a sterile neutrino into an active neutrino, or up-scattering processes of active neutrinos into a heavy state.

The analytical expressions given in appendix B.3 can approximate the loop functions in this scenario. We find that the loop functions for the dipole moments and the anapole moment/charge radius are related via a phase factor.

We present in fig. 3.11 the loop functions for the dipole moments and for the

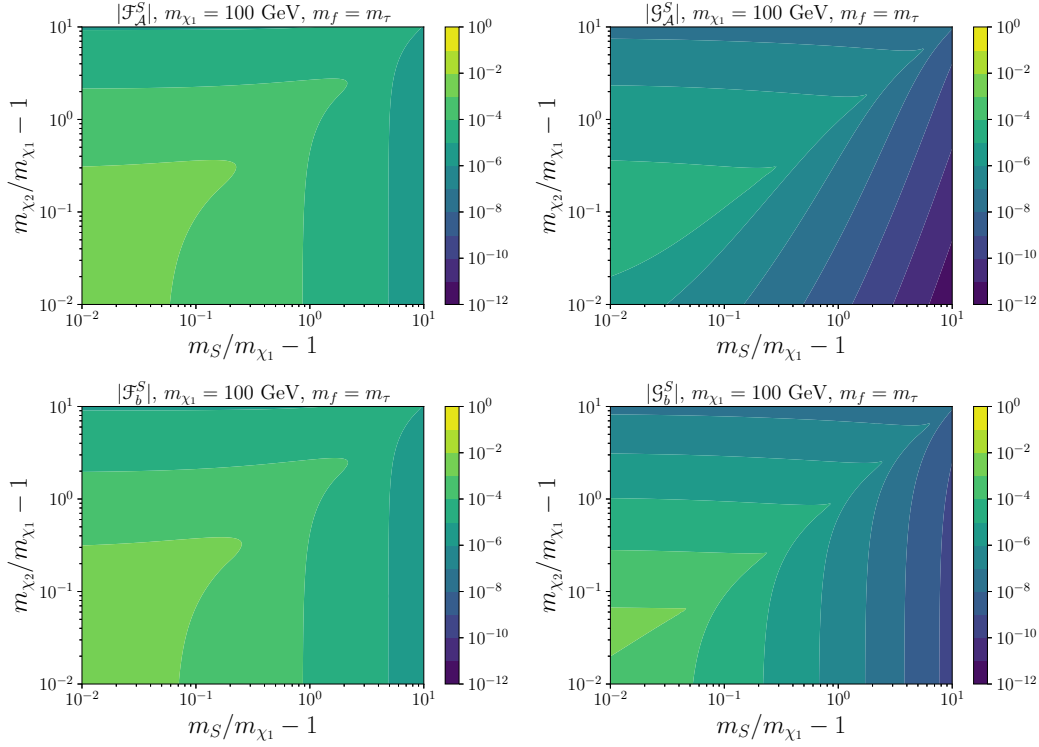


Figure 3.7: Same as fig. 3.6 but for the loop functions of the dimension-6 operators.

anapole moment/charge radius for a boson mass of $m_{S,V} = 100$ GeV and a fermion with mass $m_f = 1.1 \times m_{\chi_1}$ (left panel) or $m_f = m_\tau$ (right panel). We find that the vector loop functions are typically larger than their scalar counterparts, with some degeneracy occurring for small m_{χ_1} . In the τ -philic case, we find an enhancement at $m_{\chi_1} \sim m_{S,V}$, where the shape and scale depend on the loop function. For example, while $\mathcal{G}_{\mu,d}^S$ has a clear peak at $m_{\chi_1} \sim m_{S,V}$, $\mathcal{F}_{\mu,d}^V$ does not, and instead is approximately constant for values $m_{\chi_1} > m_{S,V}$.

3.4.3 Light external states

Now, we consider the scenario in which both external masses are light compared to the relevant scale in the loop: $m_{\chi_1}, m_{\chi_2} \ll \Lambda$. The analytical expressions of the loop functions are summarized in appendix B.4. This scenario is particularly interesting, as active (and typically sterile) neutrinos are significantly lighter than the EW scale, highlighting an important phenomenological application of these formulas. For a further discussion, see chapter 7.

We present in fig. 3.12 the absolute value of the loop functions for the magnetic

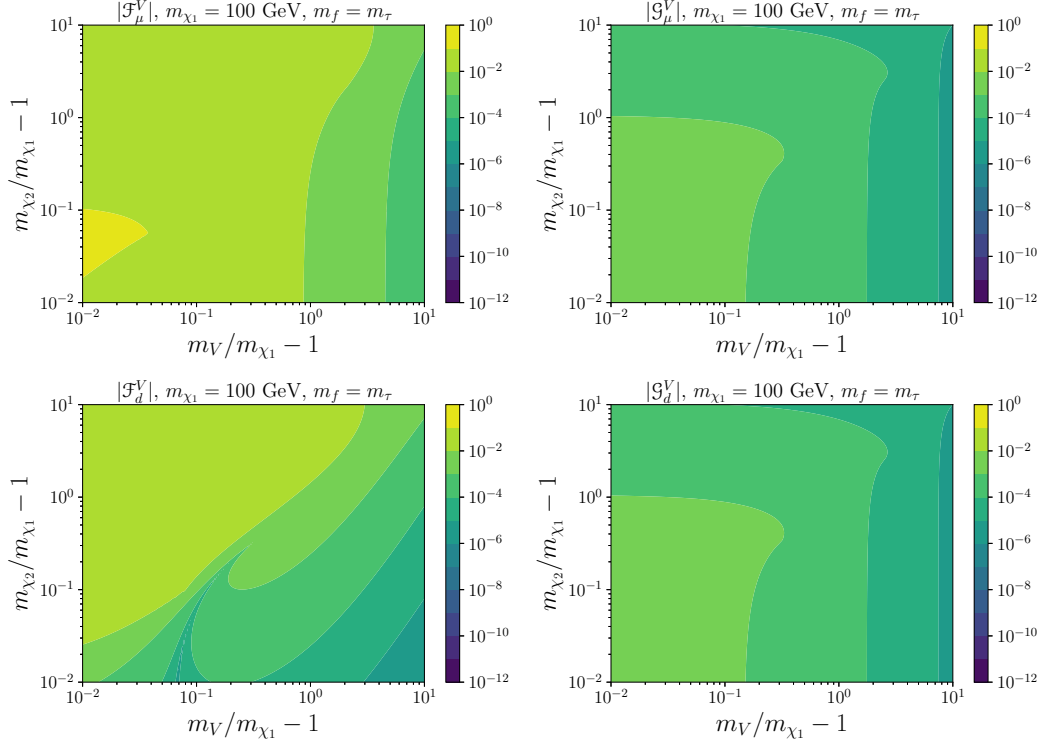


Figure 3.8: Same as fig. 3.6, but for the vector loop functions.

dipole moment and the anapole moment as a function of m_{χ_1} ; the ones for the electric dipole and charge radius look very similar to them for the parameters considered in the plot. Looking at the analytical expressions found in appendix B.4, the following relations amongst the loop functions hold:

$$\mathcal{F}_d^S/\mathcal{F}_\mu^S = i \frac{m_{\chi_1} - m_{\chi_2}}{m_{\chi_1} + m_{\chi_2}}, \quad \mathcal{F}_d^V/\mathcal{F}_\mu^V = -i \frac{m_{\chi_1} - m_{\chi_2}}{m_{\chi_1} + m_{\chi_2}}, \quad (3.62a)$$

$$\mathcal{G}_d^S/\mathcal{G}_\mu^S = i, \quad \mathcal{G}_d^V/\mathcal{G}_\mu^V = -i, \quad (3.62b)$$

$$\mathcal{F}_A^S/\mathcal{F}_b^S \simeq 1 + \mathcal{O}(m_{\chi_1} m_{\chi_2}/m_S^2), \quad \mathcal{F}_A^V/\mathcal{F}_b^V \simeq -1 + \mathcal{O}(m_{\chi_1} m_{\chi_2}/m_V^2), \quad (3.62c)$$

$$\mathcal{G}_A^S/\mathcal{G}_b^S = \frac{m_{\chi_1} - m_{\chi_2}}{m_{\chi_1} + m_{\chi_2}}, \quad \mathcal{G}_A^V/\mathcal{G}_b^V = -\frac{m_{\chi_1} - m_{\chi_2}}{m_{\chi_1} + m_{\chi_2}}. \quad (3.62d)$$

Therefore, the only significant difference is that in contrast to the anapole loop function, $\mathcal{G}_b^{S,V}$ does not vanish for $m_{\chi_1} \simeq m_{\chi_2}$. Similarly, in contrast to the magnetic dipole moment, $\mathcal{F}_d^{S,V}$ does vanish when the external masses are identical. The reason is simply, that in the diagonal limit $\mathcal{F}_d^{S,V} = \mathcal{G}_A^{S,V} = 0$.

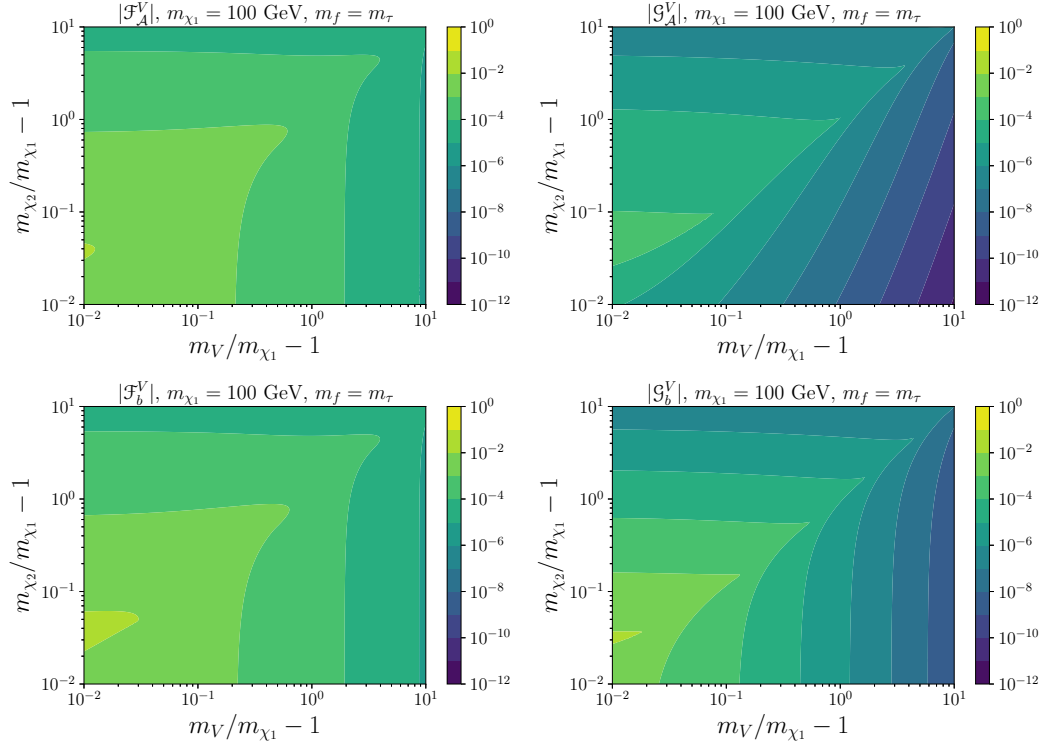


Figure 3.9: Same as fig. 3.7, but for the vector loop functions.

As can be seen from the functional behavior of these loop functions in fig. 3.12, $\mathcal{F}_\mu^{S,V}$ and $\mathcal{G}_A^{S,V}$ are proportional to the masses of the external fermions, explaining their slope in the top left panel. In the top right panel, the second external fermion has a mass of $m_{\chi_2} = 100 \text{ keV}$, such that once $m_{\chi_1} \lesssim m_{\chi_2}$, these functions become proportional to m_{χ_2} and thus independent of m_{χ_1} . This behavior can be interpreted as occurring from the fact that a mass insertion flips the helicity of the diagram. Therefore, the initial- or final-state fermion line has a mass insertion in these scenarios.

The functions $\mathcal{G}_\mu^{S,V}$, on the other hand, are proportional to the mass m_f of the charged fermion f , as can be seen in the top panels. In the bottom panels, the internal fermion mass is fixed by the mass-splitting $m_f/m_{\chi_1} = 1.1$, such that the proportionality to m_f translates into a proportionality to m_{χ_1} for $\mathcal{G}_\mu^{S,V}$.

The scale of $\mathcal{F}_A^{S,V}$ is set by $m_{S,V}^{-2}$, and as it only slightly depends on $m_{\chi_{1,2}}$, it appears primarily constant throughout all panels of fig. 3.12, with the exception being the deviation for $m_{\chi_1} \rightarrow 1 \text{ GeV}$ observable in the bottom panels.

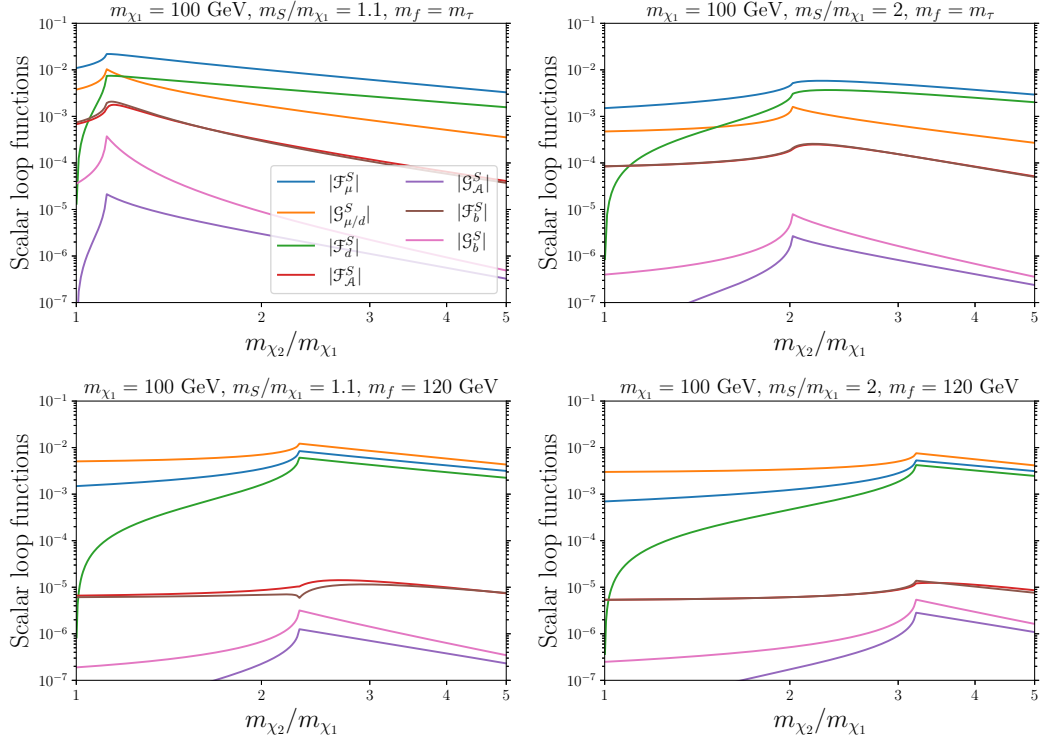


Figure 3.10: Scalar loop functions $|\mathcal{F}_M^S|$ and $|\mathcal{G}_M^S|$ as function of $\xi = m_{\chi_2}/m_{\chi_1}$ for different choices of masses.

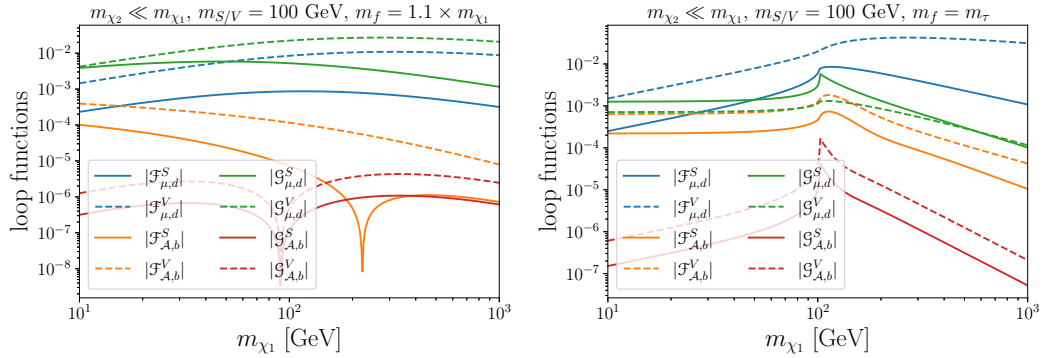


Figure 3.11: Magnetic moment- and anapole loop functions for the scenario in which $m_{\chi_2} \ll m_{\chi_1}$ with a boson of mass $m_{S,V} = 100$ GeV in the loop. The fermion mass is given by $m_f = 1.1 \times m_{\chi_1}$ (left) and $m_f = m_\tau$ (right).

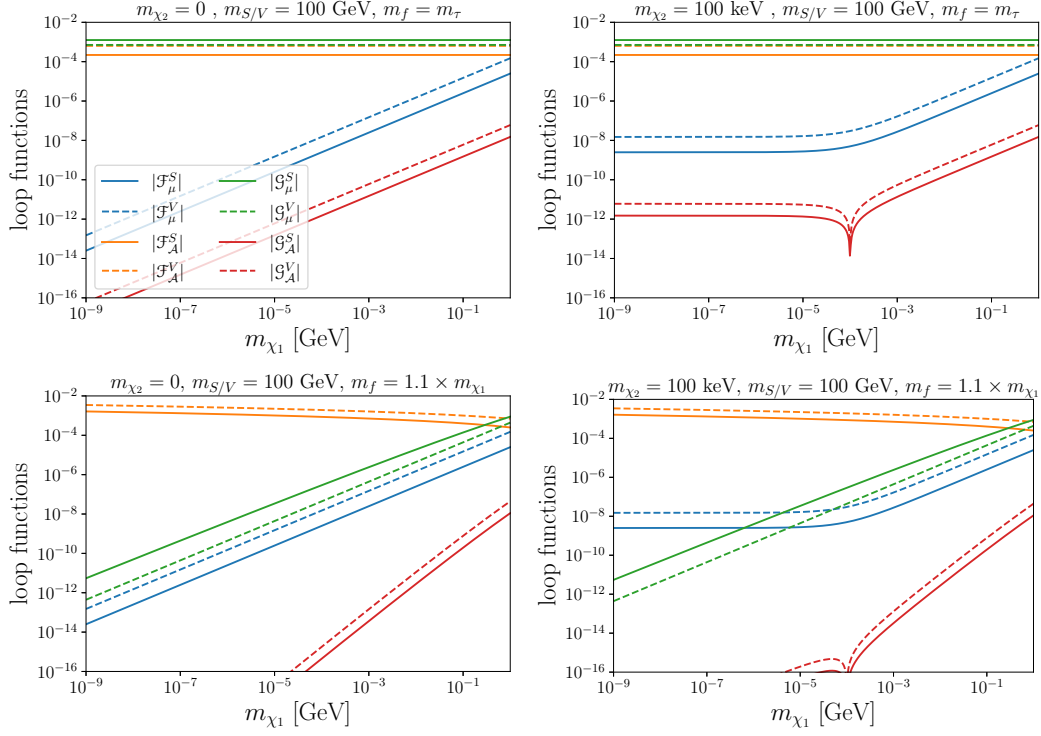


Figure 3.12: Magnetic moment- and anapole loop functions for the limit of light external fermions $m_{\chi_{1,2}} \ll m_{S,V} = 100$ GeV. Concretely, we set $m_{\chi_2} = 0$ (*left*) and $m_{\chi_2} = 100$ keV (*right*). The top row considers a tau-lepton in the loop, whereas the bottom row shows the loop functions for $m_f/m_{\chi_1} = 1.1$.

Chapter 4

Direct detection of dark matter with electromagnetic moments

In this chapter, we particularize the calculation of DM-induced signals at direct detection facilities discussed in section 2.3.2 to the case of electromagnetically interacting DM candidates. First, we revisit the calculation for the Majorana case, in which only one EM is non-zero, such that the conventional approach outlined in section 2.3.2 suffices. We introduce the non-relativistic effective field theory of DM direct detection and particularize this formalism to the case of EM interactions. In this formalism, the presence of multiple operators can be studied quantitatively, particularly the impact on the signals due to their interference. We focus on the case of Dirac DM and study its five EM interactions and the reach of the direct detection experiments on the underlying parameter space spanned by the EFT operators.

4.1 Electromagnetic interactions I: simplified approach

Here, we describe the formalism used in the derivation of the nuclear recoil direct detection limits of the anapole moment of Majorana DM candidates as presented in ref. [2]. Similar studies for the Majorana case have been conducted in refs. [206, 225, 251, 253, 265]. The direct detection phenomenology of a Dirac DM candidate having multiple EM interactions was studied in refs. [203, 206, 225, 252, 266, 267], following a similar approach.

We consider the anapole moment interaction of a Majorana DM candidate¹

$$\mathcal{L} \supset \frac{\mathcal{A}_\chi}{2} \bar{\chi} \gamma^\mu \gamma^5 \chi \partial^\nu F_{\mu\nu}, \quad (4.1)$$

which gives rise to DM-target scattering processes depicted in fig. 4.1. Concretely, we focus on the case where the target is a nucleus N . For DM-electron scattering and their reach on the EM moments, see, for example, refs. [125, 268–270]. The

¹For reasons of consistency, we kept the normalization factor of 1/2. This choice differs from the usual convention used in this work.

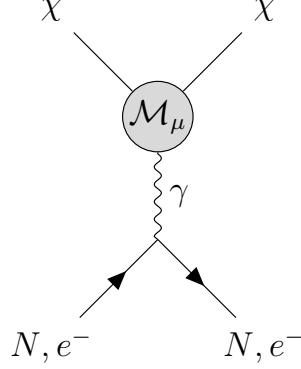


Figure 4.1: Effective interaction between χ and the target (nucleus or electron), mediated by the photon. The blob resembles the effective vertex \mathcal{M}_μ , which is proportional to the anapole moment \mathcal{A}_χ for the Majorana model.

differential cross-section reads [206, 265]

$$\frac{d\sigma}{dE_R} = \alpha \mathcal{A}_\chi^2 \left[Z^2 \left(2m_T - \left(1 + \frac{m_T}{m_\chi} \right)^2 \frac{E_R}{v^2} \right) F_{\text{SI}}^2(q^2) + \frac{1}{3} \frac{m_T}{m_N^2} \left(\frac{\bar{\mu}_T}{\mu_N} \right)^2 \frac{E_R}{v^2} F_{\text{D}}^2(q^2) \right], \quad (4.2)$$

which consists of the anapole-charge interaction, proportional to the SI form factor $F_{\text{SI}}(q^2)$ and on the form factor arising from the anapole-dipole interaction proportional to $F_{\text{D}}(q^2)$, coupling to the spins of the target. The latter can be modeled as [119]

$$F_{\text{D}}^2(q^2) = \begin{cases} (\sin(qR)/qR)^2 & \text{if } qR < 2.55 \text{ or } qR > 4.5 \\ 0.047 & 2.55 \leq qR \leq 4.5 \end{cases}. \quad (4.3)$$

Further,

$$\bar{\mu}_T = \left(\sum_i f_i \mu_i^2 \frac{S_i + 1}{S_i} \right) \quad (4.4)$$

is the weighted dipole moment of the target, where the sum runs over the isotopes i , and f_i , S_i and μ_i are respectively its elemental abundance, spin, and nuclear magnetic moment [271].

Plugging this cross-section into the expression for the differential rate for an experiment, eq. (2.42), allows the computation of scattering signals due to anapole-mediated DM interactions. In contrast to the standard approach, in which the cross-section σ_p was considered a free parameter, we can constrain the anapole moment \mathcal{A}_χ using the experimental data.² We present in fig. 4.2 the 90% C.L. exclusion limits

²The exclusion limits were derived by Ryo Nagai.

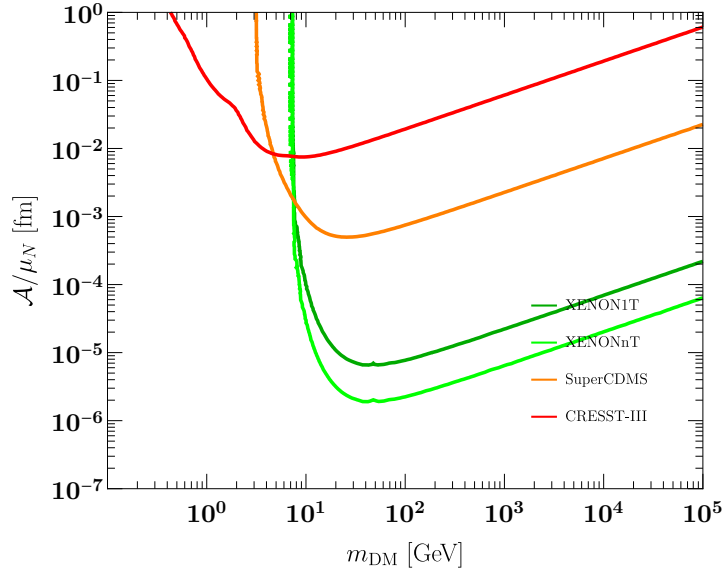


Figure 4.2: 90% C.L. exclusion limit on the anapole moment \mathcal{A}_χ .

from XENON1T [137], SuperCDMS [272], CRESST-III [273] and XENONnT [274] forecasts.³ The dominant constraints for $m_\chi \gtrsim 10$ GeV comes from XENONnT, being the most sensitive for $m_\chi \sim 40$ GeV where it constraints the anapole moment to be $\mathcal{A}_\chi \gtrsim 10^{-6} \mu_N \text{ fm}$. For smaller DM masses, SuperCDMS and CRESST-III give the leading constraints due to their lower detection thresholds.

4.2 Non-relativistic effective field theory

Before proceeding with the Dirac DM discussion, we must introduce the general formalism of the non-relativistic effective field theory (NREFT) of DM direct detection experiments.

Following refs. [275, 276], this formalism expresses the Lagrangian in terms of hermitian Galilean-invariant operators expanded in the DM halo velocity $v \sim 10^{-3}$ and the transferred momentum q . The number of possible independent operators depends on the spin of the DM candidate. For a fermionic candidate, one finds 14 independent operators at the lowest order in the expansion, which are summarized in table 4.1. The Lagrangian then consists of these operators multiplied by Wilson

³See ref. [213] for details on the detection efficiencies.

coefficients parameterizing the interaction strengths of χ to the target:

$$\mathcal{L} = \sum_{i=1}^{15} \sum_{N=n,p} c_i^N \mathcal{O}_i^N. \quad (4.5)$$

In eq. (4.5), c_i^n denotes the coupling to the neutron, and c_i^p is the coupling to the proton, typically assumed to be velocity- and momentum-independent. Alternatively, the Wilson coefficients can be expressed in terms of the nucleon's isospin as

$$c_i^0 = \frac{1}{2} (c_i^p + c_i^n), \quad c_i^1 = \frac{1}{2} (c_i^p - c_i^n). \quad (4.6)$$

In this basis, eq. (4.5) reads

$$\mathcal{L} = \sum_{i=1}^{15} \sum_{\tau=0,1} c_i^\tau \mathcal{O}_i t^\tau, \quad (4.7)$$

with $t^0 = \mathbb{1}_{2 \times 2}$ and $t^1 = \tau_3$.

In this formalism, the differential rate written in eq. (2.42) is reformulated as

$$\frac{d^2 R}{dE_R dv_T} = \sum_T N_T \frac{\rho}{m_\chi} f(\mathbf{v}_T) v_T \frac{d\sigma}{dE_R}, \quad (4.8)$$

with cross-section

$$\frac{d\sigma}{dE_R} = \frac{2m_T}{4\pi v_T^2} \left[\frac{1}{2j_\chi + 1} \frac{1}{2j_T + 1} |\mathcal{M}|^2 \right], \quad (4.9)$$

in which the amplitude $|\mathcal{M}|^2$ contains the DM model dependency. This amplitude is factorized in a part that depends on the DM physics, including the Wilson coefficients of eq. (4.5), and a part that depends on nuclear physics, as [276]

$$\frac{1}{2j_\chi + 1} \frac{1}{2j_T + 1} |\mathcal{M}|^2 = \frac{4\pi}{2j_T + 1} \sum_{\tau=0}^1 \sum_{\tau'=0}^1 \sum_k R_k^{\tau\tau'} \left[c_i^\tau, c_j^{\tau'}, (v^\perp)^2, \frac{q^2}{m_N^2} \right] W_{Tk}^{\tau\tau'}(y), \quad (4.10)$$

where $y = (qb/2)^2$ and b is the size of the nucleus. The nuclear response functions $W_{Tk}^{\tau\tau'}$ are independent of the DM physics and have been calculated, for example, in refs. [275–277]. The DM response functions $R_k^{\tau\tau'}$ are linear combinations of the Wilson coefficients; see ref. [276] for the exact analytical expressions. Then, the differential rate describing the elastic DM-nucleus scattering reads

$$\frac{dR_{\chi T}}{dE_R} = \int_{v > v_{\min}} d^3 v_T \frac{dR}{dE_R dv_T}, \quad (4.11)$$

$\mathcal{O}_1 = 1_\chi 1_N$	$\mathcal{O}_9 = i\mathbf{S}_\chi \cdot (\mathbf{S}_N \times \frac{\mathbf{q}}{m_N})$
$\mathcal{O}_3 = i\mathbf{S}_N \cdot (\frac{\mathbf{q}}{m_N} \times \mathbf{v}^\perp)$	$\mathcal{O}_{10} = i\mathbf{S}_N \cdot \frac{\mathbf{q}}{m_N}$
$\mathcal{O}_4 = \mathbf{S}_\chi \cdot \mathbf{S}_N$	$\mathcal{O}_{11} = i\mathbf{S}_\chi \cdot \frac{\mathbf{q}}{m_N}$
$\mathcal{O}_5 = i\mathbf{S}_\chi \cdot (\frac{\mathbf{q}}{m_N} \times \mathbf{v}^\perp)$	$\mathcal{O}_{12} = \mathbf{S}_\chi \cdot (\mathbf{S}_N \times \mathbf{v}^\perp)$
$\mathcal{O}_6 = (\mathbf{S}_\chi \cdot \frac{\mathbf{q}}{m_N})(\mathbf{S}_N \cdot \frac{\mathbf{q}}{m_N})$	$\mathcal{O}_{13} = i(\mathbf{S}_\chi \cdot \mathbf{v}^\perp)(\mathbf{S}_N \cdot \frac{\mathbf{q}}{m_N})$
$\mathcal{O}_7 = \mathbf{S}_N \cdot \mathbf{v}^\perp$	$\mathcal{O}_{14} = i(\mathbf{S}_\chi \cdot \frac{\mathbf{q}}{m_N})(\mathbf{S}_N \cdot \mathbf{v}^\perp)$
$\mathcal{O}_8 = \mathbf{S}_\chi \cdot \mathbf{v}^\perp$	$\mathcal{O}_{15} = -(\mathbf{S}_\chi \cdot \frac{\mathbf{q}}{m_N})((\mathbf{S}_N \times \mathbf{v}^\perp) \cdot \frac{\mathbf{q}}{m_N})$

Table 4.1: Non-relativistic Galilean-invariant operators for DM with spin 1/2, \mathcal{O}_2 vanishes at lowest order in the expansion.

where $v_{\min} = \sqrt{\frac{m_T E_R}{2\mu_T^2}}$.

As DM physics is factorized from nuclear physics, once the latter is determined, this formalism can be used to study a range of DM models by matching the relativistic operators to the Wilson coefficients of the NREFT. From a bottom-up point of view, this formalism allows a systematic study of the NREFT, in particular the consequences of multiple non-zero operators and the resulting interference effects [278–280].

4.2.1 The Migdal effect in DM direct detection

In addition to the above-described elastic nuclear recoils, the scattering process can give rise to an ionization signal by ejecting electrons via the *Migdal effect* [133, 281] proposed in 1941 by A. Migdal [132].⁴ As a DM particle scatters off a nucleus, displacing it, the electron cloud may not follow immediately. This delay leads to the energy being distributed amongst the nucleus and the electrons, such that one of the latter may be excited or ionized. The ionized electron can still yield a signal even if the energy deposited as nuclear recoil is below the detector threshold.

The differential rate of such a signal can be written in a factorized way as [133]

$$\frac{dR_{\chi T}}{dE_{\text{det}}} = \int_0^\infty dE_R \int_{v>v_{\min}} dv_T \frac{d^2 R_{\chi T}}{dE_R dv_T} \times \frac{1}{2\pi} \sum_{n,\ell} \frac{d}{dE_e} p_{n\ell \rightarrow E_e}(q_e), \quad (4.12)$$

where E_{det} is the energy at the detector, $p_{n\ell \rightarrow E_e}(q_e)$ is the ionization probability of an electron with quantum numbers (n, ℓ) with de-excitation energy $E_{n\ell}$. The ionized electron has energy E_e with average momentum q_e , which reads in the electron's rest

⁴Experimental efforts to measure the Migdal effect in xenon atoms using neutrons have been reported in refs. [282, 283].

frame $q_e = m_e \sqrt{2E_R/m_T}$. The differential rate in eq. (4.12) is given by the elastic DM-nucleus rate given in eq. (4.11). Further, the minimal velocity now reads

$$v_{\min} = \frac{m_T E_R + \mu_T E_{\text{EM}}}{\mu_T \sqrt{2m_T E_R}}, \quad (4.13)$$

where $E_{\text{EM}} = E_e + E_{nl}$ is the ionization energy deposited in the detector and is related to the total energy deposited via

$$E_{\text{det}} = E_{\text{EM}} + Q E_R, \quad (4.14)$$

where $Q = E_e/E_R$ is the quenching factor, describing the relative efficiency of nuclear recoils compared to electron recoils. This discrepancy comes mainly from nuclei and electrons traversing the detector differently; the former loses more energy in the form of heat.

Since its proposed application to DM direct searches, the Migdal effect has been used by several collaborations to extend the experimental reach to light DM particles [284–291].

Similar to the neutrino floor affecting nucleus scattering analyses, neutrino CE ν NS, the neutrino Migdal effect, and neutrino electron scattering can give rise to a background contribution in searches utilizing the DM Migdal effect [145].

4.3 Electromagnetic interactions II: within the effective field theory

4.3.1 The rate matrices

As proposed in refs. [278, 279], the scattering rate between DM and the target can be formulated in a factorized way, where the DM halo model and the detector-related physics is contained in a matrix, multiplying the coefficients c_i^T (or c_i^N) of the NREFT. In this formulation, the rate matrices can be calculated once for a specific experiment and subsequently applied to almost arbitrary DM models by matching the coefficients to the operators of the specific DM model.

To apply this approach to the case of the EM interaction, we first need to express the relativistic Lagrangian, given in eq. (3.10), within the NREFT formalism by matching to the NR Wilson coefficients. We consider the following NR operators [267]:

- At dimension-4 DM could possess a millicharge Q_χ , which could be induced by a $U(1)_{\text{dark}}$ symmetry, whose gauge boson kinetically mixes with the SM photon γ [292, 293]. The resulting millicharge is suppressed by the kinetic

mixing parameter ϵ . The NR operator reads:

$$\mathcal{O}_{\text{milli}} = e^2 \sum_{N=n,p} Q_\chi Q_N \frac{1}{q^2} \mathcal{O}_1, \quad (4.15)$$

where $Q_p = 1$ and $Q_n = 0$ are the electric charges of the proton and neutron, respectively.

- The magnetic dipole moment μ_χ and electric dipole moment d_χ are the coefficients of dimension-5 operators, which can be generated via t -channel interactions with scalars/vectors and fermions. Their NR operators read:

$$\mathcal{O}_{\text{MD}} = 2e\mu_\chi \sum_{N=n,p} \left[\frac{1}{4m_\chi} Q_N \mathcal{O}_1 + \frac{m_N}{q^2} Q_N \mathcal{O}_5 + \frac{1}{2m_N} g_N \mathcal{O}_4 - \frac{m_N}{2q^2} g_N \mathcal{O}_6 \right], \quad (4.16)$$

$$\mathcal{O}_{\text{ED}} = 2ed_\chi \sum_{N=n,p} Q_N m_N \frac{1}{q^2} \mathcal{O}_{11}, \quad (4.17)$$

with $g_p = 5.59$ and $g_n = -3.83$ being the gyromagnetic factors of the proton and neutron, respectively.

- The dimension-6 NR operators are the anapole moment \mathcal{A}_χ and the charge radius b_χ . A t -channel mediator can generate both of them. The NR operators are given by:

$$\mathcal{O}_{\text{ana}} = e\mathcal{A}_\chi \sum_{N=n,p} (2Q_N \mathcal{O}_8 - g_N \mathcal{O}_9), \quad (4.18)$$

$$\mathcal{O}_{\text{CR}} = eb_\chi \sum_{N=n,p} Q_N \mathcal{O}_1. \quad (4.19)$$

The anapole moment is only non-zero if parity is broken by the UV physics generating it.

- In principle, DM can have four dimension-7 interactions with photons (Rayleigh operators):

$$\bar{\chi}\chi F^{\mu\nu} F_{\mu\nu}, \quad \bar{\chi}\gamma^5\chi F^{\mu\nu}, \quad \bar{\chi}\chi F^{\mu\nu} \tilde{F}_{\mu\nu} F_{\mu\nu}, \quad \bar{\chi}\gamma^5\chi F^{\mu\nu} \tilde{F}_{\mu\nu}. \quad (4.20)$$

Within the EFT framework, these operators could generate signals in indirect- and collider searches of DM [294, 295] and have an impact on the relic density due to $\chi\chi \rightarrow \gamma\gamma$ annihilations [296–299]. As the Rayleigh operators do not contribute to signals at direct detection experiments, we do not include them in our analysis and discussion.

Therefore, in the NREFT, the Lagrangian describing scattering between DM and nuclei via the EM moments is given by

$$\mathcal{L}_{\text{NREFT}} = \mathcal{O}_{\text{milli}} + \mathcal{O}_{\text{ED}} + \mathcal{O}_{\text{MD}} + \mathcal{O}_{\text{ana}} + \mathcal{O}_{\text{CR}}. \quad (4.21)$$

By comparing eq. (4.21) with eq. (4.5), we obtain the Wilson coefficients in the canonical basis:

$$\begin{aligned} c_1^N &= \frac{e^2 Q_N}{q^2} Q_\chi + \frac{2eQ_N}{4m_\chi} \mu_\chi + eQ_N b_\chi, \\ c_4^N &= \frac{2eg_N}{2m_N} \mu_\chi, \quad c_5^N = \frac{2eQ_N m_N}{q^2} \mu_\chi, \quad c_6^N = -\frac{2eg_N m_N}{2q^2} \mu_\chi, \\ c_8^N &= 2eQ_N \mathcal{A}_\chi, \quad c_9^N = -eg_N \mathcal{A}_\chi, \quad c_{11}^N = \frac{2eQ_N m_N}{q^2} d_\chi, \end{aligned} \quad (4.22)$$

and all others are zero. Note that the millicharge, the magnetic moment, and the charge radius contribute to c_1^p , leading to interference terms in the expression for the rate. Further, some of the Wilson coefficients in eq. (4.22) are dependent on the momentum q^2 , such that the approach outlined in refs. [278, 279] is not directly applicable but has to be adjusted accordingly. This leads to a separate set of rate matrix elements we present and utilize in the following.

Following refs. [278, 279], the projected total count of signal events in a given DM direct detection experiment, denoted by \mathcal{E} , can be factorized as [3]

$$\mathcal{N}_{\text{sig}}^\mathcal{E} = (Q_\chi \mu_\chi d_\chi \mathcal{A}_\chi b_\chi) \begin{pmatrix} \mathbb{N}_{Q_\chi Q_\chi}^\mathcal{E} & \mathbb{N}_{Q_\chi \mu_\chi}^\mathcal{E} & 0 & 0 & \mathbb{N}_{Q_\chi b_\chi}^\mathcal{E} \\ \mathbb{N}_{Q_\chi \mu_\chi}^\mathcal{E} & \mathbb{N}_{\mu_\chi \mu_\chi}^\mathcal{E} & 0 & 0 & \mathbb{N}_{\mu_\chi b_\chi}^\mathcal{E} \\ 0 & 0 & \mathbb{N}_{d_\chi d_\chi}^\mathcal{E} & 0 & 0 \\ 0 & 0 & 0 & \mathbb{N}_{\mathcal{A}_\chi \mathcal{A}_\chi}^\mathcal{E} & 0 \\ \mathbb{N}_{Q_\chi b_\chi}^\mathcal{E} & \mathbb{N}_{\mu_\chi b_\chi}^\mathcal{E} & 0 & 0 & \mathbb{N}_{b_\chi b_\chi}^\mathcal{E} \end{pmatrix} \begin{pmatrix} Q_\chi \\ \mu_\chi \\ d_\chi \\ \mathcal{A}_\chi \\ b_\chi \end{pmatrix}, \quad (4.23)$$

where all detector specifics and astrophysical modeling of the local DM abundance are encoded in the matrix elements $\mathbb{N}_{ij}^\mathcal{E}$. We calculated the matrix elements using eq. (4.11) and eq. (4.12) for DM-nucleus elastic scattering and Migdal scattering, respectively, using WimPyDD [136].⁵ We used the ionization probabilities provided in ref. [133] for the Migdal effect calculation.

We present in fig. 4.3 the matrix elements $\mathbb{N}_{ij}^\mathcal{E}$ for the direct detection experiments XENON1T [300], LUX-ZEPLIN (LZ) [301], PICO-60 [302] and DS50 [303].⁶ The units of the individual matrix elements are such that the left-hand side in eq. (4.23) is dimensionless: $\mathbb{N}_{Q_\chi Q_\chi}^\mathcal{E}$ has no units, $\mathbb{N}_{\mu_\chi \mu_\chi}^\mathcal{E}$ and $\mathbb{N}_{d_\chi d_\chi}^\mathcal{E}$ have units of GeV^2 , and

⁵Gaurav Tomar performed this calculation.

⁶The data is available at <https://github.com/ga42puq/EMmoments-rate-matrices>.

$N_{A_\chi A_\chi}^\mathcal{E}$ and $N_{b_\chi b_\chi}^\mathcal{E}$ have units of GeV^4 . The off-diagonal element $N_{Q_\chi \mu_\chi}^\mathcal{E}$ has units of GeV^1 , $N_{Q_\chi b_\chi}^\mathcal{E}$ has units of GeV^2 and $N_{\mu_\chi b_\chi}^\mathcal{E}$ has units of GeV^3 . Note that for the matrix elements of the DS50 experiment, we present the largest rate of all bins considered. However, we treat the bins separately to derive the exclusion limits; see appendix A for more details.

With these matrix elements, we now have the tools equipped to calculate the experimental limits on all EM interactions for considering *i*) one operator at a time (which is the standard approach), and *ii*) multiple non-zero operators. Scenario *ii*) includes interference terms, leading to weaker limits as one would obtain following approach *i*).

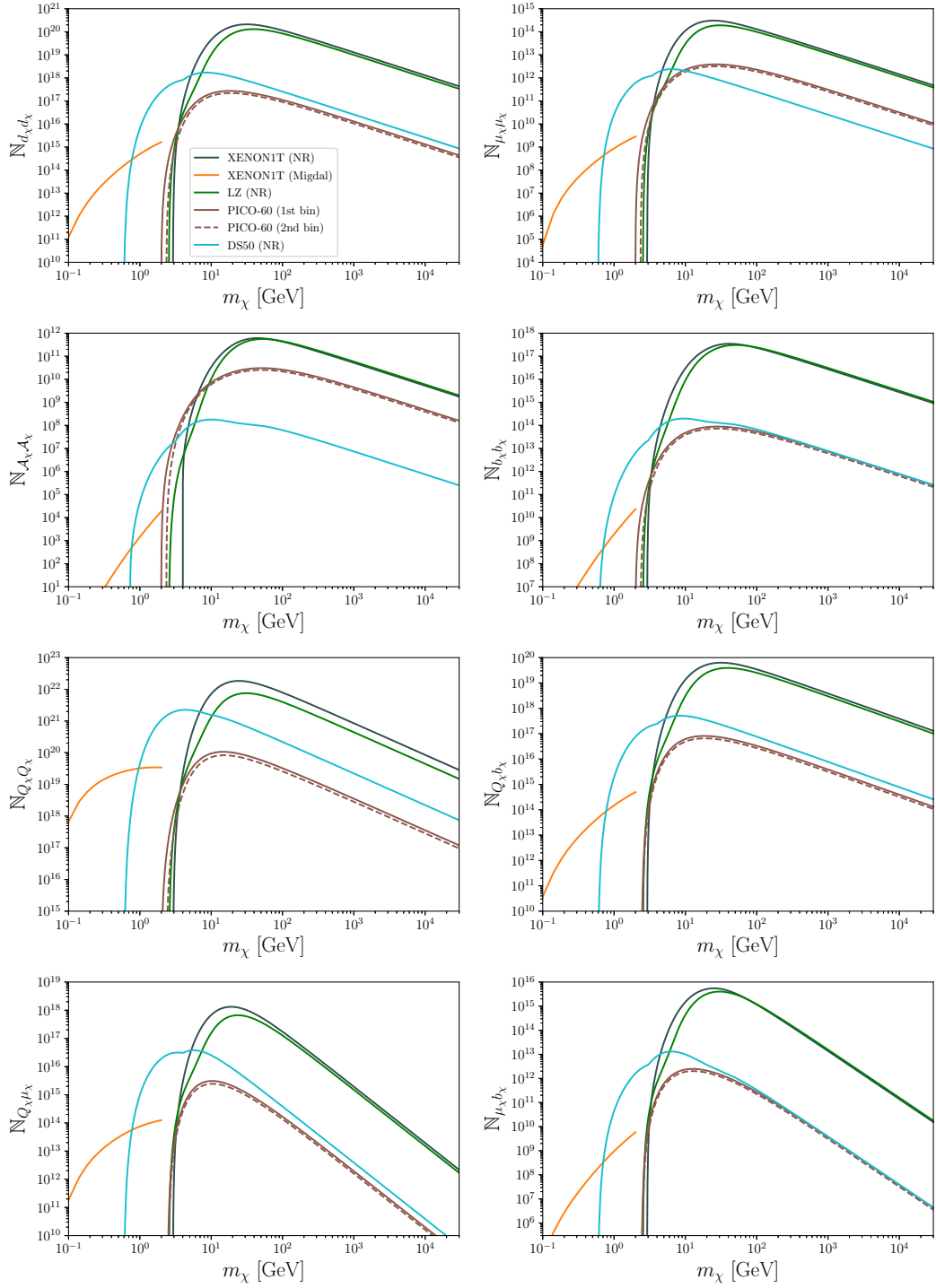


Figure 4.3: Matrix elements $N_{ij}^{\mathcal{E}}$ defined in eq. (4.23) for different experiments \mathcal{E} . See main text for details.

4.3.2 Application to one operator at a time

For demonstration, we assume that the only non-zero operator is the magnetic dipole moment, such that eq. (4.23) reduces to

$$\mathcal{N}_{\text{sig}}^{\mathcal{E}} = \mu_{\chi}^2 \times \mathbb{N}_{\mu_{\chi}\mu_{\chi}}^{\mathcal{E}}. \quad (4.24)$$

Using the measured number of counts of experiments \mathcal{E} and the provided $\mathbb{N}_{\mu_{\chi}\mu_{\chi}}^{\mathcal{E}}$ (see fig. 4.3), we can determine the 90% C.L. upper exclusion limit on the parameter μ_{χ} by comparing the predicted DM signal count with the experimental data. For more details on the statistical treatment, see appendix A. Proceeding similarly for the other EM interactions, we obtain their respective exclusion limits, which are presented in fig. 4.4.

In fig. 4.4, we also include limits from Supernova 1987A, the CMB, Voyager, and from LEP [304, 305]. Colliders operate with significantly larger energies than the DM direct detection scale defined through the momentum transfer q_{DD}^2 , resulting in the hierarchy $q_{\text{coll}}^2 \gg q_{\text{DD}}^2$. Therefore, the underlying assumption on the validity of the EFT is different in these two scenarios. Technically speaking, the exclusion limits can only be compared if both scales are smaller than the scale Λ_{loop} generating the EM moments. As can be seen from the toy model analysis in chapters 5 and 6, the relevant scales appearing in the one-loop diagrams can be of order $\Lambda_{\text{loop}} \sim 50 \text{ GeV}$, such that the collider bounds do not apply to such a model. Nevertheless, as we focus on the EFT description in this chapter, we may assume that $\Lambda_{\text{loop}}^2 \gg q_{\text{DD}}^2, q_{\text{coll}}^2$.

We further show limits from electron recoil analyses from XENON10 and XENON1T [125]⁷ and from PANDA-X [270]. Additional nuclear recoil limits from PANDA-X [267] are shown. For the anapole moment, we include the limits from SuperCDMS and CRESST-III from fig. 4.2.⁸ For the millicharge, we include nuclear recoil limits from ref. [306] and present a recast of the electron recoil limits from XENON10 [307] and SENSEI [308], assuming a massless dark photon as in ref. [122].

Amongst the direct detection experiments, we find that for all operators, the electron recoil limits provide the best constraints for $m_{\chi} \lesssim 1 \text{ GeV}$, the limits derived using the Migdal effect for $m_{\chi} \sim 1 \text{ GeV}$, and for $m_{\chi} \gtrsim 5 \text{ GeV}$ the limits derived using nuclear recoils give the strongest limits. However, the complementarity between electron scattering and the Migdal effect varies when looking at separate experiments or targets. While for the magnetic dipole, for $m_{\chi} = 2 \text{ GeV}$, the XENON1T Migdal limit is one order of magnitude above the XENON1T electron limit, for the electric dipole, it provides the dominant constraint at $m_{\chi} = 2 \text{ GeV}$. This hierarchy is in analogy to the comparison of short-range and long-range interactions and the complementarity between Migdal- and electron recoil studies for xenon-targets conducted in refs. [123,

⁷As pointed out in ref. [269], the XENON10/XENON1T limits obtained in ref. [125] might need to be adjusted slightly, weakening the exclusion bounds from these analyses.

⁸We accounted for the different vertex normalization convention.

124]. While the dominant contribution to the magnetic dipole cross-section is classified as short-range ($\sim \mathcal{O}_1$), the electric dipole may be seen as long-range interaction ($\sim \mathcal{O}_{11}/q^2 \sim 1/q$), resulting in the observed hierarchy for XENON1T [309]. Therefore, this classification also explains why the exclusion limits on the electric dipole moment are roughly two to three orders of magnitude stronger than those on the magnetic dipole moment. The strong limits on the electric dipole moment translate into relatively strong limits on CP-violating couplings in the UV theory, in which the EM moments are generated, see chapter 6.

4.3 Electromagnetic interactions II: within the effective field theory

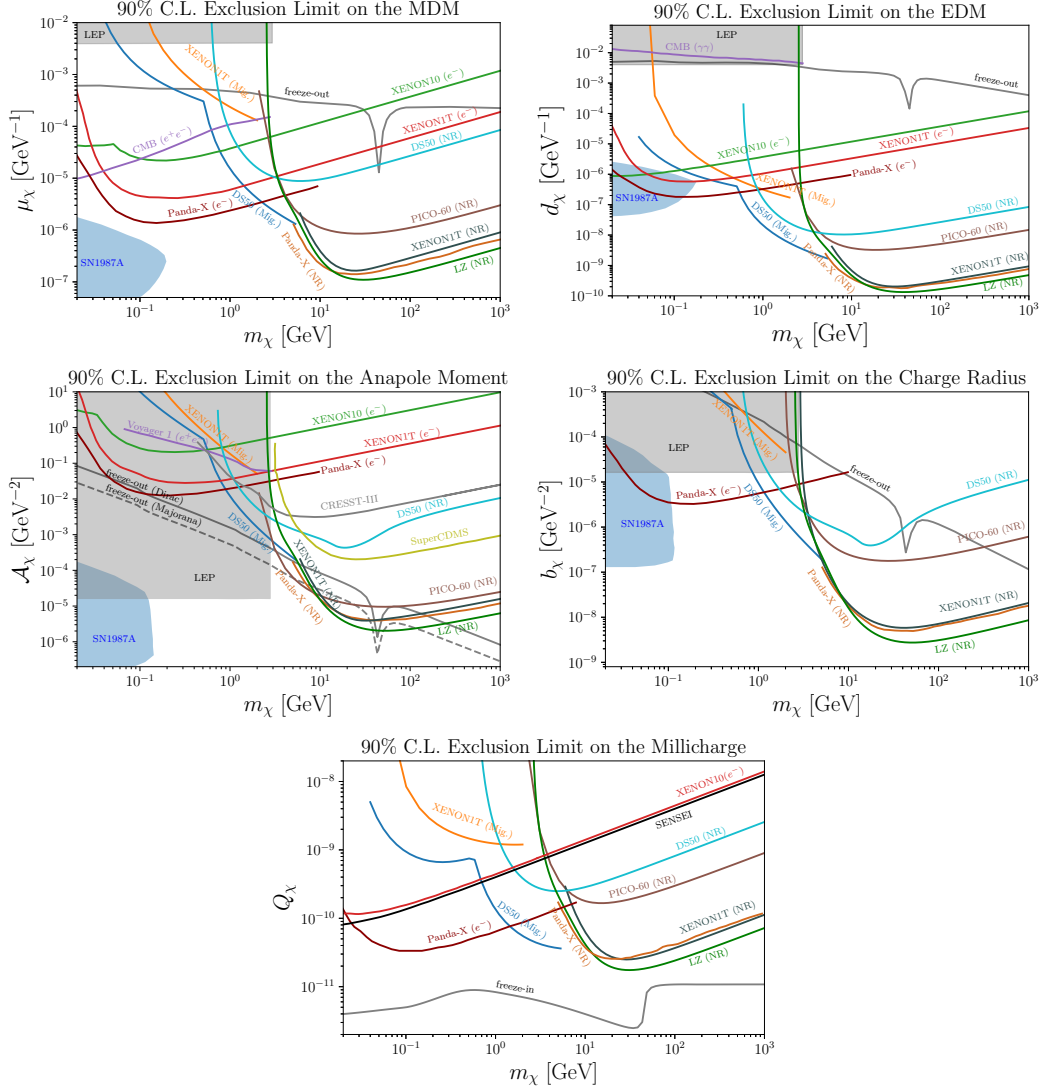


Figure 4.4: 90% C.L. limits on the EM moments of spin-1/2 DM. We also show the values of the corresponding EM moment leading to the correct DM abundance via freeze-out/freeze-in. See main text for details.

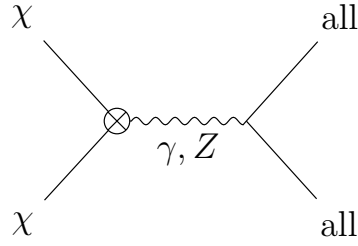


Figure 4.5: s -channel annihilation process for the EFT of DM with EM moments at lowest order.

4.3.3 Intermission: relic density in the EFT

So far, we have not specified the production mechanism of the DM candidate and simply *assumed* that χ makes up all of our galaxy’s halo DM distribution, potentially leading to the direct detection signatures described above.

In the EFT of DM with EM moments, χ has a portal interaction mediated by the photon and the Z boson. We chose a coupling to the hypercharge gauge boson B^μ instead of A^μ to avoid unphysical contributions from annihilations into vector boson, resulting in unitarity violation [218, 310], see appendix C for more details on this matter.

Both freeze-in and freeze-out processes can give rise to the correct relic abundance. At the lowest order, the s -channel annihilation shown in fig. 4.5 either annihilates the DM particles, leading to the freeze-out of its number density, or, for freeze-in, it populates the Universe steadily with χ particles via the inverse process. In fig. 4.5, the final states can be SM particles coupling to the neutral gauge bosons or, in the case of specific UV models, could contain other new degrees of freedom. Suppose these new particles generate the EM moments. In that case, they provide further portals to the SM, resulting in additional tree-level annihilation diagrams, which typically dominate over the loop-suppressed EM multipoles. Therefore, the thermal production phenomenology in such a UV model will differ drastically from the findings within the EFT framework.

The freeze-in line for the millicharge and the freeze-out line for the remaining interactions are shown in the exclusion plots for the EM moments in fig. 4.4. Apart from the anapole moment, all freeze-out thermal relics are excluded in the EFT in the whole parameter space considered. For the millicharge, the experimental reach is roughly one order of magnitude above the freeze-in line. We do not explicitly consider the freeze-in process for the dimension-full operators, as the required coupling is well below the experimental sensitivity. For example, for the dipole moments, DM can be generated by the freeze-in mechanism if $\mu_\chi, d_\chi \sim (10^{-15} - 10^{-18}) \text{ GeV}^{-1}$.

The s -channel annihilations with the Z boson are resonantly enhanced for the

center of mass energies of $\sqrt{s} \simeq m_Z$. Therefore, for $m_\chi \simeq m_Z/2 \simeq 45$ GeV, more DM is annihilated than in a photon-only model, which in turn leads to the sharp drops of the freeze-out lines in fig. 4.4. Such a resonant production only avoids the direct detection constraints on the thermal relic for the anapole moment, allowing a small unconstrained window for $m_\chi \sim 45$ GeV and $\mathcal{A}_\chi \sim 10^{-6}$ GeV $^{-2}$.

Similarly, the freeze-in line has different features in the hypercharge-coupled model. In contrast to the photon-coupled model, where the prediction is less dependent on m_χ for $m_\chi \gtrsim 1$ GeV, the presence of the additional Z channel enhances the annihilations $\text{SM SM} \rightarrow \chi\chi$ below the Z threshold at $m_\chi \leq m_Z/2$, allowing smaller values of Q_χ to generate the observed DM relic abundance. The additional Z channels are kinematically inaccessible for DM masses above this threshold, such that the freeze-in line aligns with the photon-only model prediction.

4.3.4 Application to multiple operators

For the scenario in which multiple operators are present at the same time—as is typically the case in models in which a Dirac DM candidate obtains EM moments—we can use eq. (4.23) and the approach outlined in refs. [278, 279] to obtain *conservative* limits on operators for which interference terms arise.

For the case at hand, this effect is relevant for the EM moments that appear in the c_1^N term in eq. (4.22): millicharge, magnetic moment, and charge radius. Using a quadratic approximation for the likelihood, the conservative limits can be obtained analytically using [278, 279]

$$\mathbb{M}_\alpha^{\text{max}} = \sqrt{\mathcal{N}_\mathcal{E}^{\text{sig}}(\mathbb{M}^{\text{max}})(\mathbb{N}_\mathcal{E}^{-1})_{\alpha\alpha}}, \quad (4.25)$$

where $\mathcal{N}_\mathcal{E}^{\text{sig}}(\mathbb{M}^{\text{max}})$ is the solution of

$$a_\mathcal{E} \left(\mathcal{N}_\mathcal{E}^{\text{sig}}(\mathbb{M}^{\text{max}}) \right)^2 + b_\mathcal{E} \mathcal{N}_\mathcal{E}^{\text{sig}}(\mathbb{M}^{\text{max}}) + c_\mathcal{E} - 2.71 = 0, \quad (4.26)$$

and $(\mathbb{N}_\mathcal{E}^{-1})_{\alpha\alpha}$ are the diagonal elements of the inverse rate matrices given in eq. (4.23). The coefficients for the quadratic approximation of the likelihood functions, $\{a_\mathcal{E}, b_\mathcal{E}, c_\mathcal{E}\}$, are provided in table A.2 of appendix A.

We present in fig. 4.6 the conservative limits on these operators as non-continuous lines and the naive limits are indicated by continuous lines. As values of the EM moments above the dashed and dot-dashed limits are excluded, they can be considered conservative irrespective of other EM interactions. Compared to the standard approach, the limits are weaker by a factor $\sim 2 - 5$ in the conservative approach, depending on the coupling, mass range, and experiment.

Furthermore, we can visualize the experimental reach on multiple operators in a lower-dimensional subspace by evaluating the signal rate assuming two non-zero

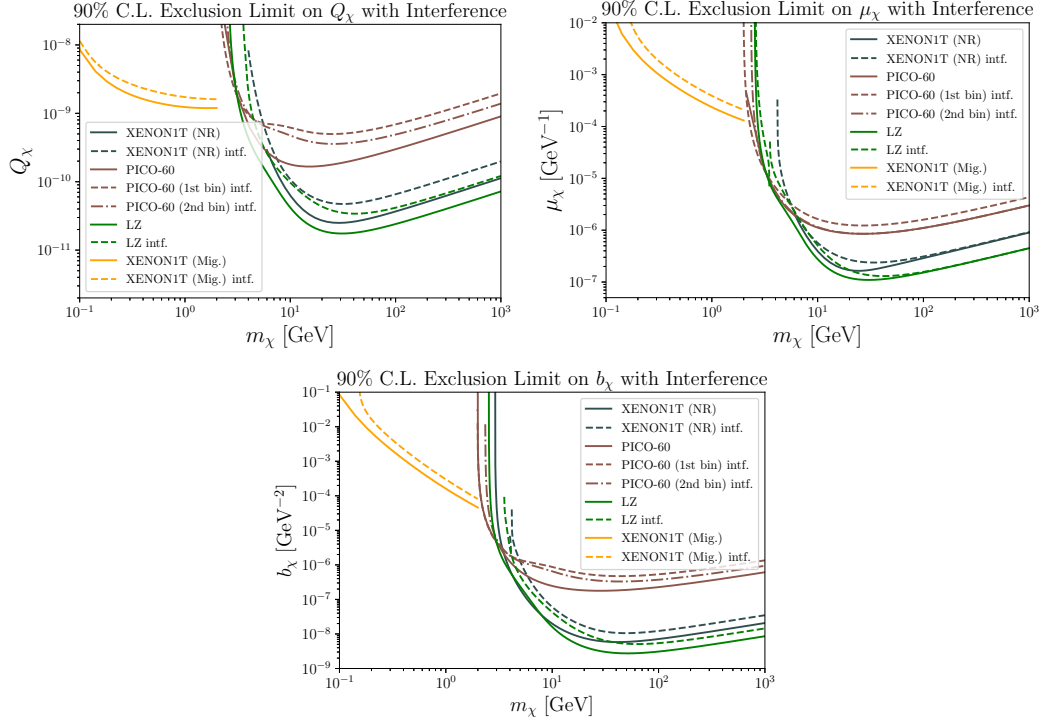


Figure 4.6: 90% C.L. exclusion limits on the millicharge, the magnetic moment and charge radius in the standard approach (*continuous*) and conservative limits in which interference terms are included (*dashed* and *dot-dashed*).

coefficients in the set $\{Q_\chi, \mu_\chi, b_\chi\}$. The overall signal rate can decrease or increase depending on the relative phase as these operators interfere, leading to ellipses in the two-dimensional space spanned by the respective coefficients.

We present in fig. 4.7 these exclusion ellipses for XENON1T, LZ, PICO-60 (1st and 2nd bin) and their combination for a Dirac DM candidate with a mass of $m_\chi = 4$ GeV. As the experiments have different sensitivities to the EM moments, the elements of the rate matrix $M_{ij}^\mathcal{E}$ vary—in particular, the off-diagonal elements—resulting in the tilt of the ellipses. XENON1T and LZ use xenon as the target material; therefore, the orientation of their exclusion ellipses is very similar. In contrast, the PICO-60 experiment uses C_3F_8 , leading to a different orientation with respect to the xenon-based ones. Due to this mismatch, the combination of these experiments leads to a significant improvement in the global exclusion limit, as visualized by the black exclusion ellipses, more than what would be gained by an increase in exposure to a single experiment.⁹

⁹We followed ref. [279] for the derivation of the combined exclusion limit.

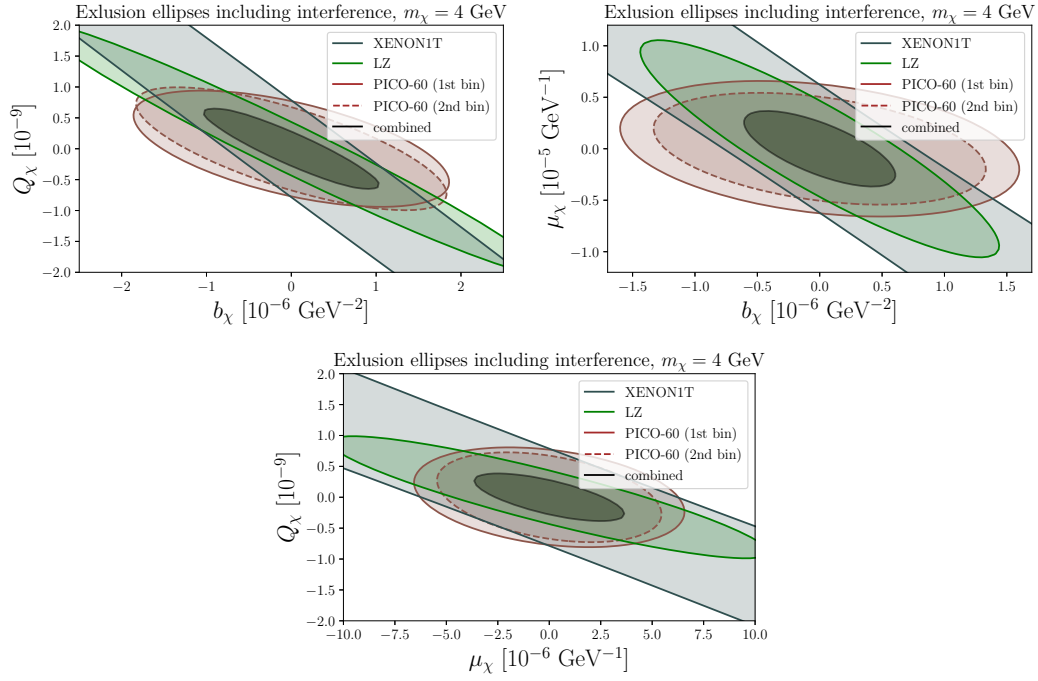


Figure 4.7: 90% exclusion ellipses for the two-dimensional subspaces spanned by $\{Q_\chi, b_\chi, \mu_\chi\}$; the colored regions are excluded by the respective experiments indicated in the legend. We also show the exclusion ellipses by statistically combining XENON1T, LZ, PICO-60 (1st bin), and PICO-60 (2nd bin).

Chapter 5

The lightest neutralino as an archetype of Majorana fermions

In chapter 3, we derived the generic expressions for the various EM interactions of a fermion in which a t -channel mediator generates them at the one-loop level. As pointed out in refs. [1, 2], one application of these model-independent results is the calculation of the anapole moment of the lightest neutralino $\tilde{\chi}_1^0$ within the minimal supersymmetric standard model (MSSM). The neutralino is a Majorana fermion, so the anapole operator is the only non-zero diagonal interaction with the EM field; further, in chapter 4, we discussed the direct detection phenomenology and derived the exclusion limits on the anapole moment from various dark matter laboratories. We found that the strongest limit excludes a fermionic dark matter candidate with mass $m_\chi \simeq 40 \text{ GeV}$ with an anapole moment of $\mathcal{A}_\chi \simeq 2 \times 10^{-6} \text{ fm } \mu_N$.

In this chapter, we want to explore the theoretical prediction for the anapole moment of the lightest neutralino within the MSSM in light of the sensitivity of the direct detection experiments. Conceptually, similar ideas have been considered in refs. [311–314]; however, here we employ the general results derived in section 3.2 for a consistent treatment of the vector contribution utilizing the background field method. Although, in general, the EM moments can also give rise to transition elements, and thus decays of neutralinos [209–211], here we focus only on the diagonal anapole moment of the lightest neutralino.

5.1 Supersymmetry in a nutshell

Before discussing the anapole moment of the lightest neutralino and its connection to direct searches of dark matter in more detail, we briefly discuss the relevant notions of supersymmetry (SUSY) to fix the notation. For a more detailed overview, see refs. [315–322].

In SUSY, spacetime symmetry is extended to include a transformation that relates bosonic and fermionic states. This extension is the only known way to circumvent the Coleman-Mandula theorem [321, 323], which prohibits the scattering matrix from having more symmetries than those from the Poincaré-group and internal symmetries.

ries. Thereby, its minimal realization, the *minimal supersymmetric standard model* (MSSM), is a theoretically well-motivated extension of the SM. Here, the SM is augmented with so-called supersymmetric partners for every field present in the SM. Furthermore, due to technical reasons, the MSSM contains two Higgs doublets, one up-type with hypercharge $Y = +1$, and one down-type with hypercharge $Y = -1$, generating the mass terms for both weak isospin configurations $T_{3L} = \pm 1$ [319].

The MSSM offers solutions to various open questions of the contemporary particle physics landscape. Prominent examples include gauge coupling unification at high energies, protecting the Higgs mass from large radiative corrections, and offering a plausible weak-scale DM candidate. The latter point is only true if R -parity, also known as *matter parity*, is conserved, stabilizing the lightest supersymmetric particle (LSP), which can thus serve as a DM candidate. This discrete symmetry is defined as

$$R_p = (-1)^{3(B-L)+2s}, \quad (5.1)$$

where B is the baryon number, L the lepton number and s is the spin. All SM particles are assigned a value of $R_p = +1$, whereas the supersymmetric partners have $R_p = -1$. In addition to stabilizing the LSP, a theory respecting R -parity has no tree-level terms giving rise to rapid proton decays [324, 325]. The proton lifetime is constrained to be $\tau \gtrsim 10^{34}$ years [326, 327], such that these R -parity violating (RPV) terms would have to be suppressed by unnaturally tiny coupling constants. To avoid such terms altogether, assuming R -parity conservation for the MSSM is common practice, which we also adapt in this chapter.

In exact SUSY, the masses of the SM particles and their supersymmetric partners are identical. As experimentally, no new scalar fields with masses of the SM fermions have been observed, SUSY cannot be realized exactly in Nature. Thus, SUSY must be broken, which must occur in a hidden sector [319]. Subsequently, the breaking has to be mediated to the visible sector, for which many mechanisms have been proposed including supergravity mediating- [316, 328], gauge mediating- [329], and anomaly mediating models [330–333].

From a practical point of view, one typically considers SUSY breaking by manually adding soft-breaking terms to the Lagrangian. These terms include soft-breaking mass- and Yukawa terms for the new degrees of freedom. These soft parameters and the mixing angles between the new states are $\mathcal{O}(100)$ unknown parameters introduced in the MSSM. Considering phenomenological input, such as the absence of new CP phases, no flavor changing neutral currents, and universality of the two first generations, the number of new parameters can be reduced to be of $\mathcal{O}(20)$ [334], which is still large enough to make phenomenological studies cumbersome.

Thus, typical approaches in phenomenological studies include only considering a subset of these parameters, as typically done in collider studies as summarized by the Particle Data Group in ref. [335], or focusing on isolated features of the model

as in refs. [336–339]. Also, theoretical ideas, such as split-SUSY [340–343], where all scalar partners are assumed to be heavy, can reduce the number of parameters. Alternatively, one can use high-dimensional parameter scans (such as in refs. [344, 345]) to study a more general situation. Related to the former approach is the idea of the RPV-3 MSSM [346, 347], where only the third generation sfermions are taken to be light to avoid experimental constraints on the first two sparticle generations while maintaining the stability of the electroweak vacuum with minimal fine-tuning. In this dissertation, however, we focus on the R -parity conserving case, except for the discussion of RPV MSSM contributions to the EM properties of neutrinos in section 7.3.5.

5.2 Particle content of the minimal supersymmetric standard model

Following ref. [319], we briefly introduce the particle content of the R -parity conserving MSSM before calculating and discussing the anapole moment of the lightest neutralino in the upcoming sections. A similar introduction can be found in ref. [1].

5.2.1 The Higgs sector

The MSSM contains two Higgs doublets

$$h_1 = \begin{pmatrix} h_1^1 \\ h_1^2 \end{pmatrix} = \begin{pmatrix} h_1^0 \\ h_1^- \end{pmatrix} \quad \text{and} \quad h_2 = \begin{pmatrix} h_2^1 \\ h_2^2 \end{pmatrix} = \begin{pmatrix} h_2^+ \\ h_2^0 \end{pmatrix}, \quad (5.2)$$

whose soft-breaking Lagrangian reads

$$-\mathcal{L}_{\text{soft}} \supset m_1^2 |h_1|^2 + m_2^2 |h_2|^2 + (m_{12}^2 h_1 \cdot h_2 + \text{h.c.}), \quad (5.3)$$

where m_1 and m_2 are respectively the masses of the up-type and down-type Higgs, and $m_{12}^2 = B\mu$, where B is the soft-breaking bilinear parameter and μ is the Higgs-higgsino mass parameter. After spontaneous symmetry breaking, the Higgs doublets acquire each a vacuum expectation value (vev):

$$\langle h_1 \rangle = \frac{1}{\sqrt{2}} \begin{pmatrix} v_1 \\ 0 \end{pmatrix}, \quad \langle h_2 \rangle = \frac{1}{\sqrt{2}} \begin{pmatrix} 0 \\ v_2 \end{pmatrix}. \quad (5.4)$$

Phenomenologically, the ratio of the two vevs,

$$\tan \beta = \frac{v_2}{v_1}, \quad (5.5)$$

with $0 < \beta < \pi/2$, is a free parameter of the theory and enters through the couplings in many observables. The Higgs potential reads at the minimum

$$V_H^{\min} = \frac{1}{32}(g'^2 + g^2)(v_1^2 - v_2^2)^2 + \frac{1}{2}m_{1h}^2 v_1^2 + \frac{1}{2}m_{2h}^2 v_2^2 - m_{12}^2 v_1 v_2, \quad (5.6)$$

where $m_{1,2h}^2 = m_{1,2}^2 + |\mu|^2$. As at the minimum $\partial V_H^{\min}/\partial v_i = 0$, one can derive the following relations [319]:

$$m_{12}^2 = -\frac{1}{2}(m_1^2 - m_2^2) \tan(2\beta) - \frac{1}{2}m_Z^2 \sin(2\beta), \quad (5.7)$$

$$|\mu|^2 = \frac{m_2^2 \sin^2 \beta - m_1^2 \cos^2 \beta}{\cos(2\beta)} - \frac{1}{2}m_Z^2. \quad (5.8)$$

The fields remaining in the low-energy theory are two neutral CP-even Higgs fields h and H with masses

$$m_{h,H}^2 = \frac{1}{2} \left(m_A^2 + m_Z^2 \mp \sqrt{(m_A^2 - m_Z^2)^2 + 4m_Z^2 m_A^2 \sin^2(2\beta)} \right), \quad (5.9)$$

where one, typically the lighter, is identified with the $m_{h_{\text{exp}}} \simeq 125$ GeV signature measured by CMS [348] and ATLAS [349]. Further, the mass spectrum consists of a CP-odd Higgs A with mass

$$m_A^2 = \frac{2m_{12}^2}{\sin 2\beta}, \quad (5.10)$$

a charged Higgs H^\pm with mass

$$m_{H^\pm}^2 = m_A^2 + m_W^2, \quad (5.11)$$

a neutral Goldstone boson G^0 , and a charged Goldstone boson G^\pm . Similar to the SM Higgs mechanism, the Goldstone modes are identified with the longitudinal degree of freedom of the gauge bosons Z and W^\pm , respectively, giving rise to their masses as

$$m_W = \frac{g}{2} \sqrt{v_1^2 + v_2^2}, \quad m_Z = \frac{\sqrt{g'^2 + g^2}}{2} \sqrt{v_1^2 + v_2^2}. \quad (5.12)$$

The relevant independent parameters for the Higgs sector can, therefore, be chosen as follows:

$$m_A \quad \text{and} \quad \tan \beta. \quad (5.13)$$

Then, all mixing angles and masses of the Higgs sector can be determined at the tree level. In general, loop effects can give large corrections to the masses [350–352], and are included in numerical tools commonly employed to study supersymmetric particle spectra such as `SuSpect` [334], `SOFTSUSY` [353], `FlexibleSUSY` [354] and `Himalaya` [355].

5.2.2 Neutralinos and charginos

The fermionic superpartners of the gauge bosons B, W^0, W^\pm , commonly referred to as *gauginos* are the *binos* \tilde{B} and the *winos* \tilde{W}^0 and \tilde{W}^\pm . As the superpartners of the Higgs doublets introduced in eq. (5.2),

$$\tilde{h}_1 = \begin{pmatrix} \tilde{h}_1^+ \\ \tilde{h}_1^- \end{pmatrix} = \begin{pmatrix} \tilde{h}_1^0 \\ \tilde{h}_1^- \end{pmatrix} \quad \text{and} \quad \tilde{h}_2 = \begin{pmatrix} \tilde{h}_2^+ \\ \tilde{h}_2^- \end{pmatrix} = \begin{pmatrix} \tilde{h}_2^+ \\ \tilde{h}_2^0 \end{pmatrix}, \quad (5.14)$$

also contain fermionic degrees of freedom; the neutral (charged) gauginos and the neutral (charged) higgsinos can mix. We can write the vector containing the neutral interaction eigenstates as

$$\psi^0 = (\tilde{B}, \tilde{W}^0, \tilde{h}_1^+, \tilde{h}_2^0), \quad (5.15)$$

where the mass matrix reads

$$\mathcal{M}^n = \begin{pmatrix} M_1 & 0 & -m_Z c_\beta s_W & m_Z s_\beta s_W \\ 0 & M_2 & m_Z c_\beta c_W & -m_Z s_\beta c_W \\ -m_Z c_\beta s_W & m_Z c_\beta c_W & 0 & -\mu \\ m_Z s_\beta s_W & -m_Z s_\beta c_W & -\mu & 0 \end{pmatrix}. \quad (5.16)$$

The parameters M_1 and M_2 are respectively the soft bino and wino masses, $s_\beta = \sin \beta$, $c_\beta = \cos \beta$, $s_W = \sin \theta_W$ and $c_W = \cos \theta_W$.

After diagonalization with a unitary 4×4 mixing matrix N , the resulting mass eigenstates are the *neutralinos* and are typically denoted by

$$\tilde{\chi}_i^0 = N_{ik} \psi_k^0, \quad (5.17)$$

satisfying $m_{\tilde{\chi}_1^0} < m_{\tilde{\chi}_2^0} < m_{\tilde{\chi}_3^0} < m_{\tilde{\chi}_4^0}$. The lightest of them, $\tilde{\chi}_1^0$, is a typical WIMP-like DM candidate, as in many models, this is the LSP in the spectrum whose stability is guaranteed by R -parity. The lightest neutralino is denoted by χ for the remaining part of this chapter.

The charged components of the winos and the higgsinos also mix, forming the *chargino* states denoted by $\tilde{\chi}_j^\pm$, with $j = 1, 2$. The mass term for the interaction eigenstates denoted by

$$\psi^+ = \begin{pmatrix} \tilde{W}^+ \\ \tilde{h}_2^+ \end{pmatrix} \quad \text{and} \quad \psi^- = \begin{pmatrix} \tilde{W}^- \\ \tilde{h}_1^- \end{pmatrix}, \quad (5.18)$$

reads

$$-\mathcal{L} \supset (\psi^-)^T X \psi^+ + \text{h.c.}, \quad (5.19)$$

where the chargino mass matrix is given by

$$X = \begin{pmatrix} M_2 & \sqrt{2} m_W \sin \beta \\ \sqrt{2} m_W \cos \beta & \mu \end{pmatrix}. \quad (5.20)$$

The mass matrix X is diagonalized by the 2×2 unitary matrices U and V as

$$U^* X V^{-1} = M_{\text{diag}}^c, \quad (5.21)$$

and the mass eigenstates are identified with

$$\chi^+ = V \psi^+ \quad \text{and} \quad \chi^- = U \psi^-. \quad (5.22)$$

The (squared) eigenvalues of the mass matrix X then read

$$m_{\tilde{\chi}_{1,2}^\pm}^2 = \frac{1}{2} \left[|M_2^2| + |\mu^2| + 2m_W^2 \mp \left((|M_2^2| - |\mu^2|)^2 + 4m_W^4 \cos^2(2\beta) + 4m_W^2 (|M_2^2| + |\mu^2| + 2 \operatorname{Re}(M_2 \mu) \sin(2\beta)) \right)^{1/2} \right], \quad (5.23)$$

i.e. in terms of the four component Dirac spinors

$$\tilde{\chi}_j^\pm = \begin{pmatrix} \tilde{\chi}_j^\pm \\ \tilde{\chi}_j^\mp T \end{pmatrix}, \quad (5.24)$$

the diagonal mass Lagrangian reads

$$-\mathcal{L} \supset m_{\tilde{\chi}_1^\pm} \tilde{\chi}_1^\pm \tilde{\chi}_1^\pm + m_{\tilde{\chi}_2^\pm} \tilde{\chi}_2^\pm \tilde{\chi}_2^\pm. \quad (5.25)$$

If M_2 and μ are real, the chargino mixing matrices can be written as

$$U = O_u \quad (5.26)$$

and

$$V = \begin{cases} O_v & \text{if } \det X > 0 \\ \sigma_3 O_v & \text{if } \det X < 0 \end{cases}, \quad (5.27)$$

with real matrices

$$O_i = \begin{pmatrix} \cos \phi_i & \sin \phi_i \\ -\sin \phi_i & \cos \phi_i \end{pmatrix}. \quad (5.28)$$

The mixing angles ϕ_u and ϕ_v are related to the new SUSY parameters as

$$\tan 2\phi_u = \frac{2\sqrt{2}m_W(\mu \sin \beta + M_2 \cos \beta)}{M_2^2 - \mu^2 - 2m_W^2 \cos(2\beta)}, \quad (5.29a)$$

$$\tan 2\phi_v = \frac{2\sqrt{2}m_W(\mu \cos \beta + M_2 \sin \beta)}{M_2^2 - \mu^2 + 2m_W^2 \cos(2\beta)}. \quad (5.29b)$$

As eq. (5.29) is invariant under $\phi_i \rightarrow \phi_i + \pi/2$, all four combinations have to be checked whether they diagonalize the chargino mass matrix given in eq. (5.20), or not [319].

As evident from the neutralino and chargino mixing matrices in eq. (5.16) and eq. (5.20) respectively, the relevant parameters which determine the masses and, via the elements of the mixing matrices, the couplings of the neutralinos and charginos with the other MSSM particles, are:

$$M_1, \quad M_2, \quad \mu, \quad \tan \beta. \quad (5.30)$$

5.2.3 Sfermion field content

Finally, we discuss the supersymmetric partners of the SM fermions. Their mass term can be cast as

$$-\mathcal{L} \supset \tilde{\mathbf{f}}^\dagger M_f^2 \tilde{\mathbf{f}}, \quad (5.31)$$

where we introduced

$$\tilde{\mathbf{f}} = \begin{pmatrix} \tilde{f}_L \\ \tilde{f}_R \end{pmatrix}, \quad (5.32)$$

with $\tilde{f}_{L(R)}$ denoting the supersymmetric partner of the left-chiral (right-chiral) SM fermion.¹ The mass matrix for the charged sleptons and squarks is given by

$$M_f^2 = \begin{pmatrix} M_{fLL}^2 & M_{fLR}^2 \\ M_{fRL}^2 & M_{fRR}^2 \end{pmatrix}, \quad (5.33)$$

with entries [356]

$$M_{fLL}^2 = m_f^2 + m_{\tilde{f}_L}^2 + m_Z^2 \cos(2\beta) (T_{3L}^f - Q_f \sin^2(\theta_W)), \quad (5.34a)$$

$$M_{fLR}^2 = m_f (A_f^* - \mu \kappa), \quad (5.34b)$$

$$M_{fRR}^2 = m_f^2 + m_{\tilde{f}_R}^2 + m_Z^2 \cos(2\beta) Q_f \sin^2(\theta_W), \quad (5.34c)$$

$$M_{fRL}^2 = m_f (A_f - \mu^* \kappa), \quad (5.34d)$$

where T_{3L}^f is the third component of the weak isospin of the fermion f , Q_f its charge in units of $e > 0$, and m_f its mass. Further, $m_{\tilde{f}_L}$ ($m_{\tilde{f}_R}$) is the left-chiral (right-chiral) soft-breaking mass, μ is the Higgs-higgsino mass parameter appearing due to the Higgs mechanism, A_f are the soft-breaking trilinear couplings, and we defined

$$\kappa = \begin{cases} 1/\tan \beta & f = \text{up-type squarks} \\ \tan \beta & f = \text{down-type squarks, } \tilde{\ell} \end{cases}. \quad (5.35)$$

¹Although we consider $\tilde{\mathbf{f}}$ to be related to a specific fermion f of a single generation, we could also interpret $\tilde{f}_{L/R}$ as three-dimensional vectors in generation space such that the resulting $\tilde{\mathbf{f}}$ describes collectively all sfermions, leading to intergenerational mixing [319]. Such a scenario, however, goes beyond the scope of this work.

Finally, for completeness, the mass matrix for the sneutrinos in the absence of right-handed neutrinos is given by

$$M_{\tilde{\nu}}^2 = \begin{pmatrix} M_{\tilde{\ell}_L}^2 + m_Z^2 T_{3L}^{\tilde{\nu}} \cos 2\beta & 0 \\ 0 & 0 \end{pmatrix}. \quad (5.36)$$

The sfermion matrix in eq. (5.33) can be diagonalized by a 2×2 orthogonal matrix,

$$O_f = \begin{pmatrix} \cos \theta_f & \sin \theta_f \\ -\sin \theta_f & \cos \theta_f \end{pmatrix}, \quad (5.37)$$

such that

$$O_f M_f^2 O_f^T = \text{diag}(m_{f_1}^2, m_{f_2}^2) \quad (5.38)$$

with $m_{f_1}^2 < m_{f_2}^2$.

Note that the off-diagonal terms of eq. (5.33) are proportional to the corresponding fermion mass, such that for practical purposes, the mixing of the first two generations can be considered to be negligible. This assumption is also experimentally motivated, as light sfermions of the first two generations would cause problematic flavor-changing neutral currents, unobserved by experiments [319, 357]. For heavy soft masses in the first two generations, these processes can be suppressed [358, 359]; see refs. [317, 319] for more details.

We conclude that at the tree level, the relevant input parameters for the sfermion sector are the soft-breaking mass parameters

$$\begin{aligned} & m_{\tilde{\ell}_L}, \quad m_{\tilde{u}_L}, \quad m_{\tilde{c}_L}, \quad m_{\tilde{t}_L}, \\ & m_{\tilde{\ell}_R}, \quad m_{\tilde{u}_R}, \quad m_{\tilde{c}_R}, \quad m_{\tilde{t}_R}, \quad m_{\tilde{d}_R}, \quad m_{\tilde{s}_R}, \quad m_{\tilde{b}_R}, \end{aligned} \quad (5.39)$$

and the trilinear soft-breaking couplings

$$A_\tau, \quad A_b, \quad A_t. \quad (5.40)$$

5.3 Anapole moment of the lightest neutralino

As demonstrated in refs. [1, 2], the anapole moment of the lightest neutralino is generated at the one-loop level by its interactions with a *i*) sfermion and fermion, *ii*) chargino and W boson (and the associated Goldstone boson), and a *iii*) chargino and Higgs boson. Depending on the couplings, mixing angles, and masses of the low-energy particle spectrum, these processes can contribute with different strengths, such that general statements about the size of the anapole moment of the lightest neutralino cannot be made. These three contributions are depicted in fig. 5.1.

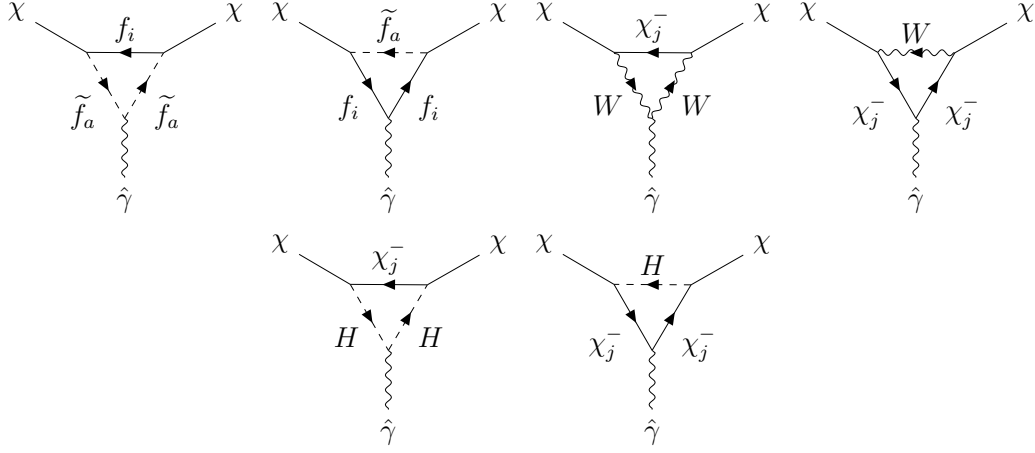


Figure 5.1: Diagrams generating the anapole moment of the lightest neutralino χ within the MSSM using the BDM. As χ is a Majorana fermion, the conjugated diagrams are kept implicit but considered in the calculation.

The relevant part of the MSSM Lagrangian describing the interaction with the (s)fermions can be formulated as [319]

$$\mathcal{L} \supset \bar{\chi} \left[\tilde{c}_L^{i,a} P_L + \tilde{c}_R^{i,a} P_R \right] \tilde{f}_a f_i + \text{h.c.} \quad (5.41)$$

Here, \tilde{f}_a describes the mass-eigenstate a of the superpartner of the fermion f_i , where i is a generation index. Assuming no intergenerational scalar mixing, the couplings between the sfermions, fermions, and χ read:

$$\tilde{c}_L^{i,1} = G^{f_i L} \cos \theta_{\tilde{f}_a} + H^{f_i R} \sin \theta_{\tilde{f}_a}, \quad (5.42a)$$

$$\tilde{c}_R^{i,1} = G^{f_i R} \sin \theta_{\tilde{f}_a} + H^{f_i L} \cos \theta_{\tilde{f}_a}, \quad (5.42b)$$

$$\tilde{c}_L^{i,2} = -G^{f_i L} \sin \theta_{\tilde{f}_a} + H^{f_i R} \cos \theta_{\tilde{f}_a}, \quad (5.42c)$$

$$\tilde{c}_R^{i,2} = G^{f_i R} \cos \theta_{\tilde{f}_a} - H^{f_i L} \sin \theta_{\tilde{f}_a}, \quad (5.42d)$$

where we defined

$$G^{f_i L} = -\sqrt{2}g \left[T_{3L}^{f_i} N_{12}^* + \tan \theta_W (Q_{f_i} - T_{3L}^{f_i}) N_{11}^* \right], \quad (5.43a)$$

$$G^{f_i R} = \sqrt{2}g \tan \theta_W Q_{f_i} N_{11}, \quad (5.43b)$$

$$H^{f_i L} = -\frac{g}{\sqrt{2}m_W} m_{f_i} \times \begin{cases} N_{14}/\sin \beta, & f_i = u\text{-type} \\ N_{13}/\cos \beta, & f_i = d\text{-type}, \ell \end{cases}, \quad (5.43c)$$

$$H^{f_i R} = H^{f_i L*}. \quad (5.43d)$$

The interactions of χ with the charged gauge boson and its associated Goldstone mode is given by [319]

$$\mathcal{L} \supset \bar{\chi} \gamma^\mu \left[v_L^j P_L + v_R^j P_R \right] \tilde{\chi}_j^- W_\mu^+ + \bar{\chi} \left[c_L^{G,j} P_L + c_R^{G,j} P_R \right] \tilde{\chi}_j^- G^+ + \text{h.c.}, \quad (5.44)$$

with

$$v_L^j = -g N_{12} U_{j1}^* - g \frac{1}{\sqrt{2}} N_{13} U_{j2}^*, \quad (5.45a)$$

$$v_R^j = -g N_{12}^* V_{j1} + g \frac{1}{\sqrt{2}} N_{14}^* V_{j2}, \quad (5.45b)$$

$$c_L^{G,j} = g \cos \beta \left[N_{13}^* U_{j1}^* - \frac{1}{\sqrt{2}} U_{j2}^* (N_{12}^* + \tan \theta_W N_{11}^*) \right], \quad (5.45c)$$

$$c_R^{G,j} = -g \sin \beta \left[N_{14} V_{j1} + \frac{1}{\sqrt{2}} V_{j2} (N_{12} + \tan \theta_W N_{11}) \right]. \quad (5.45d)$$

Finally, the interactions of the lightest neutralino with the charged Higgs boson can be written as [319]

$$\mathcal{L} \supset \bar{\chi} \left[c_L^{H,j} P_L + c_R^{H,j} P_R \right] H^+ \tilde{\chi}_j^- + \text{h.c.}, \quad (5.46)$$

with couplings

$$c_L^{H,j} = -g \sin \beta \left[N_{13}^* U_{j1}^* - \frac{1}{\sqrt{2}} U_{j2}^* (N_{12}^* + \tan \theta_W N_{11}^*) \right], \quad (5.47a)$$

$$c_R^{H,j} = -g \cos \beta \left[N_{14} V_{j1} + \frac{1}{\sqrt{2}} V_{j2} (N_{12} + \tan \theta_W N_{11}) \right]. \quad (5.47b)$$

As these interactions are parameterized following the notation of chapter 3, we can use the general results of section 3.2 to directly deduce the anapole moment of the lightest neutralino [1, 2]:

$$\mathcal{A}_\chi = \mathcal{A}_{\tilde{f}} + \mathcal{A}_W + \mathcal{A}_H, \quad (5.48)$$

where we separated the three different contributions induced respectively by the

interactions in eqs. (5.41), (5.44) and (5.46). Explicitly, they read [1, 2]:

$$\mathcal{A}_{\tilde{f}} = -\frac{e}{96\pi^2 m_\chi^2} \sum_{i,a} N_c^i Q_i \left[|c_L^{i,a}|^2 - |c_R^{i,a}|^2 \right] \mathcal{F}_3^S \left(\frac{m_{f_i}}{m_\chi}, \frac{m_{\tilde{f}_a}}{m_\chi} \right), \quad (5.49a)$$

$$\begin{aligned} \mathcal{A}_W = \frac{e}{96\pi^2 m_\chi^2} \left\{ 2 \sum_j \left[|v_L^j|^2 - |v_R^j|^2 \right] \mathcal{F}_3^V \left(\frac{m_{\tilde{\chi}_j^\pm}}{m_\chi}, \frac{m_W}{m_\chi} \right) \right. \\ \left. + \sum_j \left[|c_L^{G,j}|^2 - |c_R^{G,j}|^2 \right] \mathcal{F}_3^V \left(\frac{m_{\tilde{\chi}_j^\pm}}{m_\chi}, \frac{m_W}{m_\chi} \right) \right\}, \quad (5.49b) \end{aligned}$$

$$\mathcal{A}_H = \frac{e}{96\pi^2 m_\chi^2} \sum_j \left[|c_L^{H,j}|^2 - |c_R^{H,j}|^2 \right] \mathcal{F}_3^S \left(\frac{m_{\tilde{\chi}_j^\pm}}{m_\chi}, \frac{m_{H^+}}{m_\chi} \right). \quad (5.49c)$$

In eq. (5.49), N_c^i (Q_i) is the color factor (electric charge) of the fermion in the loop, and we used $Q_{\tilde{\chi}_j^\pm} = -1$ for the charginos. Further, the scalar- and vector anapole loop functions $\mathcal{F}_3^{S,V}$ are given in eq. (3.34) and eq. (3.35) respectively.

Note that the anapole moment identically vanishes in the supersymmetric limit, as can be checked explicitly by evaluating eq. (5.49) for vanishing soft-breaking parameters.

5.4 Analysis for simplified particle spectra

In this section, we discuss a few common simplified limiting cases of the full MSSM particle spectrum that compromise typical simplified model setups of Majorana dark matter.

5.4.1 Pure lightest neutralino and heavy scalars

The first simplified scenario is akin to minimal dark matter [360], in which dark matter is part of a specific representation of $SU(2)_L$. Here, all sfermions are assumed to be heavy and thus decouple from the low-energy theory (*i.e.* split-SUSY [340–343]). Therefore, the only interactions remaining at the low-energy scale are due to the gauge- and Higgs-related terms in the MSSM Lagrangian.

Bino limit (singlet)

The first case assumes that the lightest neutralino is a pure bino state ($N_{11} = 1$), thus a singlet under the gauge group of $SU(2)_L$. Regarding the MSSM parameters, this limit is realized if $M_1 \ll M_2, |\mu|, m_{\tilde{f}}$. Here, the lightest neutralino is practically inert and does not couple to the charged gauge boson and the charged Higgs, so the anapole moment is predicted to be very small.

Wino limit (doublet)

For the MSSM parameters satisfying $M_2 \ll M_1, |\mu|, m_{\tilde{f}}$ the lightest neutralino is a wino, interacting with the W boson via the charged wino component of the charginos. Only the W boson loop (and the Goldstone) contribute to the anapole moment in this limit. However, the couplings in this scenario are inherently P-conserving, as

$$v_L^1 \simeq -g, \quad v_R^1 \simeq -g, \quad (5.50a)$$

$$c_L^{G,1} \simeq 0, \quad c_R^{G,1} \simeq 0, \quad (5.50b)$$

such that the anapole moment is strongly suppressed in the wino DM scenario.

Higgsino limit (triplet)

Finally the higgsino limit is realized if $|\mu| \ll M_1, M_2, m_{\tilde{f}}$. The two lightest neutralinos are almost mass-degenerate, forming a pseudo-Dirac pair. The lightest chargino is comprised of the charged higgsino component. The couplings read:

$$v_L^1 \simeq -\frac{g}{2}, \quad v_R^1 \simeq \frac{g}{2}, \quad (5.51a)$$

$$c_L^{G,1} \simeq 0, \quad c_R^{G,1} \simeq 0, \quad (5.51b)$$

such that similar to the wino limit, the anapole moment is strongly suppressed. For the loop induced by the charged Higgs boson, eq. (5.46) indicates that also this contribution is suppressed and, therefore, negligible.

All in all, we find that for the pure neutralino limits (*e.g.* bino, wino, and higgsino), the anapole moment of the lightest neutralino is negligible. For it to be enhanced, one needs to introduce parity-breaking interactions, which can be achieved by either

- i)* light sfermions in the spectrum (see eq. (5.41)), or
- ii)* non-pure neutralinos with higgsino component (see eq. (5.44)).

These two options generate an anapole moment via the scalar- and vector contributions, respectively. In the generic MSSM parameter landscape, both conditions can be satisfied simultaneously.

5.4.2 Pure lightest neutralino and a light scalar

As discussed in the previous subsection, one way to generate an anapole moment is through introducing light scalar degrees of freedom. We particularize this scenario for the three pure neutralino cases. Therefore, the vector contribution is absent, as the respective couplings respect parity.

Bino and a light stau

As noted in section 5.4.1, for the case of a pure bino, the neutralino does not couple to the W - and the Higgs boson. Therefore, the only contribution to the anapole moment can be due to additional light scalars, to which the bino couples. We consider a simplified scenario in which the bino interacts with a SM fermion f and the mass-eigenstates \tilde{f}_1 and \tilde{f}_2 (where $m_{\tilde{f}_1} < m_{\tilde{f}_2}$), obtained by diagonalizing the interaction eigenstates \tilde{f}_L and \tilde{f}_R via a rotation parameterized by the mixing angle $\theta_{\tilde{f}}$. Using the general couplings of eq. (5.42), we find:

$$c_L^1 = -\sqrt{2}g \left[\tan \theta_W (Q_f - T_{3L}^f) \right] \cos \theta_{\tilde{f}}, \quad c_R^1 = \sqrt{2}g \tan \theta_W Q_f \sin \theta_{\tilde{f}}, \quad (5.52a)$$

$$c_L^2 = \sqrt{2}g \left[\tan \theta_W (Q_f - T_{3L}^f) \right] \sin \theta_{\tilde{f}}, \quad c_R^2 = \sqrt{2}g \tan \theta_W Q_f \cos \theta_{\tilde{f}}. \quad (5.52b)$$

We present in the upper left panel of fig. 5.2 a scatter plot of the anapole moment for a tau-philic bino (therefore $f = \tau$) with parameters in the range $m_\chi \in [10^1, 10^4]$ GeV, $m_{\tilde{f}_1} \in [m_\chi, 10m_\chi]$, $m_{\tilde{f}_2} \in [m_{\tilde{f}_1}, 10m_\chi]$, and $\theta_{\tilde{f}} \in [0, 2\pi]$. We employ the limit on staus from LEP [361], ATLAS [362] and the constraints from the $Z \rightarrow \text{inv.}$ width, excluding new charged particles with masses below ~ 45 GeV [363]. The latter is the cause of the fragmentation for $m_\chi \lesssim 40$ GeV in the top left panel in fig. 5.2, as here the scalar mass is constrained to be heavier than ~ 45 GeV, thus setting the overall scale of the anapole as $\mathcal{A}_\chi \sim m_S^{-2}$. For larger values, $m_\chi \gtrsim 45$ GeV, the scalar mass can be comparable to m_χ , evading the constraints. Thus, we find an enhancement of the anapole moment for small mass-splittings between the scalar and χ , defining the upper scale of \mathcal{A}_χ in fig. 5.2. Meanwhile, the lower scale is set by the largest scalar mass considered in the scan, $m_S \leq 10 \times m_\chi$. These features are smeared out by the randomness of the Yukawa coupling, further enhancing or decreasing the prediction for the anapole moment. The few points indicating strongly suppressed anapole moments correspond to cancellations between the couplings, implying accidental P-conserving interactions.

Wino and a light stau

Also, here, the anapole moment is generated by the inherent parity-violating interaction between the wino, a fermion, and the associated sfermion. The parity-violating couplings read

$$c_L^1 = -\sqrt{2}g T_{3L}^f \cos \theta_{\tilde{f}}, \quad c_R^1 = 0, \quad (5.53a)$$

$$c_L^2 = \sqrt{2}g T_{3L}^f \sin \theta_{\tilde{f}}, \quad c_R^2 = 0. \quad (5.53b)$$

We present in the top right panel of fig. 5.2 a scatter plot for similar parameter choices as discussed in the bino paragraph.

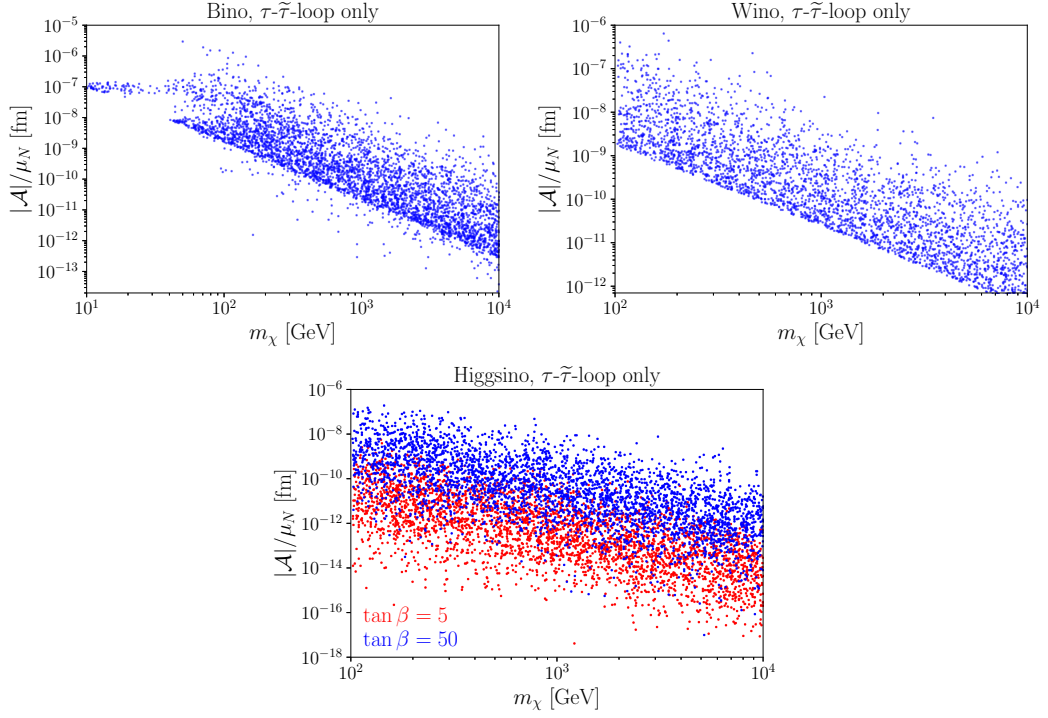


Figure 5.2: Anapole moment of the pure bino, wino, and higgsino generated by a light $\tilde{\tau}$ in units of the nucleon magneton $\mu_N = e/2m_p$. For the higgsino case, we separately show the result for $\tan \beta = 5$ ($\tan \beta = 50$) in red (blue). The presented points satisfy the constraints on staus from ATLAS [362], LEP [361] and the Z -width [363].

Higgsino and a light stau

Finally, in the scenario that the neutralino is a pure higgsino and its anapole moment is solely generated by one light sfermion in the spectrum, the couplings read:

$$c_L^1 = H^{fL} \sin \theta_{\tilde{f}}, \quad c_R^1 = H^{fL} \cos \theta_{\tilde{f}}, \quad (5.54a)$$

$$c_L^2 = H^{fL} \cos \theta_{\tilde{f}}, \quad c_R^2 = -H^{fL} \sin \theta_{\tilde{f}}, \quad (5.54b)$$

with

$$H^{fL} = -\frac{g}{2m_W} m_f \times \begin{cases} 1/\sin \beta, & f = u\text{-type} \\ 1/\cos \beta, & f = d\text{-type}, \ell \end{cases}, \quad (5.55)$$

violating parity. The expected anapole moment for the tau-philic scenario is presented in the bottom panel of fig. 5.2 for $\tan \beta = 5$ in red and $\tan \beta = 50$ in blue.

5.4.3 Mixed lightest neutralino with heavy scalars

In this scenario, the contribution from scalar particles in the loop is suppressed by their masses as $\mathcal{A}_\chi \sim m_S^{-2}$, which are negligible if the scalars are sufficiently heavy. Therefore, the only sizeable contribution in this scenario can arise from charginos and W or Higgs bosons in the loop. The only free parameters in this setup are the soft gaugino masses $M_{1,2}$, the bilinear Higgs soft parameter μ , and the ratio of the two Higgs vevs, $\tan\beta$. We employ collider constraints on charginos assuming decays via W bosons from LEP [364], setting a lower bound on the chargino mass as $m_{\tilde{\chi}_1^\pm} > 103.5$ GeV, and from ATLAS [365].

Bino-wino

First, we consider the bino-wino mixed neutralino, realized if the mass parameters satisfy $M_{1,2} \ll \mu$. In this limit, only the lighter chargino, which is a charged wino, is part of the low-energy spectrum. The couplings between the lightest neutralino, the chargino, and the W boson become:

$$v_L^1 = -gN_{12}, \quad v_R^1 = -gN_{12}^*, \quad (5.56a)$$

$$c_L^{G,1} = 0, \quad c_R^{G,2} = 0, \quad (5.56b)$$

which preserves parity and, therefore, does not generate an anapole moment. The other contribution due to the chargino and Higgs vanishes, as the former is a charged wino, thus

$$c_L^{H,1} = 0, \quad c_R^{H,1} = 0. \quad (5.57)$$

We conclude that a bino-wino without light scalars has no anapole moment.

Bino-higgsino

The mixed bino-higgsino scenario corresponds to MSSM parameters satisfying $M_1, \mu \ll M_2$. Then, the only light chargino in the spectrum is a charged higgsino. Therefore, in contrast to the bino-wino scenario, the interaction of the neutralino with the charged Higgs and chargino does not vanish. The couplings read:

$$c_L^{H,1} = g \sin\beta \tan\theta_W N_{11}^*, \quad c_R^{H,1} = -g \cos\beta \tan\theta_W N_{11}. \quad (5.58)$$

Further, the couplings between neutralino, chargino, and W boson read in this limit:

$$v_L^1 = -\frac{g}{\sqrt{2}} N_{13}, \quad v_R^1 = g \frac{g}{\sqrt{2}} N_{14}^* \quad (5.59a)$$

$$c_L^{G,1} = -\frac{g}{\sqrt{2}} \cos\beta \tan\theta_W N_{11}^*, \quad c_R^{G,2} = -\frac{g}{\sqrt{2}} \sin\beta \tan\theta_W N_{11}. \quad (5.59b)$$

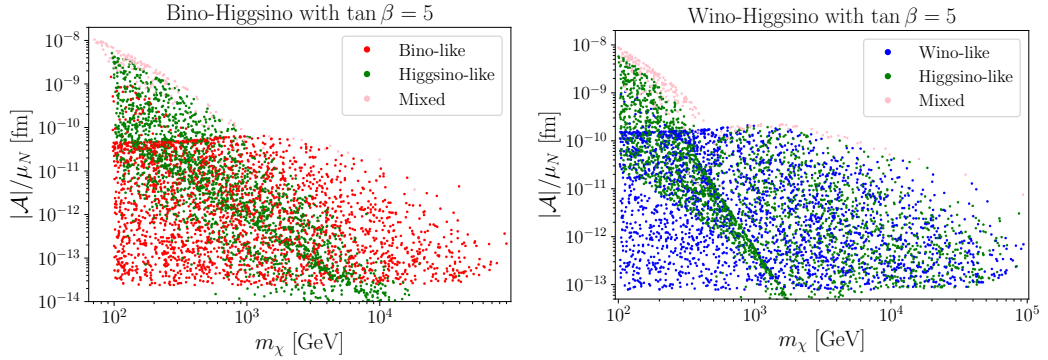


Figure 5.3: Scans over the simplified SUSY model parameters in which the lightest neutralino is a mixture of bino & higgsino (*left*) and wino & higgsino (*right*). The color denotes the dominant admixture of the neutralino. The constraints from LEP [364], ATLAS [365] and the Z -width [363] are applied.

The result of a random scan with parameters $M_1, \mu \in [100, 10^5]$ GeV and $\tan \beta = 5$ is shown in the left panel of fig. 5.3. Here, we assumed a heavy charged Higgs boson, such as to focus only on the W -chargino loop contribution to the neutralino's anapole moment. In fig. 5.3 the colors denote whether the lightest neutralino is bino-like ($|N_{11}| > 0.95$, red), higgsino-like ($\sqrt{N_{13}^2 + N_{14}^2} > 0.95$, green) or wino-like ($N_{12} > 0.95$, blue). The pink dots show the remaining points, where the lightest neutralino is an admixture of the different interaction eigenstates. As expected, the points indicating large mixing result in the largest predictions for the anapole moment, as here, the P violation is enhanced. In contrast, the bino- and wino-like scenarios lead to smaller values of the anapole, as here, the chargino is heavy, suppressing the amplitude. On the other hand, the higgsino-like scenario is enhanced because the lightest neutralino and chargino become mass-degenerate, for which the loop functions are enhanced.

The plot in the left panel of fig. 5.3 indicates that in the mixed scenario (pink dots), the neutralino can be lighter than the minimal mass-scales of the scan, given by $M_1, \mu \geq 100$ GeV. This apparent inconsistency originates from the diagonalization procedure of the neutralino mixing matrix, where multiple entries of comparable scale result in masses $m_\chi \sim 50$ GeV for the lightest neutralino. In this scenario, a relatively large mass-splitting to the chargino is realized, such that collider constraints on the chargino are evaded.

Wino-higgsino

Finally, if $M_2, \mu \ll M_1$, the lightest neutralino is a mixture of wino and higgsino, and both charginos can be light and thus contribute to the anapole moment. The couplings between the lightest neutralino, the W boson and the charginos $\tilde{\chi}_j^\pm$, $j = 1, 2$, read:

$$v_L^j = -gN_{12}U_{j1}^* - \frac{g}{\sqrt{2}}N_{13}U_{j2}^*, \quad v_R^j = -gN_{12}^*V_{j1} + \frac{g}{\sqrt{2}}N_{14}^*V_{j2}, \quad (5.60a)$$

$$c_L^{G,j} = g \cos \beta [N_{13}^*U_{j1}^* - \frac{1}{\sqrt{2}}U_{j2}^*N_{12}^*], \quad c_R^{G,j} = -g \sin \beta [N_{14}V_{j1} + \frac{1}{\sqrt{2}}V_{j2}N_{12}], \quad (5.60b)$$

being typically parity-violating. The same holds for the interaction with the charged Higgs, for which the couplings read:

$$c_L^{H,j} = -g \sin \beta [N_{13}^*U_{j1}^* - \frac{1}{\sqrt{2}}N_{12}^*U_{j2}^*], \quad c_R^{H,j} = -g \cos \beta [N_{14}V_{j1} + \frac{1}{\sqrt{2}}V_{j2}N_{12}]. \quad (5.61)$$

We present in the right panel of fig. 5.3 a parameter scan with similar choices for the input parameters as for the previous case; the conclusions are analogous to the earlier discussion. In contrast to the bino-higgsino scenario, no points with $m_\chi \leq 100$ GeV are identified, as in this scenario not only χ but also the chargino is light, which is excluded by LEP constraints [364].

5.5 Analysis within the full MSSM

For the analysis in the full MSSM, we consider a broad scan of the soft parameters defining the low-energy physics after renormalization group evolution. We apply various experimental constraints to this resulting particle spectrum to eliminate excluded points from this high-dimensional parameter space.

The scan setup is as follows: We generate a random set of input parameters defined at the scale $\Lambda = 3$ TeV according to table 5.1 and run them down to the electroweak scale using `SOFTSUSY 4.0` [353]. The resulting low-energy spectrum is checked against experimental constraints. We used the LEP constraints implemented in `micrOMEGAs v3` [366–369] and LHC limits on sparticles using `SModelS v2` [370]. Further, we used constraints on the Higgs sector using `HiggsBounds v4` [371–374] and `HiggsSignals` [375] to ensure that the physical Higgs boson in the spectrum has a mass of $123 \text{ GeV} < m_h < 127 \text{ GeV}$. Flavour constraints are included using `SuperIso v3.0` [376] and `GM2Calc` [377]. To interface the different codes with the common `SLHA` [378, 379] format, we used `PySLHA` [380] and `SLHAea` [381]. We then used the analytical formulas in eq. (5.49) to calculate the anapole moment of the

MSSM		MSSM (lepto-philic)	
Parameter	Range	Parameter	Range
M_1	[100, 2000] GeV	M_1	[100, 2000] GeV
M_2	[100, 2000] GeV	M_2	[100, 2000] GeV
M_3	[2000, 5000] GeV	M_3	3000 GeV
$A_{t,b,\tau}$	[-4000, 4000] GeV	A_t	4000 GeV
m_A	[10^3 , 10^5] GeV	$A_{b,\tau}$	0
$\tan \beta$	[3, 50]	m_A	5000 GeV
μ	[100, 2000] GeV	$\tan \beta$	50
$m_{\tilde{\ell}_{L,R}}$	[100, 2000] GeV	μ	[100, 2000] GeV
$m_{\tilde{q}_{L1,2}}$	[400, 2000] GeV	$m_{\tilde{e}_{L,R}}, m_{\tilde{\mu}_{L,R}}$	[100, 1000] GeV
$m_{\tilde{u}_{R1,2}}, m_{\tilde{d}_{R1,2}}$	[400, 2000] GeV	$m_{\tilde{\tau}_{L,R}}$	3000 GeV
$m_{\tilde{q}_{L3}}$	[300, 2000] GeV	$m_{\tilde{q}_{L1,2}}, m_{\tilde{u}_{R1,2}}, m_{\tilde{d}_{R1,2}}$	5×10^4 GeV
$m_{\tilde{u}_{R3}}, m_{\tilde{d}_{R3}}$	[300, 2000] GeV	$m_{\tilde{q}_{L3}}, m_{\tilde{u}_{R3}}, m_{\tilde{d}_{R3}}$	10^4 GeV

Table 5.1: Input parameters for the MSSM scans defined at the scale $\Lambda = 3$ TeV for the full scan (*left*) and for the smaller scan, focusing on the lepto-philic coannihilation region (*right*). For details on the meaning of each parameter, see section 5.1.

lightest neutralino using the low-energy spectrum satisfying all experimental constraints listed above.

The resulting values for the anapole moment of the lightest neutralino are presented in fig. 5.4 for the scan defined by the parameter ranges given in the left part of table 5.1. In the left panel of fig. 5.4, the color indicates the composition of the lightest neutralino. Only a few bino-like points survived the experimental constraints. While the wino-like points populate the region around $|\mathcal{A}_\chi| \sim 10^{-7} \text{ fm } \mu_N$, the higgsino-like points have maximal values around $|\mathcal{A}_\chi| \sim 10^{-8} \text{ fm } \mu_N$. Apart from the fact that also smaller values of m_χ are populated, the scenario of mixed neutralinos does not have a distinct tendency.

In the right panel of fig. 5.4, the color indicates which diagram gives the dominant contribution to the total anapole moment, *i.e.* the sfermion-fermion loop (red), the W -chargino loop (blue) or the Higgs-chargino loop (green). The remaining points are colored in pink.

Overall, the interpretation follows the discussion of the simplified setups in section 5.4: large values of the anapole are due to light scalars in the model with $\mathcal{O}(1)$ enhancement per light scalar. On the other hand, the loops with vector bosons saturate at $|\mathcal{A}_\chi| \sim 10^{-8} \text{ fm } \mu_N$. As visible, no points are found in which the Higgs contribution \mathcal{A}_H is dominant, whereas the mixed scenario populates the whole range.

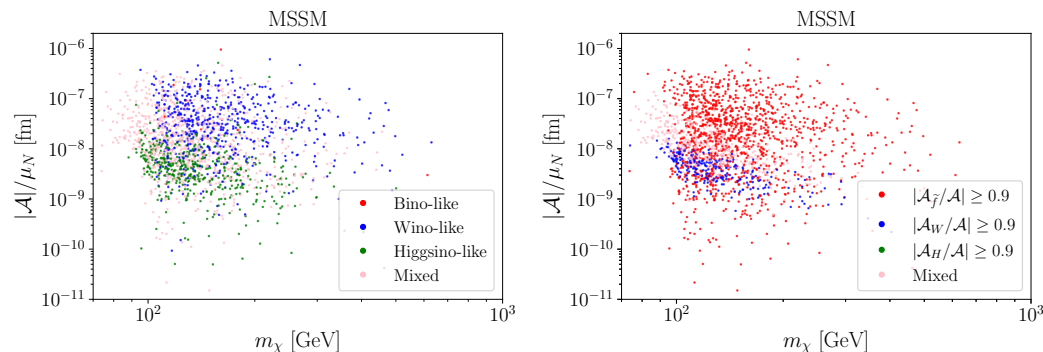


Figure 5.4: Result of the parameter scan within the MSSM using as boundary conditions the input values defined in table 5.1. In the left panel, we highlight the composition of the lightest neutralino, and in the right panel, the dominant contribution to its anapole moment. For the experimental constraints considered, see the main text.

In this full scan, we considered a high-dimensional parameter space with finite computing power, risking burying interesting features, such as resonance regions. Further, some points that survived all the above-mentioned constraints could be in tension with direct detection experiments, mainly if the squarks are light or the channels with Higgs bosons are enhanced. Albeit we covered some of the phenomenologically interesting scenarios semi-analytically in section 5.4, here we also want to consider a dedicated lower-dimensional scan, focusing on light sleptons of the first two generations while allowing all neutralino compositions. Therefore, both possibilities of an enhanced anapole moment can be realized: light sleptons and sizeable mixing among the interaction eigenstates comprising the lightest neutralino. The exact parameter ranges are summarized in the right part of table 5.1, and the resulting predictions for the anapole moment of the lightest neutralino are depicted in fig. 5.5.

As in fig. 5.4, in the left panel of fig. 5.5, the color indicates the composition of the lightest neutralino, whereas in the right panel, it indicates the dominant contribution to the anapole moment. Further, in the right panel the star indicates points which satisfy direct detection constraints from XENON1T [137], PICO-60 [302], CRESST-III [273] and DarkSide-50 [303] as recast by micrOMEGAs v5.3.41 [306, 368]. We find that most of the bino-like and wino-like points avoid the direct detection constraints while predicting large values of the anapole moment due to the light sleptons in the spectrum. In contrast, almost all mixed and higgsino-like points are excluded due to the enhanced tree-level Higgs channel in this scenario.

We do not include constraints from the dark matter relic abundance as we want

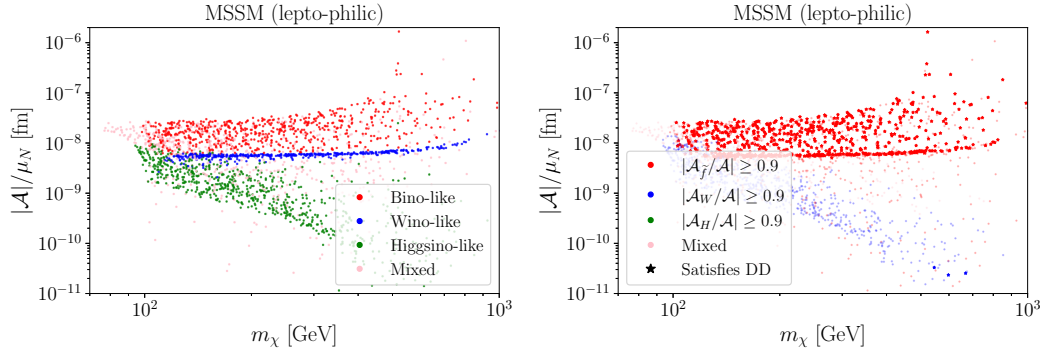


Figure 5.5: Same as fig. 5.4 but for the parameters shown in the right table of table 5.1. In the right panel, a star indicates that direct searches do not exclude this parameter point, as calculated by `micrOMEGAs v5.3.41`.

to remain agnostic about the production mechanism. Therefore, the points shown in figs. 5.4 and 5.5 may not correspond to spectra in which the lightest neutralino reproduces the measured relic abundance.

Chapter 6

Dirac dark matter with electromagnetic moments

In this chapter, we introduce a simplified toy model of Dirac DM, in which EM multipoles are generated at the one-loop level. We use the model-independent direct detection constraints derived in chapter 4 to obtain limits on the UV parameter space. We also discuss these results in light of thermal production via the standard freeze-out mechanism.

6.1 The Dirac dark matter toy model

We consider a lepto-philic DM candidate with a t -channel scalar mediator. The total Lagrangian of this theory reads:

$$\mathcal{L} = \mathcal{L}_{\text{SM}} + \mathcal{L}_{\chi} + \mathcal{L}_{\text{scalar}} + \mathcal{L}_{\text{tri.}} + \mathcal{L}_{\text{quart.}} + \mathcal{L}_{\text{portal}}. \quad (6.1)$$

Here, \mathcal{L}_{SM} is the Lagrangian of the SM, and \mathcal{L}_{χ} contains the kinetic- and mass term of the DM candidate,

$$\mathcal{L}_{\chi} = \bar{\chi}i\cancel{\partial}\chi - m_{\chi}\bar{\chi}\chi. \quad (6.2)$$

Further, $\mathcal{L}_{\text{scalar}}$ describes the scalar Lagrangian, $\mathcal{L}_{\text{tri.}}$ and $\mathcal{L}_{\text{quart.}}$ contain trilinear and quartic interactions, and $\mathcal{L}_{\text{portal}}$ contains the Yukawa interaction, providing a portal between the dark- and visible sector. We discuss these terms in the following.

From the discussion in chapter 3, we know that a portal interaction of DM with a scalar and fermion can give rise to EM interactions. Depending on the richness of this vertex structure, all or only a subset of the possible EM interactions are generated. To capture the complete phenomenological picture, the toy model should have different couplings to parameterize the Yukawa interactions between χ and the left- and right components of the SM fermion in the loop. Choosing complex couplings also allows for CP violation and, therefore, an electric dipole moment.

In the toy model here, we can achieve that by introducing couplings to the left- and right chiral parts of the SM fermion via a portal interaction

$$\mathcal{L}_{\text{portal}} = y_L \bar{\chi} S_L^{\dagger} F + y_R e^{i\phi_{\text{CP}}} \bar{\chi} S_R^{\dagger} f_R + \text{h.c.}, \quad (6.3)$$

where we introduced a $SU(2)_L$ singlet scalar field $S_R^- = S_R$ and doublet $\mathcal{S}_L = (S_L^0, S_L^-)$ coupling respectively to a SM fermion singlet f and doublet F with real couplings $y_{L/R}$. We consider a lepto-philic model, such that we can identify $F = (\nu_L, \ell_L)$ and $f = \ell_R$, where $\ell = e, \mu, \tau$ is an SM lepton. Note that we can choose y_R to carry the CP-violating phase ϕ_{CP} without loss of generality.

The Lagrangian of the scalar fields is given by

$$\mathcal{L}_{\text{scalar}} = (D_\mu \mathcal{S}_L)^\dagger (D_\mu \mathcal{S}_L) + |D_\mu S_R|^2 - m_L^2 \mathcal{S}_L^\dagger \mathcal{S}_L - m_R^2 |S_R|^2, \quad (6.4)$$

where the covariant derivatives depend on the quantum numbers of \mathcal{S}_L and S_R and we introduced soft masses $m_{L/R}^2$.

The trilinear term is given by

$$-\mathcal{L}_{\text{tri.}} = A(\mathcal{S}_L^\dagger \Phi) S_R + \text{h.c.}, \quad (6.5)$$

whose presence induces mixing between \mathcal{S}_L and S_R after electroweak symmetry breaking. This mixing is controlled by the trilinear coupling A , which we assume to be real for simplicity.

The last piece in eq. (6.1) is the quartic term

$$\begin{aligned} -\mathcal{L}_{\text{quart.}} = & \sum_{S=\mathcal{S}_L, S_R} \frac{1}{2} \lambda_0^S (S^\dagger S)^2 + \lambda_1^S (\Phi^\dagger \Phi) (S^\dagger S) \\ & + \lambda_2^{S_L} (\Phi^\dagger \mathcal{S}_L) (\mathcal{S}_L^\dagger \Phi) + \lambda_3^{S_L S_R} (\mathcal{S}_L^\dagger \mathcal{S}_L) (S_R^\dagger S_R), \end{aligned} \quad (6.6)$$

where Φ denotes the SM Higgs doublet. For the sake of simplicity, we set these quartic couplings to zero from now on, as they do not influence the EM interactions of χ . In principle, however, they appear in the scalar mixing matrix and thus impact the left-right mixing angle (see, for example, ref. [254]). We could, however, achieve a similar effect by rescaling the soft masses $m_{L/R}^2$ accordingly.

After the SM Higgs field acquires a vacuum expectation value of $v \simeq 246$ GeV, the following scalar mass matrix emerges

$$-\mathcal{L}_{\text{scalar}} \supset (S_L^* \ S_R^*) \begin{pmatrix} m_L^2 & A \frac{v}{\sqrt{2}} \\ A \frac{v}{\sqrt{2}} & m_R^2 \end{pmatrix} \begin{pmatrix} S_L \\ S_R \end{pmatrix}, \quad (6.7)$$

which can be diagonalized by a rotation

$$\begin{pmatrix} S_L \\ S_R \end{pmatrix} = \begin{pmatrix} \cos \psi & -\sin \psi \\ \sin \psi & \cos \psi \end{pmatrix} \begin{pmatrix} S_1 \\ S_2 \end{pmatrix}, \quad (6.8)$$

where the mixing angle is given by

$$\tan \psi = - \frac{\sqrt{2} A v}{m_R^2 - m_L^2 + \sqrt{2 A^2 v^2 + (m_R^2 - m_L^2)^2}}. \quad (6.9)$$

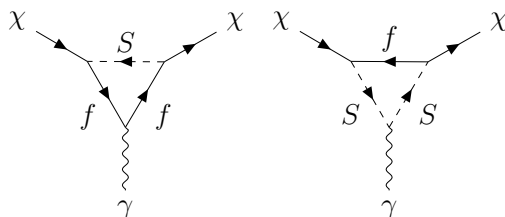


Figure 6.1: Diagrams generating the EM moments of the Dirac DM candidate in our toy model with $S = S_{1,2}$.

Thus, in this new basis, the toy model Lagrangian in eq. (6.1) has diagonal scalar mass terms,

$$\mathcal{L} \supset -m_L^2 (S_L^0)^2 - m_{S_1}^2 S_1^\dagger S_1 - m_{S_2}^2 S_2^2, \quad (6.10)$$

where the mass eigenvalues read

$$m_{S_{1,2}}^2 = \frac{1}{2} \left(m_R^2 + m_L^2 \mp \sqrt{2A^2 v^2 + (m_R^2 - m_L^2)^2} \right). \quad (6.11)$$

In analogy to the similar discussion in the SUSY context, a negative $m_{S_1}^2$ would indicate a breaking of the $SU(3)_c$ or $U(1)_{EM}$ symmetry. Even if the squared masses are positive, too large values of A can lead to unstable vacua, resulting in additional constraints from vacuum stability [382–387].

From now on, we trade the parameter set $\{m_L, m_R, A\}$ in favor of $\{m_{S_1}, m_{S_2}, \sin \psi\}$ and assume that the vacuum stability constraints are negligible.

In the mass basis, the relevant portal interaction of eq. (6.3) now reads

$$\begin{aligned} \mathcal{L}_{\text{portal}} = & \bar{\chi} \left[y_L \cos \psi P_L + y_R \sin \psi e^{i\phi_{CP}} P_R \right] S_1^* f + \text{h.c.} \\ & + \bar{\chi} \left[-y_L \sin \psi P_L + y_R \cos \psi e^{i\phi_{CP}} P_R \right] S_2^* f + \text{h.c.} \end{aligned} \quad (6.12)$$

This portal interaction, eq. (6.12), is akin to the building block Lagrangian used in section 3.2, which we used to derive the EM moments for a neutral Dirac fermion. Therefore, S_1 and S_2 generate at the one-loop level, depicted in fig. 6.1, the dipole moments, an anapole moment and a charge radius of χ .

Using the general results derived in section 3.2, we find for the magnetic- and

electric dipole moment of χ

$$\mu_\chi = -\frac{eQ_f}{32\pi^2 m_\chi} \left\{ (y_L^2 \cos^2 \psi + y_R^2 \sin^2 \psi) \mathcal{F}_1 \left(\frac{m_f}{m_\chi}, \frac{m_{S_1}}{m_\chi} \right) \right. \quad (6.13a)$$

$$\left. + 2y_L y_R \cos \psi \sin \psi \cos \phi_{\text{CP}} \mathcal{F}_2 \left(\frac{m_f}{m_\chi}, \frac{m_{S_1}}{m_\chi} \right) \right. \quad (6.13b)$$

$$\left. + (y_L^2 \sin^2 \psi + y_R^2 \cos^2 \psi) \mathcal{F}_1 \left(\frac{m_f}{m_\chi}, \frac{m_{S_2}}{m_\chi} \right) \right. \quad (6.13c)$$

$$\left. - 2y_L y_R \cos \psi \sin \psi \cos \phi_{\text{CP}} \mathcal{F}_2 \left(\frac{m_f}{m_\chi}, \frac{m_{S_2}}{m_\chi} \right) \right\} \quad (6.13d)$$

and

$$d_\chi = \frac{eQ_f}{16\pi^2 m_\chi} y_L y_R \cos \psi \sin \psi \sin \phi_{\text{CP}} \left[\mathcal{F}_2 \left(\frac{m_f}{m_\chi}, \frac{m_{S_1}}{m_\chi} \right) - \mathcal{F}_2 \left(\frac{m_f}{m_\chi}, \frac{m_{S_2}}{m_\chi} \right) \right], \quad (6.14)$$

respectively. The electric dipole moment vanishes without CP violation, *i.e.* $\sin \phi_{\text{CP}} = 0$ implies $d_\chi = 0$. Furthermore, it vanishes if the scalar masses are identical, $m_{S_1} = m_{S_2}$, or if the mixing between the gauge eigenstates is trivial, in which case $\sin \psi = 0$ or $\cos \psi = 0$, as here an appropriate field redefinition can rotate the phase away.

The anapole moment reads

$$\mathcal{A}_\chi = -\frac{eQ_f}{192\pi^2 m_\chi^2} \left\{ [y_L^2 \cos^2 \psi - y_R^2 \sin^2 \psi] \mathcal{F}_3 \left(\frac{m_f}{m_\chi}, \frac{m_{S_1}}{m_\chi} \right) \right. \quad (6.15a)$$

$$\left. + [y_L^2 \sin^2 \psi - y_R^2 \cos^2 \psi] \mathcal{F}_3 \left(\frac{m_f}{m_\chi}, \frac{m_{S_2}}{m_\chi} \right) \right\}. \quad (6.15b)$$

Note that the P violation is explicit; if the couplings of χ to the left- and right-chiral fermion in eq. (6.12) are identical, the anapole moment vanishes.

Finally, the charge radius can be expressed as

$$b_\chi = \frac{-eQ_f}{384\pi^2 m_\chi^2} \left\{ (y_L^2 \cos^2 \psi + y_R^2 \sin^2 \psi) \mathcal{F}_4 \left(\frac{m_f}{m_\chi}, \frac{m_{S_1}}{m_\chi} \right) \right. \quad (6.16a)$$

$$\left. + 2y_L y_R \cos \psi \sin \psi \cos \phi_{\text{CP}} \mathcal{F}_5 \left(\frac{m_f}{m_\chi}, \frac{m_{S_1}}{m_\chi} \right) \right. \quad (6.16b)$$

$$\left. + (y_L^2 \sin^2 \psi + y_R^2 \cos^2 \psi) \mathcal{F}_4 \left(\frac{m_f}{m_\chi}, \frac{m_{S_2}}{m_\chi} \right) \right. \quad (6.16c)$$

$$\left. - 2y_L y_R \cos \psi \sin \psi \cos \phi_{\text{CP}} \mathcal{F}_5 \left(\frac{m_f}{m_\chi}, \frac{m_{S_2}}{m_\chi} \right) \right\}. \quad (6.16d)$$

Although, in general, both scalars S_1 and S_2 contribute, from now on, we limit our discussion to the scenario in which S_2 is very heavy and can be integrated out

from the low-energy theory. In practice, the moments are mainly generated by the light scalar S_1 , as all further contributions are suppressed by some power of m_{S_2} such that even a scalar mass-splitting of a factor of a few would be enough for the contribution from S_1 to be a good approximation for the whole amplitude. Therefore, this assumption is well motivated except if the scalars are close in mass.

We can identify the relevant portal couplings in eq. (6.12) as

$$c_L \equiv y_L \cos \psi, \quad c_R \equiv y_R \sin \psi. \quad (6.17)$$

As we can interpret (c_L, c_R) as a vector in the plane of P-breaking couplings, it is useful to express them in polar coordinates as

$$c_L = c \cos \theta, \quad c_R = c \sin \theta, \quad (6.18)$$

with radius $c^2 = c_L^2 + c_R^2$ and P-violating angle $\tan \theta = c_R/c_L = y_R/y_L \tan \psi$. Then, maximal P violation corresponds to $\cos \theta = 0$ or $\sin \theta = 0$. Finally, we express the scalar mass using the mass-splitting parameter $\eta = m_{S_1}/m_\chi > 1$.

Thus, the toy model is characterized by the following set of parameters:

$$m_\chi, \quad \eta, \quad c, \quad \sin \theta, \quad \sin \phi_{\text{CP}}. \quad (6.19)$$

6.2 Constraints from direct detection signals

In section 4.3, we calculated the model-independent rate matrices, which can be used to translate limits on the EFT operators into limits on the parameter space of UV models that generate these EM interactions. Here, we apply this formalism to derive exclusion limits on the parameter space of our toy model. Similar analyses have been carried out in refs. [225, 252, 388] for a simplified version of this toy model.

For $\ell = e$, tree-level interactions with the bound electrons are introduced, leading to an additional source of recoil signatures in the detectors; therefore, it is beyond the scope of this analysis. Further, the toy model generates contributions to the electron's anomalous magnetic moment, translating into severe constraints on the electron-philic couplings [225]. Also, for $\ell = \mu$, the toy model gives a contribution to the $(g-2)_\mu$, which is of the opposite sign with respect to the discrepancy between measurement and SM prediction [225] (see section 3.1 for an overview). In contrast, the experimental limits on the dipole moments of the τ -lepton are significantly weaker [389, 390], allowing room for BSM physics. Due to this freedom, we consider the τ -philic version of the toy model for the remaining part of the analysis. In principle, however, future experimental limits on the dipole moments of the τ -lepton [391–395] could be used to infer complementary constraints on the τ -philic toy model parameter space.

For fixed values of $\sin \theta$ and $\sin \phi_{\text{CP}}$ we show in figs. 6.2 and 6.3 the regions in the two-dimensional plane spanned by m_χ and $\eta - 1$ for which a given operator gives the largest contribution to the overall signal rate for a specific experiment. We find that the anapole is always suppressed compared to the other operators. Although within the toy model, its numerical value is usually close to the value of the charge radius, the experimental sensitivity to the charge radius operator is significantly stronger, see figs. 4.3 and 4.4. As visualized in figs. 6.2 and 6.3, the assumption that only one operator gives the dominant contribution at direct detection experiments is not justified in a general setup. Further, which operator dominates depends not only on the model parameters but also on the experiment. In particular, we find that even relatively small values of the CP-violating angle, such as $\sin \phi_{\text{CP}} \sim 0.01$, can make the electric dipole contribution dominant for some experiments and for some combinations of m_χ and $\eta - 1$.

Therefore, we consider all four EM moments for calculating the exclusion limits using the factorized rate equation in eq. (4.23). The EM moments μ_χ , d_χ , \mathcal{A}_χ and b_χ are calculated as a function of the toy model parameters summarized in eq. (6.19), resulting in the number of events at the experiment \mathcal{E} , $\mathcal{N}_{\text{sig}}^\mathcal{E}$. Using the statistical methods outlined in appendix A, we derive exclusion limits on this parameter space following the non-observation of DM events. We consider two phenomenologically interesting cases: *i*) the case of maximal CP violation, and *ii*) a conservative scenario with minimal signal count with respect to P- and CP violation.

Maximal CP violation

We choose the benchmark value of $\sin \phi_{\text{CP}} = 1$ for maximal CP violation. Further, we set $\sin \theta = 1/\sqrt{2}$, corresponding to minimal P violation, as then $c_L = c_R$. Further, we set the effective coupling $c = 1$; the limits for all but DS50 would rescale appropriately as $\mathcal{N}_{\text{sig}}^\mathcal{E} \sim c^4$. For DS50, the situation is more complicated, as we employ the background subtraction procedure to calculate the exclusion limits; see appendix A for more details.

For these benchmark values, we derive the limits on $\eta - 1$ as a function of m_χ , which we present in fig. 6.4a. In this figure, we also present collider limits from $\tilde{\tau}$ searches from LEP [361], ATLAS [396] and the model-independent constraints on new light charged particles from the Z -width measurement [363].

Our analysis indicates that direct detection experiments can probe a large portion of the parameter space; particularly, relatively large mass-splittings can be probed in the CP-violating scenario. For instance, when the DM mass is around $m_\chi \simeq 10$ GeV, the obtained limits rule out scalar masses of approximately $m_{S_1} \simeq 10$ TeV. Additionally, we find that small mass-splittings in the range of $\eta \simeq \mathcal{O}(1.01 - 1.1)$ for heavier DM masses of $m_\chi \simeq \mathcal{O}(1 - 10)$ TeV are excluded. This strong sensitivity arises from the non-relativistic electric dipole operator being enhanced for low momenta,

6.2 Constraints from direct detection signals

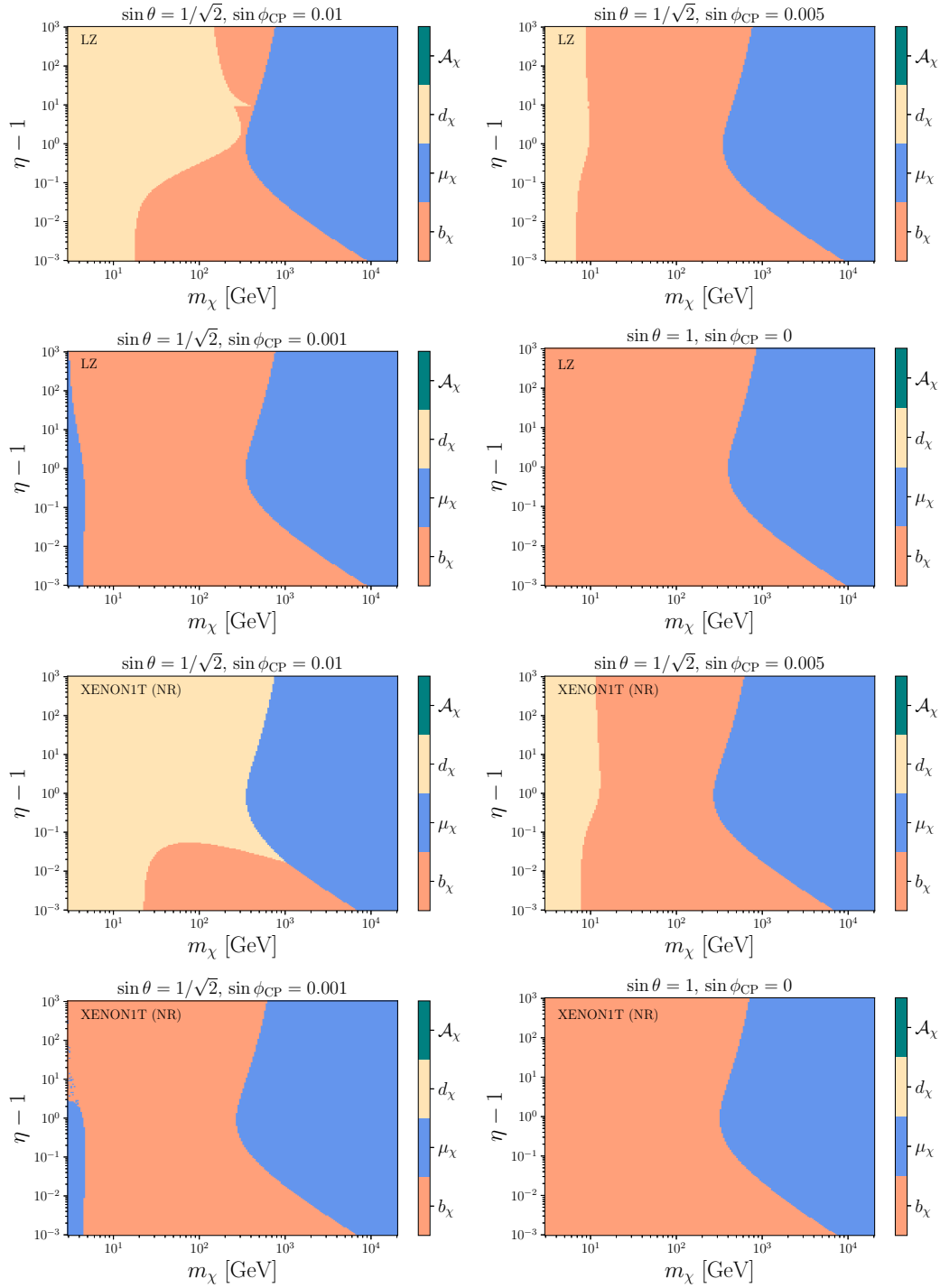


Figure 6.2: Dominant contribution to the LZ and XENON1T (NR) signal rate for specific choices of P- and CP-violating angles as indicated in each panel.

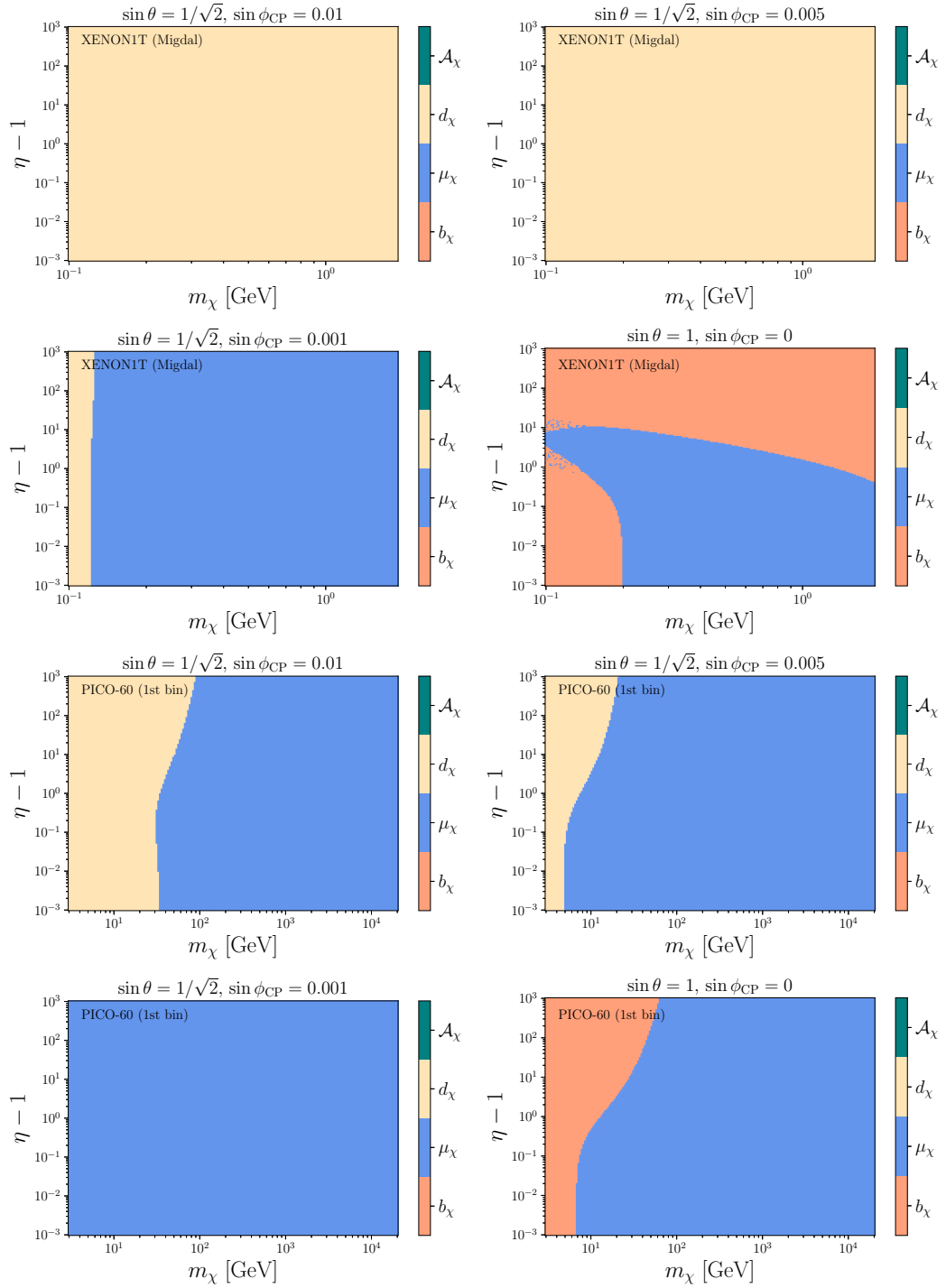


Figure 6.3: Same as fig. 6.2, but for XENON1T (Migdal) and PICO-60 (1st bin) .

see section 4.3. Consequently, when $\sin \phi_{\text{CP}} \neq 0$, the electric dipole significantly contributes to the overall signal rate, resulting in strong limits.

Conservative limits

Although the toy model we consider has only five free parameters, we have to resort to some lower dimensional parameter space by fixing, for example, the angles and c and then constraining the remaining parameters. We followed this approach for the maximal CP-violating scenario above, where the angle choice was a phenomenologically interesting edge case. In order to find more general conclusions about the phenomenology, we could conduct parameter scans, as we did for the neutralino in chapter 5. Here, we want to follow a different approach, resulting in *conservative* limits on the toy model parameter space.

For this, we define the minimized signal rate

$$\mathcal{N}_{\min}^{\mathcal{E}}(m_{\chi}, \eta, c) = \min_{\sin \theta, \sin \phi_{\text{CP}}} \mathcal{N}_{\text{sig}}^{\mathcal{E}}(m_{\chi}, \eta, c, \sin \theta, \sin \phi_{\text{CP}}), \quad (6.20)$$

which for every point in parameter space gives the minimal rate with respect to P- and CP violation. Due to the complicated dependency on the couplings, angles, and kinematic configurations, we determine this minimized rate numerically for calculating the exclusion limit; see appendix A for more details.

We present the minimized rate for the experiments under consideration in fig. 6.5 as a function of m_{χ} for $\eta = 1.1$. In each panel, the lower plot shows the solution for the angles θ and ϕ_{CP} , which minimize the signal count. The upper plot shows the total signal count in black, the different contributions from the four EM moments, and the interference term between the charge radius and the magnetic moment. We find that $\sin \phi_{\text{CP}} = 0$ always minimizes the rate. This behavior is expected as the electric dipole does not interfere with other operators and is proportional to the CP-violating angle. Thus, CP violation always increases the signal count. The P-violating case is more complicated, and no general statements about its impact on the signal count can be made. For $m_{\chi} \gtrsim 1 \text{ GeV}$ and $\eta = 1.1$, we find that $\sin \theta = -1/\sqrt{2}$ leads to a minimization for most experiments. For a different value of η , this relation changes.

We present the resulting exclusion limit in fig. 6.4b for $c = 1$. As we used the minimal rate, these limits are conservative, as any increase in $\mathcal{N}_{\text{sig}}^{\mathcal{E}}$ would result in stronger constraints. Therefore, irrespective of the amount of P- or CP violation in the toy model, the areas enclosed by the contours in the $(m_{\chi}, \eta - 1)$ plane are excluded. Even in this conservative approach, a relatively large region in parameter space is excluded, extending to $m_{\chi} \sim 4 \text{ TeV}$ for small mass-splittings $\eta \sim 1.01$. Even for $m_{\chi} \sim 1 \text{ TeV}$, scalar masses of $m_{S_1} \sim 2 \text{ TeV}$ are excluded, providing a robust and complementary handle on the toy model parameter space.

In principle, further constraints on this toy model can be derived from indirect detection searches; see, for example, refs. [251, 253, 295, 397, 398] for studies on

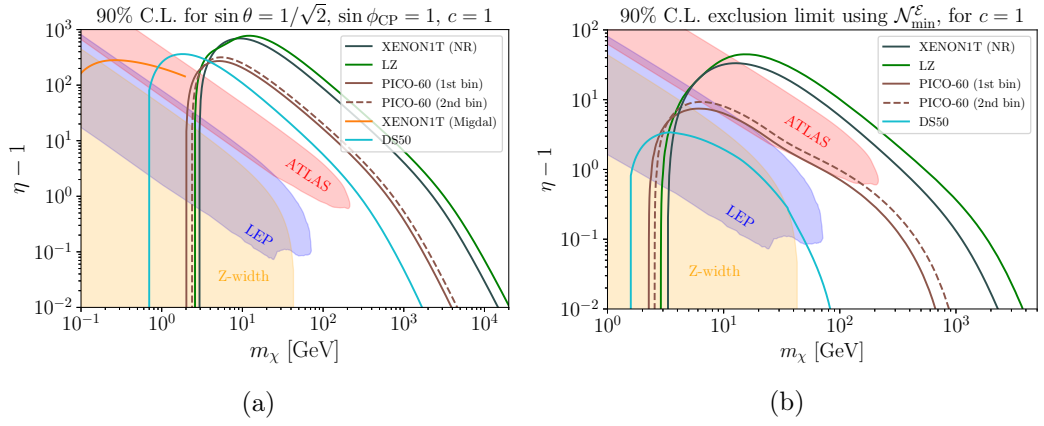


Figure 6.4: 90% C.L. exclusion limits for a model with maximal CP violation (*left*) and the P- and CP independent signal rate $\mathcal{N}_{\text{sig}}^{\mathcal{E}}$ (*right*). In both cases, we set $c = 1$. The blue and red areas show the results of stau searches by LEP [361] and ATLAS [396], respectively. The orange area shows the constraint derived from the decay width of the Z boson [363].

similar models. Such an analysis introduces further uncertainties, for example, from modeling the DM halo, which makes general statements about the interplay of direct detection, collider studies, and indirect detection experiments difficult.

6.2 Constraints from direct detection signals

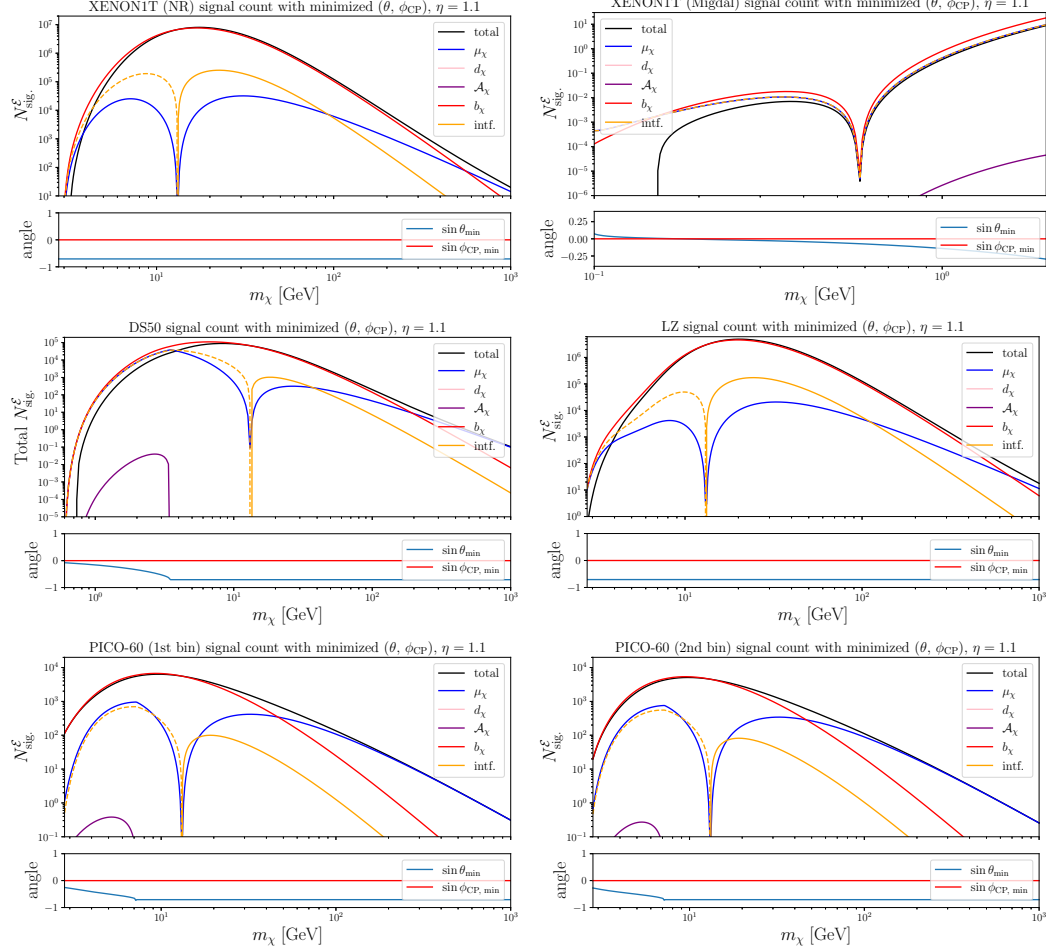


Figure 6.5: Each panel presents the signal count at a specific experiment for the minimized signal rate. The dashed line for the interference contribution indicates that this term is negative, leading to substantial cancellations for XENON1T (Migdal) and DS50. Further, we present the corresponding solutions for the P- and CP-violating angles in the respective lower sub-figures. For the DS50 experiment, we present the total signal rate, *i.e.* we summed over all nine bins.

6.3 Constraints on the thermal relic

For our toy model, we can calculate the relic abundance $\Omega_\chi h^2$ within the standard freeze-out paradigm (see section 2.2) and interpret the measured relic density $\Omega_{\text{DM}} h^2 \simeq 0.12$ [45] as a constraint, thereby fixing one of the UV model parameters.

In the regime outside the coannihilation region, the relic abundance of χ for the case in which it interacts with either S_L or S_R is driven by the tree-level t -channel annihilation diagrams depicted in fig. 6.6. The thermally averaged annihilation cross-section can be written as (see *e.g.* refs. [252, 397, 399, 400])

$$\langle\sigma v\rangle \simeq \frac{y_{L/R}^4 m_\chi^2 \sqrt{1 - (m_\tau/m_\chi)^2}}{32\pi (m_\chi^2 + m_{L/R}^2 - m_\tau^2)^2}. \quad (6.21)$$

In the coannihilation region, *i.e.* if the mass-splitting between the initial states is small, the processes $X_1 X_2 \rightarrow X_3 X_4$, with X_i being bath-particles, can become relevant. In particular, the process $\chi S_{1,2} \rightarrow X_3 X_4$ is enhanced for $\eta \lesssim 1.2$, for which the EM moments are also large. This correlation offers an interesting interplay between thermal production and the direct detection signature. As in this toy model, DM possesses EM interactions, also processes mediated by the SM neutral gauge bosons are constituents of the Boltzmann equations and should be included, as we did in the EFT analysis in section 4.3.3.

To account properly for this large number of processes, we implement our model in `FeynRules` [401–403] and use the public tool `micrOMEGAs` [368, 404] (which uses `CalcHEP` [405] internally) to solve the Boltzmann equations numerically to obtain the relic abundance of χ .

We want to provide some examples of how the relic density and direct detection experiments can give complementary constraints on the parameter space of our toy model. For the benchmark scenarios summarized in table 6.1, we use the measured relic abundance of $\Omega_{\text{DM}} h^2 \simeq 0.12$ [45] to fix one of the Yukawa couplings $y_{L/R}$ of the UV theory, which allows us to calculate the EM moments of χ . As the signal events at the direct detection laboratories only depend on the EM moments (see section 4.3), we then infer to which extent direct searches exclude this combination of parameters.

The reason for choosing the gauge Yukawa couplings $y_{L/R}$ instead of $c_{L/R}$ is that the relevant channels for thermal production inherently discriminate between the left- and right-chiral leptons. *E.g.* the process $\chi\chi \rightarrow \tau_L\tau_L$ is accompanied by the annihilation diagrams $\chi\chi \rightarrow \nu_\tau\nu_\tau$, see fig. 6.6. This is not the case for $\chi\chi \rightarrow \tau_R\tau_R$, as τ_R is a SM singlet. Therefore, taking $y_{L/R}$ as a free parameter gives control over these distinct processes relevant to thermal production.

We present in fig. 6.7 the resulting exclusion plots for the benchmark scenarios outlined in table 6.1 together with the same collider exclusion limits shown in fig. 6.4.

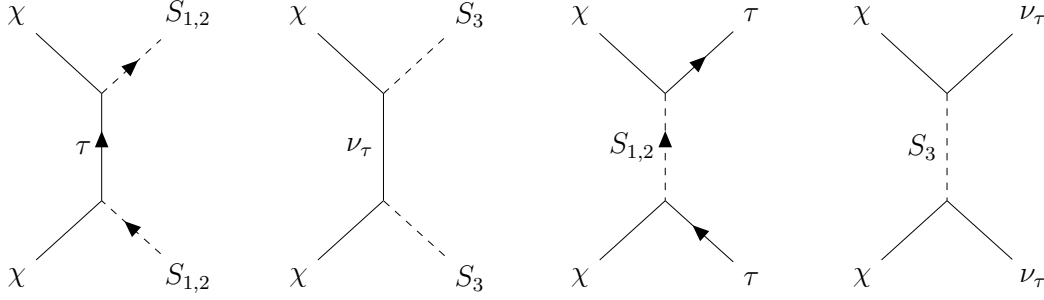


Figure 6.6: Tree-level t -channel diagrams of DM annihilation for the tau-philic toy model.

Benchmark	y_L	y_R	$\sin \psi$	$\sin \phi_{\text{CP}}$
B1	fixed	0	$1/\sqrt{2}$	0
B2	fixed	0.3	$1/\sqrt{2}$	0
B3	0	fixed	$1/\sqrt{2}$	0
B4	0.1	fixed	$1/\sqrt{2}$	0.1
B5	0.3	fixed	$1/\sqrt{2}$	1
B6	fixed	0.1	0.1	0.1

Table 6.1: Benchmarks for the two-dimensional scans of our simplified model. We scan over the masses m_χ and the lighter of the scalar soft masses m_{S_1} and fix one Yukawa coupling by requiring $\Omega_\chi h^2 = \Omega_{\text{DM}} h^2 = 0.12$ [45]. We assume that the heavier scalar can be integrated out from the low-energy theory. The benchmarks B1 and B3 have been investigated in ref. [252].

Further, the black contours indicate the value of

$$c = \sqrt{c_L^2 + c_R^2} = \sqrt{y_L^2 \cos^2 \psi + y_R^2 \sin^2 \psi} \quad (6.22)$$

required for thermal production via the freeze-out mechanism. The dot-dashed line represents $c = 0.1$, the continuous line $c = 0.4$, the dashed line $c = 1.0$, and the dotted line $c = \sqrt{4\pi}$, the perturbative limit. The dark shaded region in the lower left corners corresponds to the cases for which DM is under-abundant, typically due to too efficient coannihilations. This region is extended to larger values of η for the benchmark scenario B2 (B5), as here the Yukawa coupling is set to $y_R = 0.3$ ($y_L = 0.3$), in which case also the annihilations are too efficient, depleting the DM number density.

The presence of multiple dot-dashed countours in the lower left region in the benchmark scenario B4 comes from the fact that the solution to $c = 0.1$ is not

unique. For the value of $\sin\psi$ in this benchmark scenario, the contour is defined through $c^2 = \frac{1}{2}(y_L^2 + y_R^2)$. Therefore, $y_R = \pm y_L$ gives a solution on the contour defined by $c = y_L$ ($= 0.1$). As the couplings control the interaction strength to the left/right component of the τ -lepton, see eq. (6.12), they affect the corresponding annihilation cross-sections involving $\tau_{L/R}$. Thus, both solutions $y_R = +y_L$ and $y_R = -y_L$ result in a distinct contour for $c = 0.1$ in the $(m_\chi, \eta - 1)$ -plane.

Finally, the blue regions present the excluded regions from direct detection experiments by combining XENON1T, LZ, and PICO-60.¹ We find that for the benchmark scenarios enumerated in table 6.1, the direct detection constraints rule out a significant part of the parameter space of the thermal relic. In particular, the benchmark with large CP violation (B5) is entirely ruled out. Further, the collider studies severely constrain the low-mass region, which is not reachable by the direct detection experiments. Except for the benchmark B5, for a thermal relic, only DM masses at the TeV scale with $\mathcal{O}(1)$ mass-splittings to the scalar field are not excluded, with details depending on the benchmark considered. In all benchmarks, we find that the processes due to the EM moments, such as the s -channel diagram in fig. 4.5, at best contribute at the percent level.

In principle, there could be regions in parameter space where both production mechanisms—freeze-in and freeze-out—play a complementary role [406–408]. Further, as pointed out in ref. [408], the presence of multiple DM candidates in the dark sector can alter the production history substantially, in particular if the heavier state(s) can decay into the lighter. This constitutes an additional source term in the Boltzmann equation for the lightest DM state, effectively rendering its coupling to the SM arbitrary. In such a scenario, the halo DM particles could have large couplings to the SM, which would give large signals in terrestrial direct detection facilities. In the standard freeze-out paradigm, such a coupling would likely lead to underproduction and, therefore, be considered excluded.

¹As in section 4.3.4, we followed ref. [279] for combining the experimental constraints.

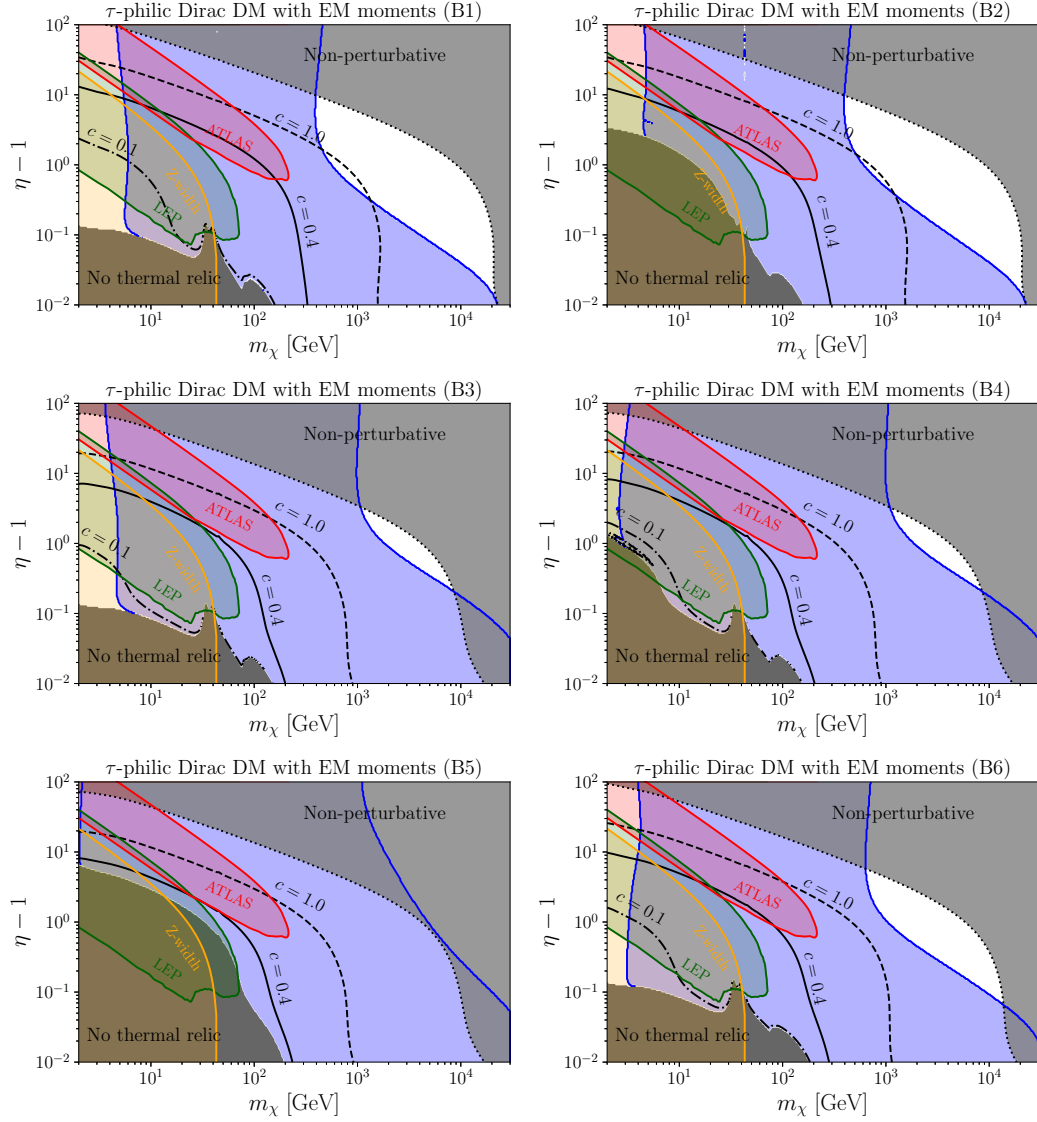


Figure 6.7: Parameter scan for the benchmark scenarios listed in table 6.1, where we fixed either y_L or y_R (with $c^2 = c_L^2 + c_R^2$) for thermal production of χ via freeze-out. We also add the collider constraints already shown in fig. 6.4. The blue-shaded region is the combined exclusion limit from LZ, XENON1T, and PICO-60; see the main text for details.

Chapter 7

Electromagnetic moments of neutrinos

Most of this dissertation focused on the EM moments of Dirac- and Majorana DM candidates and their corresponding direct detection phenomenology.

In this chapter, we aim to use the general results derived in chapter 3 to calculate the EM properties of neutrinos within the framework of the minimally extended SM and other common BSM scenarios. Additionally, we explore the case of a dark sector, in which *dark moments* of the active neutrinos are generated.

7.1 General remarks about neutrino electromagnetic moments

7.1.1 Overview of neutrino EM interactions

In the SM, neutrinos are massless neutral fermions that interact with a photon exclusively through the dimension-6 operators. BSM contributions, however, can enhance all EM interactions, making the study of neutrino EM properties a valuable probe for new physics. Depending on the specific BSM scenario, these enhancements can arise either as direct consequences of the neutrino mass-generation mechanism [228, 261, 409–412] or from other BSM frameworks, including left-right symmetric models [413–417], supersymmetric theories [416, 418, 419], leptoquark models [420], and various other proposals [421–426]. Further, two-photon interactions of neutrinos can also be generated [427], which are beyond the scope of this work. For a comprehensive review of the general properties of neutrino EM moments and their implications, see ref. [223].

The EM moments of neutrinos have different experimental signatures: In the limit of very light neutrinos, the magnetic moment flips the neutrino helicity, preventing interference terms with weak interactions for $2 \rightarrow 2$ scattering events [428]. This results in an additional term in the cross-section, which scales inversely with the neutrino energy, providing a unique spectral feature. In contrast, in the same limit, the anapole moment can be interpreted as a shift in the vector coupling or, equivalently, as a modification of the weak mixing angle [429]. Therefore, precise measurements of the weak mixing angle at small scales can probe the anapole moment [430, 431].

As mentioned in the general introduction to the EM moments in section 3.1, historically, calculating the anapole moment and the charge radius of neutrinos was challenging. The problem was, that a naive evaluation of the triangle diagrams leads to a gauge-dependent and UV-divergent expression [185–190, 192–195]. In fact, a direct calculation in the linear ξ gauge results in an anapole moment [1]

$$\mathcal{A} \sim \epsilon_{\text{UV}}^{-1} \xi + \dots, \quad (7.1)$$

with ϵ_{UV} being the small dimensional shift originating from dimensional regularization of the one-loop integral. As the SM is renormalizable and there is no corresponding counter term, this result cannot be a physical and thus measurable quantity. By considering the vertex-like topologies of the one-loop amplitude of a $2 \rightarrow 2$ process, it was realized in refs. [190, 192–194], that the unphysical terms from the triangle- and box diagrams cancel each other, resulting in a physical expression for the anapole and charge radius. Hereby, the Pinch Technique (PT) played a pivotal role, allowing the reassignment of sub-amplitudes diagrammatically. Equivalently, the background field formalism can be employed, in which the amplitude is evaluated in the background Feynman gauge [239–241].

Nowadays, the charge radius (or anapole moment) of the neutrino is its EM property closest to being measured. From reactor anti-neutrino-electron scattering events, the TEXONO collaboration obtained limits on the effective charge radius of the electron anti-neutrinos [432], which read in our convention

$$-3.5 \times 10^{-33} \text{ cm}^2 < (\bar{b}_{ee})_{\text{eff.}} < 5.5 \times 10^{-33} \text{ cm}^2, \quad (7.2)$$

where $(\bar{b}_{ee})_{\text{eff.}} = \bar{b}_{ee} + \bar{\mathcal{A}}_{ee}$ is the effective charge radius of the electron anti-neutrino. As discussed in section 3.3, the EM moments of anti-fermions can be related to the EM moments of fermions, such that we can identify $(\bar{b}_{ee})_{\text{eff.}} = -b_{ee} + \mathcal{A}_{ee} = -(b_{ee})_{\text{eff.}}$; see also ref. [429].

Meanwhile, the canonical prediction in the minimally extended SM is $(b_{ee})_{\text{eff.}} \simeq 4.14 \times 10^{-34} \text{ cm}^2$, see sections 7.2.1 and 7.2.2. As evident, the theory prediction is roughly one order of magnitude below the current experimental limit and constitutes a good observable for models beyond the SM akin to the anomalous magnetic moment of the muon. Therefore, experimental constraints on the effective charge radius of neutrinos will constitute a novel avenue to probe new physics.

The situation for the dipole moments is different. Using solar neutrinos, XENONnT obtained the leading limits on the effective magnetic dipole moment [433]

$$(\mu_{ee})_{\text{eff.}} < 6.4 \times 10^{-12} \mu_B \simeq 1.9 \times 10^{-9} \text{ GeV}^{-1}, \quad (7.3)$$

where $(\mu_{ee})_{\text{eff.}} = \mu_{ee} - id_{ee}$. The same diagrams, which resulted in a relatively large effective charge radius, predict $\mu_{\alpha\alpha} \simeq 3.2 \times 10^{-19} \left(\frac{m_\nu}{1\text{eV}}\right) \mu_B$ for a Dirac neutrino

in the minimally extended SM. Here, the theory prediction and the experimental constraints separate seven orders of magnitude.

In addition to these two experimental studies, other experiments and analyses provide constraints on the EM properties of neutrinos. These include studies of solar neutrinos in underground laboratories [434–439], coherent elastic neutrino-nucleus scattering (CE ν NS) [440–444], reactor experiments [445–448], collider searches [449–453], and beam dump experiments [454–456]. Astrophysical observations [457–467] and cosmological analyses [458, 468] also provide constraints, alongside other ideas to probe the neutrino EM properties [469–471]. It is crucial to note that comparing these different bounds is not straightforward because experiments are typically sensitive to some effective EM moment instead of the canonical moments \mathbb{M} defined in the neutrino mass basis.

Recently, the xenon-based DM direct detection experiments XENONnT [138] and PandaX-4T [139] have reported the first nuclear recoil measurements of solar neutrinos via CE ν NS. These results demonstrate their potential as neutrino telescopes and open up new avenues for exploring neutrino properties [145, 472], particularly their EM moments [437, 473]. These experimental advancements underscore the importance of understanding the theoretical predictions of extensions of the SM for the EM moments of neutrinos.

7.1.2 Assessment of the theory prediction

Before discussing the EM moments of light neutrinos in various models, we first analyze the behavior of the loop functions to better understand their overall dependence on model parameters.

As active neutrinos are very light, $m_\nu \sim 1$ eV [45, 474–476], we can use the loop functions for light external states discussed in section 3.4.3 to calculate the EM moments of neutrinos.

In fig. 7.1, we present the relevant loop functions for scalar- and vector-mediated one-loop processes that generate the EM moments as functions of the bosonic mass parameter m_S or m_V . We consider the range $10 \text{ GeV} < m_{S,V} < 10 \text{ TeV}$, motivated by the weak-scale and collider constraints, typically constraining new physics to be above the TeV-scale.

We present the scenario for masses of $m_\alpha = 0$ and $m_\beta = 1$ eV in the top row, showing the behavior for active neutrinos qualitatively. In the bottom row, we show the loop functions for $m_\alpha = 0$ and $m_\beta = 100$ keV, where the state β could be a sterile neutrino. The continuous, dashed, and dotted lines indicate an electron, muon, or tau in the loop. Note that the loop functions associated with the dimension-5 and dimension-6 operators have units of GeV^{-1} and GeV^{-2} , respectively.

For light external states, the functions $\mathcal{F}_{\mu,d}^{S,V}$ and $\mathcal{G}_{\mathcal{A},b}^{S,V}$ are relatively small, because they are proportional to $(m_\alpha \pm m_\beta)$. This behavior is the primary reason for the

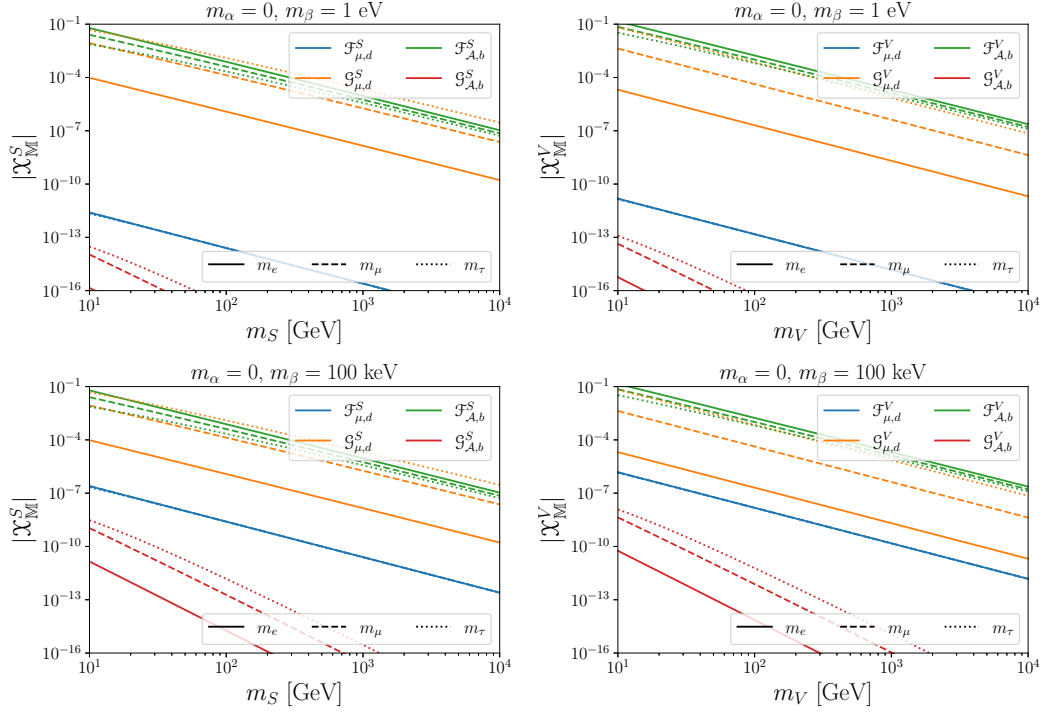


Figure 7.1: Loop functions in the limit of light external states for $m_\alpha = 0$ and $m_\beta = 1 \text{ eV}$ ($m_\beta = 100 \text{ keV}$) in the top (bottom) panel; in the left panel we show the scalar loop functions \mathcal{X}_M^S ($\mathcal{X} = \mathcal{F}, \mathcal{G}$), and in the right panels the vector loop functions \mathcal{X}_M^V . The units are GeV^{-1} (GeV^{-2}) for the dimension-5 (dimension-6) loop functions, and the continuous, dashed, and dotted lines indicate, respectively, the contribution from an electron, muon, and tau lepton.

strong suppression of neutrino dipole moments in the minimally extended SM, as we will see when discussing the theoretical predictions in sections 7.2.1 and 7.2.2. Conversely, $\mathcal{F}_{A,b}^{S,V}$ and $\mathcal{G}_{\mu,d}^{S,V}$ do not exhibit such strong suppression. These functions correspond to the anapole and charge radius operators ($\mathcal{F}_{A,b}^{S,V}$), as well as the contributions to dipole moments where the helicity flip occurs within the loop ($\mathcal{G}_{\mu,d}^{S,V}$). The latter is proportional to the internal fermion mass, which is in fig. 7.1 the lepton mass m_ℓ . Further, $\mathcal{F}_{\mu,d}^{S,V}$ is typically insensitive to the fermion mass in the loop, as these terms are suppressed by factors of $m_f^2/m_{S/V}^2$.

Therefore, just by analyzing the general loop functions for light neutrino, we can deduce that due to the hierarchy in mass scales, the dipole moments (anapole moment or charge radius) can only receive significant contributions if the $\mathcal{G}_{\mu,d}^{S,V}$ ($\mathcal{F}_{A,b}^{S,V}$) term is large.

Consequently, the EM moments of neutrinos can be enhanced if at least one of the following conditions is satisfied:

- Light degrees of freedom in the loop, *e.g.* small $m_{S,V}$,
- Dipole moments: large couplings $c_{L/R}^j(c_{R/L}^i)^*$ or $v_{L/R}^j(v_{R/L}^i)^*$,
- Anapole and charge radius: large couplings $c_{L/R}^j(c_{L/R}^i)^*$ or $v_{L/R}^j(v_{L/R}^i)^*$.

As discussed in section 3.4.3, the dimension-5 and dimension-6 loop functions for the scenario of light external masses are related straightforwardly, *cf.* eq. (3.62). Therefore, in this chapter, we mainly focus on the magnetic dipole moments and anapole moments of neutrinos. We comment on the phenomenological implications of including all relevant EM moments in section 7.3.6.

7.2 Neutrino electromagnetic moments within the SM

7.2.1 SM Dirac neutrino

To understand the relevant scale set by the SM, we first revisit the calculation of the EM moments of active Dirac neutrinos within the minimally extended SM. The relevant part of the Lagrangian reads [228]

$$\begin{aligned}\mathcal{L} &= \frac{g}{\sqrt{2}} \sum_{\ell} \left[\bar{\nu}_{\ell} \gamma^{\mu} P_L \ell W_{\mu}^{+} - \bar{\nu}_{\ell} \left(\frac{m_{\ell}}{m_W} P_R - \frac{m_{\alpha}}{m_W} P_L \right) \ell G^{+} \right] + \text{h.c.} \\ &= \frac{g}{\sqrt{2}} \sum_{\ell} \sum_{\alpha} U_{\ell\alpha}^{*} \bar{\nu}_{\alpha} \left[\gamma^{\mu} P_L \ell W_{\mu}^{+} - \left(\frac{m_{\ell}}{m_W} P_R - \frac{m_{\alpha}}{m_W} P_L \right) \ell G^{+} \right] + \text{h.c.},\end{aligned}\quad (7.4)$$

where W^{+} is the weak gauge boson with mass m_W , G^{+} is its associated Goldstone boson, $g = e/\sin\theta_W \simeq 0.44$ is the weak coupling constant, m_{α} is the mass of the neutrino mass eigenstate ν_{α} , and m_{ℓ} is the mass of the lepton ℓ which has charge $Q_{\ell} = -1$ for $\ell = e, \mu, \tau$. Finally,

$$U_{\ell\alpha} = \begin{pmatrix} 1 & 0 & 0 \\ 0 & c_{23} & s_{23} \\ 0 & -s_{23} & c_{23} \end{pmatrix} \begin{pmatrix} c_{13} & 0 & s_{13}e^{-i\delta} \\ 0 & 1 & 0 \\ -s_{13}e^{i\delta} & 0 & c_{13} \end{pmatrix} \begin{pmatrix} c_{12} & s_{12} & 0 \\ -s_{12} & c_{12} & 0 \\ 0 & 0 & 1 \end{pmatrix}\quad (7.5)$$

is the unitary PMNS [477] lepton mixing matrix for Dirac neutrinos. Here, $s_{ij} = \sin(\theta_{ij})$ and $c_{ij} = \cos(\theta_{ij})$ with $0 \leq \theta_{ij} \leq \pi/2$ being the mixing angles and δ_{CP} is the CP-violating Dirac phase.

As we calculated all EM moments in chapter 3 in full generality, we only have to read off the couplings in the canonical parameterization for the scalar- and vector interaction of eq. (3.45) and eq. (3.46) respectively. They read:

$$v_L^\alpha = \frac{g}{\sqrt{2}} U_{\ell\alpha}^*, \quad v_R^\alpha = 0, \quad (7.6a)$$

$$c_L^\alpha = \frac{g}{\sqrt{2}} U_{\ell\alpha}^* \frac{m_\alpha}{m_W}, \quad c_R^\alpha = -\frac{g}{\sqrt{2}} U_{\ell\alpha}^* \frac{m_\ell}{m_W}. \quad (7.6b)$$

The corresponding one-loop diagrams are depicted in fig. 7.2. We find for the EM moments

$$\begin{aligned} (\mathbb{M}_{\beta\alpha})^\ell = & -\frac{eG_F}{8\sqrt{2}\pi^2} U_{\ell\beta}^* U_{\ell\alpha} \left\{ (m_\alpha m_\beta \pm m_\ell^2) \mathcal{F}_{\mathbb{M}}^S \left(\frac{m_\ell}{m_\alpha}, \frac{m_W}{m_\alpha}, \frac{m_\beta}{m_\alpha} \right) \right. \\ & - m_\ell (m_\beta \pm m_\alpha) \mathcal{G}_{\mathbb{M}}^S \left(\frac{m_\ell}{m_\alpha}, \frac{m_W}{m_\alpha}, \frac{m_\beta}{m_\alpha} \right) \\ & \left. + m_W^2 \mathcal{F}_{\mathbb{M}}^V \left(\frac{m_\ell}{m_\alpha}, \frac{m_W}{m_\alpha}, \frac{m_\beta}{m_\alpha} \right) \right\}, \end{aligned} \quad (7.7)$$

where $G_F = \sqrt{2}g^2/8m_W^2$ is the Fermi constant. Particularizing eq. (7.7) to the dipole moments, we find at leading order in $m_{\alpha,\beta}$ [228, 234, 261, 478]

$$\mu_{\beta\alpha}^\ell = \frac{eG_F}{32\sqrt{2}\pi^2} (m_\alpha + m_\beta) U_{\ell\beta}^* U_{\ell\alpha} \frac{-2 + 7r^2 - 6r^4 + r^6 + 4r^4 \log r}{(-1 + r^2)^3}, \quad (7.8a)$$

$$d_{\beta\alpha}^\ell = -i \frac{eG_F}{32\sqrt{2}\pi^2} (m_\alpha - m_\beta) U_{\ell\beta}^* U_{\ell\alpha} \frac{-2 + 7r^2 - 6r^4 + r^6 + 4r^4 \log r}{(-1 + r^2)^3}, \quad (7.8b)$$

where $r = m_\ell/m_W$ and we used the loop functions summarized in appendix B.4. At leading order in r and after summing over all lepton generations, this reduces to

$$\mu_{\beta\alpha} = \frac{3eG_F}{16\sqrt{2}\pi^2} (m_\alpha + m_\beta) \left(\delta_{\alpha\beta} - \frac{1}{2} \sum_{\ell=e,\mu,\tau} U_{\ell\beta}^* U_{\ell\alpha} \frac{m_\ell^2}{m_W^2} \right), \quad (7.9a)$$

$$d_{\beta\alpha} = -i \frac{3eG_F}{16\sqrt{2}\pi^2} (m_\alpha - m_\beta) \left(\delta_{\alpha\beta} - \frac{1}{2} \sum_{\ell=e,\mu,\tau} U_{\ell\beta}^* U_{\ell\alpha} \frac{m_\ell^2}{m_W^2} \right), \quad (7.9b)$$

where we used $\sum_\ell U_{\ell\beta}^* U_{\ell\alpha} = \delta_{\alpha\beta}$. This relation may change with additional sterile neutrinos; see ref. [223].

As evident from eq. (7.9), the off-diagonal elements are suppressed by factors of $m_\ell^2/m_W^2 \lesssim 5 \times 10^{-4} m_\ell^2/m_\tau^2$ with respect to the diagonal dipole moments akin to the GIM mechanism of flavor-changing neutral currents for quarks [479].

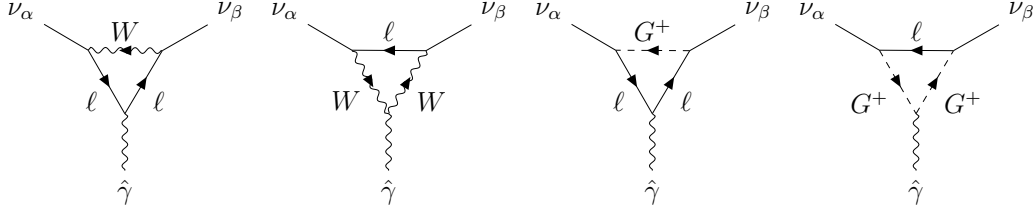


Figure 7.2: Diagrams contributing to the EM moments of neutrinos within the (minimally extended) SM in the background field formalism. The neutrinos can be both Dirac or Majorana; in the latter case, the conjugated diagrams should also be considered.

For the anapole moment and charge radius, we proceed similarly, *i.e.* we take the loop functions presented in appendix B.4 and expand them up to lowest orders in $m_{\alpha,\beta}$ and r . This results in [2, 189, 190, 480]

$$\mathcal{A}_{\beta\alpha} = -\frac{eG_F}{24\sqrt{2}\pi^2} \left(3\delta_{\alpha\beta} - 2 \sum_{\ell=e,\mu,\tau} U_{\ell\beta}^* U_{\ell\alpha} \log\left(\frac{m_\ell^2}{m_W^2}\right) \right), \quad (7.10a)$$

$$b_{\beta\alpha} = \frac{eG_F}{24\sqrt{2}\pi^2} \left(3\delta_{\alpha\beta} - 2 \sum_{\ell=e,\mu,\tau} U_{\ell\beta}^* U_{\ell\alpha} \log\left(\frac{m_\ell^2}{m_W^2}\right) \right). \quad (7.10b)$$

Therefore, the charge radius and anapole are—up to a sign and terms proportional to $m_\alpha m_\beta / m_W^2$ —equivalent. In contrast to the dipole moments, for the dimension-6 transition moments, the factors m_ℓ^2 / m_W^2 enter only via the logarithm.

As active neutrinos are relativistic and left-chiral, it is typically a good approximation to set $\gamma^5 \simeq -1$ in the interaction vertex given in eq. (3.8). Therefore, the dimension-6 part of the vertex can be interpreted as being purely of charge radius type (or equivalently purely of anapole type), with coupling $(b_{\beta\alpha})_{\text{eff.}} = b_{\beta\alpha} - \mathcal{A}_{\beta\alpha} \simeq 2b_{\beta\alpha}$. Similarly, the dimension-5 operators compose together an effective magnetic moment $(\mu_{\beta\alpha})_{\text{eff.}} = \mu_{\beta\alpha} - id_{\beta\alpha}$. As we will see below, for Majorana neutrinos, the anapole moment is twice that of a Dirac neutrino, such that the dimension-6 interactions of Dirac- and Majorana neutrinos with the photon are experimentally indistinguishable, as any corrections are neutrino-mass suppressed [481].

Before discussing the Majorana results, we briefly summarize the strength of the diagonal EM interactions of Dirac neutrinos within the minimally extended SM:

$$\mu_{\alpha\alpha} \simeq 9.5 \times 10^{-17} \left(\frac{m_\alpha}{1 \text{ eV}}\right) \text{ GeV}^{-1} \simeq 3.2 \times 10^{-19} \left(\frac{m_\alpha}{1 \text{ eV}}\right) \mu_B, \quad d_{\alpha\alpha} \simeq 0, \quad (7.11)$$

with transition moments being suppressed by further factors of m_ℓ^2 / m_W^2 due to the GIM mechanism as explained above. The anapole moments and the charge radius

read

$$\mathcal{A}_{\beta\alpha} = \sum_{\ell=e,\mu,\tau} U_{\ell\beta}^* U_{\ell\alpha} \mathcal{A}_{\ell\ell} \simeq -b_{\beta\alpha}, \quad (7.12)$$

with [190, 480]

$$\mathcal{A}_{\ell\ell} \simeq \text{diag}(-5.37, -3.11, -1.93) \times 10^{-7} \text{ GeV}^{-2} \quad (7.13a)$$

$$\simeq \text{diag}(-2.07, -1.20, -0.74) \times 10^{-34} \text{ cm}^2, \quad (7.13b)$$

such that

$$\mathcal{A}_{\beta\alpha} \simeq \begin{pmatrix} -4.35 & -1.35 & 0.66 + 0.02i \\ -1.35 & -3.41 & -0.26 + 0.01i \\ 0.66 - 0.02i & -0.26 - 0.01i & -2.65 \end{pmatrix} \times 10^{-7} \text{ GeV}^{-2}, \quad (7.14)$$

where we used for the PMNS mixing matrix the central values $\theta_{12} = 33.68^\circ$, $\theta_{23} = 48.5^\circ$, $\theta_{13} = 8.52^\circ$ and $\delta_{\text{CP}} = 177^\circ$ for normal mass ordering [78]. The imaginary parts are due to $\delta_{\text{CP}} \neq \pi\mathbb{Z}$.

7.2.2 SM Majorana neutrino

Obtaining the EM multipole moments of Majorana neutrinos generated by the same loops as the Dirac case is also straightforward using the general formulas derived in section 3.3.2. There, we found that the EM moments of Majorana fermions can be expressed as

$$(\mathbb{M}_{ji}^{S,V})^M = (\mathbb{M}_{ji}^{S,V})^D \mp (\mathbb{M}_{ji}^{S,V})^D (c_{L/R}^{i,j} \rightarrow (c_{L/R}^{i,j})^*, v_{L/R}^{i,j} \rightarrow (v_{L/R}^{i,j})^*), \quad (7.15)$$

where the upper and lower signs correspond to $\mathbb{M} = \mu, b$ and $\mathbb{M} = d, \mathcal{A}$, respectively. Using the results for the Dirac EM moments of the previous section, we find (see

ref. [234] for a derivation of the dipole moments using this notation)

$$\begin{aligned}\mu_{\beta\alpha}^{\nu^M} &= i \frac{3eG_F}{8\sqrt{2}\pi^2} (m_\alpha + m_\beta) \sum_\ell \text{Im}(U_{\ell\alpha}U_{\ell\beta}^*) \left(1 - \frac{1}{2} \frac{m_\ell^2}{m_W^2}\right) \\ &= -i \frac{3eG_F}{16\sqrt{2}\pi^2} (m_\alpha + m_\beta) \sum_\ell \text{Im}(U_{\ell\alpha}U_{\ell\beta}^*) \frac{m_\ell^2}{m_W^2},\end{aligned}\quad (7.16a)$$

$$\begin{aligned}d_{\beta\alpha}^{\nu^M} &= -i \frac{3eG_F}{8\sqrt{2}\pi^2} (m_\alpha - m_\beta) \sum_\ell \text{Re}(U_{\ell\alpha}U_{\ell\beta}^*) \left(1 - \frac{1}{2} \frac{m_\ell^2}{m_W^2}\right) \\ &= i \frac{3eG_F}{16\sqrt{2}\pi^2} (m_\alpha - m_\beta) \sum_\ell \text{Re}(U_{\ell\alpha}U_{\ell\beta}^*) \frac{m_\ell^2}{m_W^2},\end{aligned}\quad (7.16b)$$

$$\mathcal{A}_{\beta\alpha}^{\nu^M} = \frac{eG_F}{6\sqrt{2}\pi^2} \sum_\ell \text{Re}(U_{\ell\alpha}U_{\ell\beta}^*) \left(-3 + 2 \log\left(\frac{m_\ell^2}{m_W^2}\right)\right), \quad (7.16c)$$

$$b_{\beta\alpha}^{\nu^M} = -i \frac{eG_F}{6\sqrt{2}\pi^2} \sum_\ell \text{Im}(U_{\ell\alpha}U_{\ell\beta}^*) \left(-3 + 2 \log\left(\frac{m_\ell^2}{m_W^2}\right)\right), \quad (7.16d)$$

where the neutrino mixing matrix is given by

$$U = U^D D^M, \quad (7.17)$$

with the Dirac lepton mixing matrix U^D given in eq. (7.5), and the diagonal matrix

$$D^M = \text{diag}(1, e^{i\phi_{21}}, e^{i\phi_{31}}) \quad (7.18)$$

containing the physical Majorana CP phases ϕ_α .

As mentioned in section 3.3.2, instead of setting all creation phases λ_i to unity, we can keep them explicit, resulting in modified reversed diagrams [209, 226, 228, 258, 261], in which case, eq. (3.56) can be cast as

$$\mathbb{M}^M = \mathbb{M}^D \mp \lambda_{if} \times \mathbb{M}^D (\tilde{c}_{L/R} \rightarrow (\tilde{c}_{L/R})^*, \tilde{\nu}_{L/R} \rightarrow (\tilde{\nu}_{L/R})^*), \quad (7.19)$$

which is eq. (3.59). Following this convention, the EM moments read

$$\left(\mu_{\beta\alpha}^{\nu M}\right)^\ell = \frac{3eG_F}{16\sqrt{2}\pi^2}(m_\alpha + m_\beta)U_{\ell\alpha}U_{\ell\beta}^* \left(1 - \frac{1}{2}\frac{m_\ell^2}{m_W^2}\right) \left[1 - \frac{\lambda_\alpha^*\lambda_\beta U_{\ell\alpha}^*U_{\ell\beta}}{U_{\ell\alpha}U_{\ell\beta}^*}\right], \quad (7.20a)$$

$$\left(d_{\beta\alpha}^{\nu M}\right)^\ell = -i\frac{3eG_F}{16\sqrt{2}\pi^2}(m_\alpha - m_\beta)U_{\ell\alpha}U_{\ell\beta}^* \left(1 - \frac{1}{2}\frac{m_\ell^2}{m_W^2}\right) \left[1 + \frac{\lambda_\alpha^*\lambda_\beta U_{\ell\alpha}^*U_{\ell\beta}}{U_{\ell\alpha}U_{\ell\beta}^*}\right], \quad (7.20b)$$

$$\left(\mathcal{A}_{\beta\alpha}^{\nu M}\right)^\ell = \frac{eG_F}{12\sqrt{2}\pi^2}U_{\ell\alpha}U_{\ell\beta}^* \left(-3 + 2\log\left(\frac{m_\ell^2}{m_W^2}\right)\right) \left[1 + \frac{\lambda_\alpha^*\lambda_\beta U_{\ell\alpha}^*U_{\ell\beta}}{U_{\ell\alpha}U_{\ell\beta}^*}\right], \quad (7.20c)$$

$$\left(b_{\beta\alpha}^{\nu M}\right)^\ell = -\frac{eG_F}{12\sqrt{2}\pi^2}U_{\ell\alpha}U_{\ell\beta}^* \left(-3 + 2\log\left(\frac{m_\ell^2}{m_W^2}\right)\right) \left[1 - \frac{\lambda_\alpha^*\lambda_\beta U_{\ell\alpha}^*U_{\ell\beta}}{U_{\ell\alpha}U_{\ell\beta}^*}\right]. \quad (7.20d)$$

Thus, to some extent, eq. (7.20) can be considered to be more general than the expressions shown in eq. (7.16), as by using the arbitrariness of the creation phases, we can set $\lambda_\alpha = 1$ for all α . Then, we reproduce the result from eq. (7.16). However, the fraction in the square brackets is invariant under rephasing [258, 259]. It holds in the formalism in which λ_α is set to unity, in which case the neutrino mixing matrices are complex, or in which the phases are absorbed, and the lepton mixing matrix can be made real [258].

If we assume that CP is conserved, we note that the condition of CP invariance of the charged current in eq. (7.4) leads to the requirement that [258, 261]

$$U_{\ell\alpha} = U_{\ell\alpha}^* \eta_{\Xi(\alpha)}^*. \quad (7.21)$$

One finds after some algebra that the invariant quantity we encountered in eq. (7.20) can be simplified as [261]

$$\frac{\lambda_\alpha^*\lambda_\beta U_{\ell\alpha}^*U_{\ell\beta}}{U_{\ell\alpha}U_{\ell\beta}^*} = \frac{\lambda_\alpha \eta_{\Xi(\alpha)}}{\lambda_\beta \eta_{\Xi(\beta)}} = \frac{\tilde{\eta}_{\Xi(\alpha)}}{\tilde{\eta}_{\Xi(\beta)}}, \quad (7.22)$$

where $\tilde{\eta}_{\Xi(\alpha)} = \lambda_\alpha \eta_{\Xi(\alpha)} = \pm i$, with $\eta_{\Xi(\alpha)}$ being the CP phase of ν_α^M . Then, the EM

moments can be expressed as [258, 261]

$$\mu_{\beta\alpha}^{\nu M} = -\frac{3eG_F}{32\sqrt{2}\pi^2}(m_\alpha + m_\beta) \sum_\ell U_{\ell\alpha}U_{\ell\beta}^* \frac{m_\ell^2}{m_W^2} \left[1 - \frac{\tilde{\eta}_{\Xi(\alpha)}}{\tilde{\eta}_{\Xi(\beta)}} \right], \quad (7.23a)$$

$$d_{\beta\alpha}^{\nu M} = i\frac{3eG_F}{32\sqrt{2}\pi^2}(m_\alpha - m_\beta) \sum_\ell U_{\ell\alpha}U_{\ell\beta}^* \frac{m_\ell^2}{m_W^2} \left[1 + \frac{\tilde{\eta}_{\Xi(\alpha)}}{\tilde{\eta}_{\Xi(\beta)}} \right], \quad (7.23b)$$

$$\mathcal{A}_{\beta\alpha}^{\nu M} = \frac{eG_F}{12\sqrt{2}\pi^2} \sum_\ell U_{\ell\alpha}U_{\ell\beta}^* \left(-3 + 2 \log\left(\frac{m_\ell^2}{m_W^2}\right) \right) \left[1 + \frac{\tilde{\eta}_{\Xi(\alpha)}}{\tilde{\eta}_{\Xi(\beta)}} \right], \quad (7.23c)$$

$$b_{\beta\alpha}^{\nu M} = -\frac{eG_F}{6\sqrt{2}\pi^2} \sum_\ell U_{\ell\alpha}U_{\ell\beta}^* \log\left(\frac{m_\ell^2}{m_W^2}\right) \left[1 - \frac{\tilde{\eta}_{\Xi(\alpha)}}{\tilde{\eta}_{\Xi(\beta)}} \right]. \quad (7.23d)$$

From the expressions in eq. (7.23), it is clear that for Majorana neutrinos, only a diagonal anapole moment exists, which has twice the value of the anapole moment of a Dirac neutrino. Further, depending on the relative CP eigenvalues, only transition electric (magnetic) moments *and* transition anapole moments (charge radii) can exist, which are twice the value as for the Dirac case [226–228]. This observation implies that Majorana neutrinos can have a transition electric dipole moment even if CP is conserved [262, 482].

If the Majorana neutrinos are CP eigenstates, the Majorana neutrino mixing matrix U can be written as [223, 483]

$$U_{\ell\alpha} = \mathcal{O}_{\ell\alpha} e^{i\phi_\alpha} \quad (7.24)$$

with \mathcal{O} being an orthogonal matrix and ϕ_α the Majorana CP phases. They are related to the CP eigenvalues as $e^{-2i\phi_\alpha} = \tilde{\eta}_{\Xi(\alpha)}$ due to the fact that the charged current in eq. (7.4) remains invariant under rephasing [258, 259]. Thus, the relevant product of the neutrino mixing matrices we encountered in the previous discussion, for example in eq. (7.23), simplifies to

$$U_{\ell\alpha}U_{\ell\beta}^* = \mathcal{O}_{\ell\alpha}\mathcal{O}_{\ell\beta} \sqrt{\frac{\tilde{\eta}_{\Xi(\beta)}}{\tilde{\eta}_{\Xi(\alpha)}}}. \quad (7.25)$$

In particular, eq. (7.25) implies, that the product $U_{\ell\alpha}U_{\ell\beta}^*$ is either purely real ($\tilde{\eta}_{\Xi(\alpha)}/\tilde{\eta}_{\Xi(\beta)} = 1$), or purely imaginary ($\tilde{\eta}_{\Xi(\alpha)}/\tilde{\eta}_{\Xi(\beta)} = -1$) [482]. Now, we are in a position to compare both formalisms:

Without creation phases

Plugging eq. (7.25) into eq. (7.16), we find that

$$\mu_{\beta\alpha}^{\nu M} \sim -\frac{i}{16} \operatorname{Im} \left(\sqrt{\frac{\tilde{\eta}_{\Xi(\beta)}}{\tilde{\eta}_{\Xi(\alpha)}}} \right), \quad d_{\beta\alpha}^{\nu M} \sim \frac{i}{16} \operatorname{Re} \left(\sqrt{\frac{\tilde{\eta}_{\Xi(\beta)}}{\tilde{\eta}_{\Xi(\alpha)}}} \right), \quad (7.26a)$$

$$\mathcal{A}_{\beta\alpha}^{\nu M} \sim \frac{1}{6} \operatorname{Re} \left(\sqrt{\frac{\tilde{\eta}_{\Xi(\beta)}}{\tilde{\eta}_{\Xi(\alpha)}}} \right), \quad b_{\beta\alpha}^{\nu M} \sim -\frac{i}{6} \operatorname{Im} \left(\sqrt{\frac{\tilde{\eta}_{\Xi(\beta)}}{\tilde{\eta}_{\Xi(\alpha)}}} \right), \quad (7.26b)$$

where we dropped the masses, mixing matrices and couplings.

With creation phases

Using the parameterization given in eq. (7.25), eq. (7.23) becomes

$$\mu_{\beta\alpha}^{\nu M} \sim -\frac{1}{32} \sqrt{\frac{\tilde{\eta}_{\Xi(\beta)}}{\tilde{\eta}_{\Xi(\alpha)}}} \left[1 - \frac{\tilde{\eta}_{\Xi(\alpha)}}{\tilde{\eta}_{\Xi(\beta)}} \right], \quad d_{\beta\alpha}^{\nu M} \sim \frac{i}{32} \sqrt{\frac{\tilde{\eta}_{\Xi(\beta)}}{\tilde{\eta}_{\Xi(\alpha)}}} \left[1 + \frac{\tilde{\eta}_{\Xi(\alpha)}}{\tilde{\eta}_{\Xi(\beta)}} \right], \quad (7.27a)$$

$$\mathcal{A}_{\beta\alpha}^{\nu M} \sim \frac{1}{12} \sqrt{\frac{\tilde{\eta}_{\Xi(\beta)}}{\tilde{\eta}_{\Xi(\alpha)}}} \left[1 + \frac{\tilde{\eta}_{\Xi(\alpha)}}{\tilde{\eta}_{\Xi(\beta)}} \right], \quad b_{\beta\alpha}^{\nu M} \sim -\frac{1}{6} \sqrt{\frac{\tilde{\eta}_{\Xi(\beta)}}{\tilde{\eta}_{\Xi(\alpha)}}} \left[1 - \frac{\tilde{\eta}_{\Xi(\alpha)}}{\tilde{\eta}_{\Xi(\beta)}} \right]. \quad (7.27b)$$

For the possible relative CP eigenvalues of $\tilde{\eta}_{\Xi(\alpha)}/\tilde{\eta}_{\Xi(\beta)} = \pm 1$, we can confirm that both approaches give the same results for the SM-like EM moments of Majorana neutrinos.

In principle, additional diagrams may contribute, depending on the mass generation of the neutrino masses [228, 261, 410, 411]. For example, the charged Higgs component of a Higgs triplet—which gives rise to the Majorana masses—may increase the dipole moments significantly [228]. We discuss this scenario in more detail in section 7.3.1. Therefore, comparing the SM contribution of Majorana- and Dirac EM moments is generally tricky.

We conclude that the dipole moments generated by SM particles are well below the experimental reach for both Dirac- and Majorana neutrinos. The reason is that the dipoles are proportional to the neutrino masses, $\mu, d \sim (m_\alpha \pm m_\beta)$, due to the chirality flip on the external leg. In the language of the Lagrangians, this property originates from the absence of any right-handed current, resulting in the term $\sim \mathcal{G}_M^{S,V}$ vanishing. As mentioned in section 7.1.2, this term could result in large predictions for the dipole moments. Meanwhile, the weak gauge bosons suppress the anapole and charge radius, as we found them to be proportional to Fermi's constant, $\mathcal{A}, b \sim \pm G_F$. In contrast to the neutrino mass suppression we encountered for the dipole moments, this suppression is not as severe, explaining the relatively large SM prediction.

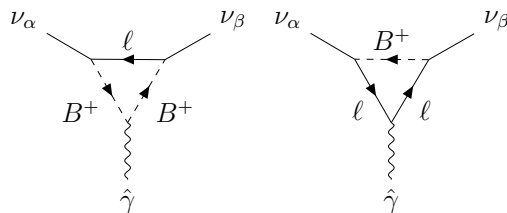


Figure 7.3: Diagrams contributing to the EM moments of Majorana neutrinos within the triplet extended SM.

7.3 Neutrino electromagnetic moments beyond the SM

7.3.1 Majorana neutrino with a Higgs triplet

A crucial difference between Dirac- and Majorana neutrinos is the inherently different mass mechanism, introducing a model-dependence in the estimation of their EM moments.

Following ref. [228], we discuss here the effect of a Higgs triplet on the EM multipoles of Majorana neutrinos. In addition to the diagrams that are present for the Dirac case and were discussed in section 7.2.2, the single-charged Higgs component B^+ contributes to the EM moments of the neutrinos via the diagrams shown in fig. 7.3.

The relevant portal interaction reads [228]

$$\mathcal{L} \supset \frac{g}{\sqrt{2}m_W} \sum_{\alpha,\ell} \bar{\nu}_\alpha U_{\ell\alpha}^* [m_\ell \tan \alpha P_R + m_\alpha \cot \alpha P_L] \ell B^+ + \text{h.c.}, \quad (7.28)$$

with mixing angle $\tan \alpha = \sqrt{2}v_3/v_2$, where v_3 (v_2) is the vev of the triplet (doublet), satisfying

$$v^2 = v_2^2 + 2v_3^2 \simeq (246 \text{ GeV})^2. \quad (7.29)$$

Experimentally, the vev of the Higgs triplet is expected to be at the GeV scale, $v_3 \sim (1 - 8) \text{ GeV}$ [484], resulting in a small mixing angle $\tan \alpha \simeq \mathcal{O}(0.005 - 0.05)$. Further,

$$B^+ = -\sin \alpha \phi^+ + \cos \alpha H^+ \quad (7.30)$$

is the orthogonal combination of the charged Higgs components. Meanwhile,

$$S^+ = \cos \alpha \phi^+ + \sin \alpha H^+ \quad (7.31)$$

is the unphysical Goldstone boson identified with the longitudinal mode of the W boson, $S^+ = G^+$.

Assuming CP-invariance, this additional contribution may be written for the magnetic dipole moment as

$$\begin{aligned} \mu_{\beta\alpha}^{\text{trip.}} = & -\frac{e}{32\pi^2} \left\{ \left[c_L^{\beta\ell} (c_L^{\alpha\ell})^* + c_R^{\beta\ell} (c_R^{\alpha\ell})^* \right] \mathcal{F}_\mu^S \left(\frac{m_\ell}{m_\alpha}, \frac{m_{B^+}}{m_\alpha}, \frac{m_\beta}{m_\alpha} \right) \right. \\ & \left. + \left[c_L^{\beta\ell} (c_R^{\alpha\ell})^* + c_R^{\beta\ell} (c_L^{\alpha\ell})^* \right] \mathcal{G}_\mu^S \left(\frac{m_\ell}{m_\alpha}, \frac{m_{B^+}}{m_\alpha}, \frac{m_\beta}{m_\alpha} \right) \right\} \left[1 - \frac{\tilde{\eta}_{\Xi(\alpha)}}{\tilde{\eta}_{\Xi(\beta)}} \right], \end{aligned} \quad (7.32)$$

with

$$c_L^{\alpha\ell} = \frac{g}{\sqrt{2}m_W} U_{\ell\alpha}^* m_\alpha \cot \alpha, \quad c_R^{\alpha\ell} = \frac{g}{\sqrt{2}m_W} U_{\ell\alpha}^* m_\ell \tan \alpha, \quad (7.33)$$

and similar expressions for the other EM moments. Expanding in $m_{\alpha,\beta}/m_W$ and introducing $x_\ell = m_\ell/m_{B^+}$, we find [228]

$$\begin{aligned} \mu_{\beta\alpha}^{\text{trip.}} = & \frac{eG_F(m_\alpha + m_\beta)}{32\sqrt{2}\pi^2} \sum_\ell U_{\ell\alpha} U_{\ell\beta}^* \frac{x_\ell^2}{(1-x_\ell^2)^3} \times \\ & \times \left[4(x_\ell^2 - 1)(x_\ell^2 - 2\log(x_\ell) - 1) \right. \\ & \left. + \tan^2(\alpha)(x_\ell^4 - 4x_\ell^2 \log(x_\ell) - 1) \right] \left[1 - \frac{\tilde{\eta}_{\Xi(\alpha)}}{\tilde{\eta}_{\Xi(\beta)}} \right]. \end{aligned} \quad (7.34)$$

For the transition case ($\alpha \neq \beta$), we can parameterize the relative enhancement of the magnetic dipole moment due to a BSM contribution as [228]

$$\frac{\mu_{\beta\alpha}^{\text{SM}} + \mu_{\beta\alpha}^{\text{BSM}}}{\mu_{\beta\alpha}^{\text{SM}}} = \frac{(c_e + c_\mu)F(0) + c_\tau F(m_\tau) + F^{\text{BSM}}}{(c_e + c_\mu)F(0) + c_\tau F(m_\tau)} \quad (7.35a)$$

$$= \frac{F(m_\tau) - F(0) + c_\tau^{-1} F^{\text{BSM}}}{F(m_\tau) - F(0)}, \quad (7.35b)$$

where $c_\ell = U_{\ell\beta}^* U_{\ell\alpha}$ and $F(m_\ell) \simeq 1 - \frac{1}{2}m_\ell^2/m_W^2$. For the Higgs triplet, the BSM contribution expanded to the lowest order in $x_\ell \ll 1$ reads

$$F^{\text{trip.}} \simeq \frac{1}{6} \sum_\ell c_\ell x_\ell^2 (4 + 4\log(x_\ell^2) - \tan^2 \alpha). \quad (7.36)$$

To estimate its size, we note that the contribution from the τ -lepton dominates, so it is a reasonable approximation to drop the contributions from the light leptons. Therefore, we can approximate

$$F^{\text{trip.}} \simeq c_\tau \frac{2}{3} \frac{m_\tau^2}{m_{B^+}^2} \left(1 + \log \left(\frac{m_\tau^2}{m_{B^+}^2} \right) \right), \quad (7.37)$$

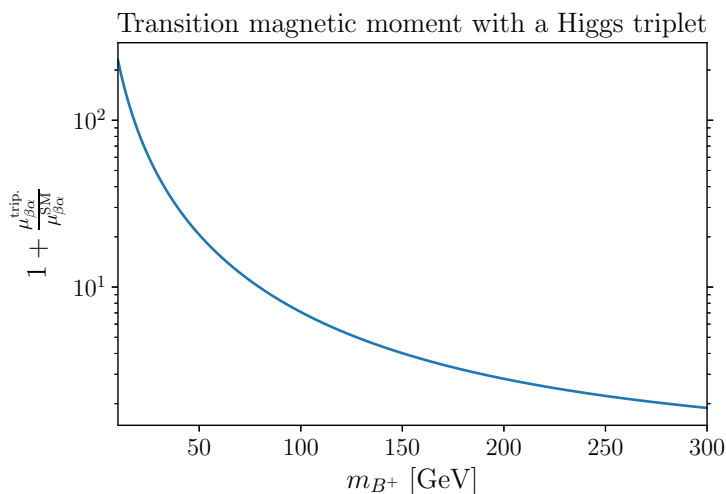


Figure 7.4: Increase in the transition magnetic moment of Majorana neutrinos in the SM with an additional Higgs triplet. The result is practically independent of $\tan\alpha$.

where we also dropped the term proportional to $\tan^2\alpha \ll 1$. Thus, the normalized BSM contribution reads [228]

$$1 + \frac{\mu_{\beta\alpha}^{\text{trip.}}}{\mu_{\beta\alpha}^{\text{SM}}} \simeq 1 - \frac{4m_W^2}{3m_{B^+}^2} \left(1 + \log\left(\frac{m_\tau^2}{m_{B^+}^2}\right) \right) > 1, \quad (7.38)$$

where we used that $\sum_\ell U_{\ell\alpha}^* U_{\ell\beta} = 0$ and the fact that $m_e, m_\mu \ll m_W, m_{B^+}$ and only kept terms up to $\mathcal{O}(m_\tau^2/m_{B^+}^2)$. In this limit, the result becomes independent of the neutrino mixing matrix.

We show in fig. 7.4 this contribution to the SM magnetic dipole moment as a function of the charged Higgs mass m_{B^+} . We see that the magnetic dipole moment is enhanced by up to roughly two orders of magnitude for $m_{B^+} \sim 10$ GeV, enhancing the corresponding decay rate by a factor of $\sim 10^4$.

The enhancement on the diagonal magnetic dipole moment depends on the mixing angles, as the sum over the lepton species now reads $\sum_\ell U_{\ell\alpha}^* U_{\ell\alpha} = 1$, leading to terms $\sim (U_{\tau\alpha}^* U_{\tau\alpha})^{-1}$ appear in the numerator and denominator of eq. (7.38).

For the anapole moment, we find

$$\mathcal{A}_{\beta\alpha}^{\text{trip.}} = -\frac{eG_F}{48\sqrt{2}\pi^2} \tan^2\alpha \sum_\ell U_{\ell\alpha} U_{\ell\beta}^* x_\ell^2 \frac{3 - 3x_\ell^2 + (2 + x_\ell^2) \log(x_\ell^2)}{(1 - x_\ell^2)^2} \left[1 + \frac{\tilde{\eta}_{\Xi(\alpha)}}{\tilde{\eta}_{\Xi(\beta)}} \right], \quad (7.39)$$

which is suppressed as $\sim x_\ell^2 \tan^2\alpha$ and, therefore, negligible.

7.3.2 Left-right symmetric model

As another example, we can calculate the EM moments of Majorana neutrinos within a left-right symmetric model. The simplest weak gauge group with this idea is $SU(2)_L \times SU(2)_R \times U(1)_{B-L}$, for details of the model, see for example refs. [261, 485].

The relevant part of the Lagrangian reads [485]

$$\begin{aligned} \mathcal{L} \supset & \frac{g}{\sqrt{2}} \bar{\nu} \gamma^\mu [\cos \xi K_L P_L - \sin \xi K_R P_R] \ell W_{1\mu}^\dagger \\ & + \frac{g}{\sqrt{2}} \bar{\nu} \gamma^\mu [\sin \xi K_L P_L + \cos \xi K_R P_R] \ell W_{2\mu}^\dagger + \text{h.c.}, \end{aligned} \quad (7.40)$$

where ξ denotes the mixing angle between the gauge bosons W_L and W_R , W_1 and W_2 are the associated mass eigenstates, and the mixing elements of the vertices read

$$K_L = V_L^{\nu\dagger} V_L^\ell, \quad K_R = V_R^{\nu\dagger} V_R^\ell, \quad (7.41)$$

where the 3×3 matrices $V_{L/R}^\ell$ diagonalize the charged leptons $\ell_{L/R}$, and the neutrino mixing matrices are such that the 6×6 matrix

$$V^\nu = \begin{pmatrix} V_L^{\nu*} \\ V_R^\nu \end{pmatrix} \quad (7.42)$$

diagonalizes the neutrinos as

$$\nu_{\ell R} = V_{\ell\alpha}^\nu \nu_{R\alpha}, \quad \nu_{\ell L} = V_{\ell\alpha}^{\nu*} \nu_{L\alpha}, \quad (7.43)$$

where $V_{L/R}^\nu$ are 6×3 mixing matrices. Finally, the physical Majorana neutrino states are

$$\nu = \nu_L + \nu_R = \nu^c. \quad (7.44)$$

Due to the experimental limits on W_R , the heavier mass eigenstate W_2 has to be heavier than ~ 2 TeV [486] (see also the discussion and references in ref. [261]), such that this contribution is mass-suppressed as $\sim m_{W_1}^2/m_{W_2}^2$ w.r.t. the SM-like contribution due to the W_1 term in eq. (7.40). Further, the \mathcal{F}_M^V terms now also receive contributions from the right-chiral interaction with coefficient proportional to $v_R^2 \sim \sin^2 \xi < 2 \times 10^{-5}$ [487], which is therefore negligible.

In principle, contributions from the two Higgs triplets and the Goldstone bosons associated with the interaction of eq. (7.40) should be considered. However, the former contribute similarly to the discussion in section 7.3.1, and the latter is negligible at the lowest order, as their couplings are suppressed by $\sim m_\nu/m_{W_1}$ or m_ℓ/m_{W_1} with respect to the interaction of eq. (7.40), as here the couplings are gauge couplings. We found a similar hierarchy in the SM, where at lowest order, the vector contributions

$\mathcal{F}_{\mathbb{M}}^V$ and $\mathcal{G}_{\mathbb{M}}^V$ are dominant, *cf.* eq. (7.7). Thus, we focus on the diagrams with vector bosons to estimate the EM moments in the left-right symmetric model.

The crucial difference in this scenario with respect to the SM is the presence of the right-chiral current in eq. (7.40), giving rise to a non-zero $\sim \mathcal{G}_{\mathbb{M}}^V$ term, which could give large contributions according to the discussion in section 7.1.2.

At the lowest order in m_ℓ and $m_{\alpha,\beta}$, the magnetic dipole moment reads

$$\mu_{\beta\alpha}^{\text{LR}} \simeq i \frac{eG_F}{\sqrt{2}} \cos \xi \sin \xi \sum_{\ell} m_{\ell} \text{Im} [(K_L)_{\ell\beta} (K_R^*)_{\ell\alpha} + (K_R)_{\ell\beta} (K_L^*)_{\ell\alpha}]. \quad (7.45)$$

In the manifest left-right symmetric model $V_L^\ell = V_R^\ell$, such that eq. (7.45) simplifies to

$$\mu_{\beta\alpha}^{\text{LR}} \simeq i \frac{eG_F}{\sqrt{2}} \cos \xi \sin \xi \sum_{\ell} m_{\ell} \text{Im} [(V_L^{\nu*})_{\ell\beta} (V_R^{\nu})_{\ell\alpha} + (V_R^{\nu*})_{\ell\beta} (V_L^{\nu})_{\ell\alpha}]. \quad (7.46)$$

The expression in eq. (7.46) is consistent with the results presented in ref. [415], where they utilized the formalism in which the creation phases are factored out to compute the decay widths of neutrinos in the left-right symmetric model assuming CP conservation. In contrast to their results, however, we are not limited to the CP-conserving scenario and thus also predict an electric dipole moment, which can be obtained by making the according replacements in eq. (7.46), *cf.* section 3.4.3.

As pointed out in refs. [261, 415], for active neutrinos eq. (7.46) may still be small owing to the small gauge boson mixing $\sin \xi$ and the small right neutrino mixings with active neutrinos—at least in the see-saw paradigm. The latter parameter, however, can be large if one of the neutrinos is sterile, *i.e.* if $\nu_\alpha = \nu_s$ or $\nu_\beta = \nu_s$. As the dipole moments are linked to the radiative decay, this would, in turn, give rise to enhanced decays $\nu_s \rightarrow \nu + \gamma$ in left-right symmetric models [488].

The anapole moment and charge radius, on the other hand, do not receive significant contributions, as also here the suppression of $v_R^2 \sim \sin^2 \xi$ renders the new term $\sim \mathcal{F}_{\mathcal{A},b}^V$ negligible. The $\mathcal{G}_{\mathcal{A},b}^V$ term is suppressed by the light neutrino mass scale, as discussed in section 7.1.2.

7.3.3 R -parity conserving MSSM

Here, we consider supersymmetric contributions to Dirac neutrinos within the MSSM (see section 5.1 for an overview), in which two additional loops contribute to the EM multipoles: *a*) chargino-slepton loops and *b*) lepton-Higgs loops, as shown in fig. 7.5. In the following section, we discuss these two contributions separately.

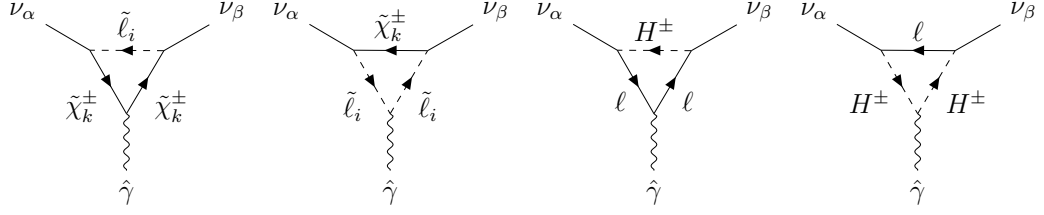


Figure 7.5: R -parity conserving MSSM contributions to the EM moments of neutrinos.

a) Chargino-slepton loops

This interaction gives rise to the one-loop coupling to the photon via the two left diagrams depicted in fig. 7.5. The relevant interaction reads [319]

$$\mathcal{L} \supset \sum_{\ell, i, k} c_R^{ik\ell} \bar{\nu}_\ell P_R \tilde{\ell}_i \tilde{\chi}_k^+ + \text{h.c.} = \sum_{\alpha, \ell, i, k} c_R^{ik\ell} U_{\ell\alpha}^* \bar{\nu}_\alpha P_R \tilde{\ell}_i \tilde{\chi}_k^- + \text{h.c.} \quad (7.47)$$

We can identify the canonical couplings as

$$c_L^{ik\ell\alpha} = 0, \quad c_R^{ik\ell\alpha} = U_{\ell\alpha}^* c_R^{ik\ell}, \quad (7.48)$$

where

$$c_R^{1k\ell} = -g\mathcal{U}_{k1} \cos\theta_{\tilde{\ell}} + \frac{gm_\ell}{\sqrt{2} \cos\beta m_W} \mathcal{U}_{k2} \sin\theta_{\tilde{\ell}}, \quad (7.49a)$$

$$c_R^{2k\ell} = g\mathcal{U}_{k1} \sin\theta_{\tilde{\ell}} + \frac{gm_\ell}{\sqrt{2} \cos\beta m_W} \mathcal{U}_{k2} \cos\theta_{\tilde{\ell}}. \quad (7.49b)$$

Then, the magnetic dipole moment reads

$$\mu_{\beta\alpha}^{(a)} = -\frac{e}{32\pi^2} \sum_{i, k, \ell} U_{\ell\alpha} U_{\ell\beta}^* |c_R^{ik\ell}|^2 \mathcal{F}_\mu^S \left(\frac{m_{\tilde{\chi}_k^\pm}}{m_\alpha}, \frac{m_{\tilde{\ell}_i}}{m_\alpha}, \frac{m_\beta}{m_\alpha} \right). \quad (7.50)$$

In contrast to the discussion of the (minimally extended) SM, the factor $\rho = m_{\tilde{\chi}_k^\pm}/m_{\tilde{\ell}_i}$ (in the SM this was m_ℓ/m_W) is not necessarily small. Therefore, we only expand the loop function in the neutrino masses, leading at the lowest order in $m_{\alpha, \beta}$ to

$$\begin{aligned} \mu_{\beta\alpha}^{(a)} &= -\frac{e}{128\pi^2} \sum_{i, k, \ell} |c_R^{ik\ell}|^2 U_{\ell\alpha} U_{\ell\beta}^* \frac{m_\alpha + m_\beta}{m_{\tilde{\ell}_i}^2} \frac{\rho^4 - 4\rho^2 \log(\rho) - 1}{(\rho^2 - 1)^3} \\ &= -\frac{e}{128\pi^2} (m_\alpha + m_\beta) \sum_{i, k, \ell} |c_R^{ik\ell}|^2 U_{\ell\alpha} U_{\ell\beta}^* \frac{m_{\tilde{\chi}_k^\pm}^4 - m_{\tilde{\ell}_i}^4 - 2m_{\tilde{\ell}_i}^2 m_{\tilde{\chi}_k^\pm}^2 \log(m_{\tilde{\chi}_k^\pm}^2/m_{\tilde{\ell}_i}^2)}{m_{\tilde{\ell}_i}^2 (m_{\tilde{\chi}_k^\pm}^2 - m_{\tilde{\ell}_i}^2)^3}. \end{aligned} \quad (7.51)$$

In the same approximation, the anapole moment reads

$$\mathcal{A}_{\beta\alpha}^{(a)} = -\frac{e}{192\pi^2} \sum_{i,k,\ell} |c_R^{ik\ell}|^2 U_{\ell\alpha} U_{\ell\beta}^* \frac{\left(m_{\tilde{\chi}_k^\pm}^2 + 2m_{\tilde{\ell}_i}^2\right) \log\left(m_{\tilde{\chi}_k^\pm}^2/m_{\tilde{\ell}_i}^2\right) - 3m_{\tilde{\chi}_k^\pm}^2 + 3m_{\tilde{\ell}_i}^2}{\left(m_{\tilde{\chi}_k^\pm}^2 - m_{\tilde{\ell}_i}^2\right)^2}. \quad (7.52)$$

We note that the contributions to the dipole moments are proportional to the neutrino masses, as the interaction is maximally parity-violating, resulting in the term $\sim \mathcal{G}_{\mu,d}^S$ vanishing. In contrast, the anapole and charge radius do not suffer from such a suppression.

To estimate the contribution to the neutrino anapole moment, we may integrate out the heavier slepton $\tilde{\ell}_2$ and chargino $\tilde{\chi}_2^\pm$. Further, we can neglect the term proportional to m_ℓ/m_W in the coupling, *viz.* $c_R^{ik\ell} \simeq -g\delta_{1i}\mathcal{U}_{k1}\cos\theta_{\tilde{\ell}}$. The contribution then reads for mass-degenerate sleptons

$$\mathcal{A}_{\beta\alpha}^{(a)} \simeq -\frac{eg^2}{192\pi^2} |\mathcal{U}_{11}|^2 \sum_{\ell} U_{\ell\alpha} U_{\ell\beta}^* \cos^2(\theta_{\tilde{\ell}}) \frac{\left(m_{\tilde{\chi}^\pm}^2 + 2m_{\tilde{\ell}}^2\right) \log\left(m_{\tilde{\chi}^\pm}^2/m_{\tilde{\ell}}^2\right) - 3m_{\tilde{\chi}^\pm}^2 + 3m_{\tilde{\ell}}^2}{\left(m_{\tilde{\chi}^\pm}^2 - m_{\tilde{\ell}}^2\right)^2} \quad (7.53)$$

where we dropped the index $i = k = 1$ of the chargino and slepton.

For a numeric estimate, we set the slepton mass to $m_{\tilde{\ell}} = 300$ GeV and for the chargino, we choose $m_{\tilde{\chi}^\pm} = 200$ GeV, resulting in¹

$$\mathcal{A}_{\alpha\alpha}^{(a)} \simeq |\mathcal{U}_{11}|^2 \sum_{\ell} U_{\ell\alpha} U_{\ell\beta}^* \cos^2(\theta_{\tilde{\ell}}) \times (7.21) \times 10^{-10} \text{ GeV}^{-2}, \quad (7.54)$$

which is smaller than the SM contribution by around three orders of magnitude. The smallness is simply because both mass scales appearing in the loop are relatively large.

From the functional behavior discussed in chapter 3 and section 7.1.2, it is evident that an enhancement is achieved if there is a small mass scale in the loop and optimally, some masses are degenerate. In the SM case, the lepton was light, so we may expect other contributions with leptons inside the loop to be comparable to the SM prediction. This is the case for the lepton-Higgs contribution.

¹These values are currently not excluded by collider limits. However, as the limits depend strongly on the assumed mass spectra, they are model-dependent. In particular, they are sensitive to the mass-splitting with respect to the lightest neutralino. See, for example, the ATLAS limits on staus [396] and charginos [489].

b) Lepton-Higgs loops

For the interaction between the neutrino, a lepton, and the charged Higgs boson, the interaction Lagrangian is given by [319]

$$\mathcal{L} \supset \frac{g}{\sqrt{2}m_W} \sum_{\ell} U_{\ell\alpha}^* \bar{\nu}_{\alpha} [m_{\nu_{\alpha}} \cot \beta P_L + m_{\ell} \tan \beta P_R] H^+ \ell, \quad (7.55)$$

where we assumed a Dirac mass term for the neutrino. The canonical couplings read

$$c_L^{\ell\alpha} = \frac{g}{\sqrt{2}m_W} U_{\ell\alpha}^* m_{\nu_{\alpha}} \cot \beta, \quad c_R^{\ell\alpha} = \frac{g}{\sqrt{2}m_W} U_{\ell\alpha}^* m_{\ell} \tan \beta. \quad (7.56)$$

We note that the analytic expression can be obtained from the result of the CP-conserving Majorana model extended with a Higgs triplet discussed in section 7.3.1 by dropping the factors $[1 \pm \tilde{\eta}_{\Xi(\alpha)}/\tilde{\eta}_{\Xi(\beta)}]$, and by making the replacements $B^+ \rightarrow H^+$ and $\tan \alpha \rightarrow \tan \beta$.

As in the MSSM (or a generic two-Higgs doublet model), the value for $\tan \beta$ is less constrained than $\tan \alpha$ for the triplet-extended SM, we may expect a more considerable contribution to the EM moments in the former model.

With $x_{\ell} = m_{\ell}/m_{H^{\pm}}$ the magnetic dipole moment therefore reads

$$\begin{aligned} \mu_{\beta\alpha}^{(b)} = & \frac{eG_F(m_{\alpha} + m_{\beta})}{32\sqrt{2}\pi^2} \sum_{\ell} U_{\ell\alpha} U_{\ell\beta}^* \frac{x_{\ell}^2}{(1-x_{\ell}^2)^3} \times \\ & \times \left[4(x_{\ell}^2 - 1)(x_{\ell}^2 - 2\log(x_{\ell}) - 1) \right. \\ & \left. + \tan^2(\beta)(x_{\ell}^4 - 4x_{\ell}^2 \log(x_{\ell}) - 1) \right], \end{aligned} \quad (7.57)$$

Being suppressed by the neutrino masses. The anapole moment is given by

$$\mathcal{A}_{\alpha\beta}^{(b)} = \frac{eG_F}{48\sqrt{2}\pi^2} \tan^2 \beta \sum_{\ell} U_{\ell\alpha} U_{\ell\beta}^* x_{\ell}^2 \frac{3 - 3x_{\ell}^2 + (2 + x_{\ell}^2) \log(x_{\ell}^2)}{(1-x_{\ell}^2)^2}. \quad (7.58)$$

If we expand the anapole moment in $m_{\ell}/m_{H^{\pm}}$, we find

$$\mathcal{A}_{\ell\ell}^{(b)} = \frac{eG_F}{48\sqrt{2}\pi^2} \tan^2 \beta \frac{m_{\ell}^2}{m_{H^{\pm}}^2} \left[3 + 2 \log\left(\frac{m_{\ell}^2}{m_{H^{\pm}}^2}\right) \right]. \quad (7.59)$$

As the SM contribution reads

$$\mathcal{A}_{\ell\ell}^{\text{SM}} = \frac{eG_F}{24\sqrt{2}\pi^2} \left[-3 + 2 \log\left(\frac{m_{\ell}^2}{m_W^2}\right) \right], \quad (7.60)$$

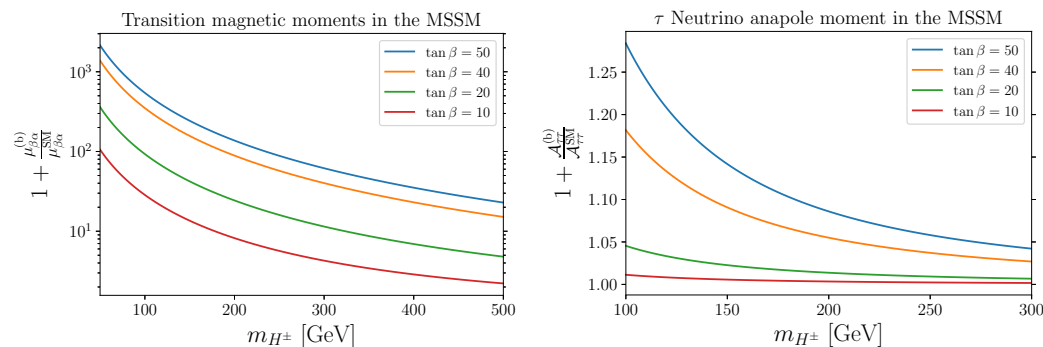


Figure 7.6: MSSM contributions to the transition magnetic dipole of neutrinos (independent of the mass eigenstates) and the anapole moment of ν_τ .

we may expect a similar order of magnitude between the Higgs-lepton contribution and the SM prediction if

$$\frac{1}{2} \left(\frac{m_\ell}{m_{H^\pm}} \tan \beta \right)^2 \simeq \mathcal{O}(1). \quad (7.61)$$

which is feasible only for $\ell = \tau$ and large $\tan \beta$.

We show in fig. 7.6 the relative correction to the anapole moment $\mathcal{A}_{\tau\tau}^{\text{SM}}$ and to the magnetic moment in analog to the discussion of the Higgs triplet extended Majorana model. We find that all EM moments are increased in this model. While the discussion for the magnetic dipole moments follows the reasonings of section 7.3.1, the anapole moment and charge radius may be enhanced by up to (10 – 30)%, depending on the details of the Higgs sector. Considering experimental constraints on the parameter space, it turns out that the low- m_{H^\pm} , high- $\tan \beta$ region is largely excluded for reasonable benchmark choices, leading to a maximal enhancement of a few percent. However, the details depend on the specifics of the benchmark scenario considered [490–492], allowing some freedom in the parameter space.

7.3.4 Leptoquarks

Leptoquarks are hypothetical particles that interact with both leptons and quarks simultaneously. There are two types of leptoquarks: scalar leptoquarks and vector leptoquarks, which are further classified based on their representation (for a comprehensive review, see ref. [493]). Of particular interest are the additional interactions they introduce between neutrinos and quarks, as such interactions can generate EM moments of neutrinos [420]. The relevant Feynman diagrams that illustrate these contributions are displayed in fig. 7.7.

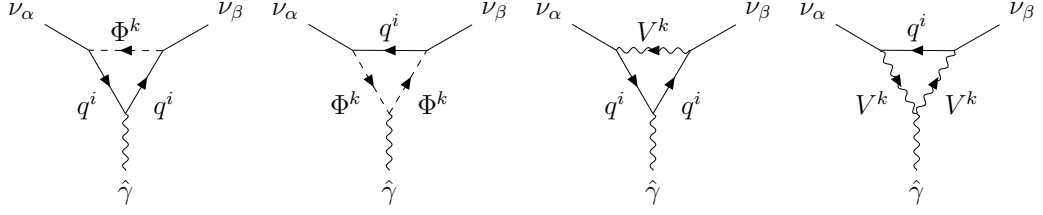


Figure 7.7: Scalar leptoquark Φ^k and vector leptoquarks V^k contributions to the EM moments of neutrinos.

Scalar leptoquarks

The interaction of the scalar leptoquark may be written as [493, 494]

$$\mathcal{L}_{\tilde{R}_2} \supset \tilde{R}_2^{2/3} V_{ik} \tilde{Y}_{2kj}^{\overline{\text{LR}}} \bar{u}_L^i \nu_R^j + \tilde{R}_2^{-1/3} \left[U_{kj} \tilde{Y}_{2ik}^{\overline{\text{RL}}} \bar{d}_R^i \nu_L^j + \tilde{Y}_{2ij}^{\overline{\text{LR}}} \bar{d}_L^i \nu_R^j \right] + \text{h.c.} \quad (7.62)$$

and

$$\mathcal{L}_{S_1} \supset S_1^{1/3} \left[U_{kj} Y_{1ik}^{\text{LL}} \bar{d}_L^i \nu_L^j + Y_{1ij}^{\text{RR}} \bar{d}_R^i \nu_R^j \right] + \text{h.c.}, \quad (7.63)$$

with CKM and PMNS matrixes V and U , respectively, and the superscript indicates the charge of the leptoquark. The Yukawa matrices \tilde{Y} constitute the new parameters of the theory. These interactions can be cast as

$$\mathcal{L} \supset \bar{\nu}_\alpha \left[c_L^{ik\alpha} P_L + c_R^{ik\alpha} P_R \right] q_i (\Phi^k)^* + \text{h.c.}, \quad (7.64)$$

where $\Phi^k = \Phi^{2/3}$ if q is an up-type quark and $\Phi^k = \Phi^{-1/3}$ for q being a down-type quark.² The coupling constants $c_L^{ik\alpha}$ and $c_R^{ik\alpha}$ depend on the representation of Φ (*i.e.* $\Phi^{2/3} = \tilde{R}_2^{2/3}$ or $\Phi^{-1/3} = \tilde{R}_2^{-1/3}$ ($S_1^{1/3}$)), and are a combination of fermion mixing matrixes and new Yukawa coupling matrixes.

The contribution to all EM moments is obtained by applying our general formulas given in eq. (3.47) by identifying the scalar mass with the leptoquark mass $m_S = m_{\text{LQ}}$, the fermion mass with a quark mass and accounting for the color factor by multiplying with N_c .

For $c_{L/R}^{ik\beta} \neq 0$, we may approximate the contribution to the dipole moments as

$$\left. \begin{aligned} \mu_{\beta\alpha}^S \\ -id_{\beta\alpha}^S \end{aligned} \right\} \simeq \frac{eQ_k N_c}{32\pi^2} \sum_{i,k=1}^3 \left[\tilde{c}_L^{ik\beta} (c_R^{ik\alpha})^* \pm c_R^{ik\beta} (c_L^{ik\alpha})^* \right] g_\mu^S \left(\frac{m_{q_i}}{m_\alpha}, \frac{m_{\text{LQ}}}{m_\alpha}, \frac{m_\beta}{m_\alpha} \right), \quad (7.65)$$

²It was pointed out in refs. [420, 495, 496] that the term with the charge-conjugated field contributes the same as if there was no charge-conjugation involved, after making the appropriate replacements for the charges and couplings. The same conclusion can be found using the formalism proposed in ref. [236].

where we dropped the first term $\sim \mathcal{F}_{\mu,d}^S$ as this is proportional to the neutrino masses and used $\mathcal{G}_d^S = i\mathcal{G}_\mu^S$. However, if $c_L^{ik\beta} \simeq 0$ or $c_R^{ik\beta} \simeq 0$, the leading contribution can come from the $\mathcal{F}_{\mu,d}^S$ term, similar to the SM situation.

For the anapole and the charge radius, we can drop the term $\sim \mathcal{G}_{\mathcal{A},b}^S$, and find

$$\left. \begin{array}{l} \mathcal{A}_{\beta\alpha}^S \\ b_{\beta\alpha}^S \end{array} \right\} \simeq \frac{eQ_k N_c}{32\pi^2} \sum_{i,k=1}^3 \left[c_L^{ik\beta} (c_L^{ik\alpha})^* \mp c_R^{ik\beta} (c_R^{ik\alpha})^* \right] \mathcal{F}_{\mathcal{A}}^S \left(\frac{m_{q_i}}{m_\alpha}, \frac{m_{\text{LQ}}}{m_\alpha}, \frac{m_\beta}{m_\alpha} \right), \quad (7.66)$$

where we used $\mathcal{F}_b^S \simeq \mathcal{F}_{\mathcal{A}}^S$.

Vector leptoquarks

Similarly, for the vector leptoquarks, the Lagrangian of the relevant representations read [493, 494]

$$\mathcal{L}_{U_1} \supset U_{1\mu}^{2/3} \left(V_{im} U_{kj} X_{1mk}^{\text{LL}} \bar{u}_L^i \gamma^\mu \nu_L^j + X_{1ij}^{\text{RR}} \bar{u}_R^i \gamma^\mu \nu_R^j \right) + \text{h.c.} \quad (7.67)$$

and

$$\mathcal{L}_{\tilde{V}_2} \supset \tilde{V}_{2\mu}^{-2/3} \left(-U_{ik} \tilde{X}_{2kj}^{\text{RL}} \bar{u}_R^i \gamma^\mu \nu_L^j + V_{ik}^T \tilde{X}_{2kj}^{\text{LR}} \bar{u}_L^i \gamma^\mu \nu_R^j \right) - \tilde{V}_{2\mu}^{1/3} \tilde{X}_{2ij}^{\text{LR}} \bar{d}_L^i \gamma^\mu \nu_R^j + \text{h.c.} \quad (7.68)$$

Again, these interactions can be cast in the canonical form:

$$\mathcal{L} \supset \bar{\nu}_\alpha \gamma^\mu \left[v_L^{i\alpha} P_L + v_R^{i\alpha} P_R \right] q^i V_\mu^{k*} + \text{h.c.} \quad (7.69)$$

Therefore, the EM moments read

$$\left. \begin{array}{l} \mu_{\beta\alpha}^V \\ id_{\beta\alpha}^V \end{array} \right\} \simeq \frac{eQ_k N_c}{32\pi^2} \sum_i \left[v_L^{i\beta} (v_R^{i\alpha})^* \pm v_R^{i\beta} (v_L^{i\alpha})^* \right] \mathcal{G}_\mu^V \left(\frac{m_{q_i}}{m_\alpha}, \frac{m_{\text{LQ}}}{m_\alpha}, \frac{m_\beta}{m_\alpha} \right) \quad (7.70)$$

$$\left. \begin{array}{l} \mathcal{A}_{\beta\alpha}^V \\ -b_{\beta\alpha}^V \end{array} \right\} \simeq \frac{eQ_k N_c}{32\pi^2} \sum_i \left[v_L^{i\beta} (v_L^{i\alpha})^* \mp v_R^{i\beta} (v_R^{i\alpha})^* \right] \mathcal{F}_{\mathcal{A}}^V \left(\frac{m_{q_i}}{m_\alpha}, \frac{m_{\text{LQ}}}{m_\alpha}, \frac{m_\beta}{m_\alpha} \right), \quad (7.71)$$

where we used $\mathcal{G}_d^V = -i\mathcal{G}_\mu^V$ and $\mathcal{F}_b^V = -\mathcal{F}_{\mathcal{A}}^V$, see section 3.4.3.

We note that specific models may lead to certain restrictions on the coupling constants. For example, in the gauge leptoquark model discussed in ref. [420], which is inspired by the model of ref. [497], the vector coupling to the right-handed quark vanishes. In this scenario, the leading contribution to the dipole moments is $\sim \mathcal{F}_{\mu,d}^V$ and therefore suppressed by the neutrino masses. Meanwhile, the anapole receives a large contribution, as this model maximally violates parity. The additional Goldstone loops are phenomenologically suppressed as $\sim m_{q_i}/m_{\text{LQ}}$ and $\sim m_\alpha/m_{\text{LQ}}$. They are,

therefore, typically negligible for an estimate of the EM moments, similar to the situation in the SM.

Leptoquarks are experimentally constrained to be in the TeV range (see for example searches from CMS [498–503] and ATLAS [504–507]), such that their contributions to the dimension-6 operators are expected to be negligible, even for $\mathcal{O}(1)$ couplings and light quarks in the loop. On the other hand, the dimension-5 operators can be enhanced as the coefficient of the $\mathcal{G}_{\mu,d}^{S,V}$ term may be of $\mathcal{O}(1)$, possibly compensating the mass suppression of the loop functions. This would be in contrast to the SM where the scalar contribution of the dipole moments due to Goldstone bosons is suppressed as $\sim m_\ell m_\nu / m_W^2$ and the vector part $\sim \mathcal{G}_{\mu,d}^V$ is absent because the weak interaction maximally violates parity.

7.3.5 R -parity violating MSSM

We saw that for leptoquarks, even with $\mathcal{O}(1)$ couplings, the contributions to the EM moments of neutrinos are typically expected to be tiny as the masses of the leptoquarks have to be of $\mathcal{O}(\text{TeV})$ to avoid collider constraints on colored particles. Therefore, if the SM fermions in the loop are leptons instead of quarks, the limits on the new colorless scalars would relax, and thus, the EM moments might be enhanced.

A model with such a structure is the R -parity violating (RPV) MSSM (see ref. [319] for an introduction and ref. [508] for a recent status report). In contrast to the R -parity conserving MSSM introduced in section 5.1, the key feature in the RPV MSSM is the addition of interactions breaking lepton- or baryon number at the tree-level.

In the superpotential, these terms are written as

$$W_{\Delta L=1} = \frac{1}{2} \lambda_{ijk} L_i L_j \bar{e}_k + \lambda'_{ijk} L_i Q_j \bar{d}_k + \mu_L^i L_i H_u, \quad (7.72a)$$

$$W_{\Delta B=1} = \frac{1}{2} \lambda''_{ijk} \bar{u}_i \bar{d}_j \bar{d}_k, \quad (7.72b)$$

where $\lambda_{ijk} = -\lambda_{jik}$ and $\lambda''_{ijk} = -\lambda''_{ikj}$ due to gauge invariance. The first two terms in eq. (7.72a) are called the LLE- and LQD term, and the term in eq. (7.72b) is the UDD term; the latter can induce proton decays.

Constraints on the couplings λ_{ijk} , λ'_{ijk} and λ''_{ijk} are strongly model dependent. To reduce the large number of new parameters introduced in the RPV MSSM, often some elements of these couplings are set to zero, and certain assumptions about the supersymmetric mass-spectrum and branching ratios are made.³ In particular, the mass-splitting between the lightest neutralino and the next-to-LSP, which may be assumed to be a slepton, is relevant for collider constraints, as for compressed spectra, the final states can be soft and thus hard to detect [509].

³See, for example, the reported studies of the Particle Data Group [335] for a comprehensive list of collider exclusion limits on the RPV SUSY spectrum, including the respective model assumptions.

Both LLE- and LQD terms of the lepton number violating superpotential contribute to the EM moments of the neutrinos, as the new scalar degrees of freedom give rise to interactions between neutrinos and the SM fermions. Here, we only discuss the LLE term in more detail. The LQD term leads to a phenomenology similar to that of leptoquarks, such that due to the strong collider constraints on squarks, the EM moments are expected to be suppressed by their mass scale.

The relevant part of the Lagrangian for the LLE term reads for $i > j$ [510]

$$-\mathcal{L}_{\text{LLE}} = \sum_{ijk, i>j} \lambda_{ijk} \left(\tilde{\ell}_{kR}^* \bar{\nu}_i^c P_L \ell_j + \tilde{\ell}_{jL} \bar{\ell}_k P_L \nu_i - \tilde{\nu}_j \bar{\ell}_k P_L \ell_i + \text{h.c.} \right). \quad (7.73)$$

The first two terms contribute to the EM moments of neutrinos. While the second term fits our canonical vertex parameterization,

$$-\mathcal{L} \supset \sum_{\alpha} \sum_{ijk, i>j} U_{i\alpha}^* \lambda_{ijk} \bar{\nu}_{\alpha} P_R \ell_k \tilde{\ell}_{jL}^* + \text{h.c.}, \quad (7.74)$$

due to the presence of the charge conjugation ν^c , the first does not. We already encountered a similar situation in the discussion of leptoquarks in section 7.3.4. The contribution can be calculated using the formalism proposed in ref. [236], which turns out to be equivalent to the contribution from the Lagrangian

$$-\mathcal{L} \supset \sum_{\alpha} \sum_{ijk, i>j} U_{i\alpha}^* \lambda_{ijk} \bar{\nu}_{\alpha} P_L \ell_j \tilde{\ell}_{kR}^* + \text{h.c.} \quad (7.75)$$

Thus, we may use eq. (7.75) to calculate the RPV contribution from the first term in eq. (7.73).

If the sleptons mix, $(\tilde{\ell}_{kL}, \tilde{\ell}_{kR})_m^T = L_{mn}^{2k-1} (\tilde{\ell}_{k1}, \tilde{\ell}_{k2})_n^T$, the overall RPV SUSY contribution can be cast in the canonical form:

$$\mathcal{L} = \bar{\nu}_{\alpha} \left[L_{2n}^{2k-1} \lambda_{ijk} P_L + L_{1n}^{2k-1} \lambda_{ikj} P_R \right] \ell_j \tilde{\ell}_{kn}^* + \text{h.c.} \quad (7.76)$$

In general, both left- and right-handed leptons can contribute to the EM multipoles of neutrinos. We will assume no sfermion mixing and consider only the right-handed part of eq. (7.76) for simplicity. The case with mixing is qualitatively similar to the leptoquark discussion in section 7.3.4. Then, the Lagrangian can be cast as

$$-\mathcal{L} \supset \sum_{\alpha} \sum_i \lambda_i U_{i\alpha}^* \bar{\nu}_{\alpha} P_R \ell \tilde{\ell}^* + \text{h.c.}, \quad (7.77)$$

where $\tilde{\ell}$ and ℓ can be any slepton or lepton to which the neutrino ν_{α} couples with strength λ_i (which can be different for each combination of leptons and sleptons). We can identify the canonical couplings as

$$c_L^{\alpha i} = 0, \quad c_R^{\alpha i} = -U_{i\alpha}^* \lambda_i. \quad (7.78)$$

As the interaction maximally violates parity, we have a similar situation as in the SM: the dipole moments are suppressed as they are proportional to the neutrino masses, whereas the anapole and charge radius are relatively large. Explicitly, we find

$$\mu_{\beta\alpha}^{\text{RPV}} = -\frac{e}{32\pi^2} \sum_i c_R^{\beta i} (c_R^{\alpha i})^* \mathcal{F}_\mu^S \left(\frac{m_\ell}{m_\alpha}, \frac{m_{\bar{\ell}}}{m_\alpha}, \frac{m_\beta}{m_\alpha} \right), \quad (7.79)$$

$$\mathcal{A}_{\beta\alpha}^{\text{RPV}} = \frac{e}{32\pi^2} \sum_i c_R^{\beta i} (c_R^{\alpha i})^* \mathcal{F}_A^S \left(\frac{m_\ell}{m_\alpha}, \frac{m_{\bar{\ell}}}{m_\alpha}, \frac{m_\beta}{m_\alpha} \right), \quad (7.80)$$

where we used $Q_f = -1$ for all leptons. Then, at lowest order in the neutrino masses, the magnetic dipole and the anapole moment reduce, respectively, to

$$\mu_{\beta\alpha}^{\text{RPV}} = -\frac{eG_F}{16\sqrt{2}\pi^2} \frac{\lambda^2 m_W^2}{g^2 m_\ell^2} (m_\alpha + m_\beta) \sum_i U_{i\alpha} U_{i\beta}^* \frac{(\rho^4 - 4\rho^2 \log(\rho) - 1)}{(\rho^2 - 1)^3}, \quad (7.81)$$

$$\mathcal{A}_{\beta\alpha}^{\text{RPV}} = \frac{eG_F}{24\sqrt{2}\pi^2} \frac{\lambda^2 m_W^2}{g^2 m_\ell^2} \sum_i U_{i\alpha} U_{i\beta}^* \frac{3 - 3\rho^2 + (2 + \rho^2) \log(\rho^2)}{(\rho^2 - 1)^2}, \quad (7.82)$$

with $\rho = m_\ell/m_{\bar{\ell}}$ and we assumed a democratic $\lambda_i = \lambda$ for all i . Following the parameterization of eq. (7.35), the relative correction to the SM contribution of the transition magnetic dipole moment can be expressed as

$$1 + \frac{\mu_{\beta\alpha}^{\text{RPV}}}{\mu_{\beta\alpha}^{\text{SM}}} \simeq \frac{F(m_\tau) - F(0) + c_\tau^{-1} F^{\text{RPV}}}{F(m_\tau) - F(0)}, \quad (7.83)$$

with

$$F^{\text{RPV}} \simeq -\sum_\ell c_\ell \frac{1}{3} \frac{\lambda^2 m_W^2}{g^2 m_\ell^2} \left[1 + m_\ell^2/m_\ell^2 \left(3 + 2 \log\left(m_\ell^2/m_\ell^2 \right) \right) \right] \quad (7.84)$$

$$\simeq -c_\tau \frac{1}{3} \frac{\lambda^2 m_W^2 m_\tau^2}{g^2 m_\ell^2 m_\ell^2} \left(3 + 2 \log\left(\frac{m_\tau^2}{m_\ell^2} \right) \right), \quad (7.85)$$

where we used the fact that the neutrino mixing matrix is unitary and therefore $\sum_\ell c_\ell = 0$ (as $\alpha \neq \beta$). Thus

$$1 + \frac{\mu_{\beta\alpha}^{\text{RPV}}}{\mu_{\beta\alpha}^{\text{SM}}} \simeq 1 + \frac{2}{3} \frac{\lambda^2 m_W^4}{g^2 m_\ell^4} \left(3 + 2 \log\left(\frac{m_\tau^2}{m_\ell^2} \right) \right) < 1. \quad (7.86)$$

The anapole moment reads

$$\mathcal{A}_{\beta\alpha}^{\text{RPV}} = \sum_\ell U_{\ell\beta}^* U_{\ell\alpha} \mathcal{A}_{\ell\ell}, \quad (7.87)$$

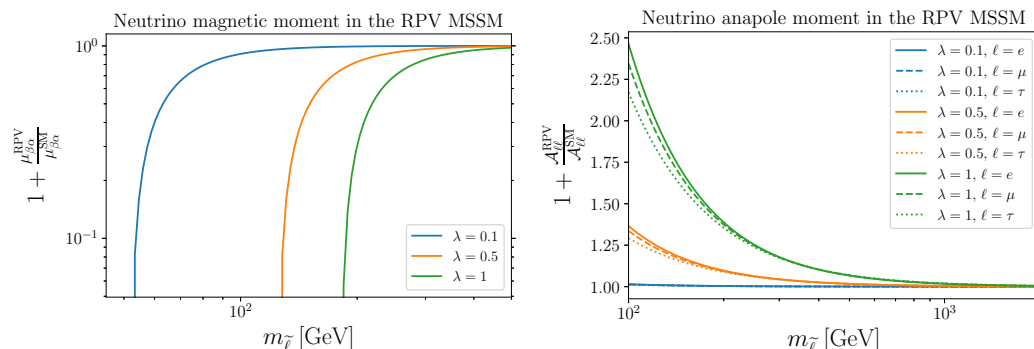


Figure 7.8: Neutrino magnetic- and anapole moments in the RPV MSSM.

where we defined

$$\mathcal{A}_{\ell\ell}^{\text{RPV}} \simeq \frac{eG_F}{24\sqrt{2}\pi^2} \frac{\lambda^2}{g^2} \frac{m_W^2}{m_{\tilde{\ell}}^2} \left(3 + 2 \log \left(\frac{m_{\tilde{\ell}}^2}{m_{\ell}^2} \right) \right), \quad (7.88)$$

which becomes sizeable for $\lambda \sim g$ and $m_{\tilde{\ell}} \sim m_W$. In practice, this may be challenging to achieve, as $\lambda \lesssim (10^{-3} - 10^{-1}) \left(\frac{m_{\tilde{\ell}}}{100 \text{ GeV}} \right)$ [319], where the exact limit depends on the triplet (ijk) and is inferred from charged-current universality and neutrino-electron scattering analyses [511–513].

We present in fig. 7.8 the normalized RPV SUSY contribution to the magnetic dipole moment and the anapole moment for $\lambda \in \{0.1, 0.5, 1\}$ in blue, orange and green respectively. Without scalar mixing, the magnetic dipole moment is small in magnitude and is found to have the opposite phase to the SM prediction. However, mixing between the scalars could lead to a contribution $\sim \mathcal{G}_{\mu}^S$, which could be dominant. The anapole moment can get $\mathcal{O}(1)$ corrections for optimistic values for the slepton mass and coupling. In contrast, the enhancement is at the percent level for more conservative values.

7.3.6 Dark electromagnetic moments

In the previous sections, we discussed models that modify the interactions between the neutrino and other SM particles by adding a mediator particle with a mass scale subject to strong experimental constraints. Therefore, the resulting contributions to the EM moments \mathbb{M} are typically suppressed by this new scale, particularly in the absence of right-handed currents.

In this section, we follow a different approach and assume the EM interactions are entirely generated in a dark sector, which is connected to the visible sector via the kinetic mixing of a dark photon with the SM photon. Therefore, the neutrinos

have *dark electromagnetic moments* in this setup. This idea has been, for example, explored in the EFT framework for the magnetic dipole operator in ref. [470], and for both dipoles and in conjunction with a neutrino mass mechanism in ref. [426]. Here, we want to explicitly calculate the EM moments due to dark sector particles in a simplified model to estimate their size.

This approach differs conceptually from the previous models, as the dark sector particles are experimentally allowed to be relatively light, enhancing the loop functions. The suppression due to the dark photon mixing parameter κ competes with this enhancement.

For the dark photon, we consider the Lagrangian [292, 293]

$$\mathcal{L} \supset -\frac{1}{4}F'_{\mu\nu}F'^{\mu\nu} + \frac{\kappa}{2}F'_{\mu\nu}F^{\mu\nu} + \frac{1}{2}m_{A'}^2 A'^2, \quad (7.89)$$

where A'_μ is the $U(1)_{\text{dark}}$ gauge boson, $F'_{\mu\nu}$ its field strength tensor, $m_{A'}$ the dark photon mass, and $F_{\mu\nu}$ is the photon field strength tensor. We will consider the massless case, and from now on, set $m_{A'} = 0$. The dark sector further contains a scalar S and a fermion ψ , charged under the $U(1)_{\text{dark}}$ symmetry described by the Lagrangian

$$\mathcal{L} \supset (D_\mu S)^\dagger (D^\mu S) - m_S^2 S^\dagger S + \bar{\psi} (i\not{D} - m_\psi) \psi, \quad (7.90)$$

where D_μ is the covariant derivative. Thus, with respect to the SM photon, these fields have a (milli-) charge $\epsilon e = \kappa e' e$, where e' is the dark photon gauge coupling.

We assume that the portal interactions with the neutrinos can be cast as

$$\mathcal{L} \supset \bar{\nu}_\alpha [c_L^\alpha P_L + c_R^\alpha P_R] \psi S^\dagger + \text{h.c.}, \quad (7.91)$$

such that the theory discriminates between the left- and right components of ψ , allowing parity violation, and, for complex couplings $c_{L/R}^\alpha$, also CP violation. This interaction generates at the one-loop level the neutrino EM moments with respect to the dark photon, which we will refer to as *dark moments*. As the dark photon mixes with the SM photon, the dark moments are transmitted to the visible sector, effectively yielding an additional contribution to the neutrino EM moments with respect to the SM photon. We depict this process in fig. 7.9.

We can obtain the analytical expressions for the dark moments by making the replacement $Q_f \rightarrow \epsilon$ in eq. (3.47) and eq. (3.48), *i.e.* we take particles ψ , S and V with millicharge ϵe (with $e > 0$) in the loop.

Therefore, the relevant parameters are the masses of the particles in the dark sector and the millicharge ϵ . We present in fig. 7.10 a collection of exclusion limits on millicharged Dirac fermions from LSND [514], proton beam dump studies from SENSEI [515] and BEBC [516], Big Bang Nucleosynthesis (BBN) [517, 518], collider limits [519], supernova cooling [520], low-energy supernovae (LESN) [521] and electron beam dump forecasts [455] for one skipper-CCD detector at BDX [522–524].

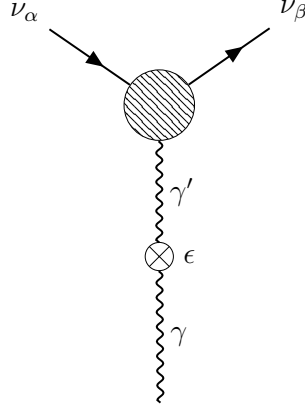


Figure 7.9: Dark moments of neutrinos, represented by the effective vertex. The kinetic mixing parameter ϵ between the dark photon γ' and the SM photon γ mediates the dark EM moments to the visible sector.

In particular, the BBN constraints on the effective number of relativistic degrees of freedom at the time of recombination, N_{eff} , lead to a lower bound on the mass of millicharged particles of $m_\psi > 8.62 \text{ MeV}$ [518]. Similar constraints on scalars and vectors are expected to be of comparable size [455], such that we will use the constraints shown in fig. 7.10 for all millicharged loop particles.

For concreteness, we consider the scenario of a scalar and a chiral fermion in the loop, such that the enhancement on the EM moments of Dirac neutrinos due to dark moments reads

$$\begin{aligned} \mathbb{M}_{\beta\alpha}^{\text{dark}} = \frac{e\epsilon}{32\pi^2} \left\{ \left[c_L^\beta c_L^\alpha \pm c_R^\beta c_R^\alpha \right] \mathcal{F}_{\mathbb{M}}^S \left(\frac{m_\psi}{m_\alpha}, \frac{m_S}{m_\alpha}, \frac{m_\beta}{m_\alpha} \right) \right. \\ \left. + \left[c_L^\beta c_R^\alpha \pm c_R^\beta c_L^\alpha \right] \mathcal{G}_{\mathbb{M}}^S \left(\frac{m_\psi}{m_\alpha}, \frac{m_S}{m_\alpha}, \frac{m_\beta}{m_\alpha} \right) \right\}. \end{aligned} \quad (7.92)$$

For a fixed value of m_ψ , we perform a log-scaled random scan over the parameters $0.01 \leq \pm c_{L/R}^{\alpha/\beta} \leq 1$, $8.62 \text{ MeV} \leq m_S \leq 20 \text{ GeV}$ and $10^{-8} \leq \epsilon \leq 10^{-2}$ taking into account all current exclusion limits for the pairs (m_ψ, ϵ) and (m_S, ϵ) collected in fig. 7.10. The EM moments generated by vector bosons are subject to model dependency due to the Goldstone contributions. Nevertheless, the EM moments generated by the vector bosons are expected to be comparable to the scalar contribution up to $\mathcal{O}(1)$ corrections.

We present in the top panels of fig. 7.11 the result of the scan for the anapole moment $\mathcal{A}_{\beta\alpha}^{\text{dark}}$ for $8.62 \text{ MeV} < m_S < 20 \text{ GeV}$ (top left panel) and $m_S = 1 \text{ GeV}$ (top right panel) together with the Dirac neutrino predictions within the SM, eq. (7.14).

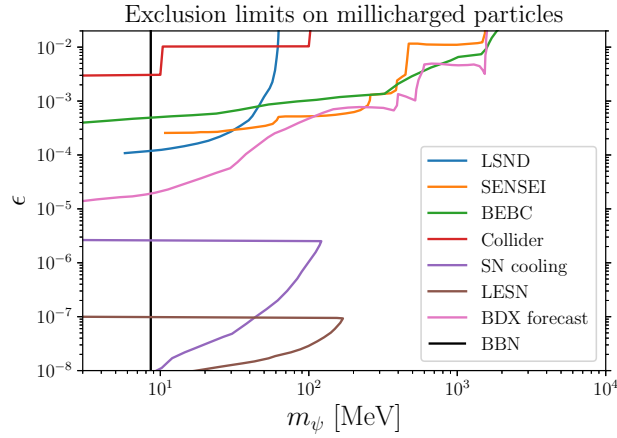


Figure 7.10: Collection of exclusion limits on millicharged particles from various terrestrial and astrophysical searches [455, 514–521]; see main text for details.

We find that the dark anapole moment can become comparable to the SM prediction if the millicharged particles in the loop are below the GeV scale.

The situation for the magnetic dipole moment in the minimally extended SM is somewhat different, as the SM value is very suppressed due to the light nature of neutrinos. In the bottom panel of fig. 7.11, we plot the dark magnetic moments from our scan and the diagonal SM prediction for Dirac neutrinos. All points $\mu_{\beta\alpha}^{\text{dark}} > 10^{-14} \text{ GeV}^{-1}$ are due to the \mathcal{G}_{μ}^S part, and for $m_{\psi} > 1 \text{ GeV}$, all predictions above $\mu_{\alpha\alpha}^{\text{SM}}$ are. As the loop functions \mathcal{G}_{M}^S and \mathcal{F}_{M}^S contribute democratically in the scan, the dominant contribution to the magnetic moment comes from the former being enhanced by its $\sim m_{\psi}$ scaling, see section 7.1.2.

The relative phase of the dark moments can become important and could lead to a reduction of the physical observable. Therefore, an observation of the anapole moment below the SM prediction would also be an indication of new physics. This potential decrease can be seen in fig. 7.12, where we present the relative enhancement to the SM prediction $\mathcal{A}_{\beta\alpha}^{\text{SM}}$ given in eq. (7.14) in the dark photon model for the diagonal (left panels) and the transition moments (right panels) for $8.62 \text{ MeV} < m_S < 20 \text{ GeV}$ (top panels) and for $m_S = 1 \text{ GeV}$ (bottom panels). For demonstration purposes, we assumed $\mathcal{A}_{\beta\alpha}^{\text{dark}} = \mathcal{A}^{\text{dark}}$, *i.e.* the same dark anapole moment for all diagonal and transition elements. The different colors indicate the different elements of the anapole matrix; see the legends. As $|\mathcal{A}_{33}^{\text{SM}}| < |\mathcal{A}_{22}^{\text{SM}}| < |\mathcal{A}_{11}^{\text{SM}}|$, the respective relative enhancement for the diagonal case is of opposite ordering; a similar statement is true for the transition moments. For the latter, we find that the relative enhancements can be larger than for the diagonal elements as we assumed a democratic BSM con-

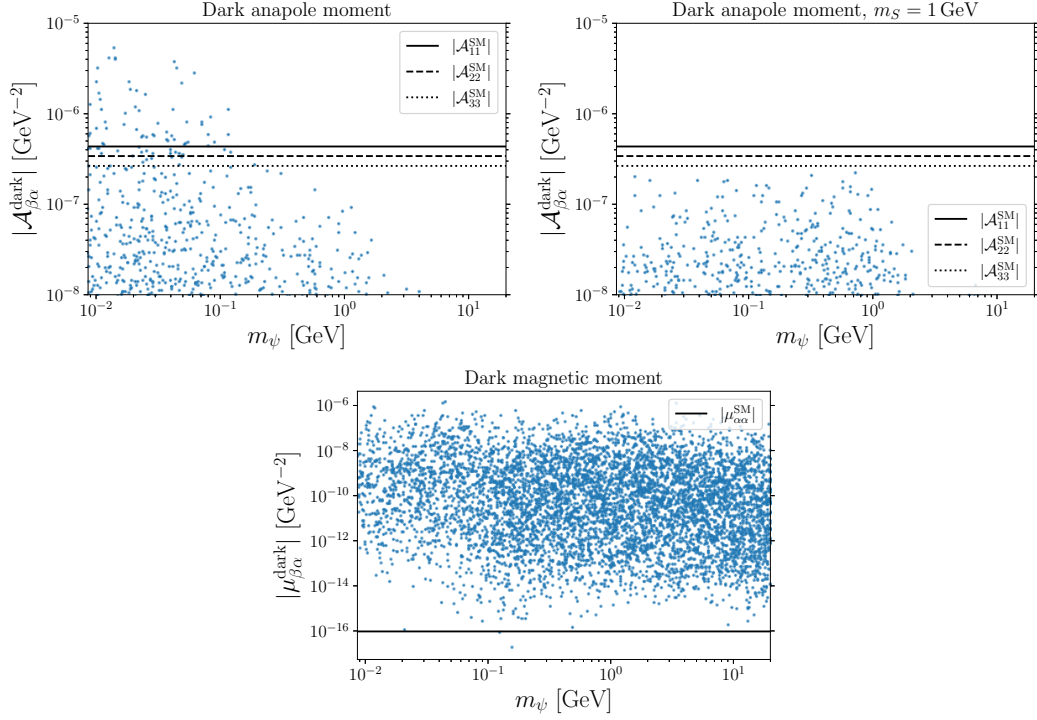


Figure 7.11: Result of the random scan for the neutrino dark anapole moment as a function of the fermion mass in the loop (*top left*), and the result of the random scan with fixed $m_S = 1$ GeV (*top right*). Further, we present the dark magnetic moment (*bottom*). For reference, we also add the absolute values of the prediction for the magnetic moment and anapole moment within the minimally extended SM for $m_\alpha = m_\beta = 1$ eV.

tribution, and because the transition moments $\mathcal{A}_{\beta\alpha}^{\text{SM}}$ ($\alpha \neq \beta$) are about one order of magnitude smaller than the diagonal elements $\mathcal{A}_{\alpha\alpha}^{\text{SM}}$.

We find that the contribution from the dark anapole moment can be up to two orders of magnitude above the SM prediction. We emphasize that the phase of the BSM contribution is important, as an opposite sign can similarly lead to a reduction of the observable anapole by a factor ~ 100 .

As mentioned in section 7.2.1, for relativistic active neutrinos, the initial beam can be approximated to be left-chiral, such that experiments are sensitive to the effective coupling

$$(b_{\beta\alpha})_{\text{eff.}} = b_{\beta\alpha} - \mathcal{A}_{\beta\alpha}, \quad (7.93)$$

with

$$\mathcal{A}_{\beta\alpha} = \mathcal{A}_{\beta\alpha}^{\text{SM}} + \mathcal{A}_{\beta\alpha}^{\text{dark}} \quad \text{and} \quad b_{\beta\alpha} = b_{\beta\alpha}^{\text{SM}} + b_{\beta\alpha}^{\text{dark}}, \quad (7.94)$$

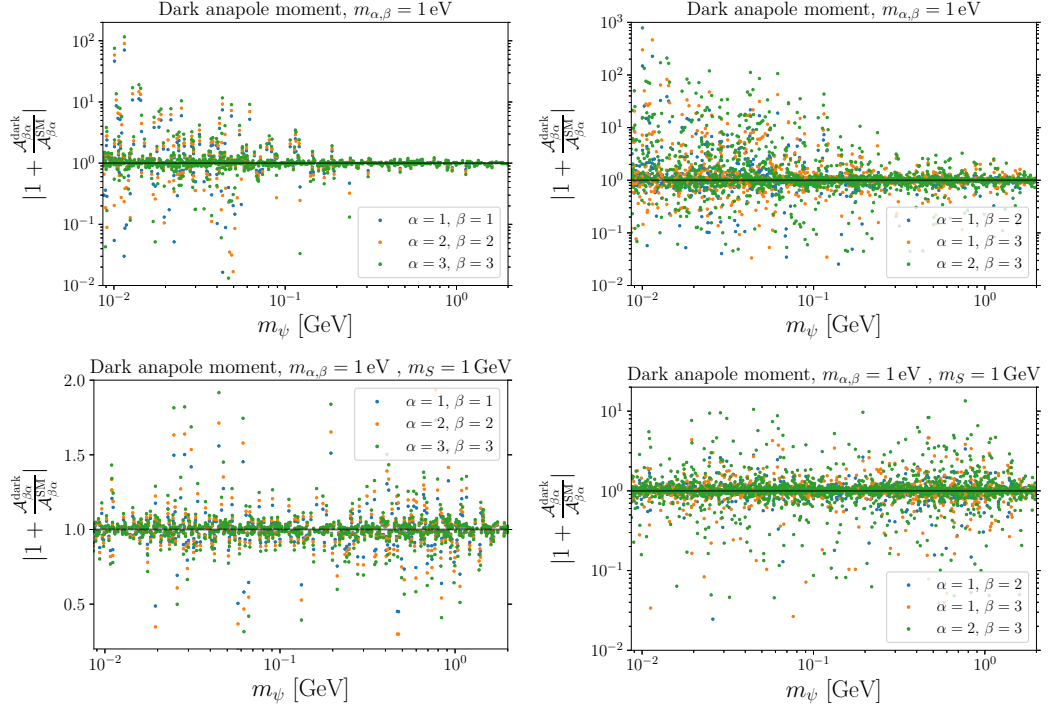


Figure 7.12: Relative enhancement of the SM anapole moments due to millicharged particles in the loop for the full random sample (*top*), and setting $m_S = 1 \text{ GeV}$ (*bottom*). We only show points which satisfy $\mathcal{A}_{\beta\alpha}^{\text{dark}}/\mathcal{A}_{\beta\alpha}^{\text{SM}} > 1\%$ as to avoid clutter; most points in the full scan do not lead to a sizeable shift to the SM prediction and are found close to the horizontal black line. Note the different axes.

where $\mathcal{A}_{\beta\alpha}^{\text{SM}} \simeq -b_{\beta\alpha}^{\text{SM}}$ is given by eq. (7.14) for normal ordering.

Therefore, to compare the theory predictions with the experiment, we have to include the corrections to both the charge radius and the anapole moment, which respectively are proportional to $(c_L^2 + c_R^2)$ and $(c_L^2 - c_R^2)$, where, for simplicity, we relabeled the couplings as $c_{L/R}^\alpha c_{L/R}^\beta \rightarrow (c_{L/R})^2$. As the terms $\mathcal{G}_{b,\mathcal{A}}^{S,V}$ are phenomenologically negligible, the phenomenology of the dimension-6 operators remains unchanged under this relabeling. Then, the additional contribution to the effective charge radius due to the dark moments reads

$$(b_{\beta\alpha}^{\text{dark}})_{\text{eff.}} = b_{\beta\alpha}^{\text{dark}} - \mathcal{A}_{\beta\alpha}^{\text{dark}} \simeq \frac{\epsilon c_R^2}{16\pi^2} \mathcal{F}_b^S \left(\frac{m_f}{m_\alpha}, \frac{m_S}{m_\alpha}, \frac{m_\beta}{m_\alpha} \right) \quad (7.95)$$

$$= \begin{cases} 2b_{\beta\alpha}^{\text{dark}}, & \text{if } c_L = 0 \\ 0, & \text{if } c_R = 0 \end{cases}, \quad (7.96)$$

up to terms of order $\mathcal{O}(m_\alpha m_\beta/m_S^2)$; we used eq. (3.62) to express \mathcal{F}_A^S in terms of \mathcal{F}_b^S .

Note that the effective charge radius vanishes if $c_L = 0$ is unique to our proposed scalar contribution. If we would consider a millicharged vector boson instead of the scalar, as then $\mathcal{F}_b^V \simeq -\mathcal{F}_A^V$, the opposite dependency emerges:

$$(b_{\beta\alpha}^{V,\text{dark}})_{\text{eff.}} = b_{\beta\alpha}^{V,\text{dark}} - \mathcal{A}_{\beta\alpha}^{V,\text{dark}} \simeq \frac{\epsilon v_L^2}{16\pi^2} \mathcal{F}_b^V \left(\frac{m_f}{m_\alpha}, \frac{m_V}{m_\alpha}, \frac{m_\beta}{m_\alpha} \right) \quad (7.97)$$

$$= \begin{cases} 0, & \text{if } v_L = 0 \\ 2b_{\beta\alpha}^{V,\text{dark}}, & \text{if } v_R = 0 \end{cases}. \quad (7.98)$$

This observation aligns with the SM weak interaction discussion in section 7.2.1.

The fact that the effective charge radius (or effective anapole moment) depends only on one of the chiral couplings in the maximal parity-violating setup is a consequence of the polarization of the initial beams for active relativistic neutrinos, which we assumed to be maximal ($\gamma_5 = -1$). Further, this feature emerges only for Dirac neutrinos; for Majorana neutrinos, only the anapole moment is non-zero, being proportional to $(c_L^2 - c_R^2)$. Therefore, if the dark sector respects parity, only the effective dimension-6 interaction of a Dirac neutrino receives a non-zero contribution.

To quantify this behavior, we show in fig. 7.13 the effective dark charge radius in units of the dark anapole $\mathcal{A}_{\beta\alpha}^{\text{dark}}$. For concreteness, we assume neutrinos with masses $m_\alpha = m_\beta = 1 \text{ eV}$. However, the exact values are not important for the dimension-6 operators, as the correction terms are $\sim m_\alpha m_\beta/m_{f,S,V}^2$ and therefore suppressed by the heavier loop scale, see appendix B.4.

The experimentally accessible effective charge radius can roughly differ by up to six orders of magnitude from the dark anapole moment, being suppressed or enhanced, depending on the P violation in the dark sector. The relative suppression occurs if $c_R \rightarrow 0$ while c_L remains large, *i.e.* the P violation in the dark sector is large. Then, the dark effective charge radius for the Dirac case becomes suppressed, whereas the anapole is $\sim |c_L|^2$. As we considered in the scan a lower bound of $|c_{L/R}| > 0.01$, in principle, the relative suppression can be even stronger. Therefore, considering only the anapole moment to estimate the experimental signature would severely overestimate the total BSM correction in this scenario.

On the other hand, if parity is conserved in the dark sector, the dark anapole moment vanishes, whereas the dark charge radius remains non-zero. This feature is captured by the enhanced points in fig. 7.13, where taking only the anapole as coupling between neutrinos and photons would significantly underestimate the total coupling strength to the photon. Finally, the clustering at $|(b_{\beta\alpha}^{\text{dark}})_{\text{eff.}}/(\mathcal{A}_{\beta\alpha}^{\text{dark}})| \simeq 2$ is because if the left coupling vanishes, $c_L \rightarrow 0$, the effective charge radius simplifies to $(b_{\beta\alpha}^{\text{dark}})_{\text{eff.}} \rightarrow 2b_{\beta\alpha}^{\text{dark}}$, see eq. (7.96).

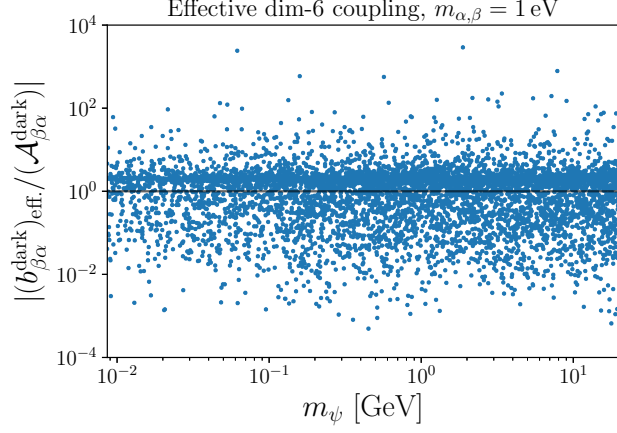


Figure 7.13: The effective charge radius $(b_{\beta\alpha}^{\text{dark}})_{\text{eff.}} = b_{\beta\alpha}^{\text{dark}} - \mathcal{A}_{\beta\alpha}^{\text{dark}}$ relative to the dark anapole only.

Overall, we find that the EM moments can receive large corrections (both positive and negative) from dark moments for millicharged particles with masses $m_{\psi} \sim 100$ MeV. The phase of this contribution is determined by the masses of the loop particles, the value of the Yukawa couplings, and the sign of the millicharge.

We conclude that, for the same dark sector parameters, a measurable difference between the Majorana- and Dirac scenario can emerge, as the effective charge radius has a different dependency on the P-violating couplings $c_{L/R}$ and $v_{L/R}$. Although we focused here on the dark moments, the findings of this section are more general and applicable to other models. In particular, correctly differentiating the effective charge radius (or effective anapole moment) from the canonical one is essential in interpreting experimental results.

Chapter 8

Summary and conclusions

Summary

Despite decades of experimental and theoretical efforts, the nature of DM remains one of the big open questions in particle physics, astrophysics, and cosmology.

In this thesis, we explored the scenario of electromagnetically interacting neutral spin-1/2 fermions, focusing on DM candidates and neutrinos. After introducing the observational evidence for DM, various production mechanisms, and current search strategies in chapter 2, we detailed in chapter 3 the model-independent one-loop calculation of all EM interactions of generic neutral spin-1/2 fermions for scalar- and vector-mediated t -channel interactions, including the transition moments. We resorted to evaluating the diagrams in the background Feynman gauge to obtain UV-convergent and gauge-independent expressions for the loops containing vector bosons. We found that in these classes of models, the fermions can possess electric- and magnetic dipole moments, charge radii, and anapole moments. These EM moments can be expressed as a product of the Yukawa coupling parameters of the UV Lagrangian and the loop functions encompassing all kinematic information. This factorization motivated our study of the loop functions individually for various phenomenologically relevant scenarios, including the diagonal case, large hierarchies between the external particles and internal states, and a large hierarchy between the two neutral fermions. Hereby, we provided relatively compact analytical expressions for these cases.

The diagonal EM moments can lead to elastic scattering events of DM particles with targets in direct detection facilities. In chapter 4, we reviewed the non-relativistic effective field theory, which allows for a model-independent study of direct detection phenomenology, and we particularized this formalism to the effective field theory of electromagnetically interacting DM. We calculated the rate matrices for XENON1T, LUX-ZEPLIN, DarkSide-50, and PICO-60, which serve as a model-independent tool for examining the interplay of different EM moments and their interference effects and used them to derive exclusion limits on the EM moments. Our findings indicate that considering experiments with different targets improves the combined experimental reach on the interfering EM moments. For individual

experiments, including the interference terms leads to conservative exclusion limits, which are weaker than those derived following the standard approach, in which only one operator is non-zero at a time.

If DM is a Majorana fermion, the only non-zero diagonal EM moment is the anapole moment. An archetypical Majorana WIMP candidate is the lightest neutralino in supersymmetric extensions of the SM. Using the model-independent results, we calculated the anapole moment of the lightest neutralino in chapter 5 for some limiting scenarios and within the entire MSSM. We found that the anapole moment can be reasonably enhanced for light scalars in the spectrum. However, in split-SUSY scenarios—where the scalar particles are heavy—the prediction falls one to two orders of magnitude below the experimental reach.

Next, in chapter 6, we examined a Dirac DM toy model consisting of two scalar t -channel mediators coupling to the τ -lepton. In this model, the DM particle can possess up to four EM moments. We used the previously introduced rate matrices to obtain limits on the UV parameter space. Since direct detection experiments are sensitive to the electric dipole operator, we found that the CP-violating parameter in the toy model faces relatively strong constraints. Further, we used a minimized signal rate to obtain conservative exclusion limits, finding that even in this scenario, the direct detection experiments probe a significant part of the parameter space, complementing collider studies. Finally, we analyzed the impact on the thermal relic, assuming standard freeze-out production for the electromagnetically interacting DM particle. The direct detection limits also yield potent constraints on this UV parameter space; the entire parameter space is excluded for the benchmark scenario with maximal CP violation.

Lastly, in chapter 7, we explored the application of the model-independent formulas to neutrinos. We revisited the predictions within the (minimally extended) SM for Dirac- and Majorana neutrinos and calculated the contributions to the EM moments in extensions of the SM, such as from a Higgs triplet, a left-right symmetric model, the R -parity conserving and R -parity violating MSSM, leptoquarks, and a dark sector. In all models except the dark sector, the additional contributions are typically suppressed by the large mass scale of new particles. The dark photon model evades these constraints, as all loop particles are millicharged dark sector particles. We found that for millicharged particles satisfying current constraints, the effective anapole moments can receive significant contributions, potentially resulting in an enhancement or suppression of the experimentally accessible neutrino anapole moment.

Conclusions

The analytical formulas for the EM moments of neutral spin-1/2 fermions offer a model-independent toolkit for calculating the EM moment matrix within various models. In this dissertation, we focused on the diagonal elements of this matrix and discussed their role in the DM direct detection phenomenology. The systematic EFT approach we followed is compelling, both in studying the EFT of electromagnetically interacting DM and in light of complete UV theories in which these EM moments are generated. Although we focused on relatively simple models, the underlying approach and its strengths can be used in more elaborate setups.

Further future avenues include the discussion of multicomponent DM models, for which inelastic scattering events may occur via the transition moments, resulting in distinct signatures in direct detection facilities or neutron star environments. In particular, for the Majorana scenario, a natural hierarchy between elastic and inelastic processes emerges, as the anapole operator exclusively governs the elastic processes, whereas the transition moments can be non-zero. For both Dirac- or Majorana candidates, these transition dipole moments can further lead to radiative decays, which result in monochromatic gamma-ray lines that could be detectable in indirect searches. Finally, the mediator particles generating the EM moments via the loop diagrams might be produced at particle colliders. Therefore, EM moments may be observed directly or indirectly through all three primary methods of non-gravitational DM searches, and the general formulas provided in this dissertation can bridge between the effective field theory and UV models to combine these search strategies.

Albeit we focused on the scenario of spin-1/2 fermions, the presented mapping between the experiment and theory could be generalized to higher-spin particles and allow for a systematic study of EM properties of particles with arbitrary spins, in particular, in terrestrial direct detection laboratories. Similarly, the calculation of the EM moments themselves could be generalized to allow for particles with different spins as external states or to calculate corrections beyond the one-loop level.

As discussed in-depth for neutrinos, our formulas can be applied to particles beyond DM candidates. Due to recent experimental advancements proving the capability of DM experiments to serve as solar neutrino telescopes, the effective anapole moment of neutrinos is expected to be tested within the foreseeable future. Investigating their EM properties could help uncover the theoretically important questions of whether neutrinos are Dirac- or Majorana fermions. Should experiments detect signatures consistent with additional EM interactions or identify an effective anapole moment that diverges from the predictions of the SM, the general formulas presented in this thesis offer a framework for interpreting these results within the context of specific UV models.

Appendix A

Derivation of exclusion limits

A.1 XENON1T, PICO-60 and LZ

For the statistical treatment of deriving the exclusion limits of XENON1T, PICO-60, and LZ, we follow the approach outlined in ref. [279]. We take the Poissonian likelihood

$$\mathcal{L} = \frac{1}{N_{\text{obs}}!} (N_{\text{sig}} + N_{\text{bck}})^{N_{\text{obs}}} \exp(-(N_{\text{sig}} + N_{\text{bck}})), \quad (\text{A.1})$$

where N_{obs} is the observed number of events, N_{bck} the reported background events, and N_{sig} is the number of events due to DM, see table A.1. The χ^2 distribution reads

$$\chi^2 = -2 \log(\mathcal{L}) = 2(N_{\text{sig}} + N_{\text{bck}} - N_{\text{obs}} \log(N_{\text{sig}} + N_{\text{bck}}) + \log(N_{\text{obs}}!)), \quad (\text{A.2})$$

with minimum

$$\chi_{\text{min.}}^2 = \begin{cases} 2(N_{\text{obs}} - N_{\text{obs.}} \log(N_{\text{obs}}) + \log(N_{\text{obs}}!)) & \text{if } N_{\text{sig}} > 0 \\ 0 & \text{else} \end{cases}. \quad (\text{A.3})$$

We then solve

$$\chi^2 - \chi_{\text{min.}}^2 = n_{\text{cl } 90\%} \quad (\text{A.4})$$

numerically for a model parameter such as an EM moment M for the EFT discussion in chapter 4, or the mass-splitting η for the t -channel toy model discussed in chapter 6. In the above equation, $n_{\text{cl } 90\%} = 2.71$ if the experiment observed at least one event, and $n_{\text{cl } 90\%} = 4.6$ if they reported zero due to the increase in the number of degrees of freedom [279].

The χ^2 distribution can be approximated via the polynomial

$$\chi^2 \simeq a_{\mathcal{E}} N_{\text{sig}}^2 + b_{\mathcal{E}} N_{\text{sig}} + c_{\mathcal{E}}, \quad (\text{A.5})$$

with minimum

$$\chi_{\text{min}}^2 = \begin{cases} c_{\mathcal{E}} - b_{\mathcal{E}}^2/(4a_{\mathcal{E}}) & \text{if } N_{\text{sig}} > 0 \\ 0 & \text{else} \end{cases}, \quad (\text{A.6})$$

Experiment	N_{obs}	N_{bkg}
XENON1T (NR)	14	7.36
XENON1T (Migdal)	49	0
LZ	0	0
PICO-60 (1st bin)	3	1
PICO-60 (2nd bin)	0	0

Table A.1: Observed events and the background prediction for the experiments described in this section. The values for XENON1T (NR) and PICO-60 are taken from ref. [279], for LZ from ref. [301] and for XENON1T (Migdal) from ref. [526].

Experiment	$a_{\mathcal{E}}$	$b_{\mathcal{E}}$	$c_{\mathcal{E}}$
XENON1T (NR)	0.09873702	-1.33278654	8.87456345
LZ	0	2	0
PICO-60 (1st bin)	0.17200563	-0.63312258	3.6519904
PICO-60 (2nd bin)	0	2	0

Table A.2: Fit parameters $\{a_{\mathcal{E}}, b_{\mathcal{E}}, c_{\mathcal{E}}\}$ for the quadratic approximation of the likelihood functions.

where the parameters $\{a_{\mathcal{E}}, b_{\mathcal{E}}, c_{\mathcal{E}}\}$ are obtained by fitting the full distribution in the region of interest and are summarized in table A.2. This approximation turns out to be extremely useful to calculate the conservative limit on the Wilson coefficients, both for individual experiments and for their combination; see refs. [278, 279, 525] for more details. We follow their approach in calculating the conservative limits on the individual EM moments presented in fig. 4.6.

We present the likelihood functions in fig. A.1; for the figure in the right panel, we set $\chi^2 = 0$ if $N_{\text{sig}} < N_{\text{obs}} - N_{\text{bkg}}$, corresponding to the upper limit on the DM signal rate.

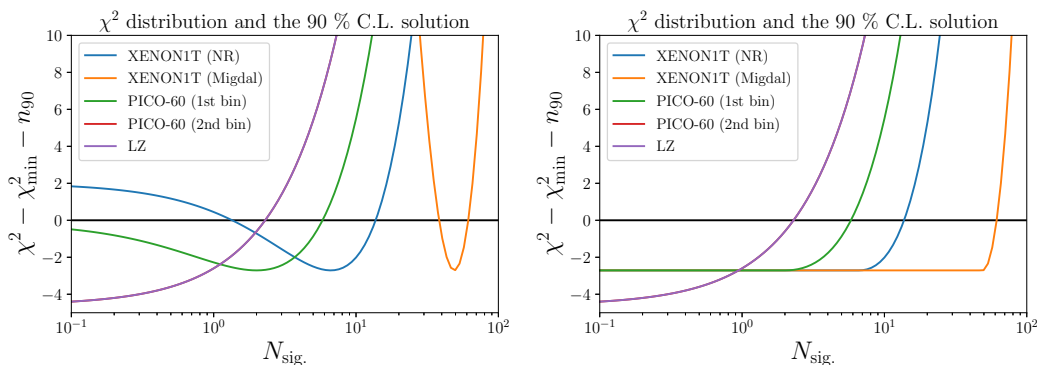


Figure A.1: Likelihood test statistic to determine the 90% C.L. exclusion limit on a given prediction for the signal rate, indicated by the intersections with the horizontal line. The likelihood distributions in the left panel result in upper- and lower limits. As we are not interested in the lower limit (*i.e.* the given signal count explains the experimental data at 90% C.L.), we use the likelihoods shown in the right panel, where only the upper limits are determined.

A.2 DarkSide-50

For the DarkSide-50 experiment, we follow the background subtraction approach [303], for which the likelihood for the standard model-independent analysis can be written as [527]

$$-2\mathcal{L} = \sum_{\text{bins } i=1}^9 \frac{(\sigma S_i + \rho b_i - x_i)^2}{\sigma_i^2}, \quad (\text{A.7})$$

where σS_i is the DM signal count, ρb_i the background, x_i the reported energy spectrum, and σ_i the associated deviation (see table A.3 for the data). The coefficients σ and ρ are free parameters.¹ Using the above likelihood function, we define the profile likelihood [527]

$$-2\mathcal{L} - (-2\mathcal{L})_{\min} = n^2, \quad (\text{A.8})$$

with $n = 1.28$ for the 90% C.L. bound. Here, $(-2\mathcal{L})_{\min}$ is obtained by numerically minimizing $-2\mathcal{L}$ with respect to σ and ρ .

In our specific setup, the DM signal count for each bin, $\mathcal{N}_{\text{sig}}^i$, is a function of the DM mass m_χ , the mass-splitting $\eta - 1 = (m_S - m_\chi)/m_\chi$ between DM and the scalar S , and the two angles $\sin\theta$ and $\sin\phi_{\text{CP}}$ parameterizing P- and CP violation,

¹However, σ may be identified with the DM-nucleon cross section in the standard analysis.

respectively. We can formulate eq. (A.7) as

$$-2\mathcal{L} = \sum_{\text{bins } i=1}^9 \frac{(\mathcal{N}_{\text{sig}}^i(m_\chi, \eta, \sin \theta, \sin \phi_{\text{CP}}) + \rho b_i - x_i)^2}{\sigma_i^2}, \quad (\text{A.9})$$

where we sum over all bins. The signal rate for each bin is calculated as

$$\mathcal{N}_{\text{sig}}^i(m_\chi, \eta, \sin \theta, \sin \phi_{\text{CP}}) = \sum_{j,k=1}^4 v_j \mathbb{N}_{jk}^i v_k, \quad (\text{A.10})$$

with $\mathbf{v} = (\mu_\chi, d_\chi, \mathcal{A}_\chi, b_\chi)$, and \mathbb{N}^i are the rate matrices introduced in section 4.3.1.

The calculation of $(-2\mathcal{L})_{\text{min}}$ needed for the evaluation of eq. (A.8) is not trivial for the derivation of exclusion limits for the toy model of chapter 6, as we dynamically subtract the background via the nuisance parameter ρ .

While for the benchmark analysis for fixed $\sin \theta$ and $\sin \phi_{\text{CP}}$ we can minimize with respect to η and ρ , for the analysis using the minimized signal rate \mathcal{N}_{min} the situation is more involved. For fixed m_χ , we are trying to minimize the likelihood w.r.t. η , $\sin \theta$, $\sin \phi_{\text{CP}}$ and ρ subject to the condition of minimizing the total signal rate

$$\mathcal{N}^{\text{tot}} = \sum_i \mathcal{N}_{\text{sig}}^i(m_\chi, \eta, \sin \theta, \sin \phi_{\text{CP}}) \quad (\text{A.11})$$

w.r.t. the angles. We can simplify this numerical minimization by noting that the electric dipole moment, controlled by $\sin \phi_{\text{CP}}$, does not interfere with the other operators. Therefore, the minimization will always yield $\sin \phi_{\text{CP}}^{\text{min}} = 0$. Meanwhile, the dependency for $\theta_{\text{min}}(m_\chi, \eta)$ is not trivial as can be seen in the right panel of fig. A.2, where we show $\sin \theta_{\text{min}}$ as function of m_χ and $\eta - 1$ obtained by minimizing the signal rate with respect to the angles. For small mass-splittings, $\sin \theta_{\text{min}}$ becomes independent of η .

To find the conservative exclusion limit using the minimized signal rate, we followed the following two approaches:

Approach A:

Whenever we evaluate eq. (A.9), we make the following replacement:

$$\mathcal{N}_{\text{sig}}^i(m_\chi, \eta, \sin \theta, \sin \phi_{\text{CP}}) \rightarrow \mathcal{N}_{\text{sig}}^i(m_\chi, \eta, \sin \theta_{\text{min}}, \sin \phi_{\text{CP}}^{\text{min}}), \quad (\text{A.12})$$

where the angles are determined by dynamically minimizing eq. (A.11) with respect to the angles while keeping the other parameters fixed. This is akin to the solutions for the angles presented in the right panel of fig. A.2, corresponding to a signal rate with dominant EM moments as shown in the left panel of fig. A.2. This process can be numerically costly, as eq. (A.11) is minimized during each evaluation of the multi-dimensional minimization of the likelihood function in eq. (A.9).

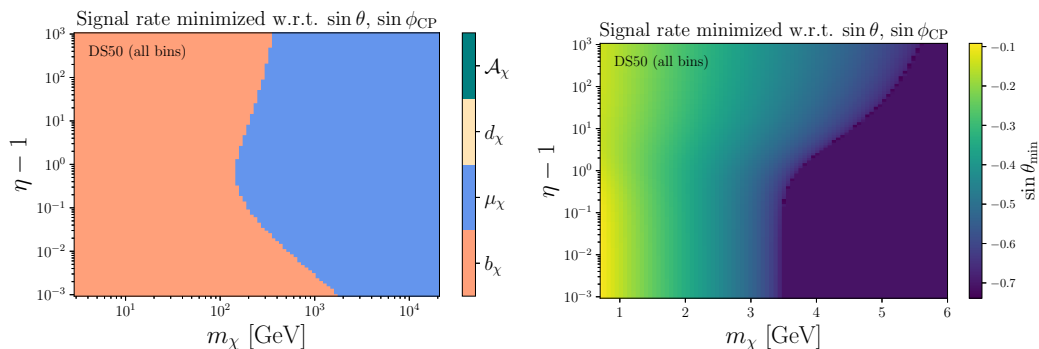


Figure A.2: Dominant EM moment in the minimized total rate (summed over all bins) for the DS50 experiment (*left*), and the corresponding solution for $\sin \theta_{\min}$ (*right*). We note that for $\eta \lesssim 2$, θ_{\min} becomes independent of η . For larger mass-splittings, there is a dependency on η in the small mass-region $3 \text{ GeV} \lesssim m_\chi \lesssim 6 \text{ GeV}$. The non-trivial shape is because the dominant contribution is the charge radius, and the appearing loop function \mathcal{F}_5^S changes sign at this threshold.

Approach B:

Alternatively, we can use that fact the experiment is sensitive to values of η in the same ballpark for which θ_{\min} does not depend on η . Therefore, we can take the one-dimensional solution of $\sin \theta_{\min}$ for $\eta = 1.1$ shown in the right panel of fig. A.3 and interpolate the data, leading to $\theta_{\min}(m_\chi)$. The corresponding total signal rate at the DS50 experiment is provided in the left panel of fig. A.3. Since both angles are expressed semi-analytically in this approach, the multi-dimensional minimization of the likelihood function in eq. (A.9) is numerically more efficient than in approach A.

Both approaches, A) dynamically finding the minimum and B) using the one-dimensional interpolation, lead to identical exclusion limits for the scenarios considered here.

Numerically minimizing eq. (A.9) with respect to η and ρ gives us its minimum, as well as the corresponding η_{\min} and ρ_{\min} , for which $(-2\mathcal{L})_{\min} = -2\mathcal{L}(\eta_{\min}, \rho_{\min})$. This ρ_{\min} is then used in the likelihood function, following the background subtraction procedure.

Then, the 90% C.L. exclusion limit on η for a fixed m_χ is obtained by solving the equation

$$-2\mathcal{L}(\eta; \rho = \rho_{\min}) - (-2\mathcal{L})_{\min} - n^2 = 0 \quad (\text{A.13})$$

for η . The angles are either fixed from the benchmark scenario considered or determined via approaches A) or B) outlined above. This way, we obtained the DS50 exclusion limits shown in fig. 6.4.

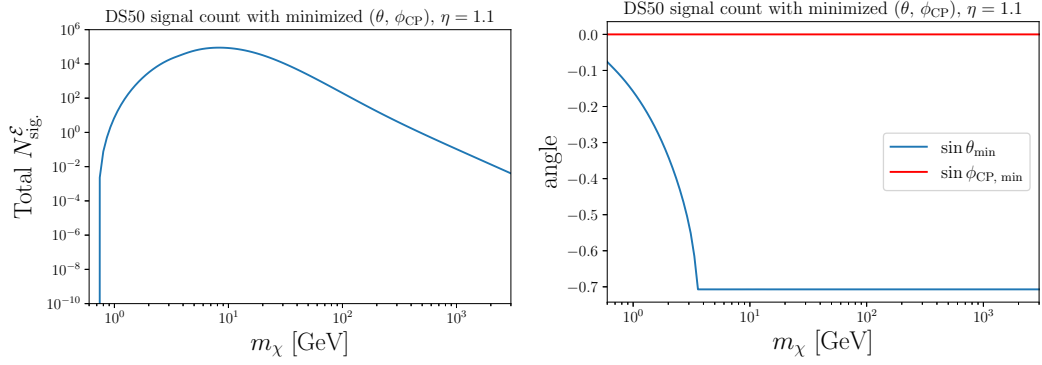


Figure A.3: Minimized total rate (summed over all bins) for the DS50 experiment (*left*) for fixed $\eta = 1.1$, and the corresponding solution for $\sin \theta_{\text{min}}$ and $\sin \phi_{\text{CP}}^{\text{min}}$ (*right*).

# Bin	x_i	σ_i	b_i
1	251.9933	15.87429	119.706074
2	226.9883	15.06613	127.083462
3	197.9644	14.06998	152.893184
4	1703.821	41.27737	1638.54481
5	2587.918	50.87158	2578.07507
6	3476.694	58.96349	3339.57099
7	4218.602	64.95076	4331.65119
8	5478.566	74.01733	5336.48678
9	7779.372	88.20074	6157.69737

Table A.3: DS50 reported events x_i , background estimate b_i and uncertainty σ_i for the i 'th bin. Data taken from Fig. 7 of ref. [303]; see also ref. [527].

Appendix B

Analytical expressions for the loop functions of the EM moments

B.1 The general loop functions

In this appendix, we present analytic expressions for the loop functions we found in the one-loop calculation of the EM moments for neutral fermions χ_1 and χ_2 with masses m_{χ_1} and m_{χ_2} , respectively.

The result is given in terms of the scalar three-point Passarino-Veltman function [528]

$$C_0(p_1^2, q^2, p_2^2, m_0, m_1, m_2) = \frac{1}{i\pi^2} \int d^n k \frac{1}{(k^2 - m_0^2)} \frac{1}{(k + p_1)^2 - m_1^2} \frac{1}{(k + p_2)^2 - m_2^2} \quad (\text{B.1})$$

and

$$\tilde{F}(\xi, \mu, \eta) = \frac{\sqrt{\lambda(\xi^2, \eta^2, \mu^2)}}{\xi^2} \log \left(\frac{\mu^2 + \eta^2 - \xi^2 + \sqrt{\lambda(\xi^2, \eta^2, \mu^2)}}{2\eta\mu} + i\epsilon \right) \quad (\text{B.2})$$

$$= \frac{2\sqrt{\lambda(\xi^2, \eta^2, \mu^2)}}{\xi^2} \operatorname{arctanh} \left(\frac{\sqrt{\lambda(\xi^2, \eta^2, \mu^2)}}{(\eta + \mu)^2 - \xi^2} + i\epsilon \right), \quad (\text{B.3})$$

where

$$\lambda(a, b, c) = a^2 + b^2 + c^2 - 2ab - 2ac - 2bc \quad (\text{B.4})$$

is the Källén function [264].

Further, for the presentation of the general results, we parameterize the loop functions $\mathcal{F}_i^{S/V}$ and $\mathcal{G}_i^{S/V}$ as

$$\mathcal{F}_i^{S/V}(\mu, \eta, \xi) = \frac{\bar{\mathcal{F}}_i^{S/V}(\mu, \eta, \xi)}{m_{\chi_1}^{(i)}(1 + \xi)^2} \quad \text{and} \quad \mathcal{G}_i^{S/V}(\mu, \eta, \xi) = \frac{\bar{\mathcal{G}}_i^{S/V}(\mu, \eta, \xi)}{m_{\chi_1}^{(i)}(1 + \xi)^2}, \quad (\text{B.5})$$

where we defined $m_{\chi_1}^{(\mu)} = m_{\chi_1}^{(d)} = m_{\chi_1}$, $m_{\chi_1}^{(\mathcal{A})} = m_{\chi_1}^{(b)} = m_{\chi_1}^2$ and $\xi = m_{\chi_2}/m_{\chi_1}$. In the following, we report the analytical results for these dimensionless loop functions $\bar{\mathcal{F}}_i^{S/V}$ and $\bar{\mathcal{G}}_i^{S/V}$.

Scalar loop functions

Magnetic dipole moment:

$$\begin{aligned} \bar{\mathcal{F}}_\mu^S(\mu, \eta, \xi) = \frac{1}{\xi(\xi-1)} & \left\{ \xi^2 \left[\tilde{F}(\xi, \mu, \eta) - \tilde{F}(1, \mu, \eta) \right] \right. \\ & + (1 - \xi^2) \left[\xi + (\eta^2 - \mu^2) \log\left(\frac{\mu}{\eta}\right) + m_{\chi_1}^2 \xi \times \right. \\ & \left. \left. \times \left(\eta^2 C_0(0, m_{\chi_1}^2, m_{\chi_1}^2 \xi^2, m_{\chi_1} \eta, m_{\chi_1} \eta, m_{\chi_1} \mu) + (\mu \leftrightarrow \eta) \right) \right] \right\}, \end{aligned} \quad (\text{B.6})$$

and

$$\bar{\mathcal{G}}_\mu^S(\mu, \eta, \xi) = -m_{\chi_1}^2 \mu (1 + \xi)^2 C_0(0, m_{\chi_1}^2, m_{\chi_1}^2 \xi^2, m_{\chi_1} \mu, m_{\chi_1} \mu, m_{\chi_1} \eta). \quad (\text{B.7})$$

Electric dipole moment:

$$\begin{aligned} \bar{\mathcal{F}}_d^S(\mu, \eta, \xi) = i \frac{(1 + \xi)}{\xi(1 - \xi)^2} & \left\{ \xi^2 \left[\tilde{F}(\xi, \mu, \eta) - \tilde{F}(1, \mu, \eta) \right] \right. \\ & - (1 - \xi^2) \left[\xi + (\mu^2 - \eta^2) \log\left(\frac{\mu}{\eta}\right) + m_{\chi_1}^2 \xi \times \right. \\ & \left. \left. \times \left(\eta^2 C_0(0, m_{\chi_1}^2, m_{\chi_1}^2 \xi^2, m_{\chi_1} \eta, m_{\chi_1} \eta, m_{\chi_1} \mu) + (\mu \leftrightarrow \eta) \right) \right] \right\}, \end{aligned} \quad (\text{B.8})$$

and

$$\bar{\mathcal{G}}_d^S(\mu, \eta, \xi) = i \bar{\mathcal{G}}_\mu^S(\mu, \eta, \xi). \quad (\text{B.9})$$

Anapole moment:

$$\begin{aligned} \bar{\mathcal{F}}_A^S(\mu, \eta, \xi) = \frac{1}{(\xi-1)^3} & \left\{ (1 + \xi) \left[(1 + 2\xi) \tilde{F}(1, \mu, \eta) - \xi(2 + \xi) \tilde{F}(\xi, \mu, \eta) \right] \right. \\ & + \frac{1 - \xi}{\xi} \left[3\xi(1 + \xi)^2 + \kappa_1^\xi \log\left(\frac{\mu}{\eta}\right) \right. \\ & + \kappa_2^\xi C_0(0, m_{\chi_1}^2, m_{\chi_1}^2 \xi^2, m_{\chi_1} \eta, m_{\chi_1} \eta, m_{\chi_1} \mu) \\ & \left. \left. + \kappa_3^\xi C_0(0, m_{\chi_1}^2, m_{\chi_1}^2 \xi^2, m_{\chi_1} \mu, m_{\chi_1} \mu, m_{\chi_1} \eta) \right] \right\}, \end{aligned} \quad (\text{B.10})$$

with

$$\kappa_1^\xi = 2(\xi(\xi + 4) + 1)(\mu^2 - \eta^2) + (\xi - 1)^2 \xi, \quad (\text{B.11})$$

$$\kappa_2^\xi = m_{\chi_1}^2 \xi [2\eta^4 + 2\eta^2((\xi + 1)^2 - 2\mu^2) + 2\mu^4 - \mu^2(\xi + 1)^2 + \xi^3 + \xi], \quad (\text{B.12})$$

$$\kappa_3^\xi = m_{\chi_1}^2 \xi [2\eta^4 - 2\eta^2(2\mu^2 + \xi^2 + 1) + 2\mu^4 + \mu^2(\xi(3\xi + 2) + 3) + 2\xi^2], \quad (\text{B.13})$$

and

$$\bar{\mathcal{G}}_{\mathcal{A}}^S(\mu, \eta, \xi) = \frac{\mu}{\xi - 1} \left\{ 2 \log \left(\frac{\mu^2}{\eta^2} \right) + m_{\chi_1}^2 \left[(1 + 2\mu^2 - 2\eta^2 + \xi^2) \times \right. \right. \\ \left. \left. C_0(0, m_{\chi_1}^2, m_{\chi_1}^2 \xi^2, m_{\chi_1} \mu, m_{\chi_1} \mu, m_{\chi_1} \eta) - (\mu \leftrightarrow \eta) \right] \right\}. \quad (\text{B.14})$$

Charge radius:

$$\bar{\mathcal{F}}_b^S(\mu, \eta, \xi) = -\frac{1}{(1 - \xi)^2(1 + \xi)} \left\{ (\xi - 1) \left[(2\xi - 1)\tilde{F}(1, \mu, \eta) + (\xi - 2)\xi\tilde{F}(\xi, \mu, \eta) \right] \right. \\ \left. + \frac{(\xi + 1)}{\xi} \left[3\xi(1 - \xi)^2 + \kappa_4^\xi \log \left(\frac{\mu}{\eta} \right) \right] \right. \\ \left. + \kappa_5^\xi C_0(0, m_{\chi_1}^2, m_{\chi_1}^2 \xi^2, m_{\chi_1} \eta, m_{\chi_1} \eta, m_{\chi_1} \mu) \right. \\ \left. + \kappa_6^\xi C_0(0, m_{\chi_1}^2, m_{\chi_1}^2 \xi^2, m_{\chi_1} \mu, m_{\chi_1} \mu, m_{\chi_1} \eta) \right] \right\}, \quad (\text{B.15})$$

with

$$\kappa_4^\xi = 2(\xi(\xi - 4) + 1)(\eta^2 - \mu^2) + (\xi + 1)^2 \xi, \quad (\text{B.16})$$

$$\kappa_5^\xi = m_{\chi_1}^2 \xi [2\eta^4 + 2\eta^2((\xi - 1)^2 - 2\mu^2) + (\mu^2 + \xi)(2\mu^2 - \xi^2 - 1)], \quad (\text{B.17})$$

$$\kappa_6^\xi = m_{\chi_1}^2 \xi [2\eta^4 - 2\eta^2(2\mu^2 + \xi^2 + 1) + 2\mu^4 + \mu^2(\xi(3\xi - 2) + 3) + 2\xi^2], \quad (\text{B.18})$$

and

$$\bar{\mathcal{G}}_b^S(\mu, \eta, \xi) = -\mu \frac{(1 + \xi)}{(1 - \xi)^2} \left\{ 2 \log \left(\frac{\mu^2}{\eta^2} \right) + m_{\chi_1}^2 \left[(1 + 2\mu^2 - 2\eta^2 + \xi^2) \times \right. \right. \\ \left. \left. C_0(0, m_{\chi_1}^2, m_{\chi_1}^2 \xi^2, m_{\chi_1} \mu, m_{\chi_1} \mu, m_{\chi_1} \eta) - (\mu \leftrightarrow \eta) \right] \right\}. \quad (\text{B.19})$$

We present in figs. B.1 to B.3 a numerical evaluation of the loop functions for fixed mass splittings of $\xi = 1.1$, $\xi = 2$ and $\xi = 10$, respectively. Note that the numerical evaluation of the EM loop functions presented here can lead to a loss of precision due to non-exact numerical cancellations. For example, in fig. B.1 this can be seen from the unstable behavior of $|\mathcal{F}_{\mathcal{A}/b}^S|$ for large m_S/m_{χ_1} or large m_f/m_{χ_1} , resulting in non-continuous, divergent and thus unphysical behavior. From comparison with figs. B.2 and B.3, it becomes clear that this unphysical behavior relaxes the larger m_{χ_2} becomes. Therefore, it is advised to use analytical approximations of the loop functions for scenarios of large mass splittings.

Appendix B Analytical expressions for the loop functions of the EM moments

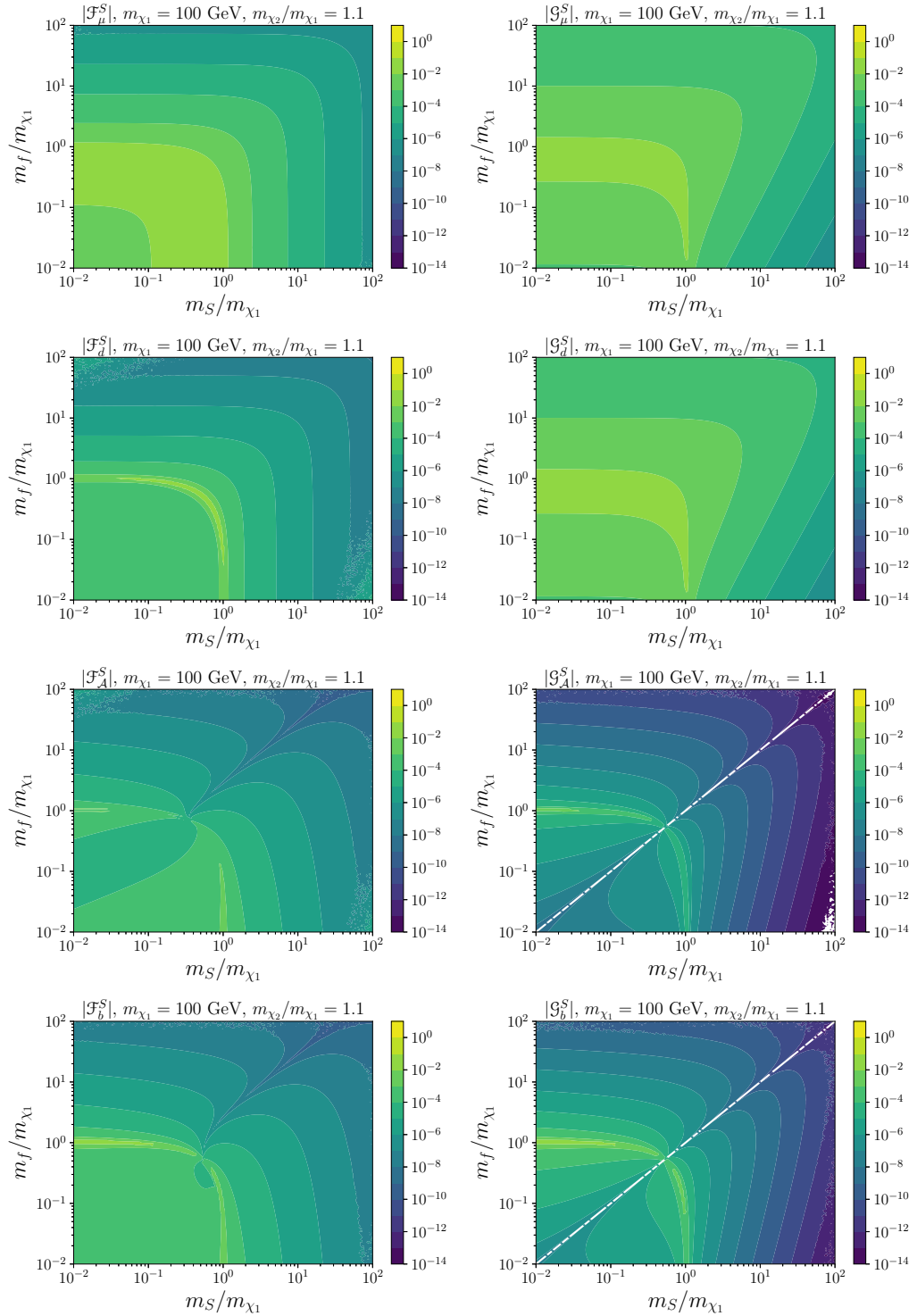


Figure B.1: Generic scalar loop functions for $m_{\chi_1} = 100$ GeV and $m_{\chi_2} = 1.1 \times m_{\chi_1}$.

B.1 The general loop functions

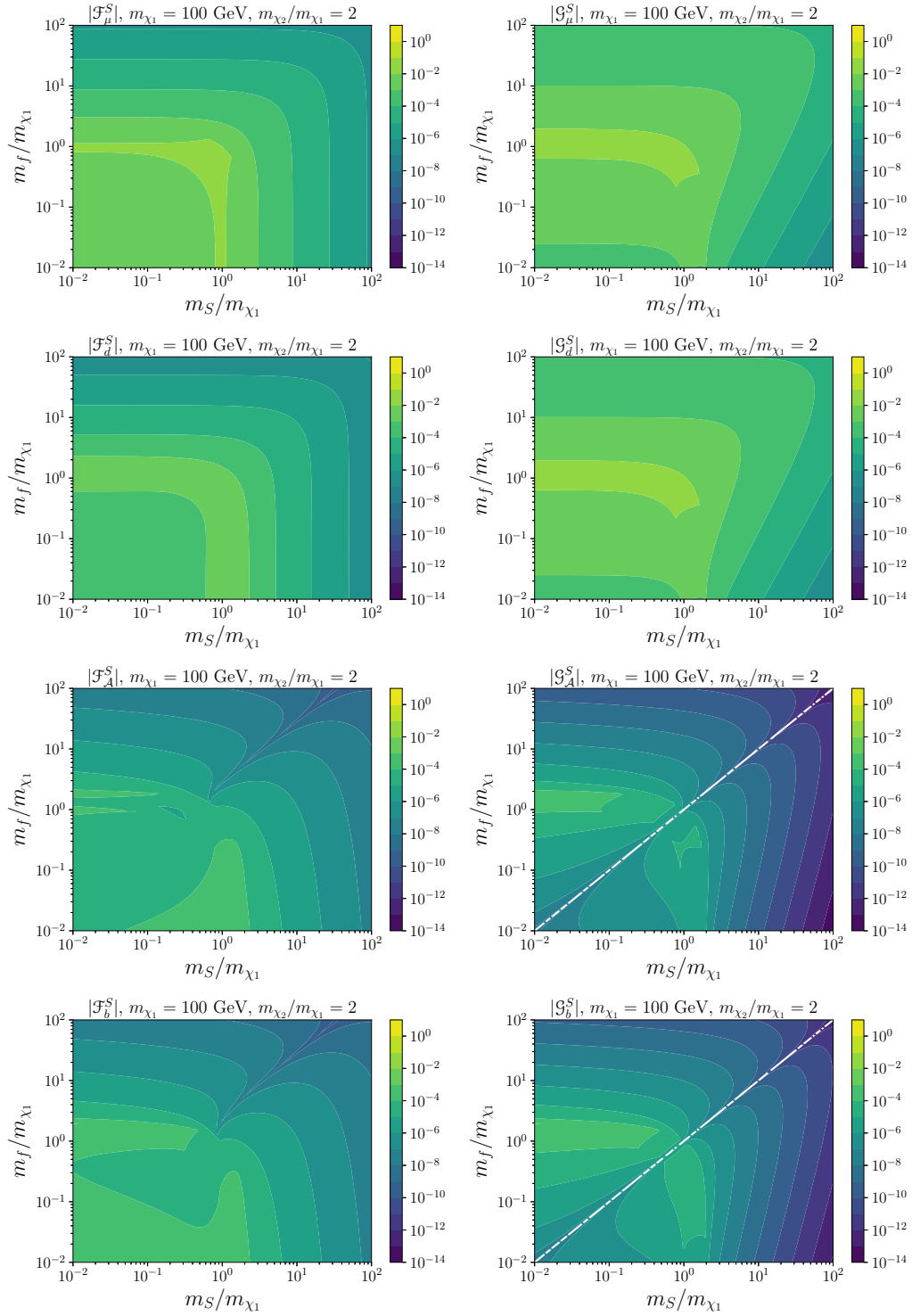


Figure B.2: Generic scalar loop functions for $m_{\chi_1} = 100$ GeV and $m_{\chi_2} = 2m_{\chi_1}$.

Appendix B Analytical expressions for the loop functions of the EM moments

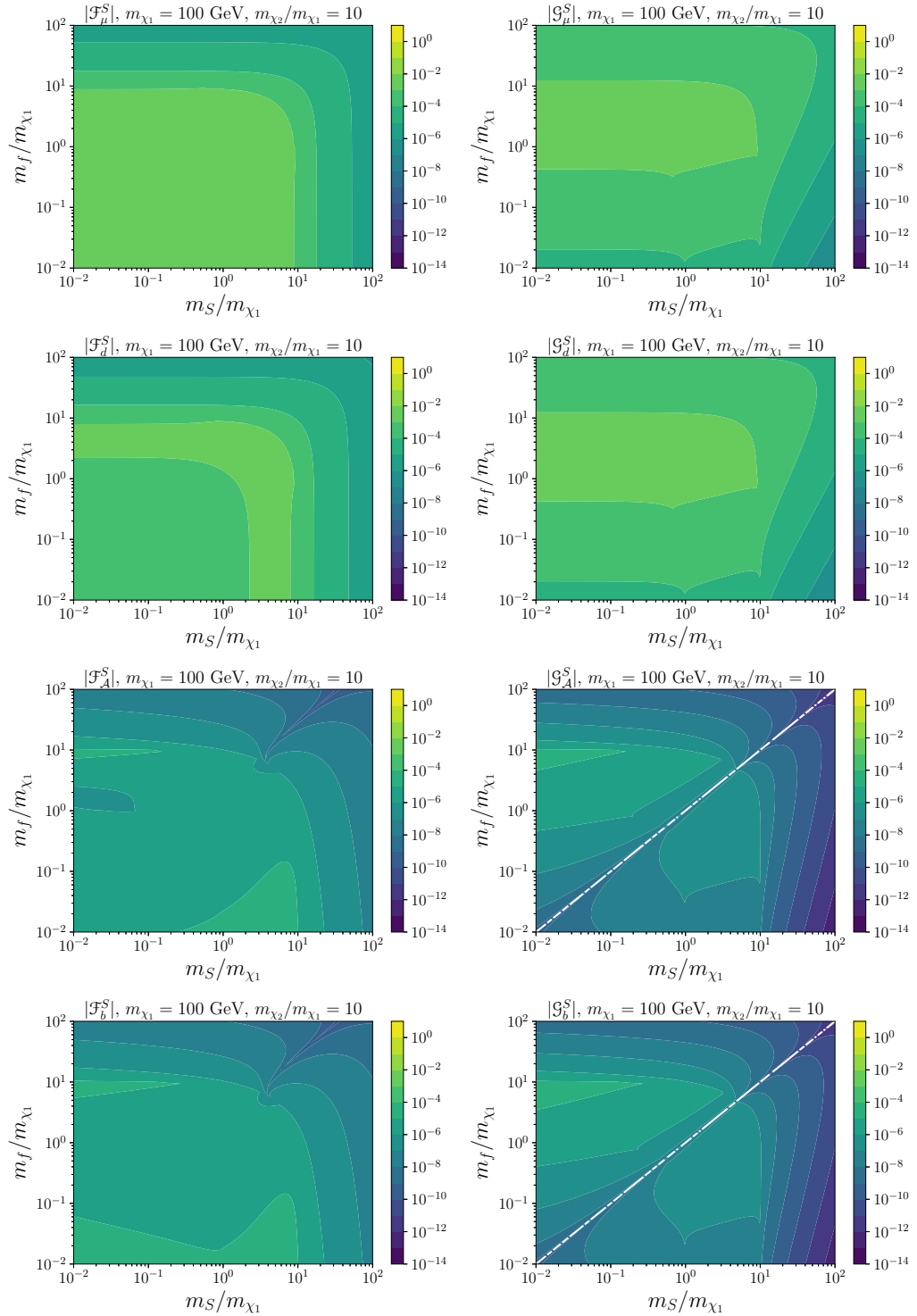


Figure B.3: Generic scalar loop functions for $m_{\chi_1} = 100$ GeV and $m_{\chi_2} = 10 \times m_{\chi_1}$.

Vector loop functions

Magnetic dipole moment:

$$\begin{aligned} \bar{\mathcal{F}}_\mu^V(\mu, \eta, \xi) = \frac{2}{\xi(\xi-1)} & \left\{ \xi^2 \left(-\tilde{F}(1, \mu, \eta) + \tilde{F}(\xi, \mu, \eta) \right) \right. \\ & + (\xi^2 - 1) \left[-\xi + (\eta^2 - \mu^2) \log\left(\frac{\eta}{\mu}\right) + m_{\chi_1}^2 \xi \times \right. \\ & \times \left(((1 + \xi^2) - \eta^2) C_0(0, m_{\chi_1}^2, m_{\chi_1}^2 \xi^2, m_{\chi_1} \eta, m_{\chi_1} \eta, m_{\chi_1} \mu) \right. \\ & \left. \left. - \mu^2 C_0(0, m_{\chi_1}^2, m_{\chi_1}^2 \xi^2, m_{\chi_1} \mu, m_{\chi_1} \mu, m_{\chi_1} \eta) \right) \right] \left. \right\}, \quad (\text{B.20}) \end{aligned}$$

and

$$\bar{\mathcal{G}}_\mu^V(\mu, \eta, \xi) = -4m_{\chi_1}^2 \mu (1 + \xi)^2 C_0(0, m_{\chi_1}^2, m_{\chi_1}^2 \xi^2, m_{\chi_1} \eta, m_{\chi_1} \eta, m_{\chi_1} \mu). \quad (\text{B.21})$$

Electric dipole moment:

$$\begin{aligned} \bar{\mathcal{F}}_d^V(\mu, \eta, \xi) = i \frac{2(1 + \xi)}{\xi(1 - \xi)^2} & \left\{ \xi^2 \left(\tilde{F}(1, \mu, \eta) - \tilde{F}(\xi, \mu, \eta) \right) \right. \\ & + (\xi^2 - 1) \left[-\xi + (\eta^2 - \mu^2) \log\left(\frac{\mu}{\eta}\right) \right. \\ & - m_{\chi_1}^2 \xi (\eta - \xi + 1) (\eta + \xi - 1) \times \\ & \quad \times C_0(0, m_{\chi_1}^2, m_{\chi_1}^2 \xi^2, m_{\chi_1} \eta, m_{\chi_1} \eta, m_{\chi_1} \mu) \\ & \left. \left. + \mu^2 C_0(0, m_{\chi_1}^2, m_{\chi_1}^2 \xi^2, m_{\chi_1} \mu, m_{\chi_1} \mu, m_{\chi_1} \eta) \right] \right\}, \quad (\text{B.22}) \end{aligned}$$

and

$$\bar{\mathcal{G}}_d^V(\mu, \eta, \xi) = -i \bar{\mathcal{G}}_\mu^V(\mu, \eta, \xi). \quad (\text{B.23})$$

Anapole moment:

$$\begin{aligned} \bar{\mathcal{F}}_A^V(\mu, \eta, \xi) = -\frac{2}{(1 - \xi)^3} & \left\{ -(1 + \xi)(1 + 2\xi) \tilde{F}(1, \mu, \eta) \right. \\ & + \xi(1 + \xi)(2 + \xi) \tilde{F}(\xi, \mu, \eta) \\ & + \frac{\xi - 1}{\xi} \left[3\xi(1 + \xi)^2 + \kappa_7^\xi \log\left(\frac{\mu}{\eta}\right) \right. \\ & + \kappa_8^\xi C_0(0, m_{\chi_1}^2, m_{\chi_1}^2 \xi^2, m_{\chi_1} \eta, m_{\chi_1} \eta, m_{\chi_1} \mu) \\ & \left. \left. + \kappa_9^\xi C_0(0, m_{\chi_1}^2, m_{\chi_1}^2 \xi^2, m_{\chi_1} \mu, m_{\chi_1} \mu, m_{\chi_1} \eta) \right] \right\}, \quad (\text{B.24}) \end{aligned}$$

with

$$\kappa_7^\xi = -2\eta^2(\xi(\xi + 4) + 1) + 2\mu^2(\xi(\xi + 4) + 1) + (\xi - 1)^2\xi, \quad (\text{B.25})$$

$$\begin{aligned} \kappa_8^\xi = m_{\chi_1}^2 \xi [2\eta^4 + 2\eta^2((\xi + 1)^2 - 2\mu^2) + 2\mu^4 \\ - \mu^2(\xi + 1)^2 + \xi^2(-\xi^2 + \xi + 2) + \xi - 1], \end{aligned} \quad (\text{B.26})$$

$$\kappa_9^\xi = m_{\chi_1}^2 \xi [2\eta^4 - 2\eta^2(2\mu^2 + \xi^2 + 1) + 2\mu^4 + \mu^2(\xi(3\xi + 2) + 3) + 2\xi^2], \quad (\text{B.27})$$

and

$$\begin{aligned} \bar{\mathcal{G}}_A^V(\mu, \eta, \xi) = \frac{4\mu}{\xi - 1} \left\{ 2 \log\left(\frac{\mu^2}{\eta^2}\right) + m_{\chi_1}^2 \left[(1 - 2\eta^2 + 2\mu^2 + \xi^2) \times \right. \right. \\ \left. \left. C_0(0, m_{\chi_1}^2, m_{\chi_1}^2 \xi^2, m_{\chi_1} \mu, m_{\chi_1} \mu, m_{\chi_1} \eta) - (\mu \leftrightarrow \eta) \right] \right\}. \end{aligned} \quad (\text{B.28})$$

Charge radius:

$$\begin{aligned} \bar{\mathcal{F}}_b^V(\mu, \eta, \xi) = -\frac{2}{(1 - \xi)^2(1 + \xi)} \left\{ (\xi - 1)(2\xi - 1) \tilde{F}(1, \mu, \eta) \right. \\ + (\xi - 1)(\xi - 2) \xi \tilde{F}(\xi, \mu, \eta) \\ + \frac{1 + \xi}{\xi} \left[3(1 - \xi)^2 \xi + \kappa_{10}^\xi \log\left(\frac{\mu}{\eta}\right) \right. \\ + \kappa_{11}^\xi C_0(0, m_{\chi_1}^2, m_{\chi_1}^2 \xi^2, m_{\chi_1} \eta, m_{\chi_1} \eta, m_{\chi_1} \mu) \\ \left. \left. + \kappa_{12}^\xi C_0(0, m_{\chi_1}^2, m_{\chi_1}^2 \xi^2, m_{\chi_1} \mu, m_{\chi_1} \mu, m_{\chi_1} \eta) \right] \right\}, \end{aligned} \quad (\text{B.29})$$

with

$$\kappa_{10}^\xi = 2\eta^2((\xi - 4)\xi + 1) - 2\mu^2((\xi - 4)\xi + 1) + \xi(\xi + 1)^2, \quad (\text{B.30})$$

$$\begin{aligned} \kappa_{11}^\xi = m_{\chi_1}^2 \xi \left[-2\eta^4 + 2\eta^2(2\mu^2 - (\xi - 1)^2) - 2\mu^4 + \mu^2(\xi - 1)^2 \right. \\ \left. + \xi^2(\xi^2 + \xi - 2) + \xi + 1 \right], \end{aligned} \quad (\text{B.31})$$

$$\kappa_{12}^\xi = m_{\chi_1}^2 \xi [2\eta^4 - 2\eta^2(2\mu^2 + \xi^2 + 1) + 2\mu^4 + \mu^2(\xi(3\xi - 2) + 3) + 2\xi^2], \quad (\text{B.32})$$

and

$$\bar{\mathcal{G}}_b^V = \frac{4\mu(\xi + 1)}{(\xi - 1)^2} \left\{ 2 \log\left(\frac{\mu^2}{\eta^2}\right) + m_{\chi_1}^2 \left[(1 - 2\eta^2 + 2\mu^2 + \xi^2) \times \right. \right. \quad (\text{B.33})$$

$$\left. \left. C_0(0, m_{\chi_1}^2, m_{\chi_1}^2 \xi^2, m_{\chi_1} \mu, m_{\chi_1} \mu, m_{\chi_1} \eta) - (\mu \leftrightarrow \eta) \right] \right\}. \quad (\text{B.34})$$

B.1 The general loop functions

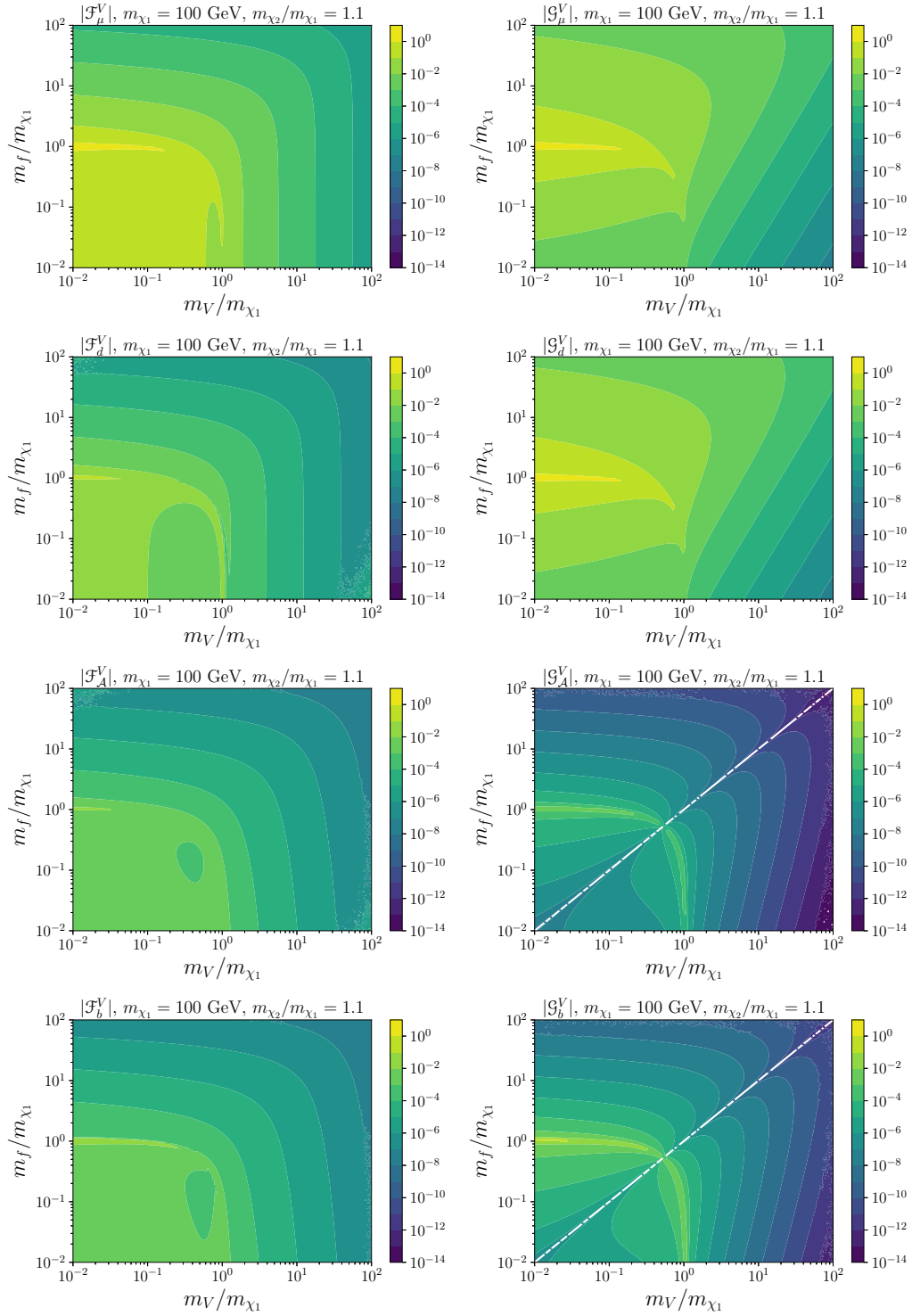


Figure B.4: Generic vector loop functions for $m_{\chi_1} = 100 \text{ GeV}$ and $m_{\chi_2} = 1.1 \times m_{\chi_1}$.

Appendix B Analytical expressions for the loop functions of the EM moments

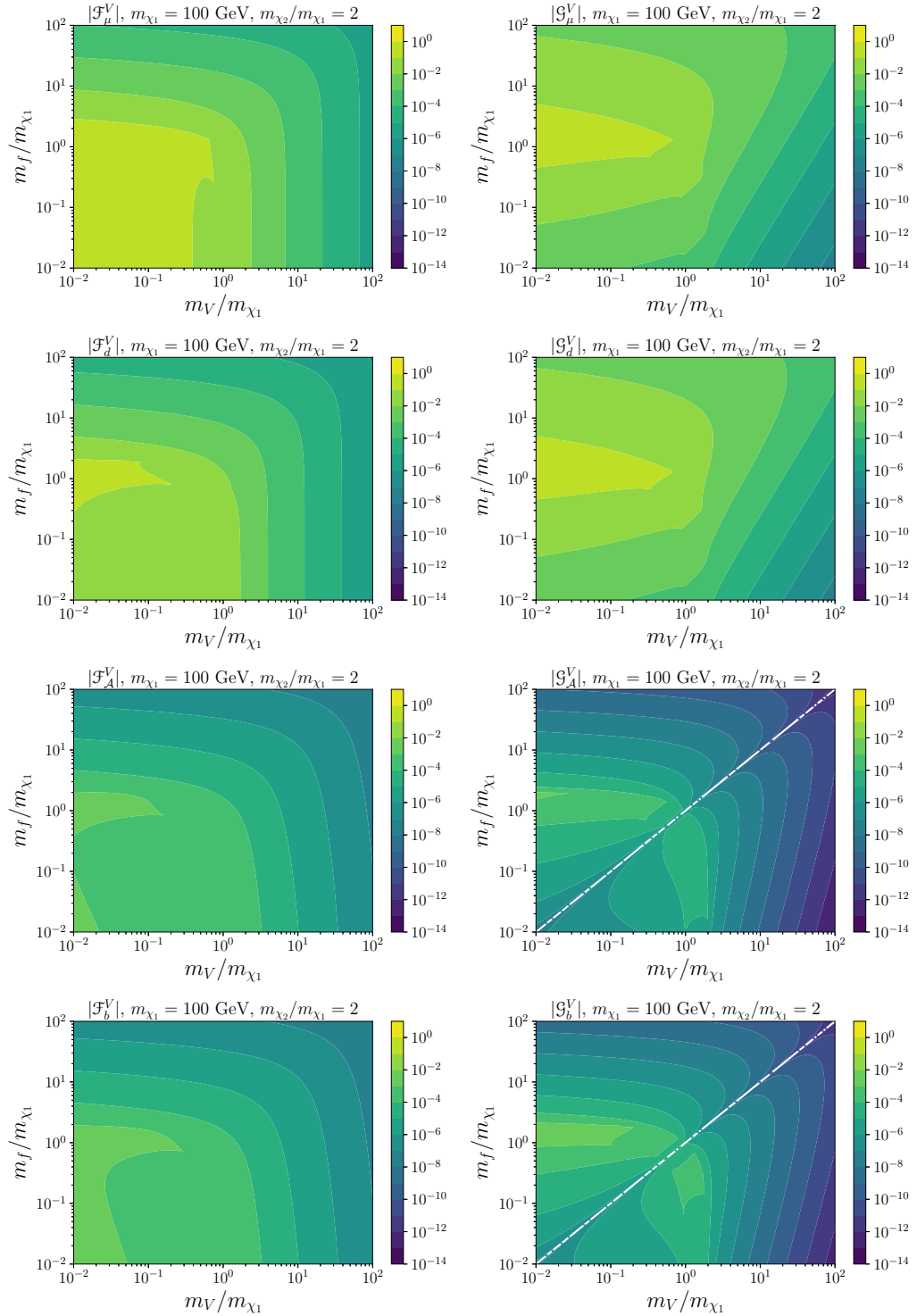


Figure B.5: Generic vector loop functions for $m_{\chi_1} = 100$ GeV and $m_{\chi_2} = 2m_{\chi_1}$.

B.1 The general loop functions

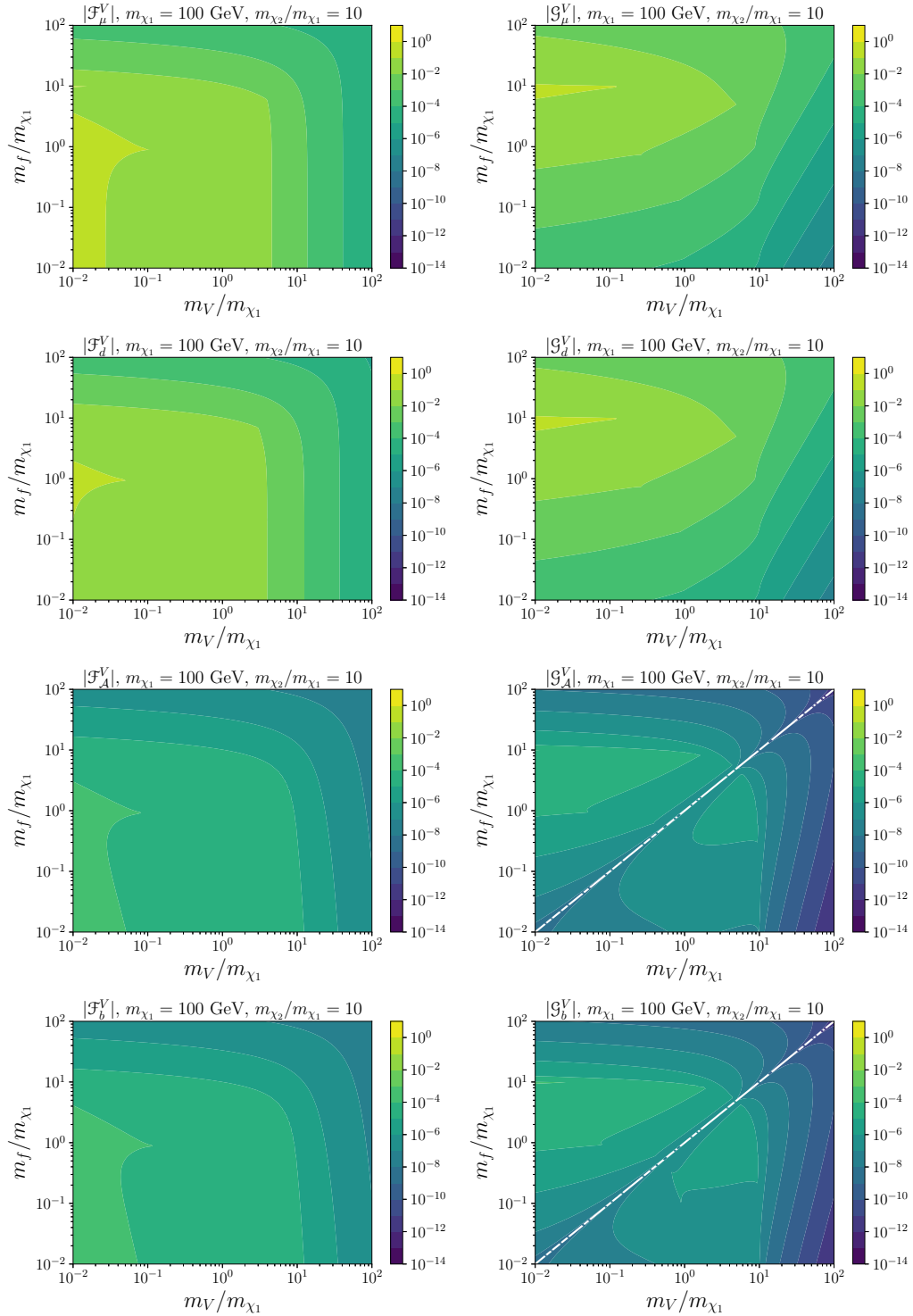


Figure B.6: Generic vector loop functions for $m_{\chi_1} = 100$ GeV and $m_{\chi_2} = 10 \times m_{\chi_1}$.

B.2 Limit of identical external states

Here, we summarize the loop functions for the diagonal case with $m_{\chi_1} = m_{\chi_2} \equiv m_\chi$, *i.e.* when $\xi = 1$. We introduce

$$\Delta = \lambda(1, \eta^2, \mu^2) = (\mu^2 - \eta^2 + 1)^2 - 4\mu^2, \quad (\text{B.35})$$

and

$$f(\mu, \eta) = \frac{1}{\Delta} \tilde{F}(1, \mu, \eta) = \frac{1}{\sqrt{\Delta}} \operatorname{arctanh} \left(\frac{\sqrt{\Delta}}{\eta^2 + \mu^2 - 1} \right). \quad (\text{B.36})$$

Note that expressions for the EM moments summarized here agree with the results presented section 3.2.3. Still, for completeness, we will provide them here again in the canonical normalization.

Scalar loop functions

Magnetic dipole moment:

$$\mathcal{F}_\mu^S = -\frac{1}{m_\chi} \left[(\Delta + \eta^2 + \mu^2 - 1) f(\mu, \eta) + (\eta^2 - \mu^2) \log \left(\frac{\mu}{\eta} \right) + 1 \right], \quad (\text{B.37})$$

and

$$\mathcal{G}_\mu^S = -\frac{\mu}{m_\chi} \left[(-\eta^2 + \mu^2 - 1) f(\mu, \eta) + \log \left(\frac{\eta}{\mu} \right) \right]. \quad (\text{B.38})$$

Electric dipole moment:

$$\mathcal{F}_d^S = 0, \quad \mathcal{G}_d^S = i\mathcal{G}_\mu^S. \quad (\text{B.39})$$

Anapole moment:

$$\mathcal{F}_A^S = \frac{1}{6m_\chi^2} \left[(-3\eta^2 + 3\mu^2 - 1) f(\mu, \eta) + 3 \log \left(\frac{\eta}{\mu} \right) \right], \quad \mathcal{G}_A^S = 0. \quad (\text{B.40})$$

Charge radius:

$$\begin{aligned} \mathcal{F}_b^S = \frac{1}{6\Delta m_\chi^2} & \left[\Delta (8\eta^2 - 8\mu^2 + 1) \log \left(\frac{\eta}{\mu} \right) - 2 (4\Delta + \eta^2 + 3\mu^2 - 1) \right. \\ & \left. + f(\mu, \eta) \left(\mu^2 (-7\Delta + 12\eta^2 - 4) + \Delta (-8\Delta - 9\eta^2 + 5) + 4\mu^4 \right) \right], \end{aligned} \quad (\text{B.41})$$

and

$$\begin{aligned} \mathcal{G}_b^S = \frac{2\mu}{3\Delta m_\chi^2} & \left[\Delta \log \left(\frac{\mu}{\eta} \right) + \eta^2 - \mu^2 + f(\mu, \eta) \times \right. \\ & \left. \times (-\mu^2 (\Delta + 2\eta^2 + 3) + (\Delta - 1) (\eta^2 - 1) + 2\mu^4) \right]. \end{aligned} \quad (\text{B.42})$$

Vector loop functions

Magnetic dipole moment:

$$\mathcal{F}_\mu^V = -\frac{2}{m_\chi} \left[(\Delta - \eta^2 + 3\mu^2 + 1) f(\mu, \eta) + (\mu^2 - \eta^2 + 2) \log\left(\frac{\eta}{\mu}\right) + 1 \right], \quad (\text{B.43})$$

and

$$\mathcal{G}_\mu^V = -\frac{4\mu}{m_\chi} \left[(\eta^2 - \mu^2 - 1) f(\mu, \eta) + \log\left(\frac{\mu}{\eta}\right) \right]. \quad (\text{B.44})$$

Electric dipole moment:

$$\mathcal{F}_d^V = 0, \quad \mathcal{G}_d^V = -i\mathcal{G}_\mu^V. \quad (\text{B.45})$$

Anapole moment:

$$\mathcal{F}_A^V = \frac{1}{3m_\chi^2} \left[(-3\eta^2 + 3\mu^2 + 7) f(\mu, \eta) + 3 \log\left(\frac{\eta}{\mu}\right) \right], \quad \mathcal{G}_A^V = 0. \quad (\text{B.46})$$

Charge radius:

$$\begin{aligned} \mathcal{F}_b^V = \frac{1}{3\Delta m_\chi^2} & \left[\Delta (-8\eta^2 + 8\mu^2 + 5) \log\left(\frac{\mu}{\eta}\right) - 2(4\Delta + \eta^2 + 3\mu^2 - 1) \right. \\ & \left. - f(\mu, \eta) \left(\mu^2 (13\Delta - 12\eta^2 + 4) + \Delta (8\Delta + 3\eta^2 + 1) - 4\mu^4 \right) \right], \end{aligned} \quad (\text{B.47})$$

and

$$\begin{aligned} \mathcal{G}_b^V = \frac{8\mu}{3\Delta m_\chi^2} & \left[\Delta \log\left(\frac{\eta}{\mu}\right) - \eta^2 + \mu^2 + f(\mu, \eta) \times \right. \\ & \left. \times \left(\mu^2 (\Delta + 2\eta^2 + 3) - (\Delta - 1) (\eta^2 - 1) - 2\mu^4 \right) \right]. \end{aligned} \quad (\text{B.48})$$

B.3 Large mass splitting between external states

Here, we consider the scenario for which $m_{\chi_1} \gg m_{\chi_2}$ and introduce the abbreviations $\alpha = \sqrt{\Delta - \eta^2 + \mu^2 + 1}$ and $\beta = \sqrt{\Delta + \eta^2 - \mu^2 + 1}$.

Scalar loop functions

Magnetic dipole moment:

$$\mathcal{F}_\mu^S = \frac{1}{m_{\chi_1}} \left[\eta^2 \left(\text{Li}_2 \left(\frac{2}{2-\alpha} \right) + \text{Li}_2 \left(\frac{2}{\beta} \right) - \text{Li}_2 \left(1 - \frac{\mu^2}{\eta^2} \right) \right) + \mu^2 \left(\text{Li}_2 \left(\frac{2}{2-\beta} \right) + \text{Li}_2 \left(\frac{2}{\alpha} \right) - \text{Li}_2 \left(1 - \frac{\eta^2}{\mu^2} \right) \right) - 1 \right], \quad (\text{B.49})$$

and

$$\mathcal{G}_\mu^S = \frac{\mu}{m_{\chi_1}} \left(\text{Li}_2 \left(\frac{2}{\alpha} \right) + \text{Li}_2 \left(\frac{2}{2-\beta} \right) - \text{Li}_2 \left(1 - \frac{\eta^2}{\mu^2} \right) \right). \quad (\text{B.50})$$

Electric dipole moment:

$$\mathcal{F}_d^S = i\mathcal{F}_\mu^S, \quad \mathcal{G}_d^S = i\mathcal{G}_\mu^S. \quad (\text{B.51})$$

Anapole moment:

$$\begin{aligned} \mathcal{F}_\mathcal{A}^S = \frac{1}{m_{\chi_1}^2} & \left[-\Delta f(\mu, \eta) - (3\mu^2 - 3\eta^2 + 1) \log \left(\frac{\mu}{\eta} \right) - 3 \right. \\ & + (2\Delta + 6\eta^2 + 3\mu^2 - 2) \left(\text{Li}_2 \left(\frac{2}{2-\alpha} \right) + \text{Li}_2 \left(\frac{2}{\beta} \right) - \text{Li}_2 \left(1 - \frac{\mu^2}{\eta^2} \right) \right) \\ & \left. + (2\Delta + 2\eta^2 + 7\mu^2 - 2) \left(\text{Li}_2 \left(\frac{2}{2-\beta} \right) + \text{Li}_2 \left(\frac{2}{\alpha} \right) - \text{Li}_2 \left(1 - \frac{\eta^2}{\mu^2} \right) \right) \right], \end{aligned} \quad (\text{B.52})$$

and

$$\begin{aligned} \mathcal{G}_\mathcal{A}^S = \frac{\mu}{m_{\chi_1}^2} & \left[4 \log \left(\frac{\eta}{\mu} \right) + (\alpha - \beta - 1) \left(\text{Li}_2 \left(\frac{2}{2-\alpha} \right) + \text{Li}_2 \left(\frac{2}{\beta} \right) - \text{Li}_2 \left(1 - \frac{\mu^2}{\eta^2} \right) \right) \right. \\ & \left. + (\alpha - \beta + 1) \left(\text{Li}_2 \left(\frac{2}{2-\beta} \right) + \text{Li}_2 \left(\frac{2}{\alpha} \right) - \text{Li}_2 \left(1 - \frac{\eta^2}{\mu^2} \right) \right) \right]. \end{aligned} \quad (\text{B.53})$$

Charge radius:

$$\mathcal{F}_b^S = \mathcal{F}_\mathcal{A}^S, \quad \mathcal{G}_b^S = \mathcal{G}_\mathcal{A}^S. \quad (\text{B.54})$$

Vector loop functions

Magnetic dipole moment:

$$\begin{aligned} \mathcal{F}_\mu^V = \frac{2}{m_{\chi_1}} & \left[\mu^2 \left(\text{Li}_2 \left(\frac{2}{2-\beta} \right) + \text{Li}_2 \left(\frac{2}{\alpha} \right) - \text{Li}_2 \left(1 - \frac{\eta^2}{\mu^2} \right) \right) \right. \\ & \left. (\eta^2 - 1) \left[\text{Li}_2 \left(\frac{2}{2-\alpha} \right) + \text{Li}_2 \left(\frac{2}{\beta} \right) - \text{Li}_2 \left(1 - \frac{\mu^2}{\eta^2} \right) \right] - 1 \right], \end{aligned} \quad (\text{B.55})$$

and

$$\mathcal{G}_\mu^V = \frac{4\mu}{m_{\chi_1}} \left(\text{Li}_2 \left(\frac{2}{2-\alpha} \right) + \text{Li}_2 \left(\frac{2}{\beta} \right) - \text{Li}_2 \left(1 - \frac{\mu^2}{\eta^2} \right) \right). \quad (\text{B.56})$$

Electric dipole moment:

$$\mathcal{F}_d^V = -i\mathcal{F}_\mu^V, \quad \mathcal{G}_d^V = -i\mathcal{G}_\mu^V. \quad (\text{B.57})$$

Anapole moment:

$$\begin{aligned} \mathcal{F}_\mathcal{A}^V = \frac{2}{m_{\chi_1}^2} & \left[\Delta f(\mu, \eta) + (-3\eta^2 + 3\mu^2 + 1) \log \left(\frac{\mu}{\eta} \right) + 3 \right. \\ & - \lambda_1 \left(\text{Li}_2 \left(\frac{2}{\alpha} \right) + \text{Li}_2 \left(-\frac{2}{\beta-2} \right) - \text{Li}_2 \left(1 - \frac{\eta^2}{\mu^2} \right) \right) \\ & \left. + \lambda_2 \left(\text{Li}_2 \left(-\frac{2}{\alpha-2} \right) + \text{Li}_2 \left(\frac{2}{\beta} \right) - \text{Li}_2 \left(1 - \frac{\mu^2}{\eta^2} \right) \right) \right], \quad (\text{B.58}) \end{aligned}$$

with

$$\lambda_1 = 2(\eta^4 - \eta^2(2\mu^2 + 1) + \mu^4) + 3\mu^2, \quad (\text{B.59})$$

$$\lambda_2 = -2(\eta^4 + \eta^2(1 - 2\mu^2) + \mu^4) + \mu^2 + 1, \quad (\text{B.60})$$

and

$$\begin{aligned} \mathcal{G}_\mathcal{A}^V = \frac{4\mu}{m_{\chi_1}^2} & \left[4 \log \left(\frac{\eta}{\mu} \right) + (\alpha - \beta - 1) \left(\text{Li}_2 \left(\frac{2}{2-\alpha} \right) + \text{Li}_2 \left(\frac{2}{\beta} \right) - \text{Li}_2 \left(1 - \frac{\mu^2}{\eta^2} \right) \right) \right. \\ & \left. + (\alpha - \beta + 1) \left(\text{Li}_2 \left(\frac{2}{2-\beta} \right) + \text{Li}_2 \left(\frac{2}{\alpha} \right) - \text{Li}_2 \left(1 - \frac{\eta^2}{\mu^2} \right) \right) \right]. \quad (\text{B.61}) \end{aligned}$$

Charge radius:

$$\mathcal{F}_b^V = -\mathcal{F}_\mathcal{A}^V, \quad \mathcal{G}_b^V = -\mathcal{G}_\mathcal{A}^S. \quad (\text{B.62})$$

B.4 Light external mass limit

Here, we expand the loop functions presented in appendix B.1 for the limit in which the masses of the external fermions are small compared to the relevant mass scale in the loop. We keep the leading order terms in m_{χ_1} and m_{χ_2} , and introduce the abbreviations $\rho = m_f/m_S$ and $r = m_f/m_V$.

Scalar loop functions

Magnetic dipole moment:

$$\mathcal{F}_\mu^S = \frac{(m_{\chi_1} + m_{\chi_2}) (\rho^4 - 2\rho^2 \log(\rho^2) - 1)}{4m_S^2 (\rho^2 - 1)^3}, \quad \mathcal{G}_\mu^S = \frac{\rho (\rho^2 - \log(\rho^2) - 1)}{m_S (\rho^2 - 1)^2}. \quad (\text{B.63})$$

Electric dipole moment:

$$\mathcal{F}_d^S = i \frac{(m_{\chi_1} - m_{\chi_2}) (\rho^4 - 2\rho^2 \log(\rho^2) - 1)}{4m_S^2 (\rho^2 - 1)^3}, \quad \mathcal{G}_d^S = i \frac{\rho (\rho^2 - \log(\rho^2) - 1)}{m_S (\rho^2 - 1)^2}. \quad (\text{B.64})$$

Anapole moment:

$$\begin{aligned} \mathcal{F}_A^S &= \frac{-3\rho^2 + (\rho^2 + 2) \log(\rho^2) + 3}{6m_S^2 (\rho^2 - 1)^2} \\ &\quad - \frac{m_{\chi_1} m_{\chi_2}}{36m_S^4 (\rho^2 - 1)^5} [-19\rho^6 - 9\rho^4 + 27\rho^2 + 6(\rho^4 + 5\rho^2 + 2)\rho^2 \log(\rho^2) + 1], \end{aligned} \quad (\text{B.65})$$

and

$$\mathcal{G}_A^S = \frac{\rho(m_{\chi_1} - m_{\chi_2}) (-3\rho^4 + (\rho^4 + 4\rho^2 + 1) \log(\rho^2) + 3)}{6m_S^3 (\rho^2 - 1)^4}. \quad (\text{B.66})$$

Charge radius:

$$\begin{aligned} \mathcal{F}_b^S &= \frac{-3\rho^2 + (\rho^2 + 2) \log(\rho^2) + 3}{6m_S^2 (\rho^2 - 1)^2} \\ &\quad + \frac{m_{\chi_1} m_{\chi_2}}{36m_S^4 (\rho^2 - 1)^5} [-19\rho^6 - 9\rho^4 + 27\rho^2 + 6(\rho^4 + 5\rho^2 + 2)\rho^2 \log(\rho^2) + 1], \end{aligned} \quad (\text{B.67})$$

and

$$\mathcal{G}_b^S = \frac{\rho(m_{\chi_1} + m_{\chi_2}) (-3\rho^4 + (\rho^4 + 4\rho^2 + 1) \log(\rho^2) + 3)}{6m_S^3 (\rho^2 - 1)^4}. \quad (\text{B.68})$$

Vector loop functions

Magnetic dipole moment:

$$\mathcal{F}_\mu^V = -\frac{(m_{\chi_1} + m_{\chi_2}) (-5r^4 + 8r^2 + (4r^4 - 2r^2) \log(r^2) - 3)}{2m_V^2 (r^2 - 1)^3}, \quad (\text{B.69})$$

and

$$\mathcal{G}_\mu^V = r \frac{4(-r^2 + r^2 \log(r^2) + 1)}{m_V (r^2 - 1)^2}. \quad (\text{B.70})$$

Electric dipole moment:

$$\mathcal{F}_d^V = i \frac{(m_{\chi_1} - m_{\chi_2}) (-5r^4 + 8r^2 + (4r^4 - 2r^2) \log(r^2) - 3)}{2m_V^2 (r^2 - 1)^3}, \quad (\text{B.71})$$

and

$$\mathcal{G}_d^V = -r \frac{4i (-r^2 + r^2 \log(r^2) + 1)}{m_V (r^2 - 1)^2}. \quad (\text{B.72})$$

Anapole moment:

$$\begin{aligned} \mathcal{F}_A^V &= -\frac{3(r^2 - 1) + (2 - 5r^2) \log(r^2)}{3m_V^2 (r^2 - 1)^2} \\ &+ \frac{m_{\chi_1} m_{\chi_2}}{18m_V^4 (r^2 - 1)^5} [-19r^6 - 9r^4 + 27r^2 + 6(r^4 + 5r^2 + 2)r^2 \log(r^2) + 1], \end{aligned} \quad (\text{B.73})$$

and

$$\mathcal{G}_A^V = \frac{2r(m_{\chi_1} - m_{\chi_2}) (-3r^4 + (r^4 + 4r^2 + 1) \log(r^2) + 3)}{3m_V^3 (r^2 - 1)^4}. \quad (\text{B.74})$$

Charge radius:

$$\begin{aligned} \mathcal{F}_b^V &= \frac{3(r^2 - 1) + (2 - 5r^2) \log(r^2)}{3m_V^2 (r^2 - 1)^2} \\ &+ \frac{m_{\chi_1} m_{\chi_2}}{18m_V^4 (r^2 - 1)^5} [-19r^6 - 9r^4 + 27r^2 + 6(r^4 + 5r^2 + 2)r^2 \log(r^2) + 1], \end{aligned} \quad (\text{B.75})$$

and

$$\mathcal{G}_b^V = -\frac{2r(m_{\chi_1} + m_{\chi_2}) (-3r^4 + (r^4 + 4r^2 + 1) \log(r^2) + 3)}{3m_V^3 (r^2 - 1)^4}. \quad (\text{B.76})$$

Appendix C

Electromagnetic- vs. hypercharge moments

Here, we provide more details on the issue of defining the EM moments with respect to the photon field A^μ .

Concretely, we consider the Dirac DM toy model, in which χ interacts with the photon field A^μ or the hypercharge gauge boson B^μ . The effective Lagrangian reads

$$\mathcal{L}_{\text{eff}} = \frac{\mu_\chi}{2} \bar{\chi} \sigma^{\mu\nu} \chi X_{\mu\nu} + \frac{d_\chi}{2} i \bar{\chi} \sigma^{\mu\nu} \gamma^5 \chi X_{\mu\nu} + b_\chi \bar{\chi} \gamma^\mu \chi \partial^\nu X_{\mu\nu} + \mathcal{A}_\chi \bar{\chi} \gamma^\mu \gamma^5 \chi \partial^\nu X_{\mu\nu}, \quad (\text{C.1})$$

where the vector field is $X^\mu = A^\mu$ or $X^\mu = B^\mu$, $X^{\mu\nu} = \partial^\mu X^\nu - \partial^\nu X^\mu$ is the respective field strength tensor, and the coefficients are the EM moments as discussed in chapter 3. Note that in this formulation, the term *EM moment* is ambiguously defined; in practice, one should keep either A^μ or B^μ as a reference. Throughout this work, we consider the moments w.r.t. A^μ , even if we consider DM interacting with the hypercharge gauge boson (see the `FeynRules` [401–403] implementation below). After electroweak symmetry breaking, the photon and hypercharge gauge boson are related, $B^\mu = \cos \theta_W A^\mu - \sin \theta_W Z^\mu$, where θ_W denotes the Weinberg angle. Thus, the respective moments are trivially related to each other.

The crucial difference between the photon- and the hypercharge model is that for the latter, the low energy EFT consists of photon- and Z mediated processes with couplings given by the EM moments, resulting in important theoretical and phenomenological consequences [310]:

- The presence of the Z channel leads to resonant thermal production via s -channel diagrams, if $m_\chi \simeq m_Z/2$.
- The DM annihilation cross-section in the photon-mediated version leads to non-unitary growth in the high-energy regime caused by the $\chi\chi \rightarrow WW$ sub-amplitude.
- Similarly, the absence of the Z channel causes an incorrect enhancement of the two-jet topology due to vector boson fusion at particle colliders.

The unphysical behavior described in the last two points is mitigated if the Z contribution is included, taming the total amplitude and restoring the SM gauge invariance. Therefore, adapting the hypercharge model when considering thermal production, indirect signals, or collider phenomenology is crucial. For direct detection experiments, on the other hand, the addition of the Z diagrams does not alter the phenomenology, as the additional diagrams are sufficiently suppressed by the Z boson propagator, as $\mathcal{M}_Z \sim m_Z^{-2}$

Often, the relic density is computed with the help of public numerical tools such as micrOMEGAs [368, 404], madDM [529] or DarkSUSY [530]. Here we will focus on micrOMEGAs v5.3.41 and madDM v3.2 within Madgraph5_aMC@NLO v2.9.16 [531].

We created a FeynRules [401–403] model file, generating CalcHEP [405] and Madgraph5_aMC@NLO output files for micrOMEGAs and madDM, respectively. The Lagrangian for electromagnetically interacting DM given in eq. (3.10) is written for the photon model as:

```
LDM := I DMbar.Ga[mu].del[DM,mu] - mdm DMbar.DM;
Ledm := (I/2) dedm DMbar.(I/2 Ga[mu].Ga[nu] - I/2 Ga[nu].Ga[mu])
      .Ga[5].DM FS[A,mu,nu];
Lmdm := (1/2) dmdm DMbar.(I/2 Ga[mu].Ga[nu] - I/2 Ga[nu].Ga[mu])
      .DM FS[A,mu,nu];
Lana := dana DMbar.Ga[mu].Ga[5].DM del[FS[A,mu,nu],nu];
Lcr := dcr DMbar.Ga[mu].DM del[FS[A,mu,nu],nu];
Lmilli := ee Qchi DMbar.Ga[mu].DM A[mu];

LBSM := LDM + Ledm + Lmdm + Lana + Lcr + Lmilli;
```

For the hypercharge model, we replace the photon with the hypercharge gauge boson:

```
LDM := I DMbar.Ga[mu].del[DM,mu] - mdm DMbar.DM;
Ledm := (I/2) dedm DMbar.(I/2 Ga[mu].Ga[nu] - I/2 Ga[nu].Ga[mu])
      .Ga[5].DM FS[B,mu,nu] (1/cw);
Lmdm := (1/2) dmdm DMbar.(I/2 Ga[mu].Ga[nu] - I/2 Ga[nu].Ga[mu])
      .DM FS[B,mu,nu] (1/cw);
Lana := dana DMbar.Ga[mu].Ga[5].DM del[FS[B,mu,nu],nu] (1/cw);
Lcr := dcr DMbar.Ga[mu].DM del[FS[B,mu,nu],nu] (1/cw);
Lmilli := ee Qchi DMbar.Ga[mu].DM B[mu] (1/cw);

LBSM := LDM + Ledm + Lmdm + Lana + Lcr + Lmilli;
```

We then calculate the relic density using the respective numerical tool, utilizing a numerical minimizer to find the value of the EM needed for the DM candidate

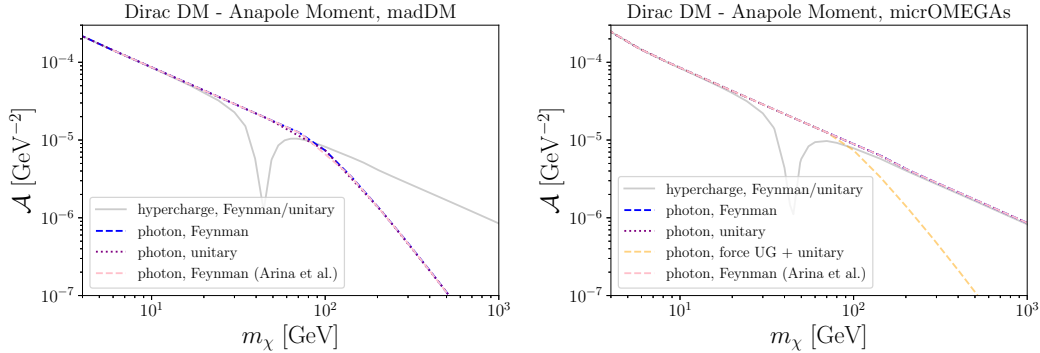


Figure C.1: Anapole moment required for thermal dark matter production via the freeze-out mechanism using `madDM` (*left*) and `micrOMEGAs` (*right*) for different input models and gauge-choices. The “force UG” in the right panel’s legend refers to the `forceUG=true` statement within `micrOMEGAs`’ `main.c` file.

to match with today’s observed relic abundance of $\Omega_{\text{DM}}h^2 \simeq 0.12$ [45]. We also cross-check our implementation with the model files of ref. [310].¹

In fig. C.1, we show the results for the anapole moment, but the implications are similar for the other EM moments. The different gauge choices in the legend describe the choice within the `FeynRules` SM file, whereas `forceUG=true` describes the boolean in the `main.c` file used for the `micrOMEGAs` routines. Notably, both codes agree for the hypercharge model, shown as a gray line, irrespective of the gauge set in the `FeynRules` model file, as it should.

For the photon model, `madDM` reproduces the ill behavior mentioned above, *i.e.* the $\chi\chi \rightarrow WW$ annihilation cross-section seems enhanced for $m_\chi \gtrsim 100$ GeV, leading to a smaller anapole moment to obtain $\Omega_\chi h^2 = 0.12$. However, coupling only to the photon violates the SM gauge group, so an unphysical behavior is unsurprising. In contrast, using `micrOMEGAs`, this behavior is only found when the switch `forceUG=true` is used, and the other choices for the gauges coincide with the hypercharge line beyond the resonance. Therefore, these codes do not consistently treat the photon-mediated model.

An analytical calculation of the relic density in the hypercharge anapole scenario was conducted in ref. [218], confirming that the hypercharge model results in physical cross-sections and, therefore, agrees with the findings of ref. [310].² In particular, the blue dashed line in the right panel of fig. C.1, indicating the photon model in the Feynman gauge calculated with `micrOMEGAs`, is coinciding with the correct hypercharge model prediction only accidentally.

¹Available at <https://feynrules.irmp.ucl.ac.be/wiki/EWFF4DM>.

²We thank Jaehoon Jeong for helpful discussions on this matter.

These findings underscore the importance of working in the framework of the hypercharge moments in favor of the electromagnetic moments for the freeze-out calculation. For a consistent formulation of electromagnetically interacting DM, one has to include the trivially related diagrams where the Z boson replaces the photon.

Bibliography

- [1] Merlin Emanuel Reichard. »Anapole Moment of Majorana Fermions and Implications for Direct Detection of Neutralino Dark Matter«. MA thesis. Garching, Germany: Technische Universität München, 2021.
- [2] Alejandro Ibarra, Merlin Reichard and Ryo Nagai. »Anapole moment of Majorana fermions and implications for direct detection of neutralino dark matter«. In: *JHEP* 01 (2023), p. 086. DOI: 10.1007/JHEP01(2023)086. arXiv: 2207.01014 [hep-ph].
- [3] Alejandro Ibarra, Merlin Reichard and Gaurav Tomar. »Probing dark matter electromagnetic properties in direct detection experiments«. In: *JCAP* 02 (2025), p. 072. DOI: 10.1088/1475-7516/2025/02/072. arXiv: 2408.15760 [hep-ph].
- [4] Gerard Jungman, Marc Kamionkowski and Kim Griest. »Supersymmetric dark matter«. In: *Phys. Rept.* 267 (1996), pp. 195–373. DOI: 10.1016/0370-1573(95)00058-5. arXiv: hep-ph/9506380.
- [5] Lars Bergström. »Nonbaryonic dark matter: Observational evidence and detection methods«. In: *Rept. Prog. Phys.* 63 (2000), p. 793. DOI: 10.1088/0034-4885/63/5/2r3. arXiv: hep-ph/0002126.
- [6] Gianfranco Bertone, Dan Hooper and Joseph Silk. »Particle dark matter: Evidence, candidates and constraints«. In: *Phys. Rept.* 405 (2005), pp. 279–390. DOI: 10.1016/j.physrep.2004.08.031. arXiv: hep-ph/0404175.
- [7] Jonathan L. Feng. »Dark Matter Candidates from Particle Physics and Methods of Detection«. In: *Ann. Rev. Astron. Astrophys.* 48 (2010), pp. 495–545. DOI: 10.1146/annurev-astro-082708-101659. arXiv: 1003.0904 [astro-ph.CO].
- [8] Marco Cirelli, Alessandro Strumia and Jure Zupan. »Dark Matter«. In: (June 2024). arXiv: 2406.01705 [hep-ph].
- [9] Martin Bauer and Tilman Plehn. *Yet Another Introduction to Dark Matter: The Particle Physics Approach*. Vol. 959. Lecture Notes in Physics. Springer, 2019. DOI: 10.1007/978-3-030-16234-4. arXiv: 1705.01987 [hep-ph].
- [10] Giuseppe Bertin. *Visible and Dark Matter in the Universe*. Cambridge University Press, Dec. 2022. ISBN: 978-1-009-02336-8, 978-1-316-51931-8. DOI: 10.1017/9781009023368.

- [11] V. C. Rubin, N. Thonnard and W. K. Ford Jr. »Rotational properties of 21 SC galaxies with a large range of luminosities and radii, from NGC 4605 /R = 4kpc/ to UGC 2885 /R = 122 kpc/«. In: *Astrophys. J.* 238 (1980), p. 471. DOI: 10.1086/158003.
- [12] M. Milgrom. »A Modification of the Newtonian dynamics: Implications for galaxies«. In: *Astrophys. J.* 270 (1983), pp. 371–383. DOI: 10.1086/161131.
- [13] M. Milgrom. »A Modification of the Newtonian dynamics as a possible alternative to the hidden mass hypothesis«. In: *Astrophys. J.* 270 (1983), pp. 365–370. DOI: 10.1086/161130.
- [14] M. Milgrom. »A modification of the Newtonian dynamics: implications for galaxy systems«. In: *Astrophys. J.* 270 (1983), pp. 384–389. DOI: 10.1086/161132.
- [15] R. H. Sanders. »Resolving the virial discrepancy in clusters of galaxies with modified newtonian dynamics«. In: *Astrophys. J. Lett.* 512 (1999), p. L23. DOI: 10.1086/311865. arXiv: astro-ph/9807023.
- [16] Anthony Aguirre, Joop Schaye and Eliot Quataert. »Problems for MOND in clusters and the Ly-alpha forest«. In: *Astrophys. J.* 561 (2001), p. 550. DOI: 10.1086/323376. arXiv: astro-ph/0105184.
- [17] R. H. Sanders. »Clusters of galaxies with modified Newtonian dynamics (MOND)«. In: *Mon. Not. Roy. Astron. Soc.* 342 (2003), p. 901. DOI: 10.1046/j.1365-8711.2003.06596.x. arXiv: astro-ph/0212293.
- [18] Etienne Pointecouteau and Joseph Silk. »New Constraints on MOND from galaxy clusters«. In: *Mon. Not. Roy. Astron. Soc.* 364 (2005), pp. 654–658. DOI: 10.1111/j.1365-2966.2005.09590.x. arXiv: astro-ph/0505017.
- [19] Ruth Kelleher and Federico Lelli. »Galaxy clusters in Milgromian dynamics: Missing matter, hydrostatic bias, and the external field effect«. In: *Astron. Astrophys.* 688 (2024), A78. DOI: 10.1051/0004-6361/202449968. arXiv: 2405.08557 [astro-ph.CO].
- [20] K. C. Freeman. »On the disks of spiral and SO Galaxies«. In: *Astrophys. J.* 160 (1970), p. 811. DOI: 10.1086/150474.
- [21] Julio F. Navarro, Carlos S. Frenk and Simon D. M. White. »The Structure of cold dark matter halos«. In: *Astrophys. J.* 462 (1996), pp. 563–575. DOI: 10.1086/177173. arXiv: astro-ph/9508025.
- [22] Julio F. Navarro, Carlos S. Frenk and Simon D. M. White. »A Universal density profile from hierarchical clustering«. In: *Astrophys. J.* 490 (1997), pp. 493–508. DOI: 10.1086/304888. arXiv: astro-ph/9611107.

- [23] James Binney and Scott Tremaine. *Galactic dynamics*. Vol. 13. Princeton university press, 2011.
- [24] Yoshiaki Sofue. »Rotation curve decomposition for size–mass relations of bulge, disk, and dark halo components in spiral galaxies«. In: *Publications of the Astronomical Society of Japan* 68.1 (Oct. 2015), p. 2. ISSN: 0004-6264. DOI: 10.1093/pasj/psv103. eprint: https://academic.oup.com/pasj/article-pdf/68/1/2/54679780/pasj_68_1_2.pdf. URL: <https://doi.org/10.1093/pasj/psv103>.
- [25] Fritz Zwicky. »Die Rotverschiebung von extragalaktischen Nebeln«. In: *Helvetica Physica Acta* (Nov. 1933).
- [26] Heinz Andernach and Fritz Zwicky. *English and Spanish Translation of Zwicky's (1933) The Redshift of Extragalactic Nebulae*. 2017. arXiv: 1711.01693 [astro-ph.IM].
- [27] F. Zwicky. »On the Masses of Nebulae and of Clusters of Nebulae«. In: *Astrophys. J.* 86 (1937), pp. 217–246. DOI: 10.1086/143864.
- [28] Craig L. Sarazin. »X-ray emission from clusters of galaxies«. In: *Rev. Mod. Phys.* 58 (1986), pp. 1–115. DOI: 10.1103/RevModPhys.58.1.
- [29] Piero Rosati, Stefano Borgani and Colin Norman. »The evolution of x-ray clusters of galaxies«. In: *Ann. Rev. Astron. Astrophys.* 40 (2002), pp. 539–577. DOI: 10.1146/annurev.astro.40.120401.150547. arXiv: astro-ph/0209035.
- [30] S. Ettori et al. »Mass profiles of Galaxy Clusters from X-ray analysis«. In: *Space Sci. Rev.* 177 (2013), pp. 119–154. DOI: 10.1007/s11214-013-9976-7. arXiv: 1303.3530 [astro-ph.CO].
- [31] Douglas Clowe et al. »A direct empirical proof of the existence of dark matter«. In: *Astrophys. J. Lett.* 648 (2006), pp. L109–L113. DOI: 10.1086/508162. arXiv: astro-ph/0608407.
- [32] Marusa Bradac et al. »Revealing the properties of dark matter in the merging cluster MACSJ0025.4-1222«. In: *Astrophys. J.* 687 (2008), p. 959. DOI: 10.1086/591246. arXiv: 0806.2320 [astro-ph].
- [33] David Harvey et al. »The non-gravitational interactions of dark matter in colliding galaxy clusters«. In: *Science* 347 (2015), pp. 1462–1465. DOI: 10.1126/science.1261381. arXiv: 1503.07675 [astro-ph.CO].
- [34] Maxim Markevitch et al. »Direct constraints on the dark matter self-interaction cross-section from the merging galaxy cluster 1E0657-56«. In: *Astrophys. J.* 606 (2004), pp. 819–824. DOI: 10.1086/383178. arXiv: astro-ph/0309303.

- [35] Arno A. Penzias and Robert Woodrow Wilson. »A Measurement of excess antenna temperature at 4080-Mc/s«. In: *Astrophys. J.* 142 (1965), pp. 419–421. DOI: 10.1086/148307.
- [36] George F. Smoot et al. »Structure in the COBE differential microwave radiometer first year maps«. In: *Astrophys. J. Lett.* 396 (1992), pp. L1–L5. DOI: 10.1086/186504.
- [37] B. Ryden. *Introduction to cosmology*. Cambridge University Press, 1970. ISBN: 978-1-107-15483-4, 978-1-316-88984-8, 978-1-316-65108-7. DOI: 10.1017/9781316651087.
- [38] Edward W. Kolb. *The Early Universe*. Vol. 69. Taylor and Francis, May 2019. ISBN: 978-0-429-49286-0, 978-0-201-62674-2. DOI: 10.1201/9780429492860.
- [39] Scott Dodelson. *Modern Cosmology*. Amsterdam: Academic Press, 2003. ISBN: 978-0-12-219141-1.
- [40] A. Friedman. »On the Curvature of space«. In: *Z. Phys.* 10 (1922), pp. 377–386. DOI: 10.1007/BF01332580.
- [41] Georges Lemaitre. »A Homogeneous Universe of Constant Mass and Increasing Radius accounting for the Radial Velocity of Extra-galactic Nebulæ«. In: *Mon. Not. Roy. Astron. Soc.* 91.5 (1931), pp. 483–490. DOI: 10.1093/mnras/91.5.483.
- [42] R. K. Sachs and A. M. Wolfe. »Perturbations of a cosmological model and angular variations of the microwave background«. In: *Astrophys. J.* 147 (1967), pp. 73–90. DOI: 10.1007/s10714-007-0448-9.
- [43] C. L. Bennett et al. »The Microwave Anisotropy Probe (MAP) mission«. In: *Astrophys. J.* 583 (2003), pp. 1–23. DOI: 10.1086/345346. arXiv: astro-ph/0301158.
- [44] »The Scientific programme of Planck«. In: (Apr. 2006). Ed. by J. Tauber et al. arXiv: astro-ph/0604069.
- [45] N. Aghanim et al. »Planck 2018 results. VI. Cosmological parameters«. In: *Astron. Astrophys.* 641 (2020). [Erratum: *Astron. Astrophys.* 652, C4 (2021)], A6. DOI: 10.1051/0004-6361/201833910. arXiv: 1807.06209 [astro-ph.CO].
- [46] F. Bernardeau et al. »Large scale structure of the universe and cosmological perturbation theory«. In: *Phys. Rept.* 367 (2002), pp. 1–248. DOI: 10.1016/S0370-1573(02)00135-7. arXiv: astro-ph/0112551.
- [47] Marc Davis et al. »The Evolution of Large Scale Structure in a Universe Dominated by Cold Dark Matter«. In: *Astrophys. J.* 292 (1985). Ed. by M. A. Srednicki, pp. 371–394. DOI: 10.1086/163168.

- [48] A. A. Vlasov. »The vibrational properties of an electron gas«. In: *Usp. Fiz. Nauk* 93.11 (1967), pp. 444–470. DOI: 10.3367/UFNr.0093.196711f.0444. URL: <https://ufn.ru/ru/articles/1967/11/f/>.
- [49] Paolo Gondolo and Graciela Gelmini. »Cosmic abundances of stable particles: Improved analysis«. In: *Nucl. Phys. B* 360 (1991), pp. 145–179. DOI: 10.1016/0550-3213(91)90438-4.
- [50] Nicolás Bernal et al. »The Dawn of FIMP Dark Matter: A Review of Models and Constraints«. In: *Int. J. Mod. Phys. A* 32.27 (2017), p. 1730023. DOI: 10.1142/S0217751X1730023X. arXiv: 1706.07442 [hep-ph].
- [51] Johannes Paul Joachim Herms. »Thermal Relics of Non-Minimal Dark Sectors«. en. PhD thesis. Technische Universität München, 2020, p. 128. URL: <https://mediatum.ub.tum.de/1554515>.
- [52] Yonit Hochberg. »SIMP Dark Matter«. In: *SciPost Phys. Lect. Notes* 59 (2022), p. 1. DOI: 10.21468/SciPostPhysLectNotes.59.
- [53] Jonathan L. Feng. »The WIMP paradigm: Theme and variations«. In: *SciPost Phys. Lect. Notes* 71 (2023), p. 1. DOI: 10.21468/SciPostPhysLectNotes.71. arXiv: 2212.02479 [hep-ph].
- [54] Lawrence J. Hall et al. »Freeze-In Production of FIMP Dark Matter«. In: *JHEP* 03 (2010), p. 080. DOI: 10.1007/JHEP03(2010)080. arXiv: 0911.1120 [hep-ph].
- [55] Wayne Hu, Rennan Barkana and Andrei Gruzinov. »Cold and fuzzy dark matter«. In: *Phys. Rev. Lett.* 85 (2000), pp. 1158–1161. DOI: 10.1103/PhysRevLett.85.1158. arXiv: astro-ph/0003365.
- [56] Lam Hui et al. »Ultralight scalars as cosmological dark matter«. In: *Phys. Rev. D* 95.4 (2017), p. 043541. DOI: 10.1103/PhysRevD.95.043541. arXiv: 1610.08297 [astro-ph.CO].
- [57] John Preskill, Mark B. Wise and Frank Wilczek. »Cosmology of the Invisible Axion«. In: *Phys. Lett. B* 120 (1983). Ed. by M. A. Srednicki, pp. 127–132. DOI: 10.1016/0370-2693(83)90637-8.
- [58] L. F. Abbott and P. Sikivie. »A Cosmological Bound on the Invisible Axion«. In: *Phys. Lett. B* 120 (1983). Ed. by M. A. Srednicki, pp. 133–136. DOI: 10.1016/0370-2693(83)90638-X.
- [59] Michael Dine and Willy Fischler. »The Not So Harmless Axion«. In: *Phys. Lett. B* 120 (1983). Ed. by M. A. Srednicki, pp. 137–141. DOI: 10.1016/0370-2693(83)90639-1.

- [60] Daniel J. H. Chung, Edward W. Kolb and Antonio Riotto. »Nonthermal supermassive dark matter«. In: *Phys. Rev. Lett.* 81 (1998), pp. 4048–4051. DOI: 10.1103/PhysRevLett.81.4048. arXiv: hep-ph/9805473.
- [61] Daniel J. H. Chung, Edward W. Kolb and Antonio Riotto. »Production of massive particles during reheating«. In: *Phys. Rev. D* 60 (1999), p. 063504. DOI: 10.1103/PhysRevD.60.063504. arXiv: hep-ph/9809453.
- [62] Alejandro Ibarra. »Indirect dark matter detection«. In: *Acta Phys. Polon. B* 43 (2012). Ed. by Michal Praszalowicz, pp. 2199–2224. DOI: 10.5506/APhysPolB.43.2199.
- [63] J. Buckley et al. »Working Group Report: WIMP Dark Matter Indirect Detection«. In: *Snowmass 2013: Snowmass on the Mississippi*. Oct. 2013. arXiv: 1310.7040 [astro-ph.HE].
- [64] Tracy R. Slatyer. »Les Houches Lectures on Indirect Detection of Dark Matter«. In: *SciPost Phys. Lect. Notes* 53 (2022), p. 1. DOI: 10.21468/SciPostPhysLectNotes.53. arXiv: 2109.02696 [hep-ph].
- [65] Christian Bierlich et al. »A comprehensive guide to the physics and usage of PYTHIA 8.3«. In: *SciPost Phys. Codeb.* 2022 (2022), p. 8. DOI: 10.21468/SciPostPhysCodeb.8. arXiv: 2203.11601 [hep-ph].
- [66] M. Bahr et al. »Herwig++ Physics and Manual«. In: *Eur. Phys. J. C* 58 (2008), pp. 639–707. DOI: 10.1140/epjc/s10052-008-0798-9. arXiv: 0803.0883 [hep-ph].
- [67] Johannes Bellm et al. »Herwig 7.0/Herwig++ 3.0 release note«. In: *Eur. Phys. J. C* 76.4 (2016), p. 196. DOI: 10.1140/epjc/s10052-016-4018-8. arXiv: 1512.01178 [hep-ph].
- [68] S. Agostinelli et al. »GEANT4 - A Simulation Toolkit«. In: *Nucl. Instrum. Meth. A* 506 (2003), pp. 250–303. DOI: 10.1016/S0168-9002(03)01368-8.
- [69] W. B. Atwood et al. »The Large Area Telescope on the Fermi Gamma-ray Space Telescope Mission«. In: *Astrophys. J.* 697 (2009), pp. 1071–1102. DOI: 10.1088/0004-637X/697/2/1071. arXiv: 0902.1089 [astro-ph.IM].
- [70] M. Ajello et al. »Fermi Large Area Telescope Performance after 10 Years of Operation«. In: *Astrophys. J. Supp.* 256.1 (2021), p. 12. DOI: 10.3847/1538-4365/ac0ceb. arXiv: 2106.12203 [astro-ph.IM].
- [71] H. Abdalla et al. »The H.E.S.S. Galactic plane survey«. In: *Astron. Astrophys.* 612 (2018), A1. DOI: 10.1051/0004-6361/201732098. arXiv: 1804.02432 [astro-ph.HE].

- [72] M. Ackermann et al. »Searching for Dark Matter Annihilation from Milky Way Dwarf Spheroidal Galaxies with Six Years of Fermi Large Area Telescope Data«. In: *Phys. Rev. Lett.* 115.23 (2015), p. 231301. DOI: 10 . 1103/PhysRevLett.115.231301. arXiv: 1503.02641 [astro-ph.HE].
- [73] A. Albert et al. »Searching for Dark Matter Annihilation in Recently Discovered Milky Way Satellites with Fermi-LAT«. In: *Astrophys. J.* 834.2 (2017), p. 110. DOI: 10 . 3847/1538 - 4357/834/2/110. arXiv: 1611 . 03184 [astro-ph.HE].
- [74] M. Ackermann et al. »The Fermi Galactic Center GeV Excess and Implications for Dark Matter«. In: *Astrophys. J.* 840.1 (2017), p. 43. DOI: 10 . 3847/1538-4357/aa6cab. arXiv: 1704.03910 [astro-ph.HE].
- [75] H. Abdallah et al. »Search for γ -Ray Line Signals from Dark Matter Annihilations in the Inner Galactic Halo from 10 Years of Observations with H.E.S.S.« In: *Phys. Rev. Lett.* 120.20 (2018), p. 201101. DOI: 10 . 1103/PhysRevLett . 120.201101. arXiv: 1805.05741 [astro-ph.HE].
- [76] H. Abdalla et al. »Searches for gamma-ray lines and 'pure WIMP' spectra from Dark Matter annihilations in dwarf galaxies with H.E.S.S.« In: *JCAP* 11 (2018), p. 037. DOI: 10.1088/1475-7516/2018/11/037. arXiv: 1810.00995 [astro-ph.HE].
- [77] Alessandro Strumia and Francesco Vissani. »Neutrino masses and mixings and...« In: (June 2006). arXiv: hep-ph/0606054.
- [78] Ivan Esteban et al. »NuFit-6.0: updated global analysis of three-flavor neutrino oscillations«. In: *JHEP* 12 (2024), p. 216. DOI: 10.1007/JHEP12(2024)216. arXiv: 2410.05380 [hep-ph].
- [79] J. Ahrens et al. »Icecube - the next generation neutrino telescope at the south pole«. In: *Nucl. Phys. B Proc. Suppl.* 118 (2003). Ed. by F. von Feilitzsch and N. Schmitz, pp. 388–395. DOI: 10 . 1016/S0920 - 5632(03) 01337 - 9. arXiv: astro-ph/0209556.
- [80] R. Abbasi et al. »Search for dark matter from the Galactic halo with the IceCube Neutrino Telescope«. In: *Phys. Rev. D* 84 (2011), p. 022004. DOI: 10.1103/PhysRevD.84.022004. arXiv: 1101.3349 [astro-ph.HE].
- [81] R. Abbasi et al. »Search for Neutrinos from Annihilating Dark Matter in the Direction of the Galactic Center with the 40-String IceCube Neutrino Observatory«. In: (Oct. 2012). arXiv: 1210.3557 [hep-ex].
- [82] M. G. Aartsen et al. »IceCube Search for Dark Matter Annihilation in nearby Galaxies and Galaxy Clusters«. In: *Phys. Rev. D* 88 (2013), p. 122001. DOI: 10.1103/PhysRevD.88.122001. arXiv: 1307.3473 [astro-ph.HE].

- [83] M. G. Aartsen et al. »Search for Dark Matter Annihilation in the Galactic Center with IceCube-79«. In: *Eur. Phys. J. C* 75.10 (2015), p. 492. DOI: 10.1140/epjc/s10052-015-3713-1. arXiv: 1505.07259 [astro-ph.HE].
- [84] M. G. Aartsen et al. »First search for dark matter annihilations in the Earth with the IceCube Detector«. In: *Eur. Phys. J. C* 77.2 (2017), p. 82. DOI: 10.1140/epjc/s10052-016-4582-y. arXiv: 1609.01492 [astro-ph.HE].
- [85] M. G. Aartsen et al. »Search for Neutrinos from Dark Matter Self-Annihilations in the center of the Milky Way with 3 years of IceCube/DeepCore«. In: *Eur. Phys. J. C* 77.9 (2017), p. 627. DOI: 10.1140/epjc/s10052-017-5213-y. arXiv: 1705.08103 [hep-ex].
- [86] A. Albert et al. »Combined search for neutrinos from dark matter self-annihilation in the Galactic Center with ANTARES and IceCube«. In: *Phys. Rev. D* 102.8 (2020), p. 082002. DOI: 10.1103/PhysRevD.102.082002. arXiv: 2003.06614 [astro-ph.HE].
- [87] R. Abbasi et al. »Search for neutrino lines from dark matter annihilation and decay with IceCube«. In: *Phys. Rev. D* 108.10 (2023), p. 102004. DOI: 10.1103/PhysRevD.108.102004. arXiv: 2303.13663 [astro-ph.HE].
- [88] A. Kappes. »KM3NeT: A Next Generation Neutrino Telescope in the Mediterranean Sea«. In: (Nov. 2007). arXiv: 0711.0563 [astro-ph].
- [89] S. Adrian-Martinez et al. »Letter of intent for KM3NeT 2.0«. In: *J. Phys. G* 43.8 (2016), p. 084001. DOI: 10.1088/0954-3899/43/8/084001. arXiv: 1601.07459 [astro-ph.IM].
- [90] S. Aiello et al. »First Searches for Dark Matter with the KM3NeT Neutrino Telescopes«. In: (Nov. 2024). arXiv: 2411.10092 [astro-ph.HE].
- [91] V. S. Berezinsky et al. *Astrophysics of cosmic rays*. Ed. by V. L. Ginzburg. 1990.
- [92] Andrea Vittino et al. »Breaks in interstellar spectra of positrons and electrons derived from time-dependent AMS data«. In: *Phys. Rev. D* 100.4 (2019), p. 043007. DOI: 10.1103/PhysRevD.100.043007. arXiv: 1904.05899 [astro-ph.HE].
- [93] Yoann Génolini et al. »Indications for a high-rigidity break in the cosmic-ray diffusion coefficient«. In: *Phys. Rev. Lett.* 119.24 (2017), p. 241101. DOI: 10.1103/PhysRevLett.119.241101. arXiv: 1706.09812 [astro-ph.HE].
- [94] Eun-Suk Seo and Vladimir S Ptuskin. »Stochastic reacceleration of cosmic rays in the interstellar medium«. In: *The Astrophysical Journal*, vol. 431, no. 2, pt. 1, p. 705-714 431 (1994), pp. 705–714.

- [95] W. R. Webber, M. A. Lee and M. Gupta. »Propagation of cosmic-ray nuclei in a diffusing galaxy with convective halo and thin matter disk«. In: *Astrophys. J.* 390 (1992), p. 96. DOI: 10.1086/171262.
- [96] Enrico Fermi. »On the Origin of the Cosmic Radiation«. In: *Phys. Rev.* 75 (1949), pp. 1169–1174. DOI: 10.1103/PhysRev.75.1169.
- [97] Y. Génolini et al. »Cosmic-ray transport from AMS-02 boron to carbon ratio data: Benchmark models and interpretation«. In: *Phys. Rev. D* 99.12 (2019), p. 123028. DOI: 10.1103/PhysRevD.99.123028. arXiv: 1904.08917 [astro-ph.HE].
- [98] A. W. Strong and I. V. Moskalenko. »Propagation of cosmic-ray nucleons in the galaxy«. In: *Astrophys. J.* 509 (1998), pp. 212–228. DOI: 10.1086/306470. arXiv: astro-ph/9807150.
- [99] A.E. Vladimirov et al. »GALPROP WebRun: An internet-based service for calculating galactic cosmic ray propagation and associated photon emissions«. In: *Computer Physics Communications* 182.5 (May 2011), pp. 1156–1161. ISSN: 0010-4655. DOI: 10.1016/j.cpc.2011.01.017. URL: <http://dx.doi.org/10.1016/j.cpc.2011.01.017>.
- [100] Carmelo Evoli et al. »Cosmic-Ray Nuclei, Antiprotons and Gamma-rays in the Galaxy: a New Diffusion Model«. In: *JCAP* 10 (2008). [Erratum: *JCAP* 04, E01 (2016)], p. 018. DOI: 10.1088/1475-7516/2008/10/018. arXiv: 0807.4730 [astro-ph].
- [101] Carmelo Evoli et al. »Cosmic-ray propagation with *DRAGON2*: I. numerical solver and astrophysical ingredients«. In: *JCAP* 02 (2017), p. 015. DOI: 10.1088/1475-7516/2017/02/015. arXiv: 1607.07886 [astro-ph.HE].
- [102] Oscar Adriani et al. »An anomalous positron abundance in cosmic rays with energies 1.5–100 GeV«. In: *Nature* 458 (2009), pp. 607–609. DOI: 10.1038/nature07942. arXiv: 0810.4995 [astro-ph].
- [103] M. Aguilar et al. »First Result from the Alpha Magnetic Spectrometer on the International Space Station: Precision Measurement of the Positron Fraction in Primary Cosmic Rays of 0.5–350 GeV«. In: *Phys. Rev. Lett.* 110 (2013), p. 141102. DOI: 10.1103/PhysRevLett.110.141102.
- [104] L. Accardo et al. »High Statistics Measurement of the Positron Fraction in Primary Cosmic Rays of 0.5–500 GeV with the Alpha Magnetic Spectrometer on the International Space Station«. In: *Phys. Rev. Lett.* 113 (2014), p. 121101. DOI: 10.1103/PhysRevLett.113.121101.
- [105] X. Chi, E. C. M. Young and K. S. Cheng. »Pulsar-wind origin of cosmic ray positrons«. In: *Astrophys. J. Lett.* 459 (1995), pp. L83–L86. DOI: 10.1086/309943.

- [106] Dan Hooper, Pasquale Blasi and Pasquale Dario Serpico. »Pulsars as the Sources of High Energy Cosmic Ray Positrons«. In: *JCAP* 01 (2009), p. 025. DOI: 10.1088/1475-7516/2009/01/025. arXiv: 0810.1527 [astro-ph].
- [107] C. Grimani. »Pulsar birthrate set by cosmic-ray positron observations«. In: *Astron. Astrophys.* 418 (2004), pp. 649–653. DOI: 10.1051/0004-6361:20040044.
- [108] Pasquale Blasi. »The origin of the positron excess in cosmic rays«. In: *Phys. Rev. Lett.* 103 (2009), p. 051104. DOI: 10.1103/PhysRevLett.103.051104. arXiv: 0903.2794 [astro-ph.HE].
- [109] Nima Arkani-Hamed et al. »A Theory of Dark Matter«. In: *Phys. Rev. D* 79 (2009), p. 015014. DOI: 10.1103/PhysRevD.79.015014. arXiv: 0810.0713 [hep-ph].
- [110] Ilias Cholis et al. »The PAMELA Positron Excess from Annihilations into a Light Boson«. In: *JCAP* 12 (2009), p. 007. DOI: 10.1088/1475-7516/2009/12/007. arXiv: 0810.5344 [astro-ph].
- [111] Yasunori Nomura and Jesse Thaler. »Dark Matter through the Axion Portal«. In: *Phys. Rev. D* 79 (2009), p. 075008. DOI: 10.1103/PhysRevD.79.075008. arXiv: 0810.5397 [hep-ph].
- [112] Alejandro Ibarra and David Tran. »Decaying Dark Matter and the PAMELA Anomaly«. In: *JCAP* 02 (2009), p. 021. DOI: 10.1088/1475-7516/2009/02/021. arXiv: 0811.1555 [hep-ph].
- [113] Alejandro Ibarra and David Tran. »Antimatter Signatures of Gravitino Dark Matter Decay«. In: *JCAP* 07 (2008), p. 002. DOI: 10.1088/1475-7516/2008/07/002. arXiv: 0804.4596 [astro-ph].
- [114] Lars Bergstrom, Torsten Bringmann and Joakim Edsjo. »New Positron Spectral Features from Supersymmetric Dark Matter - a Way to Explain the PAMELA Data?«. In: *Phys. Rev. D* 78 (2008), p. 103520. DOI: 10.1103/PhysRevD.78.103520. arXiv: 0808.3725 [astro-ph].
- [115] Daniel Feldman, Zuowei Liu and Pran Nath. »PAMELA Positron Excess as a Signal from the Hidden Sector«. In: *Phys. Rev. D* 79 (2009), p. 063509. DOI: 10.1103/PhysRevD.79.063509. arXiv: 0810.5762 [hep-ph].
- [116] Wilfried Buchmuller et al. »Probing Gravitino Dark Matter with PAMELA and Fermi«. In: *JCAP* 09 (2009), p. 021. DOI: 10.1088/1475-7516/2009/09/021. arXiv: 0906.1187 [hep-ph].
- [117] Alejandro Ibarra, David Tran and Christoph Weniger. »Indirect Searches for Decaying Dark Matter«. In: *Int. J. Mod. Phys. A* 28 (2013), p. 1330040. DOI: 10.1142/S0217751X13300408. arXiv: 1307.6434 [hep-ph].

- [118] Alejandro Ibarra and Sebastian Wild. »Prospects of antideuteron detection from dark matter annihilations or decays at AMS-02 and GAPS«. In: *JCAP* 02 (2013), p. 021. DOI: 10.1088/1475-7516/2013/02/021. arXiv: 1209.5539 [hep-ph].
- [119] J. D. Lewin and P. F. Smith. »Review of mathematics, numerical factors, and corrections for dark matter experiments based on elastic nuclear recoil«. In: *Astropart. Phys.* 6 (1996), pp. 87–112. DOI: 10.1016/S0927-6505(96)00047-3.
- [120] Eugenio Del Nobile. »The Theory of Direct Dark Matter Detection: A Guide to Computations«. In: (Apr. 2021). DOI: 10.1007/978-3-030-95228-0. arXiv: 2104.12785 [hep-ph].
- [121] Rouven Essig, Jeremy Mardon and Tomer Volansky. »Direct Detection of Sub-GeV Dark Matter«. In: *Phys. Rev. D* 85 (2012), p. 076007. DOI: 10.1103/PhysRevD.85.076007. arXiv: 1108.5383 [hep-ph].
- [122] Timon Emken et al. »Direct Detection of Strongly Interacting Sub-GeV Dark Matter via Electron Recoils«. In: *JCAP* 09 (2019), p. 070. DOI: 10.1088/1475-7516/2019/09/070. arXiv: 1905.06348 [hep-ph].
- [123] Daniel Baxter, Yonatan Kahn and Gordan Krnjaic. »Electron Ionization via Dark Matter-Electron Scattering and the Migdal Effect«. In: *Phys. Rev. D* 101.7 (2020), p. 076014. DOI: 10.1103/PhysRevD.101.076014. arXiv: 1908.00012 [hep-ph].
- [124] Rouven Essig et al. »Relation between the Migdal Effect and Dark Matter-Electron Scattering in Isolated Atoms and Semiconductors«. In: *Phys. Rev. Lett.* 124.2 (2020), p. 021801. DOI: 10.1103/PhysRevLett.124.021801. arXiv: 1908.10881 [hep-ph].
- [125] Riccardo Catena et al. »Atomic responses to general dark matter-electron interactions«. In: *Phys. Rev. Res.* 2.3 (2020), p. 033195. DOI: 10.1103/PhysRevResearch.2.033195. arXiv: 1912.08204 [hep-ph].
- [126] Yonit Hochberg, Yue Zhao and Kathryn M. Zurek. »Superconducting Detectors for Superlight Dark Matter«. In: *Phys. Rev. Lett.* 116.1 (2016), p. 011301. DOI: 10.1103/PhysRevLett.116.011301. arXiv: 1504.07237 [hep-ph].
- [127] Yonit Hochberg et al. »Detecting Superlight Dark Matter with Fermi-Degenerate Materials«. In: *JHEP* 08 (2016), p. 057. DOI: 10.1007/JHEP08(2016)057. arXiv: 1512.04533 [hep-ph].
- [128] Rouven Essig et al. »Direct Detection of sub-GeV Dark Matter with Semiconductor Targets«. In: *JHEP* 05 (2016), p. 046. DOI: 10.1007/JHEP05(2016)046. arXiv: 1509.01598 [hep-ph].

- [129] Stephen Derenzo et al. »Direct Detection of sub-GeV Dark Matter with Scintillating Targets«. In: *Phys. Rev. D* 96.1 (2017), p. 016026. DOI: 10.1103/PhysRevD.96.016026. arXiv: 1607.01009 [hep-ph].
- [130] Yonit Hochberg et al. »Directional detection of dark matter with two-dimensional targets«. In: *Phys. Lett. B* 772 (2017), pp. 239–246. DOI: 10.1016/j.physletb.2017.06.051. arXiv: 1606.08849 [hep-ph].
- [131] Yonit Hochberg et al. »Detection of sub-MeV Dark Matter with Three-Dimensional Dirac Materials«. In: *Phys. Rev. D* 97.1 (2018), p. 015004. DOI: 10.1103/PhysRevD.97.015004. arXiv: 1708.08929 [hep-ph].
- [132] A Migdal et al. »Ionization of atoms accompanying α - and β -decay«. In: *J. Phys. USSR* 4 (1941), p. 449.
- [133] Masahiro Ibe et al. »Migdal Effect in Dark Matter Direct Detection Experiments«. In: *JHEP* 03 (2018), p. 194. DOI: 10.1007/JHEP03(2018)194. arXiv: 1707.07258 [hep-ph].
- [134] Richard H. Helm. »Inelastic and Elastic Scattering of 187-MeV Electrons from Selected Even-Even Nuclei«. In: *Phys. Rev.* 104 (1956), pp. 1466–1475. DOI: 10.1103/PhysRev.104.1466.
- [135] J. Engel. »Nuclear form-factors for the scattering of weakly interacting massive particles«. In: *Phys. Lett. B* 264 (1991), pp. 114–119. DOI: 10.1016/0370-2693(91)90712-Y.
- [136] Injun Jeong et al. »WimPyDD: An object-oriented Python code for the calculation of WIMP direct detection signals«. In: *Comput. Phys. Commun.* 276 (2022), p. 108342. DOI: 10.1016/j.cpc.2022.108342. arXiv: 2106.06207 [hep-ph].
- [137] E. Aprile et al. »Dark Matter Search Results from a One Ton-Year Exposure of XENON1T«. In: *Phys. Rev. Lett.* 121.11 (2018), p. 111302. DOI: 10.1103/PhysRevLett.121.111302. arXiv: 1805.12562 [astro-ph.CO].
- [138] Elena Aprile et al. »First Indication of Solar B8 Neutrinos via Coherent Elastic Neutrino-Nucleus Scattering with XENONnT«. In: *Phys. Rev. Lett.* 133.19 (2024), p. 191002. DOI: 10.1103/PhysRevLett.133.191002. arXiv: 2408.02877 [nucl-ex].
- [139] Zihao Bo et al. »First Indication of Solar B8 Neutrinos through Coherent Elastic Neutrino-Nucleus Scattering in PandaX-4T«. In: *Phys. Rev. Lett.* 133.19 (2024), p. 191001. DOI: 10.1103/PhysRevLett.133.191001. arXiv: 2407.10892 [hep-ex].
- [140] Jocelyn Monroe and Peter Fisher. »Neutrino Backgrounds to Dark Matter Searches«. In: *Phys. Rev. D* 76 (2007), p. 033007. DOI: 10.1103/PhysRevD.76.033007. arXiv: 0706.3019 [astro-ph].

- [141] J. D. Vergados and H. Ejiri. »Can Solar Neutrinos be a Serious Background in Direct Dark Matter Searches?« In: *Nucl. Phys. B* 804 (2008), pp. 144–159. DOI: 10.1016/j.nuclphysb.2008.06.004. arXiv: 0805.2583 [hep-ph].
- [142] Louis E. Strigari. »Neutrino Coherent Scattering Rates at Direct Dark Matter Detectors«. In: *New J. Phys.* 11 (2009), p. 105011. DOI: 10.1088/1367-2630/11/10/105011. arXiv: 0903.3630 [astro-ph.CO].
- [143] A. Gutlein et al. »Solar and atmospheric neutrinos: Background sources for the direct dark matter search«. In: *Astropart. Phys.* 34 (2010), pp. 90–96. DOI: 10.1016/j.astropartphys.2010.06.002. arXiv: 1003.5530 [hep-ph].
- [144] Ciaran A. J. O’Hare. »New Definition of the Neutrino Floor for Direct Dark Matter Searches«. In: *Phys. Rev. Lett.* 127.25 (2021), p. 251802. DOI: 10.1103/PhysRevLett.127.251802. arXiv: 2109.03116 [hep-ph].
- [145] Tarak Nath Maity. »Neutrinos as background and signal in Migdal search«. In: (Dec. 2024). arXiv: 2412.17649 [hep-ph].
- [146] »LHC Machine«. In: *JINST* 3 (2008). Ed. by Lyndon Evans and Philip Bryant, S08001. DOI: 10.1088/1748-0221/3/08/S08001.
- [147] Pran Nath et al. »The Hunt for New Physics at the Large Hadron Collider«. In: *Nucl. Phys. B Proc. Suppl.* 200-202 (2010). Ed. by George Alverson, Pran Nath and Brent D. Nelson, pp. 185–417. DOI: 10.1016/j.nuclphysbps.2010.03.001. arXiv: 1001.2693 [hep-ph].
- [148] G. Aad et al. »The ATLAS Experiment at the CERN Large Hadron Collider«. In: *JINST* 3 (2008), S08003. DOI: 10.1088/1748-0221/3/08/S08003.
- [149] S. Chatrchyan et al. »The CMS Experiment at the CERN LHC«. In: *JINST* 3 (2008), S08004. DOI: 10.1088/1748-0221/3/08/S08004.
- [150] A. Augusto Alves Jr. et al. »The LHCb Detector at the LHC«. In: *JINST* 3 (2008), S08005. DOI: 10.1088/1748-0221/3/08/S08005.
- [151] Roel Aaij et al. »LHCb Detector Performance«. In: *Int. J. Mod. Phys. A* 30.07 (2015), p. 1530022. DOI: 10.1142/S0217751X15300227. arXiv: 1412.6352 [hep-ex].
- [152] Arvind Rajaraman et al. »LHC Bounds on Interactions of Dark Matter«. In: *Phys. Rev. D* 84 (2011), p. 095013. DOI: 10.1103/PhysRevD.84.095013. arXiv: 1108.1196 [hep-ph].
- [153] Daniel Abercrombie et al. »Dark Matter benchmark models for early LHC Run-2 Searches: Report of the ATLAS/CMS Dark Matter Forum«. In: *Phys. Dark Univ.* 27 (2020). Ed. by Antonio Boveia et al., p. 100371. DOI: 10.1016/j.dark.2019.100371. arXiv: 1507.00966 [hep-ex].

- [154] Jim Alexander et al. »Dark Sectors 2016 Workshop: Community Report«. In: Aug. 2016. arXiv: 1608.08632 [hep-ph].
- [155] Aram Hayrapetyan et al. »Dark sector searches with the CMS experiment«. In: (May 2024). arXiv: 2405.13778 [hep-ex].
- [156] E. E. Radescu. »Comments on the Electromagnetic Properties of Majorana Fermions«. In: *Phys. Rev. D* 32 (1985), p. 1266. DOI: 10.1103/PhysRevD.32.1266.
- [157] Jose F. Nieves and Palash B. Pal. »Electromagnetic Properties of Neutrinos in a Medium«. In: *Phys. Rev. D* 40 (1989), p. 1693. DOI: 10.1103/PhysRevD.40.1693.
- [158] Juan Carlos D’Olivo, Jose F. Nieves and Palash B. Pal. »Electromagnetic Properties of Neutrinos in a Background of Electrons«. In: *Phys. Rev. D* 40 (1989), p. 3679. DOI: 10.1103/PhysRevD.40.3679.
- [159] Julian S. Schwinger. »On Quantum electrodynamics and the magnetic moment of the electron«. In: *Phys. Rev.* 73 (1948), pp. 416–417. DOI: 10.1103/PhysRev.73.416.
- [160] Tatsumi Aoyama et al. »Tenth-Order QED Contribution to the Electron $g-2$ and an Improved Value of the Fine Structure Constant«. In: *Phys. Rev. Lett.* 109 (2012), p. 111807. DOI: 10.1103/PhysRevLett.109.111807. arXiv: 1205.5368 [hep-ph].
- [161] Tatsumi Aoyama et al. »Tenth-Order Electron Anomalous Magnetic Moment — Contribution of Diagrams without Closed Lepton Loops«. In: *Phys. Rev. D* 91.3 (2015). [Erratum: *Phys.Rev.D* 96, 019901 (2017)], p. 033006. DOI: 10.1103/PhysRevD.91.033006. arXiv: 1412.8284 [hep-ph].
- [162] X. Fan et al. »Measurement of the Electron Magnetic Moment«. In: *Phys. Rev. Lett.* 130.7 (2023), p. 071801. DOI: 10.1103/PhysRevLett.130.071801. arXiv: 2209.13084 [physics.atom-ph].
- [163] G. W. Bennett et al. »Final Report of the Muon E821 Anomalous Magnetic Moment Measurement at BNL«. In: *Phys. Rev. D* 73 (2006), p. 072003. DOI: 10.1103/PhysRevD.73.072003. arXiv: hep-ex/0602035.
- [164] D. P. Aguillard et al. »Measurement of the Positive Muon Anomalous Magnetic Moment to 0.20 ppm«. In: *Phys. Rev. Lett.* 131.16 (2023), p. 161802. DOI: 10.1103/PhysRevLett.131.161802. arXiv: 2308.06230 [hep-ex].
- [165] Sz. Borsanyi et al. »Leading hadronic contribution to the muon magnetic moment from lattice QCD«. In: *Nature* 593.7857 (2021), pp. 51–55. DOI: 10.1038/s41586-021-03418-1. arXiv: 2002.12347 [hep-lat].

- [166] T. Blum et al. »Update of Euclidean windows of the hadronic vacuum polarization«. In: *Phys. Rev. D* 108.5 (2023), p. 054507. DOI: 10.1103/PhysRevD.108.054507. arXiv: 2301.08696 [hep-lat].
- [167] Takeo Moroi. »The Muon anomalous magnetic dipole moment in the minimal supersymmetric standard model«. In: *Phys. Rev. D* 53 (1996). [Erratum: *Phys.Rev.D* 56, 4424 (1997)], pp. 6565–6575. DOI: 10.1103/PhysRevD.53.6565. arXiv: hep-ph/9512396.
- [168] Fred Jegerlehner and Andreas Nyffeler. »The Muon $g-2$ «. In: *Phys. Rept.* 477 (2009), pp. 1–110. DOI: 10.1016/j.physrep.2009.04.003. arXiv: 0902.3360 [hep-ph].
- [169] T. Aoyama et al. »The anomalous magnetic moment of the muon in the Standard Model«. In: *Phys. Rept.* 887 (2020), pp. 1–166. DOI: 10.1016/j.physrep.2020.07.006. arXiv: 2006.04822 [hep-ph].
- [170] G. Colangelo et al. »Prospects for precise predictions of a_μ in the Standard Model«. In: (Mar. 2022). arXiv: 2203.15810 [hep-ph].
- [171] Gerard 't Hooft. »Naturalness, chiral symmetry, and spontaneous chiral symmetry breaking«. In: *NATO Sci. Ser. B* 59 (1980). Ed. by Gerard 't Hooft et al., pp. 135–157. DOI: 10.1007/978-1-4684-7571-5_9.
- [172] Matthew D. Schwartz. *Quantum Field Theory and the Standard Model*. Cambridge University Press, Mar. 2014. ISBN: 978-1-107-03473-0, 978-1-107-03473-0.
- [173] R. J. Crewther et al. »Chiral Estimate of the Electric Dipole Moment of the Neutron in Quantum Chromodynamics«. In: *Phys. Lett. B* 88 (1979). [Erratum: *Phys.Lett.B* 91, 487 (1980)], p. 123. DOI: 10.1016/0370-2693(79)90128-X.
- [174] C. A. Baker et al. »An Improved experimental limit on the electric dipole moment of the neutron«. In: *Phys. Rev. Lett.* 97 (2006), p. 131801. DOI: 10.1103/PhysRevLett.97.131801. arXiv: hep-ex/0602020.
- [175] R. D. Peccei and Helen R. Quinn. »CP Conservation in the Presence of Instantons«. In: *Phys. Rev. Lett.* 38 (1977), pp. 1440–1443. DOI: 10.1103/PhysRevLett.38.1440.
- [176] R. D. Peccei and Helen R. Quinn. »Constraints Imposed by CP Conservation in the Presence of Instantons«. In: *Phys. Rev. D* 16 (1977), pp. 1791–1797. DOI: 10.1103/PhysRevD.16.1791.
- [177] Arturo Cisneros. »Effect of neutrino magnetic moment on solar neutrino observations«. In: *Astrophys. Space Sci.* 10 (1971), pp. 87–92. DOI: 10.1007/BF00654607.

- [178] L. B. Okun, M. B. Voloshin and M. I. Vysotsky. »Neutrino Electrodynamics and Possible Effects for Solar Neutrinos«. In: *Sov. Phys. JETP* 64 (1986), pp. 446–452.
- [179] L. B. Okun, M. B. Voloshin and M. I. Vysotsky. »Electromagnetic Properties of Neutrino and Possible Semiannual Variation Cycle of the Solar Neutrino Flux«. In: *Sov. J. Nucl. Phys.* 44 (1986), p. 440.
- [180] M. B. Voloshin and M. I. Vysotsky. »Neutrino Magnetic Moment and Time Variation of Solar Neutrino Flux«. In: *Sov. J. Nucl. Phys.* 44 (1986), p. 544.
- [181] Voloshin, B. B. and Vysotsky, M.I., and Okun, L. B. »Possible electromagnetic properties of the neutrino and variations of the solar neutrino flux«. In: *Soviet Physics Uspekhi* 29.11 (Nov. 1986), p. 1070. DOI: 10.1070/PU1986v029n11ABEH003654. URL: <https://dx.doi.org/10.1070/PU1986v029n11ABEH003654>.
- [182] Yakov Borisovich Zel'Dovich. »Electromagnetic interaction with parity violation«. In: *Sov. Phys. JETP* 6.6 (1958), pp. 1184–1186.
- [183] C. S. Wood et al. »Measurement of parity nonconservation and an anapole moment in cesium«. In: *Science* 275 (1997), pp. 1759–1763. DOI: 10.1126/science.275.5307.1759.
- [184] K. Tsigitkin et al. »Observation of a Large Atomic Parity Violation Effect in Ytterbium«. In: *Phys. Rev. Lett.* 103 (2009), p. 071601. DOI: 10.1103/PhysRevLett.103.071601. arXiv: 0906.3039 [physics.atom-ph].
- [185] S. Y. Lee. »Higher-order corrections to leptonic processes and the renormalization of weinberg's theory of weak interactions in the unitary gauge«. In: *Phys. Rev. D* 6 (1972), pp. 1701–1717. DOI: 10.1103/PhysRevD.6.1701.
- [186] William A. Bardeen, R. Gastmans and B. E. Lautrup. »Static quantities in Weinberg's model of weak and electromagnetic interactions«. In: *Nucl. Phys. B* 46 (1972), pp. 319–331. DOI: 10.1016/0550-3213(72)90218-0.
- [187] J. L. Lucio, A. Rosado and A. Zepeda. »A Characteristic Size for the Neutrino«. In: *Phys. Rev. D* 31 (1985), p. 1091. DOI: 10.1103/PhysRevD.31.1091.
- [188] M. J. Musolf and Barry R. Holstein. »Observability of the anapole moment and neutrino charge radius«. In: *Phys. Rev. D* 43 (1991), pp. 2956–2970. DOI: 10.1103/PhysRevD.43.2956.
- [189] A. Rosado. »Physical electroweak anapole moment for the neutrino«. In: *Phys. Rev. D* 61 (2000), p. 013001. DOI: 10.1103/PhysRevD.61.013001.
- [190] J. Bernabeu et al. »On the charge radius of the neutrino«. In: *Phys. Rev. D* 62 (2000), p. 113012. DOI: 10.1103/PhysRevD.62.113012. arXiv: hep-ph/0008114.

- [191] Norman Dombey and A.D. Kennedy. »A calculation of the electron anapole moment«. In: *Physics Letters B* 91.3 (1980), pp. 428–430. ISSN: 0370-2693. DOI: [https://doi.org/10.1016/0370-2693\(80\)91013-8](https://doi.org/10.1016/0370-2693(80)91013-8). URL: <https://www.sciencedirect.com/science/article/pii/0370269380910138>.
- [192] J. Bernabeu, J. Papavassiliou and J. Vidal. »The Neutrino charge radius is a physical observable«. In: *Nucl. Phys. B* 680 (2004), pp. 450–478. DOI: 10.1016/j.nuclphysb.2003.12.025. arXiv: hep-ph/0210055.
- [193] J. Papavassiliou, J. Bernabeu and J. Vidal. »On the definition and observability of the neutrino charge radius«. In: *Nucl. Phys. B Proc. Suppl.* 114 (2003). Ed. by A. Morales, J. Morales and S. Cebrian, pp. 197–201. DOI: 10.1016/S0920-5632(02)01905-9. arXiv: hep-ph/0210312.
- [194] J. Papavassiliou et al. »The Effective neutrino charge radius«. In: *Eur. Phys. J. C* 33 (2004), S865–S867. DOI: 10.1140/epjcd/s2003-03-920-7. arXiv: hep-ph/0310028.
- [195] Kazuo Fujikawa and Robert Shrock. »On a neutrino electroweak radius«. In: *Phys. Rev. D* 69 (2004), p. 013007. DOI: 10.1103/PhysRevD.69.013007. arXiv: hep-ph/0309329.
- [196] Maxim Dvornikov and Alexander Studenikin. »Electric charge and magnetic moment of massive neutrino«. In: *Phys. Rev. D* 69 (2004), p. 073001. DOI: 10.1103/PhysRevD.69.073001. arXiv: hep-ph/0305206.
- [197] Kazuo Fujikawa and Robert Shrock. »Comment on ‘Observability of the neutrino charge radius’«. In: (Mar. 2003). arXiv: hep-ph/0303188.
- [198] J. Bernabeu, J. Papavassiliou and J. Vidal. »Reply to the comment by Fujikawa and Shrock on the observability of the neutrino charge radius«. In: (Mar. 2003). arXiv: hep-ph/0303202.
- [199] Maxim Pospelov and Tonnis ter Veldhuis. »Direct and indirect limits on the electromagnetic form-factors of WIMPs«. In: *Phys. Lett. B* 480 (2000), pp. 181–186. DOI: 10.1016/S0370-2693(00)00358-0. arXiv: hep-ph/0003010.
- [200] Kris Sigurdson et al. »Dark-matter electric and magnetic dipole moments«. In: *Phys. Rev. D* 70 (2004). [Erratum: Phys.Rev.D 73, 089903 (2006)], p. 083501. DOI: 10.1103/PhysRevD.70.083501. arXiv: astro-ph/0406355.
- [201] Eduard Masso, Subhendra Mohanty and Soumya Rao. »Dipolar Dark Matter«. In: *Phys. Rev. D* 80 (2009), p. 036009. DOI: 10.1103/PhysRevD.80.036009. arXiv: 0906.1979 [hep-ph].

- [202] Vernon Barger, Wai-Yee Keung and Danny Marfatia. »Electromagnetic properties of dark matter: Dipole moments and charge form factor«. In: *Phys. Lett. B* 696 (2011), pp. 74–78. DOI: 10.1016/j.physletb.2010.12.008. arXiv: 1007.4345 [hep-ph].
- [203] Tom Banks, Jean-Francois Fortin and Scott Thomas. »Direct Detection of Dark Matter Electromagnetic Dipole Moments«. In: (July 2010). arXiv: 1007.5515 [hep-ph].
- [204] A. Liam Fitzpatrick and Kathryn M. Zurek. »Dark Moments and the DAMA-CoGeNT Puzzle«. In: *Phys. Rev. D* 82 (2010), p. 075004. DOI: 10.1103/PhysRevD.82.075004. arXiv: 1007.5325 [hep-ph].
- [205] Neal Weiner and Itay Yavin. »How Dark Are Majorana WIMPs? Signals from MiDM and Rayleigh Dark Matter«. In: *Phys. Rev. D* 86 (2012), p. 075021. DOI: 10.1103/PhysRevD.86.075021. arXiv: 1206.2910 [hep-ph].
- [206] Eugenio Del Nobile et al. »Direct detection of Light Anapole and Magnetic Dipole DM«. In: *JCAP* 06 (2014), p. 002. DOI: 10.1088/1475-7516/2014/06/002. arXiv: 1401.4508 [hep-ph].
- [207] Sunghyun Kang et al. »Anapole Dark Matter after DAMA/LIBRA-phase2«. In: *JCAP* 11 (2018), p. 040. DOI: 10.1088/1475-7516/2018/11/040. arXiv: 1808.04112 [hep-ph].
- [208] Thomas Hambye and Xun-Jie Xu. »Dark matter electromagnetic dipoles: the WIMP expectation«. In: *JHEP* 11 (2021), p. 156. DOI: 10.1007/JHEP11(2021)156. arXiv: 2106.01403 [hep-ph].
- [209] Howard E. Haber and Daniel Wyler. »RADIATIVE NEUTRALINO DECAY«. In: *Nucl. Phys. B* 323 (1989), pp. 267–310. DOI: 10.1016/0550-3213(89)90143-0.
- [210] Herbi K. Dreiner et al. »Searching for a single photon from lightest neutralino decays in R-parity-violating supersymmetry at FASER«. In: *JHEP* 02 (2023), p. 120. DOI: 10.1007/JHEP02(2023)120. arXiv: 2207.05100 [hep-ph].
- [211] Florian Domingo and Herbi K. Dreiner. »Decays of a bino-like particle in the low-mass regime«. In: *SciPost Phys.* 14.5 (2023), p. 134. DOI: 10.21468/SciPostPhys.14.5.134. arXiv: 2205.08141 [hep-ph].
- [212] Mathias Garny et al. »Gamma-Ray Lines from Radiative Dark Matter Decay«. In: *JCAP* 01 (2011), p. 032. DOI: 10.1088/1475-7516/2011/01/032. arXiv: 1011.3786 [hep-ph].
- [213] Junji Hisano, Alejandro Ibarra and Ryo Nagai. »Direct detection of vector dark matter through electromagnetic multipoles«. In: *JCAP* 10 (2020), p. 015. DOI: 10.1088/1475-7516/2020/10/015. arXiv: 2007.03216 [hep-ph].

- [214] Xiaoyong Chu et al. »Multipole vector dark matter below the GeV scale«. In: *Phys. Rev. D* 108.1 (2023), p. 015029. DOI: 10.1103/PhysRevD.108.015029. arXiv: 2303.13643 [hep-ph].
- [215] F. Boudjema et al. »The Gravitino electromagnetic form-factor in N=1 broken supergravity«. In: *Phys. Lett. B* 255 (1991), pp. 249–254. DOI: 10.1016/0370-2693(91)90243-J.
- [216] Onur Yonar. *Anapole Dark Matter Direct Detection and Gravitinos*. Talk presented at DESY Theory Workshop 2024: Whispers from the Dark Universe - Particles & Fields in the Gravitational Wave Era, DESY Hamburg. Sept. 2024.
- [217] Onur Yonar. »Anapole Direct Detection of Spin-3/2 Majorana Fermions, Gravitinos and Beyond«. MA thesis. Garching, Germany: Technische Universität München, 2024.
- [218] Seong Youl Choi et al. »Hunting for hypercharge anapole dark matter in all spin scenarios«. In: *Phys. Rev. D* 109.9 (2024), p. 096001. DOI: 10.1103/PhysRevD.109.096001. arXiv: 2401.02855 [hep-ph].
- [219] Boris Kayser. »Majorana Neutrinos and their Electromagnetic Properties«. In: *Phys. Rev. D* 26 (1982), p. 1662. DOI: 10.1103/PhysRevD.26.1662.
- [220] M. Fukugita and T. Yanagida. *Physics of neutrinos and applications to astrophysics*. Theoretical and Mathematical Physics. Berlin, Germany: Springer-Verlag, 2003. ISBN: 978-3-662-05119-1, 978-3-540-43800-7, 978-3-642-07851-4. DOI: 10.1007/978-3-662-05119-1.
- [221] Marek Nowakowski, E. A. Paschos and J. M. Rodriguez. »All electromagnetic form-factors«. In: *Eur. J. Phys.* 26 (2005), pp. 545–560. DOI: 10.1088/0143-0807/26/4/001. arXiv: physics/0402058.
- [222] C. Brogini, C. Giunti and A. Studenikin. »Electromagnetic Properties of Neutrinos«. In: *Adv. High Energy Phys.* 2012 (2012), p. 459526. DOI: 10.1155/2012/459526. arXiv: 1207.3980 [hep-ph].
- [223] Carlo Giunti and Alexander Studenikin. »Neutrino electromagnetic interactions: a window to new physics«. In: *Rev. Mod. Phys.* 87 (2015), p. 531. DOI: 10.1103/RevModPhys.87.531. arXiv: 1403.6344 [hep-ph].
- [224] Joshua Ellis. »TikZ-Feynman: Feynman diagrams with TikZ«. In: *Comput. Phys. Commun.* 210 (2017), pp. 103–123. DOI: 10.1016/j.cpc.2016.08.019. arXiv: 1601.05437 [hep-ph].
- [225] Joachim Kopp, Lisa Michaels and Juri Smirnov. »Loopy Constraints on Leptophilic Dark Matter and Internal Bremsstrahlung«. In: *JCAP* 04 (2014), p. 022. DOI: 10.1088/1475-7516/2014/04/022. arXiv: 1401.6457 [hep-ph].

- [226] Jose F. Nieves. »Electromagnetic Properties of Majorana Neutrinos«. In: *Phys. Rev. D* 26 (1982), p. 3152. DOI: 10.1103/PhysRevD.26.3152.
- [227] J. Schechter and J. W. F. Valle. »Majorana Neutrinos and Magnetic Fields«. In: *Phys. Rev. D* 24 (1981). [Erratum: *Phys.Rev.D* 25, 283 (1982)], pp. 1883–1889. DOI: 10.1103/PhysRevD.25.283.
- [228] Palash B. Pal and Lincoln Wolfenstein. »Radiative Decays of Massive Neutrinos«. In: *Phys. Rev. D* 25 (1982), p. 766. DOI: 10.1103/PhysRevD.25.766.
- [229] C. Itzykson and J. B. Zuber. *Quantum Field Theory*. International Series In Pure and Applied Physics. New York: McGraw-Hill, 1980. ISBN: 978-0-486-44568-7.
- [230] Andrzej Czarnecki and Bernd Krause. »Electroweak corrections to the muon anomalous magnetic moment«. In: *Nucl. Phys. B Proc. Suppl.* 51 (1996). Ed. by J. Blumlein, F. Jegerlehner and T. Riemann, pp. 148–153. DOI: 10.1016/S0920-5632(96)90019-5. arXiv: hep-ph/9606393.
- [231] Andrzej Czarnecki and Bernd Krause. »On the dipole moments of fermions at two loops«. In: *Acta Phys. Polon. B* 28 (1997). Ed. by S. Jadach, M. Skrzypek and Z. Was, pp. 829–834. arXiv: hep-ph/9611299.
- [232] Hiren H. Patel. »Package-X: A Mathematica package for the analytic calculation of one-loop integrals«. In: *Comput. Phys. Commun.* 197 (2015), pp. 276–290. DOI: 10.1016/j.cpc.2015.08.017. arXiv: 1503.01469 [hep-ph].
- [233] Herbi K. Dreiner, Howard E. Haber and Stephen P. Martin. *From Spinors to Supersymmetry*. Cambridge, UK: Cambridge University Press, July 2023. ISBN: 978-1-139-04974-0. DOI: 10.1017/9781139049740.
- [234] Robert E. Shrock. »Electromagnetic Properties and Decays of Dirac and Majorana Neutrinos in a General Class of Gauge Theories«. In: *Nucl. Phys. B* 206 (1982), pp. 359–379. DOI: 10.1016/0550-3213(82)90273-5.
- [235] Ansgar Denner et al. »Compact Feynman rules for Majorana fermions«. In: *Phys. Lett. B* 291 (1992), pp. 278–280. DOI: 10.1016/0370-2693(92)91045-B.
- [236] Ansgar Denner et al. »Feynman rules for fermion number violating interactions«. In: *Nucl. Phys. B* 387 (1992), pp. 467–481. DOI: 10.1016/0550-3213(92)90169-C.
- [237] H. Novales-Sanchez et al. »Effects of physics beyond the standard model on the neutrino charge radius: an effective Lagrangian approach«. In: *Phys. Rev. D* 78 (2008), p. 073014. DOI: 10.1103/PhysRevD.78.073014. arXiv: 0805.4177 [hep-ph].

- [238] Daniele Binosi and Joannis Papavassiliou. »Pinch technique: Theory and applications«. In: *Physics Reports* 479.1 (2009), pp. 1–152. ISSN: 0370-1573. DOI: <https://doi.org/10.1016/j.physrep.2009.05.001>. URL: <https://www.sciencedirect.com/science/article/pii/S0370157309001409>.
- [239] Ansgar Denner, G. Weiglein and S. Dittmaier. »Gauge invariance of Green functions: Background field method versus pinch technique«. In: *Phys. Lett. B* 333 (1994), pp. 420–426. DOI: 10.1016/0370-2693(94)90162-7. arXiv: [hep-ph/9406204](https://arxiv.org/abs/hep-ph/9406204).
- [240] Joannis Papavassiliou. »On the connection between the pinch technique and the background field method«. In: *Phys. Rev. D* 51 (1995), pp. 856–861. DOI: 10.1103/PhysRevD.51.856. arXiv: [hep-ph/9410385](https://arxiv.org/abs/hep-ph/9410385).
- [241] Shoji Hashimoto et al. »The Background field method: Alternative way of deriving the pinch technique’s results«. In: *Phys. Rev. D* 50 (1994), pp. 7066–7076. DOI: 10.1103/PhysRevD.50.7066. arXiv: [hep-ph/9406271](https://arxiv.org/abs/hep-ph/9406271).
- [242] Tomohiro Abe et al. »Gauge invariant Barr-Zee type contributions to fermionic EDMs in the two-Higgs doublet models«. In: *JHEP* 01 (2014). [Erratum: *JHEP* 04, 161 (2016)], p. 106. DOI: 10.1007/JHEP01(2014)106. arXiv: [1311.4704](https://arxiv.org/abs/1311.4704) [[hep-ph](https://arxiv.org/abs/hep-ph)].
- [243] Wolfgang Altmannshofer et al. »Electron EDM in the complex two-Higgs doublet model«. In: *Phys. Rev. D* 102.11 (2020), p. 115042. DOI: 10.1103/PhysRevD.102.115042. arXiv: [2009.01258](https://arxiv.org/abs/2009.01258) [[hep-ph](https://arxiv.org/abs/hep-ph)].
- [244] L. G. Cabral-Rosetti, G. Lopez Castro and J. Pestieau. »One loop electroweak corrections to the muon anomalous magnetic moment using the pinch technique«. In: (Nov. 2002). arXiv: [hep-ph/0211437](https://arxiv.org/abs/hep-ph/0211437).
- [245] Ansgar Denner, Georg Weiglein and Stefan Dittmaier. »Application of the background field method to the electroweak standard model«. In: *Nucl. Phys. B* 440 (1995), pp. 95–128. DOI: 10.1016/0550-3213(95)00037-S. arXiv: [hep-ph/9410338](https://arxiv.org/abs/hep-ph/9410338).
- [246] R. Mertig, M. Böhm and A. Denner. »Feyn Calc - Computer-algebraic calculation of Feynman amplitudes«. In: *Computer Physics Communications* 64.3 (1991), pp. 345–359. ISSN: 0010-4655. DOI: [https://doi.org/10.1016/0010-4655\(91\)90130-D](https://doi.org/10.1016/0010-4655(91)90130-D). URL: <https://www.sciencedirect.com/science/article/pii/001046559190130D>.
- [247] Vladyslav Shtabovenko, Rolf Mertig and Frederik Orellana. »New Developments in FeynCalc 9.0«. In: *Comput. Phys. Commun.* 207 (2016), pp. 432–444. DOI: 10.1016/j.cpc.2016.06.008. arXiv: [1601.01167](https://arxiv.org/abs/1601.01167) [[hep-ph](https://arxiv.org/abs/hep-ph)].

- [248] Vladyslav Shtabovenko, Rolf Mertig and Frederik Orellana. »FeynCalc 9.3: New features and improvements«. In: *Comput. Phys. Commun.* 256 (2020), p. 107478. DOI: 10.1016/j.cpc.2020.107478. arXiv: 2001.04407 [hep-ph].
- [249] Hiren H. Patel. »Package-X 2.0: A Mathematica package for the analytic calculation of one-loop integrals«. In: *Comput. Phys. Commun.* 218 (2017), pp. 66–70. DOI: 10.1016/j.cpc.2017.04.015. arXiv: 1612.00009 [hep-ph].
- [250] Vladyslav Shtabovenko. »FeynHelpers: Connecting FeynCalc to FIRE and Package-X«. In: *Comput. Phys. Commun.* 218 (2017), pp. 48–65. DOI: 10.1016/j.cpc.2017.04.014. arXiv: 1611.06793 [physics.comp-ph].
- [251] Mathias Garny, Alejandro Ibarra and Stefan Vogl. »Signatures of Majorana dark matter with t-channel mediators«. In: *Int. J. Mod. Phys. D* 24.07 (2015), p. 1530019. DOI: 10.1142/S0218271815300190. arXiv: 1503.01500 [hep-ph].
- [252] Alejandro Ibarra and Sebastian Wild. »Dirac dark matter with a charged mediator: a comprehensive one-loop analysis of the direct detection phenomenology«. In: *JCAP* 05 (2015), p. 047. DOI: 10.1088/1475-7516/2015/05/047. arXiv: 1503.03382 [hep-ph].
- [253] Pearl Sandick, Kuver Sinha and Fei Teng. »Simplified Dark Matter Models with Charged Mediators: Prospects for Direct Detection«. In: *JHEP* 10 (2016), p. 018. DOI: 10.1007/JHEP10(2016)018. arXiv: 1608.00642 [hep-ph].
- [254] Junji Hisano, Ryo Nagai and Natsumi Nagata. »Singlet Dirac Fermion Dark Matter with Mediators at Loop«. In: *JHEP* 12 (2018), p. 059. DOI: 10.1007/JHEP12(2018)059. arXiv: 1808.06301 [hep-ph].
- [255] Michael J. Baker and Andrea Thamm. »Leptonic WIMP Coannihilation and the Current Dark Matter Search Strategy«. In: *JHEP* 10 (2018), p. 187. DOI: 10.1007/JHEP10(2018)187. arXiv: 1806.07896 [hep-ph].
- [256] Juan Herrero-Garcia, Emiliano Molinaro and Michael A. Schmidt. »Dark matter direct detection of a fermionic singlet at one loop«. In: *Eur. Phys. J. C* 78.6 (2018). [Erratum: None 82, 53 (2022)], p. 471. DOI: 10.1140/epjc/s10052-018-5935-5. arXiv: 1803.05660 [hep-ph].
- [257] Shi-Ping He. »Handbook of the analytic and expansion formulae for the muon magnetic dipole moment«. In: (Aug. 2023). arXiv: 2308.07133 [hep-ph].
- [258] Boris Kayser. »CPT, CP, and c Phases and their Effects in Majorana Particle Processes«. In: *Phys. Rev. D* 30 (1984), p. 1023. DOI: 10.1103/PhysRevD.30.1023.
- [259] Boris Kayser. »CP EFFECTS WHEN NEUTRINOS ARE THEIR OWN ANTI-PARTICLES«. In: *Adv. Ser. Direct. High Energy Phys.* 3 (1989), pp. 334–361. DOI: 10.1142/9789814503280_0008.

- [260] Palash B. Pal. »Dirac, Majorana and Weyl fermions«. In: *Am. J. Phys.* 79 (2011), pp. 485–498. DOI: 10.1119/1.3549729. arXiv: 1006.1718 [hep-ph].
- [261] Rabindra N Mohapatra and Palash B Pal. *Massive Neutrinos in Physics and Astrophysics*. 3rd. WORLD SCIENTIFIC, 2004. DOI: 10.1142/5024. eprint: <https://www.worldscientific.com/doi/pdf/10.1142/5024>. URL: <https://www.worldscientific.com/doi/abs/10.1142/5024>.
- [262] Boris Kayser and Alfred S. Goldhaber. »CPT and CP Properties of Majorana Particles, and the Consequences«. In: *Phys. Rev. D* 28 (1983), p. 2341. DOI: 10.1103/PhysRevD.28.2341.
- [263] T. Hahn and M. Perez-Victoria. »Automatized one loop calculations in four-dimensions and D-dimensions«. In: *Comput. Phys. Commun.* 118 (1999), pp. 153–165. DOI: 10.1016/S0010-4655(98)00173-8. arXiv: hep-ph/9807565.
- [264] Gunnar Källén and Eugen Merzbacher. »Elementary particle physics«. In: *Physics Today* 18.6 (1965), pp. 56–58.
- [265] Chiu Man Ho and Robert J. Scherrer. »Anapole Dark Matter«. In: *Phys. Lett. B* 722 (2013), pp. 341–346. DOI: 10.1016/j.physletb.2013.04.039. arXiv: 1211.0503 [hep-ph].
- [266] Prateek Agrawal et al. »Flavored Dark Matter, and Its Implications for Direct Detection and Colliders«. In: *Phys. Rev. D* 86 (2012), p. 055002. DOI: 10.1103/PhysRevD.86.055002. arXiv: 1109.3516 [hep-ph].
- [267] Xuyang Ning et al. »Limits on the luminance of dark matter from xenon recoil data«. In: *Nature* 618.7963 (2023), pp. 47–50. DOI: 10.1038/s41586-023-05982-0.
- [268] Riccardo Catena et al. »Crystal responses to general dark matter-electron interactions«. In: *Phys. Rev. Res.* 3.3 (2021), p. 033149. DOI: 10.1103/PhysRevResearch.3.033149. arXiv: 2105.02233 [hep-ph].
- [269] Jin-Han Liang et al. »Revisiting general dark matter-bound-electron interactions«. In: *Phys. Rev. D* 110.9 (2024), p. L091701. DOI: 10.1103/PhysRevD.110.L091701. arXiv: 2405.04855 [hep-ph].
- [270] Jin-Han Liang et al. »A systematic investigation on dark matter-electron scattering in effective field theories«. In: *JHEP* 07 (2024), p. 279. DOI: 10.1007/JHEP07(2024)279. arXiv: 2406.10912 [hep-ph].
- [271] Spencer Chang, Neal Weiner and Itay Yavin. »Magnetic Inelastic Dark Matter«. In: *Phys. Rev. D* 82 (2010), p. 125011. DOI: 10.1103/PhysRevD.82.125011. arXiv: 1007.4200 [hep-ph].

- [272] R. Agnese et al. »Search for Low-Mass Weakly Interacting Massive Particles with SuperCDMS«. In: *Phys. Rev. Lett.* 112.24 (2014), p. 241302. DOI: 10.1103/PhysRevLett.112.241302. arXiv: 1402.7137 [hep-ex].
- [273] A. H. Abdelhameed et al. »First results from the CRESST-III low-mass dark matter program«. In: *Phys. Rev. D* 100.10 (2019), p. 102002. DOI: 10.1103/PhysRevD.100.102002. arXiv: 1904.00498 [astro-ph.CO].
- [274] E. Aprile et al. »Physics reach of the XENON1T dark matter experiment«. In: *JCAP* 04 (2016), p. 027. DOI: 10.1088/1475-7516/2016/04/027. arXiv: 1512.07501 [physics.ins-det].
- [275] A. Liam Fitzpatrick et al. »The Effective Field Theory of Dark Matter Direct Detection«. In: *JCAP* 02 (2013), p. 004. DOI: 10.1088/1475-7516/2013/02/004. arXiv: 1203.3542 [hep-ph].
- [276] Nikhil Anand, A. Liam Fitzpatrick and W. C. Haxton. »Weakly interacting massive particle-nucleus elastic scattering response«. In: *Phys. Rev. C* 89.6 (2014), p. 065501. DOI: 10.1103/PhysRevC.89.065501. arXiv: 1308.6288 [hep-ph].
- [277] Riccardo Catena and Bodo Schwabe. »Form factors for dark matter capture by the Sun in effective theories«. In: *JCAP* 04 (2015), p. 042. DOI: 10.1088/1475-7516/2015/04/042. arXiv: 1501.03729 [hep-ph].
- [278] Anja Brenner, Alejandro Ibarra and Andreas Rappelt. »Conservative constraints on the effective theory of dark matter-nucleon interactions from IceCube: the impact of operator interference«. In: *JCAP* 07 (2021), p. 012. DOI: 10.1088/1475-7516/2021/07/012. arXiv: 2011.02929 [hep-ph].
- [279] Anja Brenner et al. »Complementarity of experiments in probing the non-relativistic effective theory of dark matter-nucleon interactions«. In: *JCAP* 06.06 (2022), p. 026. DOI: 10.1088/1475-7516/2022/06/026. arXiv: 2203.04210 [hep-ph].
- [280] Sunghyun Kang, Injun Jeong and Stefano Scopel. »Bracketing the direct detection exclusion plot for a WIMP of spin one half in non-relativistic effective theory«. In: *Astropart. Phys.* 151 (2023), p. 102854. DOI: 10.1016/j.astropartphys.2023.102854. arXiv: 2209.03646 [hep-ph].
- [281] R. Bernabei et al. »On electromagnetic contributions in WIMP quests«. In: *Int. J. Mod. Phys. A* 22 (2007), pp. 3155–3168. DOI: 10.1142/S0217751X07037093. arXiv: 0706.1421 [astro-ph].
- [282] Jingke Xu et al. »Search for the Migdal effect in liquid xenon with keV-level nuclear recoils«. In: *Phys. Rev. D* 109.5 (2024), p. L051101. DOI: 10.1103/PhysRevD.109.L051101. arXiv: 2307.12952 [hep-ex].

- [283] H. M. Araújo et al. »The MIGDAL experiment: Measuring a rare atomic process to aid the search for dark matter«. In: *Astropart. Phys.* 151 (2023), p. 102853. DOI: 10.1016/j.astropartphys.2023.102853. arXiv: 2207.08284 [hep-ex].
- [284] D. S. Akerib et al. »Results of a Search for Sub-GeV Dark Matter Using 2013 LUX Data«. In: *Phys. Rev. Lett.* 122.13 (2019), p. 131301. DOI: 10.1103/PhysRevLett.122.131301. arXiv: 1811.11241 [astro-ph.CO].
- [285] E. Armengaud et al. »Searching for low-mass dark matter particles with a massive Ge bolometer operated above-ground«. In: *Phys. Rev. D* 99.8 (2019), p. 082003. DOI: 10.1103/PhysRevD.99.082003. arXiv: 1901.03588 [astro-ph.GA].
- [286] Nicole F. Bell et al. »Migdal effect and photon bremsstrahlung in effective field theories of dark matter direct detection and coherent elastic neutrino-nucleus scattering«. In: *Phys. Rev. D* 101.1 (2020), p. 015012. DOI: 10.1103/PhysRevD.101.015012. arXiv: 1905.00046 [hep-ph].
- [287] Gaurav Tomar, Sunghyun Kang and Stefano Scopel. »Low-mass extension of direct detection bounds on WIMP-quark and WIMP-gluon effective interactions using the Migdal effect«. In: *Astropart. Phys.* 150 (2023), p. 102851. DOI: 10.1016/j.astropartphys.2023.102851. arXiv: 2210.00199 [hep-ph].
- [288] Nicole F. Bell et al. »Low-mass inelastic dark matter direct detection via the Migdal effect«. In: *Phys. Rev. D* 104.7 (2021), p. 076013. DOI: 10.1103/PhysRevD.104.076013. arXiv: 2103.05890 [hep-ph].
- [289] Jiwei Li et al. »Spin-dependent sub-GeV inelastic dark matter-electron scattering and Migdal effect. Part I. Velocity independent operator«. In: *JCAP* 04 (2023), p. 020. DOI: 10.1088/1475-7516/2023/04/020. arXiv: 2210.15474 [hep-ph].
- [290] P. Agnes et al. »Search for Dark-Matter–Nucleon Interactions via Migdal Effect with DarkSide-50«. In: *Phys. Rev. Lett.* 130.10 (2023), p. 101001. DOI: 10.1103/PhysRevLett.130.101001. arXiv: 2207.11967 [hep-ex].
- [291] Sunghyun Kang, Stefano Scopel and Gaurav Tomar. »Low-mass constraints on WIMP effective models of inelastic scattering using the Migdal effect«. In: *JCAP* 01 (2025), p. 035. DOI: 10.1088/1475-7516/2025/01/035. arXiv: 2407.16187 [hep-ph].
- [292] Peter Galison and Aneesh Manohar. »TWO Z's OR NOT TWO Z's?« In: *Phys. Lett. B* 136 (1984), pp. 279–283. DOI: 10.1016/0370-2693(84)91161-4.
- [293] Bob Holdom. »Two U(1)'s and Epsilon Charge Shifts«. In: *Phys. Lett. B* 166 (1986), pp. 196–198. DOI: 10.1016/0370-2693(86)91377-8.

- [294] Neal Weiner and Itay Yavin. »UV completions of magnetic inelastic and Rayleigh dark matter for the Fermi Line(s)«. In: *Phys. Rev. D* 87.2 (2013), p. 023523. DOI: 10.1103/PhysRevD.87.023523. arXiv: 1209.1093 [hep-ph].
- [295] Bradley J. Kavanagh, Paolo Panci and Robert Ziegler. »Faint Light from Dark Matter: Classifying and Constraining Dark Matter-Photon Effective Operators«. In: *JHEP* 04 (2019), p. 089. DOI: 10.1007/JHEP04(2019)089. arXiv: 1810.00033 [hep-ph].
- [296] David C. Latimer. »Two-photon interactions with Majorana fermions«. In: *Phys. Rev. D* 94.9 (2016), p. 093010. DOI: 10.1103/PhysRevD.94.093010. arXiv: 1706.05071 [hep-ph].
- [297] David C. Latimer. »Anapole dark matter annihilation into photons«. In: *Phys. Rev. D* 95.9 (2017), p. 095023. DOI: 10.1103/PhysRevD.95.095023. arXiv: 1706.08029 [hep-ph].
- [298] Kiana Walter, Kobi Hall and David C. Latimer. »Aligning a Majorana fermion’s anapole moment with an external current through photon emission mediated by the fermion’s generalized polarizabilities«. In: *Phys. Rev. D* 106.9 (2022), p. 096021. DOI: 10.1103/PhysRevD.106.096021. arXiv: 2211.07742 [hep-ph].
- [299] Lukas Karoly and David C. Latimer. »The impact of electric currents on Majorana dark matter at freeze out«. In: (July 2023). arXiv: 2307.08769 [hep-ph].
- [300] E. Aprile et al. »First Dark Matter Search Results from the XENON1T Experiment«. In: *Phys. Rev. Lett.* 119.18 (2017), p. 181301. DOI: 10.1103/PhysRevLett.119.181301. arXiv: 1705.06655 [astro-ph.CO].
- [301] J. Aalbers et al. »First Dark Matter Search Results from the LUX-ZEPLIN (LZ) Experiment«. In: *Phys. Rev. Lett.* 131.4 (2023), p. 041002. DOI: 10.1103/PhysRevLett.131.041002. arXiv: 2207.03764 [hep-ex].
- [302] C. Amole et al. »Dark Matter Search Results from the Complete Exposure of the PICO-60 C₃F₈ Bubble Chamber«. In: *Phys. Rev. D* 100.2 (2019), p. 022001. DOI: 10.1103/PhysRevD.100.022001. arXiv: 1902.04031 [astro-ph.CO].
- [303] P. Agnes et al. »Low-Mass Dark Matter Search with the DarkSide-50 Experiment«. In: *Phys. Rev. Lett.* 121.8 (2018), p. 081307. DOI: 10.1103/PhysRevLett.121.081307. arXiv: 1802.06994 [astro-ph.HE].
- [304] Jean-Francois Fortin and Tim M. P. Tait. »Collider Constraints on Dipole-Interacting Dark Matter«. In: *Phys. Rev. D* 85 (2012), p. 063506. DOI: 10.1103/PhysRevD.85.063506. arXiv: 1103.3289 [hep-ph].

- [305] Xiaoyong Chu, Josef Pradler and Lukas Semmelrock. »Light dark states with electromagnetic form factors«. In: *Phys. Rev. D* 99.1 (2019), p. 015040. DOI: 10.1103/PhysRevD.99.015040. arXiv: 1811.04095 [hep-ph].
- [306] Genevieve Belanger, Ali Mjallal and Alexander Pukhov. »Recasting direct detection limits within micrOMEGAs and implication for non-standard Dark Matter scenarios«. In: *Eur. Phys. J. C* 81.3 (2021), p. 239. DOI: 10.1140/epjc/s10052-021-09012-z. arXiv: 2003.08621 [hep-ph].
- [307] Rouven Essig, Tomer Volansky and Tien-Tien Yu. »New Constraints and Prospects for sub-GeV Dark Matter Scattering off Electrons in Xenon«. In: *Phys. Rev. D* 96.4 (2017), p. 043017. DOI: 10.1103/PhysRevD.96.043017. arXiv: 1703.00910 [hep-ph].
- [308] Liron Barak et al. »SENSEI: Direct-Detection Results on sub-GeV Dark Matter from a New Skipper-CCD«. In: *Phys. Rev. Lett.* 125.17 (2020), p. 171802. DOI: 10.1103/PhysRevLett.125.171802. arXiv: 2004.11378 [astro-ph.CO].
- [309] Gaurav Tomar. *Searching for Sub-GeV dark matter using the Migdal effect*. Talk presented at the 17th International Conference on Interconnections between Particle Physics and Cosmology (PPC2024), Hyderabad, India. Oct. 2024.
- [310] Chiara Arina et al. »Light and Darkness: consistently coupling dark matter to photons via effective operators«. In: *Eur. Phys. J. C* 81.3 (2021), p. 223. DOI: 10.1140/epjc/s10052-021-09010-1. arXiv: 2005.12789 [hep-ph].
- [311] Luis G. Cabral-Rosetti, Myriam Mondragon and Esteban Reyes-Perez. »Toroidal Dipole Moment of the Lightest Neutralino in the cMSSM«. In: (June 2012). arXiv: 1206.5052 [hep-ph].
- [312] L. G. Cabral-Rosetti, M. Mondragon and E. Reyes Perez. »Toroidal dipole moment of the lightest neutralino in the MSSM«. In: *J. Phys. Conf. Ser.* 315 (2011). Ed. by David Delepine, p. 012007. DOI: 10.1088/1742-6596/315/1/012007.
- [313] L. G. Cabral-Rosetti, M. Mondragón and E. A. Reyes Pérez. »Toroidal dipole moment of the LSP in the cMSSM«. In: *J. Phys. Conf. Ser.* 485 (2014). Ed. by Myriam Mondragón et al., p. 012019. DOI: 10.1088/1742-6596/485/1/012019.
- [314] Luis G. Cabral-Rosetti, Myriam Mondragón and Esteban Reyes-Pérez. »Anapole moment of the lightest neutralino in the cMSSM«. In: *Nucl. Phys. B* 907 (2016), pp. 1–17. DOI: 10.1016/j.nuclphysb.2016.03.025. arXiv: 1504.01213 [hep-ph].

- [315] Pierre Fayet and S. Ferrara. »Supersymmetry«. In: *Phys. Rept.* 32 (1977), pp. 249–334. DOI: 10.1016/0370-1573(77)90066-7.
- [316] Hans Peter Nilles. »Supersymmetry, Supergravity and Particle Physics«. In: *Phys. Rept.* 110 (1984), pp. 1–162. DOI: 10.1016/0370-1573(84)90008-5.
- [317] Stephen P. Martin. »A Supersymmetry primer«. In: *Adv. Ser. Direct. High Energy Phys.* 18 (1998). Ed. by Gordon L. Kane, pp. 1–98. DOI: 10.1142/9789812839657_0001. arXiv: hep-ph/9709356.
- [318] Steven Weinberg. *The quantum theory of fields. Vol. 3: Supersymmetry*. Cambridge University Press, June 2013. ISBN: 978-0-521-67055-5.
- [319] M. Drees, R. Godbole and P. Roy. *Theory and phenomenology of sparticles: An account of four-dimensional N=1 supersymmetry in high energy physics*. 2004.
- [320] Ian J. R. Aitchison. »Supersymmetry and the MSSM: An Elementary introduction«. In: (May 2005). arXiv: hep-ph/0505105.
- [321] J. Terning. *Modern supersymmetry: Dynamics and duality*. 2006. DOI: 10.1093/acprof:oso/9780198567639.001.0001.
- [322] Fernando Quevedo, Sven Krippendorff and Oliver Schlotterer. »Cambridge Lectures on Supersymmetry and Extra Dimensions«. In: (Nov. 2010). arXiv: 1011.1491 [hep-th].
- [323] Rudolf Haag, Jan T. Lopuszanski and Martin Sohnius. »All Possible Generators of Supersymmetries of the s Matrix«. In: *Nucl. Phys. B* 88 (1975), p. 257. DOI: 10.1016/0550-3213(75)90279-5.
- [324] Steven Weinberg. »Supersymmetry at Ordinary Energies. 1. Masses and Conservation Laws«. In: *Phys. Rev. D* 26 (1982), p. 287. DOI: 10.1103/PhysRevD.26.287.
- [325] N. Sakai and Tsutomu Yanagida. »Proton Decay in a Class of Supersymmetric Grand Unified Models«. In: *Nucl. Phys. B* 197 (1982), p. 533. DOI: 10.1016/0550-3213(82)90457-6.
- [326] K. Abe et al. »Search for proton decay via $p \rightarrow e^+\pi^0$ and $p \rightarrow \mu^+\pi^0$ in 0.31 megaton-years exposure of the Super-Kamiokande water Cherenkov detector«. In: *Phys. Rev. D* 95.1 (2017), p. 012004. DOI: 10.1103/PhysRevD.95.012004. arXiv: 1610.03597 [hep-ex].
- [327] M. Tanaka et al. »Search for proton decay into three charged leptons in 0.37 megaton-years exposure of the Super-Kamiokande«. In: *Phys. Rev. D* 101.5 (2020), p. 052011. DOI: 10.1103/PhysRevD.101.052011. arXiv: 2001.08011 [hep-ex].

- [328] Ali H. Chamseddine, Richard L. Arnowitt and Pran Nath. »Locally Supersymmetric Grand Unification«. In: *Phys. Rev. Lett.* 49 (1982), p. 970. DOI: 10.1103/PhysRevLett.49.970.
- [329] Michael Dine, Ann E. Nelson and Yuri Shirman. »Low-energy dynamical supersymmetry breaking simplified«. In: *Phys. Rev. D* 51 (1995), pp. 1362–1370. DOI: 10.1103/PhysRevD.51.1362. arXiv: hep-ph/9408384.
- [330] Lisa Randall and Raman Sundrum. »Out of this world supersymmetry breaking«. In: *Nucl. Phys. B* 557 (1999), pp. 79–118. DOI: 10.1016/S0550-3213(99)00359-4. arXiv: hep-th/9810155.
- [331] Gian F. Giudice et al. »Gaugino mass without singlets«. In: *JHEP* 12 (1998), p. 027. DOI: 10.1088/1126-6708/1998/12/027. arXiv: hep-ph/9810442.
- [332] Alex Pomarol and Riccardo Rattazzi. »Sparticle masses from the superconformal anomaly«. In: *JHEP* 05 (1999), p. 013. DOI: 10.1088/1126-6708/1999/05/013. arXiv: hep-ph/9903448.
- [333] Jonathan A. Bagger, Takeo Moroi and Erich Poppitz. »Anomaly mediation in supergravity theories«. In: *JHEP* 04 (2000), p. 009. DOI: 10.1088/1126-6708/2000/04/009. arXiv: hep-th/9911029.
- [334] Abdelhak Djouadi, Jean-Loic Kneur and Gilbert Moultaka. »SuSpect: A Fortran code for the supersymmetric and Higgs particle spectrum in the MSSM«. In: *Comput. Phys. Commun.* 176 (2007), pp. 426–455. DOI: 10.1016/j.cpc.2006.11.009. arXiv: hep-ph/0211331.
- [335] S. Navas et al. »Review of particle physics«. In: *Phys. Rev. D* 110.3 (2024), p. 030001. DOI: 10.1103/PhysRevD.110.030001.
- [336] Gino Isidori et al. »Flavour physics at large $\tan(\beta)$ with a Bino-like LSP«. In: *Phys. Rev. D* 75 (2007), p. 115019. DOI: 10.1103/PhysRevD.75.115019. arXiv: hep-ph/0703035.
- [337] S. Heinemeyer, O. Stal and G. Weiglein. »Interpreting the LHC Higgs Search Results in the MSSM«. In: *Phys. Lett. B* 710 (2012), pp. 201–206. DOI: 10.1016/j.physletb.2012.02.084. arXiv: 1112.3026 [hep-ph].
- [338] Karim Benakli et al. »The Di-Photon Excess in a Perturbative SUSY Model«. In: *Nucl. Phys. B* 911 (2016), pp. 127–162. DOI: 10.1016/j.nuclphysb.2016.07.027. arXiv: 1605.05313 [hep-ph].
- [339] Martin Beneke, Stefan Lederer and Clara Peset. »Electroweak resummation of neutralino dark-matter annihilation into high-energy photons«. In: *JHEP* 01 (2023), p. 171. DOI: 10.1007/JHEP01(2023)171. arXiv: 2211.14341 [hep-ph].

- [340] James D. Wells. »Implications of supersymmetry breaking with a little hierarchy between gauginos and scalars«. In: *11th International Conference on Supersymmetry and the Unification of Fundamental Interactions*. June 2003. arXiv: [hep-ph/0306127](#).
- [341] Nima Arkani-Hamed and Savvas Dimopoulos. »Supersymmetric unification without low energy supersymmetry and signatures for fine-tuning at the LHC«. In: *JHEP* 06 (2005), p. 073. DOI: [10.1088/1126-6708/2005/06/073](#). arXiv: [hep-th/0405159](#).
- [342] G. F. Giudice and A. Romanino. »Split supersymmetry«. In: *Nucl. Phys. B* 699 (2004). [Erratum: *Nucl.Phys.B* 706, 487–487 (2005)], pp. 65–89. DOI: [10.1016/j.nuclphysb.2004.08.001](#). arXiv: [hep-ph/0406088](#).
- [343] N. Arkani-Hamed et al. »Aspects of split supersymmetry«. In: *Nucl. Phys. B* 709 (2005), pp. 3–46. DOI: [10.1016/j.nuclphysb.2004.12.026](#). arXiv: [hep-ph/0409232](#).
- [344] Manimala Chakraborti et al. » $(g-2)_\mu$ and SUSY dark matter: direct detection and collider search complementarity«. In: *Eur. Phys. J. C* 82.5 (2022), p. 483. DOI: [10.1140/epjc/s10052-022-10414-w](#). arXiv: [2112.01389 \[hep-ph\]](#).
- [345] Manimala Chakraborti, Sven Heinemeyer and Ipsita Saha. »Consistent Excesses in the Search for $\tilde{\chi}_2^0 \tilde{\chi}_1^\pm$: Wino/bino vs. Higgsino Dark Matter«. In: *Eur. Phys. J. C* 84.8 (2024), p. 812. DOI: [10.1140/epjc/s10052-024-13180-z](#). arXiv: [2403.14759 \[hep-ph\]](#).
- [346] Christopher Brust et al. »SUSY, the Third Generation and the LHC«. In: *JHEP* 03 (2012), p. 103. DOI: [10.1007/JHEP03\(2012\)103](#). arXiv: [1110.6670 \[hep-ph\]](#).
- [347] P. S. Bhupal Dev, Amarjit Soni and Fang Xu. »Hints of natural supersymmetry in flavor anomalies?«. In: *Phys. Rev. D* 106.1 (2022), p. 015014. DOI: [10.1103/PhysRevD.106.015014](#). arXiv: [2106.15647 \[hep-ph\]](#).
- [348] Serguei Chatrchyan et al. »Observation of a New Boson at a Mass of 125 GeV with the CMS Experiment at the LHC«. In: *Phys. Lett. B* 716 (2012), pp. 30–61. DOI: [10.1016/j.physletb.2012.08.021](#). arXiv: [1207.7235 \[hep-ex\]](#).
- [349] Georges Aad et al. »Observation of a new particle in the search for the Standard Model Higgs boson with the ATLAS detector at the LHC«. In: *Phys. Lett. B* 716 (2012), pp. 1–29. DOI: [10.1016/j.physletb.2012.08.020](#). arXiv: [1207.7214 \[hep-ex\]](#).
- [350] Howard E. Haber and Ralf Hempfling. »The Renormalization group improved Higgs sector of the minimal supersymmetric model«. In: *Phys. Rev. D* 48 (1993), pp. 4280–4309. DOI: [10.1103/PhysRevD.48.4280](#). arXiv: [hep-ph/9307201](#).

- [351] Howard E. Haber, Ralf Hempfling and Andre H. Hoang. »Approximating the radiatively corrected Higgs mass in the minimal supersymmetric model«. In: *Z. Phys. C* 75 (1997), pp. 539–554. DOI: 10.1007/s002880050498. arXiv: hep-ph/9609331.
- [352] P. Kant et al. »Light MSSM Higgs boson mass to three-loop accuracy«. In: *JHEP* 08 (2010), p. 104. DOI: 10.1007/JHEP08(2010)104. arXiv: 1005.5709 [hep-ph].
- [353] B. C. Allanach. »SOFTSUSY: a program for calculating supersymmetric spectra«. In: *Comput. Phys. Commun.* 143 (2002), pp. 305–331. DOI: 10.1016/S0010-4655(01)00460-X. arXiv: hep-ph/0104145 [hep-ph].
- [354] Peter Athron et al. »FlexibleSUSY—A spectrum generator generator for supersymmetric models«. In: *Comput. Phys. Commun.* 190 (2015), pp. 139–172. DOI: 10.1016/j.cpc.2014.12.020. arXiv: 1406.2319 [hep-ph].
- [355] Robert V. Harlander, Jonas Klappert and Alexander Voigt. »Higgs mass prediction in the MSSM at three-loop level in a pure $\overline{\text{DR}}$ context«. In: *Eur. Phys. J. C* 77.12 (2017), p. 814. DOI: 10.1140/epjc/s10052-017-5368-6. arXiv: 1708.05720 [hep-ph].
- [356] W. Hollik and H. Rzehak. »The Sfermion mass spectrum of the MSSM at the one loop level«. In: *Eur. Phys. J. C* 32 (2003), pp. 127–133. DOI: 10.1140/epjc/s2003-01387-9. arXiv: hep-ph/0305328.
- [357] F. Gabbiani et al. »A Complete analysis of FCNC and CP constraints in general SUSY extensions of the standard model«. In: *Nucl. Phys. B* 477 (1996), pp. 321–352. DOI: 10.1016/0550-3213(96)00390-2. arXiv: hep-ph/9604387.
- [358] Michael Dine, Alex Kagan and Stuart Samuel. »Naturalness in Supersymmetry, or Raising the Supersymmetry Breaking Scale«. In: *Phys. Lett. B* 243 (1990), pp. 250–256. DOI: 10.1016/0370-2693(90)90847-Y.
- [359] K. Agashe and M. Graesser. »Supersymmetry breaking and the supersymmetric flavor problem: An Analysis of decoupling the first two generation scalars«. In: *Phys. Rev. D* 59 (1999), p. 015007. DOI: 10.1103/PhysRevD.59.015007. arXiv: hep-ph/9801446.
- [360] Marco Cirelli, Nicolao Fornengo and Alessandro Strumia. »Minimal dark matter«. In: *Nucl. Phys. B* 753 (2006), pp. 178–194. DOI: 10.1016/j.nuclphysb.2006.07.012. arXiv: hep-ph/0512090.
- [361] J. Abdallah et al. »Searches for supersymmetric particles in e^+e^- collisions up to 208-GeV and interpretation of the results within the MSSM«. In: *Eur. Phys. J. C* 31 (2003), pp. 421–479. DOI: 10.1140/epjc/s2003-01355-5. arXiv: hep-ex/0311019.

- [362] Georges Aad et al. »Search for direct stau production in events with two hadronic τ -leptons in $\sqrt{s} = 13$ TeV pp collisions with the ATLAS detector«. In: *Phys. Rev. D* 101.3 (2020), p. 032009. DOI: 10.1103/PhysRevD.101.032009. arXiv: 1911.06660 [hep-ex].
- [363] S. Schael et al. »Precision electroweak measurements on the Z resonance«. In: *Phys. Rept.* 427 (2006), pp. 257–454. DOI: 10.1016/j.physrep.2005.12.006. arXiv: hep-ex/0509008.
- [364] LEP2 SUSY Working Group. *Combined LEP Chargino Results, up to 208 GeV for large m_0* . https://lepsusy.web.cern.ch/lepsusy/www/inos_moriond01/charginos_pub.html. Accessed: 2025-02-17. 2001.
- [365] Georges Aad et al. »Search for direct pair production of sleptons and charginos decaying to two leptons and neutralinos with mass splittings near the W -boson mass in $\sqrt{s} = 13$ TeV pp collisions with the ATLAS detector«. In: *JHEP* 06 (2023), p. 031. DOI: 10.1007/JHEP06(2023)031. arXiv: 2209.13935 [hep-ex].
- [366] G. Belanger et al. »MicrOMEGAs: A Program for calculating the relic density in the MSSM«. In: *Comput. Phys. Commun.* 149 (2002), pp. 103–120. DOI: 10.1016/S0010-4655(02)00596-9. arXiv: hep-ph/0112278.
- [367] G. Belanger et al. »micrOMEGAs: Version 1.3«. In: *Comput. Phys. Commun.* 174 (2006), pp. 577–604. DOI: 10.1016/j.cpc.2005.12.005. arXiv: hep-ph/0405253.
- [368] G. Belanger et al. »micrOMEGAs_3: A program for calculating dark matter observables«. In: *Comput. Phys. Commun.* 185 (2014), pp. 960–985. DOI: 10.1016/j.cpc.2013.10.016. arXiv: 1305.0237 [hep-ph].
- [369] D. Barducci et al. »Collider limits on new physics within micrOMEGAs_4.3«. In: *Comput. Phys. Commun.* 222 (2018), pp. 327–338. DOI: 10.1016/j.cpc.2017.08.028. arXiv: 1606.03834 [hep-ph].
- [370] Gaël Alguero et al. »Constraining new physics with SModelS version 2«. In: *JHEP* 08 (2022), p. 068. DOI: 10.1007/JHEP08(2022)068. arXiv: 2112.00769 [hep-ph].
- [371] Philip Bechtle et al. »HiggsBounds: Confronting Arbitrary Higgs Sectors with Exclusion Bounds from LEP and the Tevatron«. In: *Comput. Phys. Commun.* 181 (2010), pp. 138–167. DOI: 10.1016/j.cpc.2009.09.003. arXiv: 0811.4169 [hep-ph].
- [372] Philip Bechtle et al. »HiggsBounds 2.0.0: Confronting Neutral and Charged Higgs Sector Predictions with Exclusion Bounds from LEP and the Tevatron«. In: *Comput. Phys. Commun.* 182 (2011), pp. 2605–2631. DOI: 10.1016/j.cpc.2011.07.015. arXiv: 1102.1898 [hep-ph].

- [373] Philip Bechtle et al. »Recent Developments in HiggsBounds and a Preview of HiggsSignals«. In: *PoS CHARGED2012* (2012). Ed. by Rikard Enberg and Arnaud Ferrari, p. 024. DOI: 10.22323/1.156.0024. arXiv: 1301.2345 [hep-ph].
- [374] Philip Bechtle et al. »HiggsBounds-4: Improved Tests of Extended Higgs Sectors against Exclusion Bounds from LEP, the Tevatron and the LHC«. In: *Eur. Phys. J. C* 74.3 (2014), p. 2693. DOI: 10.1140/epjc/s10052-013-2693-2. arXiv: 1311.0055 [hep-ph].
- [375] Oscar Stål and Tim Stefaniak. »Constraining extended Higgs sectors with HiggsSignals«. In: *PoS EPS-HEP2013* (2013), p. 314. DOI: 10.22323/1.180.0314. arXiv: 1310.4039 [hep-ph].
- [376] F. Mahmoudi. »SuperIso v3.0, flavor physics observables calculations: Extension to NMSSM«. In: *Comput. Phys. Commun.* 180 (2009), pp. 1718–1719. DOI: 10.1016/j.cpc.2009.05.001.
- [377] Peter Athron et al. »GM2Calc: Precise MSSM prediction for $(g - 2)$ of the muon«. In: *Eur. Phys. J. C* 76.2 (2016), p. 62. DOI: 10.1140/epjc/s10052-015-3870-2. arXiv: 1510.08071 [hep-ph].
- [378] Peter Z. Skands et al. »SUSY Les Houches accord: Interfacing SUSY spectrum calculators, decay packages, and event generators«. In: *JHEP* 07 (2004), p. 036. DOI: 10.1088/1126-6708/2004/07/036. arXiv: hep-ph/0311123.
- [379] B. C. Allanach et al. »SUSY Les Houches Accord 2«. In: *Comput. Phys. Commun.* 180 (2009), pp. 8–25. DOI: 10.1016/j.cpc.2008.08.004. arXiv: 0801.0045 [hep-ph].
- [380] Andy Buckley. »PySLHA: a Pythonic interface to SUSY Les Houches Accord data«. In: *Eur. Phys. J. C* 75.10 (2015), p. 467. DOI: 10.1140/epjc/s10052-015-3638-8. arXiv: 1305.4194 [hep-ph].
- [381] Frank S. Thomas. *SLHAea - containers for SUSY Les Houches Accord input/output*. GitHub repository. 2025. URL: <https://github.com/fthomas/slhaea> (visited on 19/02/2025).
- [382] J. A. Casas, A. Lleyda and C. Munoz. »Strong constraints on the parameter space of the MSSM from charge and color breaking minima«. In: *Nucl. Phys. B* 471 (1996), pp. 3–58. DOI: 10.1016/0550-3213(96)00194-0. arXiv: hep-ph/9507294.
- [383] Toby Falk et al. »New constraints on superpartner masses«. In: *Phys. Lett. B* 367 (1996), pp. 183–187. DOI: 10.1016/0370-2693(95)01430-6. arXiv: hep-ph/9510308.

- [384] Howard Baer, Michal Brhlik and Diego Castano. »Constraints on the minimal supergravity model from nonstandard vacua«. In: *Phys. Rev. D* 54 (1996), pp. 6944–6956. DOI: 10.1103/PhysRevD.54.6944. arXiv: hep-ph/9607465.
- [385] J. Alberto Casas. »Charge and color breaking«. In: *Adv. Ser. Direct. High Energy Phys.* 21 (2010). Ed. by Gordon L. Kane, pp. 469–493. DOI: 10.1142/9789814307505_0012. arXiv: hep-ph/9707475.
- [386] Junji Hisano and Shohei Sugiyama. »Charge-breaking constraints on left-right mixing of stau’s«. In: *Phys. Lett. B* 696 (2011). [Erratum: Phys.Lett.B 719, 472–473 (2013)], pp. 92–96. DOI: 10.1016/j.physletb.2010.12.013. arXiv: 1011.0260 [hep-ph].
- [387] Teppei Kitahara and Takahiro Yoshinaga. »Stau with Large Mass Difference and Enhancement of the Higgs to Diphoton Decay Rate in the MSSM«. In: *JHEP* 05 (2013), p. 035. DOI: 10.1007/JHEP05(2013)035. arXiv: 1303.0461 [hep-ph].
- [388] Xuyang Ning et al. »Search for lepton portal dark matter in the PandaX-4T experiment«. In: (Aug. 2024). arXiv: 2408.14730 [hep-ex].
- [389] R. Escribano and E. Masso. »Improved bounds on the electromagnetic dipole moments of the τ lepton«. In: *Phys. Lett. B* 395 (1997), pp. 369–372. DOI: 10.1016/S0370-2693(97)00059-2. arXiv: hep-ph/9609423.
- [390] Aram Hayrapetyan et al. »Observation of $\gamma\gamma \rightarrow \tau\tau$ in proton-proton collisions and limits on the anomalous electromagnetic moments of the τ lepton«. In: *Rept. Prog. Phys.* 87.10 (2024), p. 107801. DOI: 10.1088/1361-6633/ad6fcb. arXiv: 2406.03975 [hep-ex].
- [391] ZeQiang Wang. »Probing τ lepton dipole moments at future Muon Colliders«. In: *PoS ICHEP2024* (2025), p. 327. DOI: 10.22323/1.476.0327. arXiv: 2410.12663 [hep-ph].
- [392] Kartik Bhide and Valerie Lang. »Probing optimal measurements of the electromagnetic dipole moments of the τ lepton«. In: (Oct. 2024). arXiv: 2410.23070 [hep-ph].
- [393] H. Denizli, A. Senol and M. Köksal. »Constraints on τ electromagnetic moments via tau pair production at the Muon colliders«. In: (Aug. 2024). arXiv: 2408.16106 [hep-ph].
- [394] Xulei Sun, Xiaorong Zhou and Yongcheng Wu. »Search for the Electric Dipole Moment of the Tau Lepton at the Super Tau-Charm Facility«. In: (Nov. 2024). arXiv: 2411.19469 [hep-ex].
- [395] Xiao-Gang He et al. »Precise measurement of CP violating τ EDM through $e^+e^- \rightarrow \gamma^*, \psi(2s) \rightarrow \tau^+\tau^-$ «. In: (Jan. 2025). arXiv: 2501.06687 [hep-ph].

- [396] »Search for electroweak SUSY production in final states with two τ -leptons in $\sqrt{s} = 13$ TeV pp collisions with the ATLAS detector«. In: (2023).
- [397] Torsten Bringmann et al. »Fermi LAT Search for Internal Bremsstrahlung Signatures from Dark Matter Annihilation«. In: *JCAP* 07 (2012), p. 054. DOI: 10.1088/1475-7516/2012/07/054. arXiv: 1203.1312 [hep-ph].
- [398] Mathias Garny et al. »Majorana Dark Matter with a Coloured Mediator: Collider vs Direct and Indirect Searches«. In: *JHEP* 06 (2014), p. 169. DOI: 10.1007/JHEP06(2014)169. arXiv: 1403.4634 [hep-ph].
- [399] Qing-Hong Cao, Ernest Ma and Gabe Shaughnessy. »Dark Matter: The Leptonic Connection«. In: *Phys. Lett. B* 673 (2009), pp. 152–155. DOI: 10.1016/j.physletb.2009.02.015. arXiv: 0901.1334 [hep-ph].
- [400] Mathias Garny, Alejandro Ibarra and Stefan Vogl. »Antiproton constraints on dark matter annihilations from internal electroweak bremsstrahlung«. In: *JCAP* 07 (2011), p. 028. DOI: 10.1088/1475-7516/2011/07/028. arXiv: 1105.5367 [hep-ph].
- [401] Neil D. Christensen and Claude Duhr. »FeynRules - Feynman rules made easy«. In: *Comput. Phys. Commun.* 180 (2009), pp. 1614–1641. DOI: 10.1016/j.cpc.2009.02.018. arXiv: 0806.4194 [hep-ph].
- [402] Neil D. Christensen et al. »A Comprehensive approach to new physics simulations«. In: *Eur. Phys. J. C* 71 (2011), p. 1541. DOI: 10.1140/epjc/s10052-011-1541-5. arXiv: 0906.2474 [hep-ph].
- [403] Adam Alloul et al. »FeynRules 2.0 - A complete toolbox for tree-level phenomenology«. In: *Comput. Phys. Commun.* 185 (2014), pp. 2250–2300. DOI: 10.1016/j.cpc.2014.04.012. arXiv: 1310.1921 [hep-ph].
- [404] Geneviève Bélanger et al. »micrOMEGAs5.0 : Freeze-in«. In: *Comput. Phys. Commun.* 231 (2018), pp. 173–186. DOI: 10.1016/j.cpc.2018.04.027. arXiv: 1801.03509 [hep-ph].
- [405] Alexander Belyaev, Neil D. Christensen and Alexander Pukhov. »CalcHEP 3.4 for collider physics within and beyond the Standard Model«. In: *Comput. Phys. Commun.* 184 (2013), pp. 1729–1769. DOI: 10.1016/j.cpc.2013.01.014. arXiv: 1207.6082 [hep-ph].
- [406] Xiaoyong Chu, Thomas Hambye and Michel H. G. Tytgat. »The Four Basic Ways of Creating Dark Matter Through a Portal«. In: *JCAP* 05 (2012), p. 034. DOI: 10.1088/1475-7516/2012/05/034. arXiv: 1112.0493 [hep-ph].
- [407] Thomas Hambye et al. »Dark matter from dark photons: a taxonomy of dark matter production«. In: *Phys. Rev. D* 100.9 (2019), p. 095018. DOI: 10.1103/PhysRevD.100.095018. arXiv: 1908.09864 [hep-ph].

- [408] Johannes Herms and Alejandro Ibarra. »Production and signatures of multi-flavour dark matter scenarios with t-channel mediators«. In: *JCAP* 10 (2021), p. 026. DOI: 10.1088/1475-7516/2021/10/026. arXiv: 2103.10392 [hep-ph].
- [409] M. B. Voloshin. »On Compatibility of Small Mass with Large Magnetic Moment of Neutrino«. In: *Sov. J. Nucl. Phys.* 48 (1988), p. 512.
- [410] K. Enqvist, J. Maalampi and A. Masiero. »MAGNETIC MOMENTS IN THE SEESAW MODEL«. In: *Phys. Lett. B* 222 (1989), pp. 453–458. DOI: 10.1016/0370-2693(89)90343-2.
- [411] Marc Sher and Shuquan Nie. »Large electric dipole moments of heavy neutrinos«. In: *Phys. Rev. D* 65 (2002), p. 093018. DOI: 10.1103/PhysRevD.65.093018. arXiv: hep-ph/0201220.
- [412] Nicole F. Bell. »How Magnetic is the Neutrino?« In: *Int. J. Mod. Phys. A* 22 (2007). Ed. by Bruce H. J. McKellar and Raymond R. Volkas, pp. 4891–4899. DOI: 10.1142/S0217751X07038256. arXiv: 0707.1556 [hep-ph].
- [413] M. A. B. Beg, W. J. Marciano and M. Ruderman. »Properties of Neutrinos in a Class of Gauge Theories«. In: *Phys. Rev. D* 17 (1978), p. 1395. DOI: 10.1103/PhysRevD.17.1395.
- [414] J. Maalampi, K. Mursula and M. Roos. »On the Possible Evidence for a Radiatively Decaying Neutrino«. In: *Phys. Rev. Lett.* 56 (1986). Ed. by Z. Ajduk, p. 1031. DOI: 10.1103/PhysRevLett.56.1031.
- [415] Utpal Chattopadhyay and Palash B. Pal. »Radiative Neutrino Decay in Left-right Models«. In: *Phys. Rev. D* 34 (1986), p. 3444. DOI: 10.1103/PhysRevD.34.3444.
- [416] Malcolm J. Duncan et al. »Restrictions on the Neutrino Magnetic Dipole Moment«. In: *Phys. Lett. B* 191 (1987), pp. 304–308. DOI: 10.1016/0370-2693(87)90260-7.
- [417] Rabindra N. Mohapatra. »Left-right Symmetry and Finite One Loop Dirac Neutrino Mass«. In: *Phys. Lett. B* 201 (1988), pp. 517–524. DOI: 10.1016/0370-2693(88)90610-7.
- [418] Zhao-Yang Zhang et al. »Transition magnetic moment of Majorana neutrinos in the triplets next-to-minimal MSSM«. In: *Phys. Rev. D* 110.1 (2024), p. 015035. DOI: 10.1103/PhysRevD.110.015035. arXiv: 2406.18323 [hep-ph].
- [419] Long Ruan et al. »Transition magnetic moment about neutrinos«. In: (July 2024). arXiv: 2407.05741 [hep-ph].

- [420] Bolaños-Carrera, A. and Guiot-Lomelí, M. and Tavares-Velasco, G. »Neutrino charge radius and electromagnetic dipole moments via scalar and vector leptoquarks«. In: *Eur. Phys. J. C* 84.3 (2024), p. 217. DOI: 10.1140/epjc/s10052-024-12495-1. arXiv: 2308.07493 [hep-ph].
- [421] Riccardo Barbieri and Rabindra N. Mohapatra. »A Neutrino With a Large Magnetic Moment and a Naturally Small Mass«. In: *Phys. Lett. B* 218 (1989), pp. 225–229. DOI: 10.1016/0370-2693(89)91423-8.
- [422] K. S. Babu and Rabindra N. Mohapatra. »Large transition magnetic moment of the neutrino from horizontal symmetry«. In: *Phys. Rev. D* 42 (1990), pp. 3778–3793. DOI: 10.1103/PhysRevD.42.3778.
- [423] K. S. Babu and Rabindra N. Mohapatra. »Radiative fermion masses and large neutrino magnetic moment: A Unified picture«. In: *Phys. Rev. D* 43 (1991), pp. 2278–2282. DOI: 10.1103/PhysRevD.43.2278.
- [424] Stephen M. Barr, E. M. Freire and A. Zee. »A Mechanism for large neutrino magnetic moments«. In: *Phys. Rev. Lett.* 65 (1990), pp. 2626–2629. DOI: 10.1103/PhysRevLett.65.2626.
- [425] B. K. Pal. »Zee model on Majorana neutrino mass and magnetic moment«. In: *Phys. Rev. D* 44 (1991), pp. 2261–2264. DOI: 10.1103/PhysRevD.44.2261.
- [426] Manfred Lindner, Branimir Radovčić and Johannes Welter. »Revisiting Large Neutrino Magnetic Moments«. In: *JHEP* 07 (2017), p. 139. DOI: 10.1007/JHEP07(2017)139. arXiv: 1706.02555 [hep-ph].
- [427] J. Liu. »Low-energy neutrino two photon interactions«. In: *Phys. Rev. D* 44 (1991), pp. 2879–2891. DOI: 10.1103/PhysRevD.44.2879.
- [428] P. Vogel and J. Engel. »Neutrino Electromagnetic Form-Factors«. In: *Phys. Rev. D* 39 (1989), p. 3378. DOI: 10.1103/PhysRevD.39.3378.
- [429] Konstantin A. Kouzakov and Alexander I. Studenikin. »Electromagnetic properties of massive neutrinos in low-energy elastic neutrino-electron scattering«. In: *Phys. Rev. D* 95.5 (2017). [Erratum: *Phys.Rev.D* 96, 099904 (2017)], p. 055013. DOI: 10.1103/PhysRevD.95.055013. arXiv: 1703.00401 [hep-ph].
- [430] Gustavo F. S. Alves et al. »Measuring the weak mixing angle at SBND«. In: (Sept. 2024). arXiv: 2409.07430 [hep-ph].
- [431] Tarak Nath Maity and Celine Boehm. »First measurement of the weak mixing angle in direct detection experiments«. In: (Sept. 2024). arXiv: 2409.04385 [hep-ph].

- [432] M. Deniz et al. »Measurement of $\text{Nu}(e)\text{-bar}$ -Electron Scattering Cross-Section with a CsI(Tl) Scintillating Crystal Array at the Kuo-Sheng Nuclear Power Reactor«. In: *Phys. Rev. D* 81 (2010), p. 072001. DOI: 10.1103/PhysRevD.81.072001. arXiv: 0911.1597 [hep-ex].
- [433] E. Aprile et al. »Search for New Physics in Electronic Recoil Data from XENONnT«. In: *Phys. Rev. Lett.* 129.16 (2022), p. 161805. DOI: 10.1103/PhysRevLett.129.161805. arXiv: 2207.11330 [hep-ex].
- [434] Amir N. Khan. »Can Nonstandard Neutrino Interactions explain the XENON1T spectral excess?« In: *Phys. Lett. B* 809 (2020), p. 135782. DOI: 10.1016/j.physletb.2020.135782. arXiv: 2006.12887 [hep-ph].
- [435] Yu-Feng Li and Shuo-yu Xia. »Probing neutrino magnetic moments and the Xenon1T excess with coherent elastic solar neutrino scattering«. In: *Phys. Rev. D* 106.9 (2022), p. 095022. DOI: 10.1103/PhysRevD.106.095022. arXiv: 2203.16525 [hep-ph].
- [436] Thomas Schwemmer and Tien-Tien Yu. »Detecting beyond the standard model interactions of solar neutrinos in low-threshold dark matter detectors«. In: *Phys. Rev. D* 106.1 (2022), p. 015002. DOI: 10.1103/PhysRevD.106.015002. arXiv: 2202.01254 [hep-ph].
- [437] Carlo Giunti and Christoph A. Ternes. *Testing neutrino electromagnetic properties at current and future dark matter experiments*. 2023. DOI: 10.1103/PhysRevD.108.095044. arXiv: 2309.17380 [hep-ph].
- [438] Mehmet Demirci and M. Fauzi Mustamin. »Probing active-sterile neutrino transition magnetic moment on coherent elastic solar neutrino-nucleus scattering«. In: *Eur. Phys. J. C* 85.1 (2025), p. 1. DOI: 10.1140/epjc/s10052-024-13679-5. arXiv: 2412.03140 [hep-ph].
- [439] Pablo M. Candela et al. »Up-scattering production of a sterile fermion at DUNE: complementarity with spallation source and direct detection experiments«. In: *JHEP* 10 (2024), p. 032. DOI: 10.1007/JHEP10(2024)032. arXiv: 2404.12476 [hep-ph].
- [440] Matteo Cadeddu et al. »Neutrino Charge Radii From Coherent Elastic Neutrino-nucleus Scattering«. In: *Phys. Rev. D* 98.11 (2018). [Erratum: *Phys.Rev.D* 101, 059902 (2020)], p. 113010. DOI: 10.1142/9789811233913_0013. arXiv: 1810.05606 [hep-ph].
- [441] Patrick D. Bolton et al. »Probing active-sterile neutrino transition magnetic moments with photon emission from $\text{CE}\nu\text{NS}$ «. In: *Phys. Rev. D* 106.3 (2022), p. 035036. DOI: 10.1103/PhysRevD.106.035036. arXiv: 2110.02233 [hep-ph].

- [442] Amir N. Khan. » $\sin^2 \theta_W$ and neutrino electromagnetic interactions in $CE\bar{\nu}_eNS$ with different quenching factors«. In: (Mar. 2022). arXiv: 2203.08892 [hep-ph].
- [443] M. Atzori Corona et al. »Momentum dependent flavor radiative corrections to the coherent elastic neutrino-nucleus scattering for the neutrino charge-radius determination«. In: *JHEP* 05 (2024), p. 271. DOI: 10.1007/JHEP05(2024)271. arXiv: 2402.16709 [hep-ph].
- [444] Konstantin A. Kouzakov, Fedor M. Lazarev and Alexander I. Studenikin. »Electromagnetic interactions in elastic neutrino-nucleon scattering«. In: (Dec. 2024). arXiv: 2412.02169 [hep-ph].
- [445] Jihn E. Kim, V. S. Mathur and S. Okubo. »Electromagnetic properties of the neutrino from neutral-current experiments«. In: *Phys. Rev. D* 9 (1974), pp. 3050–3053. DOI: 10.1103/PhysRevD.9.3050.
- [446] Assen V. Kyuldjiev. »Searching for Effects of Neutrino Magnetic Moments at Reactors and Accelerators«. In: *Nucl. Phys. B* 243 (1984), pp. 387–397. DOI: 10.1016/0550-3213(84)90482-6.
- [447] Jiunn-Wei Chen et al. »Constraining neutrino electromagnetic properties by germanium detectors«. In: *Phys. Rev. D* 91.1 (2015), p. 013005. DOI: 10.1103/PhysRevD.91.013005. arXiv: 1411.0574 [hep-ph].
- [448] Alexander Parada and G. Sanchez Garcia. »Probing neutrino millicharges at the European Spallation Source«. In: (Sept. 2024). arXiv: 2409.10652 [hep-ph].
- [449] Manish Kumar Sharma, Saumyen Kundu and Prasanta Kumar Das. »Exploring the Electromagnetically Interacting Dark Matter at the International Linear Collider«. In: (Nov. 2023). arXiv: 2311.17220 [hep-ph].
- [450] Eung Jin Chun, Sanjoy Mandal and Rojalin Padhan. »Collider imprints of a right handed neutrino magnetic moment operator«. In: *Phys. Rev. D* 109.11 (2024), p. 115002. DOI: 10.1103/PhysRevD.109.115002. arXiv: 2401.05174 [hep-ph].
- [451] Michele Frigerio and Natascia Vignaroli. »Muon collider probes of Majorana neutrino dipole moments and masses«. In: (Sept. 2024). arXiv: 2409.02721 [hep-ph].
- [452] Luc Bojorquez-Lopez et al. »The Neutrino Slice at Muon Colliders«. In: (Dec. 2024). arXiv: 2412.14115 [hep-ph].
- [453] Vedran Brdar et al. »Collider Prospects for the Neutrino Magnetic Moment Portal«. In: (Feb. 2025). arXiv: 2502.07024 [hep-ph].

- [454] Ki-Young Choi et al. »Probing the mixing between sterile and tau neutrinos in the SHiP experiment«. In: *JHEP* 06 (2024), p. 166. DOI: 10 . 1007/JHEP06(2024)166. arXiv: 2403.04191 [hep-ph].
- [455] Rouven Essig et al. »Probing Millicharged Particles at an Electron Beam Dump with Ultralow-Threshold Sensors«. In: (Dec. 2024). arXiv: 2412.09652 [hep-ph].
- [456] Enrico Bertuzzo and Michele Frigerio. »Two portals to GeV sterile neutrinos : dipole versus mixing«. In: (Dec. 2024). arXiv: 2412.10101 [hep-ph].
- [457] Peter Sutherland et al. »Astrophysical Limitations on Possible Tensor Contributions to Weak Neutral Current Interactions«. In: *Phys. Rev. D* 13 (1976), p. 2700. DOI: 10.1103/PhysRevD.13.2700.
- [458] M. Fukugita and S. Yazaki. »Reexamination of Astrophysical and Cosmological Constraints on the Magnetic Moment of Neutrinos«. In: *Phys. Rev. D* 36 (1987), p. 3817. DOI: 10.1103/PhysRevD.36.3817.
- [459] G. G. Raffelt. »New bound on neutrino dipole moments from globular cluster stars«. In: *Phys. Rev. Lett.* 64 (1990), pp. 2856–2858. DOI: 10 . 1103/PhysRevLett.64.2856.
- [460] G. G. Raffelt. »Limits on neutrino electromagnetic properties: An update«. In: *Phys. Rept.* 320 (1999), pp. 319–327. DOI: 10.1016/S0370-1573(99)00074-5.
- [461] L. Oberauer et al. »Supernova bounds on neutrino radiative decays«. In: *Astropart. Phys.* 1 (1993), pp. 377–386. DOI: 10.1016/0927-6505(93)90004-W.
- [462] S. Arceo-Diaz et al. »Constraint on the magnetic dipole moment of neutrinos by the tip-RGB luminosity in ω -Centauri«. In: *Astropart. Phys.* 70 (2015), pp. 1–11. DOI: 10.1016/j.astropartphys.2015.03.006.
- [463] Artem Popov and Alexander Studenikin. »Neutrino eigenstates and flavour, spin and spin-flavour oscillations in a constant magnetic field«. In: *Eur. Phys. J. C* 79.2 (2019), p. 144. DOI: 10.1140/epjc/s10052-019-6657-z. arXiv: 1902.08195 [hep-ph].
- [464] Artem Popov and Alexander Studenikin. »High-energy neutrinos flavour composition as a probe of neutrino magnetic moments«. In: (Apr. 2024). arXiv: 2404.02027 [hep-ph].
- [465] Vedran Brdar et al. »Neutrino magnetic moment portal and supernovae: New constraints and multimessenger opportunities«. In: *Phys. Rev. D* 107.7 (2023), p. 073005. DOI: 10.1103/PhysRevD.107.073005. arXiv: 2302.10965 [hep-ph].

- [466] Noah Franz, Mitchell Dennis and Jeremy Sakstein. »Tip of the Red Giant Branch Bounds on the Neutrino Magnetic Dipole Moment Revisited«. In: (July 2023). arXiv: 2307.13050 [hep-ph].
- [467] Garv Chauhan et al. »Probing the sterile neutrino dipole portal with SN1987A and low-energy supernovae«. In: *Phys. Rev. D* 110.1 (2024), p. 015007. DOI: 10.1103/PhysRevD.110.015007. arXiv: 2402.01624 [hep-ph].
- [468] E. Grohs and A. B. Balantekin. »Implications on cosmology from Dirac neutrino magnetic moments«. In: *Phys. Rev. D* 107.12 (2023), p. 123502. DOI: 10.1103/PhysRevD.107.123502. arXiv: 2303.06576 [hep-ph].
- [469] Ryan Plestid. »Luminous solar neutrinos I: Dipole portals«. In: *Phys. Rev. D* 104 (2021), p. 075027. DOI: 10.1103/PhysRevD.104.075027. arXiv: 2010.04193 [hep-ph].
- [470] Tong Li, Jiajun Liao and Rui-Jia Zhang. »Dark magnetic dipole property in fermionic absorption by nucleus and electrons«. In: *JHEP* 05 (2022), p. 071. DOI: 10.1007/JHEP05(2022)071. arXiv: 2201.11905 [hep-ph].
- [471] Shao-Feng Ge and Pedro Pasquini. »Disentangle neutrino electromagnetic properties with atomic radiative pair emission«. In: *JHEP* 12 (2023), p. 083. DOI: 10.1007/JHEP12(2023)083. arXiv: 2306.12953 [hep-ph].
- [472] D. Aristizabal Sierra, N. Mishra and L. Strigari. »Implications of first neutrino-induced nuclear recoil measurements in direct detection experiments«. In: (Sept. 2024). arXiv: 2409.02003 [hep-ph].
- [473] Valentina De Romeri et al. »Neutrino electromagnetic properties and sterile dipole portal in light of the first solar CE ν NS data«. In: (Dec. 2024). arXiv: 2412.14991 [hep-ph].
- [474] Nathalie Palanque-Delabrouille et al. »Constraint on neutrino masses from SDSS-III/BOSS Ly α forest and other cosmological probes«. In: *JCAP* 02 (2015), p. 045. DOI: 10.1088/1475-7516/2015/02/045. arXiv: 1410.7244 [astro-ph.CO].
- [475] M. Aker et al. »Improved Upper Limit on the Neutrino Mass from a Direct Kinematic Method by KATRIN«. In: *Phys. Rev. Lett.* 123.22 (2019), p. 221802. DOI: 10.1103/PhysRevLett.123.221802. arXiv: 1909.06048 [hep-ex].
- [476] M. Aker et al. »Direct neutrino-mass measurement with sub-electronvolt sensitivity«. In: *Nature Phys.* 18.2 (2022), pp. 160–166. DOI: 10.1038/s41567-021-01463-1. arXiv: 2105.08533 [hep-ex].
- [477] Ziro Maki, Masami Nakagawa and Shoichi Sakata. »Remarks on the unified model of elementary particles«. In: *Prog. Theor. Phys.* 28 (1962), pp. 870–880. DOI: 10.1143/PTP.28.870.

- [478] Benjamin W. Lee and Robert E. Shrock. »Natural Suppression of Symmetry Violation in Gauge Theories: Muon - Lepton and Electron Lepton Number Nonconservation«. In: *Phys. Rev. D* 16 (1977), p. 1444. DOI: 10.1103/PhysRevD.16.1444.
- [479] S. L. Glashow, J. Iliopoulos and L. Maiani. »Weak Interactions with Lepton-Hadron Symmetry«. In: *Phys. Rev. D* 2 (1970), pp. 1285–1292. DOI: 10.1103/PhysRevD.2.1285.
- [480] L. G. Cabral-Rosetti, M. Moreno and A. Rosado. »Dirac neutrino anapole moment«. In: *AIP Conf. Proc.* 623.1 (2002). Ed. by J. Lorenzo Diaz-Cruz et al., pp. 347–350. DOI: 10.1063/1.1489777. arXiv: hep-ph/0206083.
- [481] M. Zralek. »On the possibilities of distinguishing Dirac from Majorana neutrinos«. In: *Acta Phys. Polon. B* 28 (1997). Ed. by K. Kolodziej, pp. 2225–2257. arXiv: hep-ph/9711506.
- [482] Lincoln Wolfenstein. »CP Properties of Majorana Neutrinos and Double beta Decay«. In: *Phys. Lett. B* 107 (1981), pp. 77–79. DOI: 10.1016/0370-2693(81)91151-5.
- [483] Carlo Giunti and Chung W. Kim. *Fundamentals of Neutrino Physics and Astrophysics*. Oxford University Press, Mar. 2007. ISBN: 9780198508717. DOI: 10.1093/acprof:oso/9780198508717.001.0001. URL: <https://doi.org/10.1093/acprof:oso/9780198508717.001.0001>.
- [484] Shinya Kanemura and Kei Yagyu. »Radiative corrections to electroweak parameters in the Higgs triplet model and implication with the recent Higgs boson searches«. In: *Phys. Rev. D* 85 (2012), p. 115009. DOI: 10.1103/PhysRevD.85.115009. arXiv: 1201.6287 [hep-ph].
- [485] P. Duka, J. Gluza and M. Zralek. »Quantization and renormalization of the manifest left-right symmetric model of electroweak interactions«. In: *Annals Phys.* 280 (2000), pp. 336–408. DOI: 10.1006/aphy.1999.5988. arXiv: hep-ph/9910279.
- [486] Miha Nemevsek et al. »First Limits on Left-Right Symmetry Scale from LHC Data«. In: *Phys. Rev. D* 83 (2011), p. 115014. DOI: 10.1103/PhysRevD.83.115014. arXiv: 1103.1627 [hep-ph].
- [487] John F. Donoghue and Barry R. Holstein. »STRONG BOUNDS ON WEAK COUPLINGS«. In: *Phys. Lett. B* 113 (1982), pp. 382–386. DOI: 10.1016/0370-2693(82)90769-9.
- [488] Rabindra N. Mohapatra and Shmuel Nussinov. »CONSTRAINTS ON DECAYING RIGHT-HANDED MAJORANA NEUTRINOS FROM SN1987a OBSERVATIONS«. In: *Phys. Rev. D* 39 (1989), pp. 1378–1385. DOI: 10.1103/PhysRevD.39.1378.

- [489] Georges Aad et al. »Searches for new phenomena in events with two leptons, jets, and missing transverse momentum in 139 fb⁻¹ of $\sqrt{s} = 13$ TeV $p\bar{p}$ collisions with the ATLAS detector«. In: *Eur. Phys. J. C* 83.6 (2023), p. 515. DOI: 10.1140/epjc/s10052-023-11434-w. arXiv: 2204.13072 [hep-ex].
- [490] M. Carena et al. »MSSM Higgs Boson Searches at the LHC: Benchmark Scenarios after the Discovery of a Higgs-like Particle«. In: *Eur. Phys. J. C* 73.9 (2013), p. 2552. DOI: 10.1140/epjc/s10052-013-2552-1. arXiv: 1302.7033 [hep-ph].
- [491] Georges Aad et al. »Search for charged Higgs bosons decaying via $H^\pm \rightarrow \tau^\pm \nu$ in fully hadronic final states using pp collision data at $\sqrt{s} = 8$ TeV with the ATLAS detector«. In: *JHEP* 03 (2015), p. 088. DOI: 10.1007/JHEP03(2015)088. arXiv: 1412.6663 [hep-ex].
- [492] Morad Aaboud et al. »Search for charged Higgs bosons decaying via $H^\pm \rightarrow \tau^\pm \nu_\tau$ in the τ +jets and τ +lepton final states with 36 fb⁻¹ of pp collision data recorded at $\sqrt{s} = 13$ TeV with the ATLAS experiment«. In: *JHEP* 09 (2018), p. 139. DOI: 10.1007/JHEP09(2018)139. arXiv: 1807.07915 [hep-ex].
- [493] I. Doršner et al. »Physics of leptoquarks in precision experiments and at particle colliders«. In: *Phys. Rept.* 641 (2016), pp. 1–68. DOI: 10.1016/j.physrep.2016.06.001. arXiv: 1603.04993 [hep-ph].
- [494] W. Buchmuller, R. Ruckl and D. Wyler. »Leptoquarks in Lepton - Quark Collisions«. In: *Phys. Lett. B* 191 (1987). [Erratum: *Phys.Lett.B* 448, 320–320 (1999)], pp. 442–448. DOI: 10.1016/0370-2693(87)90637-x.
- [495] A. Bolaños, R. Sánchez-Vélez and G. Tavares-Velasco. »Flavor changing neutral current decays $t \rightarrow cX$ ($X = \gamma, g, Z, H$) and $t \rightarrow c\bar{\ell}\ell$ ($\ell = \mu, \tau$) via scalar leptoquarks«. In: *Eur. Phys. J. C* 79.8 (2019), p. 700. DOI: 10.1140/epjc/s10052-019-7211-8. arXiv: 1907.05877 [hep-ph].
- [496] A. Bolaños-Carrera, R. Sánchez-Vélez and G. Tavares-Velasco. »Rare decay $t \rightarrow c\gamma\gamma$ via scalar leptoquark doublets«. In: *Phys. Rev. D* 107.9 (2023), p. 095018. DOI: 10.1103/PhysRevD.107.095018. arXiv: 2208.05064 [hep-ph].
- [497] Luca Di Luzio, Admir Greljo and Marco Nardecchia. »Gauge leptoquark as the origin of B-physics anomalies«. In: *Phys. Rev. D* 96.11 (2017), p. 115011. DOI: 10.1103/PhysRevD.96.115011. arXiv: 1708.08450 [hep-ph].
- [498] Albert M Sirunyan et al. »Search for pair production of first-generation scalar leptoquarks at $\sqrt{s} = 13$ TeV«. In: *Phys. Rev. D* 99.5 (2019), p. 052002. DOI: 10.1103/PhysRevD.99.052002. arXiv: 1811.01197 [hep-ex].

- [499] Albert M Sirunyan et al. »Search for pair production of second-generation leptoquarks at $\sqrt{s} = 13$ TeV«. In: *Phys. Rev. D* 99.3 (2019), p. 032014. DOI: 10.1103/PhysRevD.99.032014. arXiv: 1808.05082 [hep-ex].
- [500] Albert M Sirunyan et al. »Search for leptoquarks coupled to third-generation quarks in proton-proton collisions at $\sqrt{s} = 13$ TeV«. In: *Phys. Rev. Lett.* 121.24 (2018), p. 241802. DOI: 10.1103/PhysRevLett.121.241802. arXiv: 1809.05558 [hep-ex].
- [501] Albert M Sirunyan et al. »Search for third-generation scalar leptoquarks decaying to a top quark and a τ lepton at $\sqrt{s} = 13$ TeV«. In: *Eur. Phys. J. C* 78 (2018), p. 707. DOI: 10.1140/epjc/s10052-018-6143-z. arXiv: 1803.02864 [hep-ex].
- [502] Albert M Sirunyan et al. »Search for singly and pair-produced leptoquarks coupling to third-generation fermions in proton-proton collisions at $s=13$ TeV«. In: *Phys. Lett. B* 819 (2021), p. 136446. DOI: 10.1016/j.physletb.2021.136446. arXiv: 2012.04178 [hep-ex].
- [503] Armen Tumasyan et al. »Inclusive nonresonant multilepton probes of new phenomena at $\sqrt{s}=13$ TeV«. In: *Phys. Rev. D* 105.11 (2022), p. 112007. DOI: 10.1103/PhysRevD.105.112007. arXiv: 2202.08676 [hep-ex].
- [504] Georges Aad et al. »Search for pairs of scalar leptoquarks decaying into quarks and electrons or muons in $\sqrt{s} = 13$ TeV pp collisions with the ATLAS detector«. In: *JHEP* 10 (2020), p. 112. DOI: 10.1007/JHEP10(2020)112. arXiv: 2006.05872 [hep-ex].
- [505] Georges Aad et al. »Search for pair production of scalar leptoquarks decaying into first- or second-generation leptons and top quarks in proton-proton collisions at $\sqrt{s} = 13$ TeV with the ATLAS detector«. In: *Eur. Phys. J. C* 81.4 (2021), p. 313. DOI: 10.1140/epjc/s10052-021-09009-8. arXiv: 2010.02098 [hep-ex].
- [506] Georges Aad et al. »Search for new phenomena in pp collisions in final states with tau leptons, b-jets, and missing transverse momentum with the ATLAS detector«. In: *Phys. Rev. D* 104.11 (2021), p. 112005. DOI: 10.1103/PhysRevD.104.112005. arXiv: 2108.07665 [hep-ex].
- [507] Georges Aad et al. »Search for supersymmetry in final states with missing transverse momentum and charm-tagged jets using 139 fb^{-1} of proton-proton collisions at $\sqrt{s} = 13$ TeV with the ATLAS detector«. In: (Oct. 2024). arXiv: 2410.17824 [hep-ex].
- [508] Arghya Choudhury, Arpita Mondal and Subhadeep Mondal. »Status of R-parity violating SUSY«. In: (Feb. 2024). DOI: 10.1140/epjs/s11734-024-01100-x. arXiv: 2402.04040 [hep-ph].

- [509] Georges Aad et al. »Search for supersymmetry in events with four or more charged leptons in 139 fb^{-1} of $\sqrt{s} = 13 \text{ TeV}$ pp collisions with the ATLAS detector«. In: *JHEP* 07 (2021), p. 167. DOI: 10.1007/JHEP07(2021)167. arXiv: 2103.11684 [hep-ex].
- [510] Peter Richardson. »Simulations of R-parity Violating SUSY Models«. PhD thesis. Oxford U., 2000. arXiv: hep-ph/0101105.
- [511] R. Barbier et al. »Report of the group on the R-parity violation«. In: (Oct. 1998). arXiv: hep-ph/9810232.
- [512] R. Barbier et al. »R-parity violating supersymmetry«. In: *Phys. Rept.* 420 (2005), pp. 1–202. DOI: 10.1016/j.physrep.2005.08.006. arXiv: hep-ph/0406039.
- [513] Francesca Borzumati et al. »Lightest neutralino decays in R(p) violating models with dominant lambda-prime and lambda couplings«. In: *JHEP* 07 (2002), p. 037. DOI: 10.1088/1126-6708/2002/07/037. arXiv: hep-ph/0108244.
- [514] Gabriel Magill et al. »Millicharged particles in neutrino experiments«. In: *Phys. Rev. Lett.* 122.7 (2019), p. 071801. DOI: 10.1103/PhysRevLett.122.071801. arXiv: 1806.03310 [hep-ph].
- [515] Liron Barak et al. »Search by the SENSEI Experiment for Millicharged Particles Produced in the NuMI Beam«. In: *Phys. Rev. Lett.* 133.7 (2024), p. 071801. DOI: 10.1103/PhysRevLett.133.071801. arXiv: 2305.04964 [hep-ex].
- [516] Giacomo Marocco and Subir Sarkar. »Blast from the past: Constraints on the dark sector from the BEBC WA66 beam dump experiment«. In: *SciPost Phys.* 10.2 (2021), p. 043. DOI: 10.21468/SciPostPhys.10.2.043. arXiv: 2011.08153 [hep-ph].
- [517] Céline Boehm, Matthew J. Dolan and Christopher McCabe. »A Lower Bound on the Mass of Cold Thermal Dark Matter from Planck«. In: *JCAP* 08 (2013), p. 041. DOI: 10.1088/1475-7516/2013/08/041. arXiv: 1303.6270 [hep-ph].
- [518] Cyril Creque-Sarbinowski et al. »Direct millicharged dark matter cannot explain the EDGES signal«. In: *Phys. Rev. D* 100.2 (2019), p. 023528. DOI: 10.1103/PhysRevD.100.023528. arXiv: 1903.09154 [astro-ph.CO].
- [519] Sacha Davidson, Steen Hannestad and Georg Raffelt. »Updated bounds on millicharged particles«. In: *JHEP* 05 (2000), p. 003. DOI: 10.1088/1126-6708/2000/05/003. arXiv: hep-ph/0001179.
- [520] Jae Hyeok Chang, Rouven Essig and Samuel D. McDermott. »Supernova 1987A Constraints on Sub-GeV Dark Sectors, Millicharged Particles, the QCD Axion, and an Axion-like Particle«. In: *JHEP* 09 (2018), p. 051. DOI: 10.1007/JHEP09(2018)051. arXiv: 1803.00993 [hep-ph].

- [521] Changqian Li et al. »Low-Energy Supernova Constraints on Millicharged Particles«. In: (Aug. 2024). arXiv: 2408.04953 [hep-ph].
- [522] M. Battaglieri et al. »Dark matter search in a Beam-Dump eXperiment (BDX) at Jefferson Lab«. In: (June 2014). arXiv: 1406.3028 [physics.ins-det].
- [523] M. Battaglieri et al. »Dark Matter Search in a Beam-Dump eXperiment (BDX) at Jefferson Lab«. In: (July 2016). arXiv: 1607.01390 [hep-ex].
- [524] D. Snowden-Ifft et al. »Beam-Dump Dark Matter Search Utilizing a Low-Threshold, Directional Dark Matter Detector (BDX-DRIFT) at Jefferson Lab«. In: 2019. URL: <https://api.semanticscholar.org/CorpusID:210924875>.
- [525] Anja Sabine Brenner. »Model- and halo-independent limits on the dark matter-nucleon interaction«. PhD thesis. Munich, Tech. U., 2023.
- [526] E. Aprile et al. »Search for Light Dark Matter Interactions Enhanced by the Migdal Effect or Bremsstrahlung in XENON1T«. In: *Phys. Rev. Lett.* 123.24 (2019), p. 241803. DOI: 10.1103/PhysRevLett.123.241803. arXiv: 1907.12771 [hep-ex].
- [527] Sunghyun Kang et al. »Present and projected sensitivities of Dark Matter direct detection experiments to effective WIMP-nucleus couplings«. In: *Astropart. Phys.* 109 (2019), pp. 50–68. DOI: 10.1016/j.astropartphys.2019.02.006. arXiv: 1805.06113 [hep-ph].
- [528] G. Passarino and M. J. G. Veltman. »One Loop Corrections for $e^+ e^-$ Annihilation Into $\mu^+ \mu^-$ in the Weinberg Model«. In: *Nucl. Phys. B* 160 (1979), pp. 151–207. DOI: 10.1016/0550-3213(79)90234-7.
- [529] Federico Ambrogio et al. »MadDM v.3.0: a Comprehensive Tool for Dark Matter Studies«. In: *Phys. Dark Univ.* 24 (2019), p. 100249. DOI: 10.1016/j.dark.2018.11.009. arXiv: 1804.00044 [hep-ph].
- [530] P. Gondolo et al. »DarkSUSY: Computing supersymmetric dark matter properties numerically«. In: *JCAP* 07 (2004), p. 008. DOI: 10.1088/1475-7516/2004/07/008. arXiv: astro-ph/0406204.
- [531] J. Alwall et al. »The automated computation of tree-level and next-to-leading order differential cross sections, and their matching to parton shower simulations«. In: *JHEP* 07 (2014), p. 079. DOI: 10.1007/JHEP07(2014)079. arXiv: 1405.0301 [hep-ph].